Dipl.-Ing. Benjamin Lang, BSc.

Photoacoustic and Photothermal Absorption Spectroscopy in Humidity and Water Content Measurement

DOCTORAL THESIS

to achieve the university degree of

Doktor der Technischen Wissenschaften

submitted to

Graz University of Technology

Supervisor:

Univ.-Prof. Mag.rer.nat.Dr.rer.nat. Alexander Bergmann
Institute of Electrical Measurement and Sensor Systems

Graz, November 2020

AFFIDAVIT

I declare that I have authored this thesis independently, that I have not used other than the declared sources/resources, and that I have explicitly indicated all material which has been quoted either literally or by content from the sources used. The text document uploaded to TUGRAZonline is identical to the present doctoral thesis.

Dipl.-Ing. Benjamin Lang, BSc.
Graz, November 2020

ACKNOWLEDGEMENTS

I want to gratefully acknowledge and sincerely thank my supervisor, Alexander Bergmann, for giving me the opportunity of conducting this Ph.D. thesis and for the tireless sharing of his knowledge and interest. I would like to express my deepest gratitude for the thoughtful, carefully considered guidance, the personal encouragement and the inordinate amount of time he has given me to conclude this thesis. The unique and encouraging working environment he created and maintained throughout the years has given me countless opporunities to learn in every possible way.

I want thank all colleagues and friends at the Institute of Electrical Measurement and Sensor Systems, Alex, Anton, Georg, Johanna, Julia, Mario, Markus B., Markus K., Martin, Monika, Paul, Philipp, Reinhard, Sitaram, Stefan, Tanja, Thomas, Theresa and Ulrich, for the inspired ideas, the stimulating discussions, the consistent support, the shared knowledge and laughs. I would also like to thank Esther, Julia and Sitaram for their technical and administrative support. In particular, I thank Martin for the open and honest discussions and the time spent after work or on weekends. I also want to thank Philipp for his guidance and expertise, openly shared with me during the countless discussions.

I also would like to express my gratitude to all my former colleagues from the Institute of Aviation at FH Joanneum and from TRN at AVL, first and foremost, Andreas K., Andreas T., Lukas, Jordi, Reinhard, Simon, Stefan, Wolfgang B. and Wolfgang H.. They all have contributed to me enjoying the time at both places and have continuously shared their expertise and support. I am also grateful to the people involved, for making AquaSense and this dissertation possible. At this point I would also like to thank the staff of RTA, especially Hermann, Michael and Wolfgang B. for their support while preparing and conducting the AquaSense measurements at their facility, as well as for their shared expertise with regard to AquaPhase and JOICE.

I want to thank my family for their support and encouraging words throughout. And most of all, I thank my wife, Katrin, for her seemingly endless patience, joy and love.

ABSTRACT

Certification of aircraft for flight in icing conditions has crucial safety relevance, as fuselage, wing, rotor, engine or air data probe icing may heavily impact performance, stability and operation. On that account, international aviation authorities require certification for intentional and inadvertent flight into icing conditions. Recent recognition of the risk arising from several hazardous meteorological conditions has led to legislation changes in icing certification requirements, leading to a corresponding demand for suitable water content measurement instrumentation at certification facilities.

This thesis has been carried out with the goal of contributing to the advancement of accurate reference instrumentation for experimentally simulated icing conditions containing significant fractions of supercooled drops greater than 50 µm in diameter (supercooled large drops, SLDs). As part of the FFG TAKEOFF project AquaSense, the development of an isokinetic evaporator probe sampling system in combination with precision hygrometers for condensed water content measurement in such icing wind tunnel-generated cloud and precipitation conditions was carried out. Main focus was put on the development, theoretical description, as well as laboratory and field characterization of the hygrometer integrated in the newly developed instrument, which employs near-infrared diode laser-based photoacoustic spectroscopy, promising to fulfill measurement requirements in accuracy, dynamic range, selectivity and robustness. A considerable part addresses the previously unsatisfactorily described collisional relaxation phenomena of water vapor in air in the photoacoustic signal generation process, which give rise to increased complexity in the calibration process of photoacoustic, as well as photothermal hygrometers. By introducing a theoretical description of these processes, a reproducible prediction of the sensitivity of photoacoustic and photothermal water vapor gas analyzers has been achieved, where the latter detection principle is also shown to provide an alternative, fast response optical gas sensing technique, which can provide the necessary accuracy and operating range, and offers potential for size reduction down to miniaturization.

By intercomparison with state-of-the-art isokinetic evaporator and hot-wire-based water content instrumentation, together with evaluation of the measurement uncertainties of the final instrument and the individual components, achievable accuracies equivalent to the reference isokinetic probe instrumentation have been demonstrated in SLD conditions. Showing partial fulfillment with the demanding accuracy requirements of the targeted certification conditions

and recommended icing wind tunnel calibration practices proves the suitability of the device and the technology to water content measurement in aviation certification-relevant simulated atmospheric icing environments.

TABLE OF CONTENTS

LIST OF FIGURES

NOMENCLATURE

Acronyms / Abbreviations

AM	Amplitude Modulation
ARP	Aerospace Recommended Practice
BWV	Background Water Vapor
CEPAS	Cantilever-Enhanced Photoacoustic Spectroscopy
CFD	Computational Fluid Dynamics
CRDS	Cavity Ring-Down Spectroscopy
CWC	(Total) Condensed Water Content
CW	Continuous Wave
DFB	Distributed Feedback
EASA	European Aviation Safety Agency
FAA	Federal Aviation Administration
FPE	Fabry-Pérot Etalon
ICI	Ice Crystal Icing
IKP	Isokinetic Evaporator Probe
IR	Infrared
IWC	Ice Water Content
IWT	Icing Wind Tunnel
LII	Light Induced Incandescence
LWC	Liquid Water Content
NDIR	Non-Dispersive Infrared
NIR	Near Infrared
NNEA	Normalized Noise-Equivalent Asorption Coefficient
PA	Photoacoustic

PAS	Photoacoustic Spectroscopy
PTS	Photothermal Spectroscopy
QEPAS	Quartz-Enhanced Photoacoustic Spectroscopy
RTA	Rail Tech Arsenal (Fahrzeugversuchsanlage GmbH)
SCR	Computational Fluid Dynamics
SLD	Supercooled Large Drop
slpm	Standard Liter Per Minute (unit; reference conditions: 273.15 K and 1013.25 hPa)
SNR	Signal-to-Noise Ratio
TDLAS	Tunable Diode Laser Absorption Spectroscopy
TWC	Total Water Content
UV	Ultra-Violet
VIS	Visible
WM	Wavelength Modulation

PREFACE

This thesis consists of two parts. In Part I, Chapter 1 first presents the aircraft icing related motivation, aims and the scope of the thesis. Chapters 2 and 3 provide some theoretical background to the spectroscopic methods and an overview of the experimental methods behind the application specific implementation. These chapters are intended to give a coarse background to the results put forward in the second part of the thesis. The discussion and outlook given in Chapters 4 and 5, and this thesis in general, are based on the following publications, presented in Part II, which are published in or submitted to international peer-reviewed journals:

Paper I Lang, B., Breitegger, P., Brunnhofer, G. et al.: Molecular relaxation effects on vibrational water vapor photoacoustic spectroscopy in air. Appl. Phys. B 126, 64, doi.org/10.1007/s00340-020-7409-3, 2020.

Paper II Lang, B., Breitfuss, W., Schweighart, S. et al.: Photoacoustic hygrometer for icing wind tunnel water content measurement: Design, analysis and intercomparison, Atmos. Meas. Tech. Discuss., doi.org/10.5194/amt-2020-295, in review, 2020.

Paper III Breitegger, P., Lang, B. and Bergmann, A.: Intensity Modulated Photothermal Measurements of NO2 with a Compact Fiber-Coupled Fabry–Pérot Interferometer, Sensors, 19(15), 3341, doi.org/10.3390/s19153341, 2019.

Paper I and **Paper III** have undergone a peer-review process and are published. **Paper II** is, at the time of submission of this thesis, still in peer-review and is published as a pre-print only (the version attached). The contributions of this thesis' author to the mentioned publications are stated directly before each article in Part II. Other additional scientific contributions are listed in Appendix A.

Part I

Preamble

CHAPTER 1

INTRODUCTION

1.1 Motivation

Measurement and quantification of atmospheric water in its various forms is a fundamental task, common to many scientific questions and engineering applications. Aside from the key importance of water in countless microscopic and macroscopic atmospheric and climatic processes, as well as Earth's radiation budget [4–7], atmospheric water in the global water cycle substantially affects man-made structures, devices and vehicles (power plants and lines, road traffic, marine vessels, aircraft, etc.) when deposited as ice on these objects [8–11]. In-flight aircraft icing, in particular, has crucial safety relevance, as fuselage, wing, rotor, engine or air data probe icing may heavily impact aerodynamic or thrust performance, stability and the operation of an aircraft and, in the fortunately infrequent worst case, may cause full loss of control with a fatal outcome [12–17]. On that account, international aviation authorities require certification for intentional and inadvertent flight into icing conditions [18, 19]. Recognition and characterization of additional hazardous conditions [12, 20–22] has advanced the fundamental understanding of atmospheric processes and has led to changes in the certification requirements for large airplanes in 2015 [23, 24]. The interest concerning previously insufficiently characterized conditions [25] has initiated an advancement and development of airborne measurement instrumentation and technology better capable of detecting and characterizing related meteorological and cloud microphysical conditions in the atmosphere [26–29]. In addition to airborne characterization, measurement equipment is required ensuring accurate replication of such conditions within on-ground test infrastructure used for certification, validation and development of aerodynamic components, general air data probes, ice detection and ice protection systems [30], as well as for fundamental icing research [31]. The repeatable and reproducible experimental simulation of representative test environments highly benefits the continuous performance optimization of many aircraft components, e.g., the development of safe and energy-efficient ice protection systems, resulting in demanded reductions in fuel consumption and emissions. Similar energy-efficient solutions are sought for in power plant applications (i.e., wind turbines) and require testing and validation in controlled environments [32]. Experimental simulation means moreover prove valuable for fast and less expensive gathering of ice accretion data, advancing the development and validation of three-dimensional numerical ice accretion models, codes and tools necessary for the future cost-effective development and optimization of reliable, safe and efficient aircraft [33–35].

1.2 Problem Statement

Icing Wind Tunnel Calibration

Several meteorological conditions mainly responsible for ice accretion on aircraft are currently known, well documented and, to a large extent, covered by certification regulations. Historically, regulatory specifications of atmospheric icing conditions (envelopes) by aviation authorities first encompassed "classical" icing, i.e., accretion of cloud supercooled liquid water droplets with mean effective diameters in the range of 15 to 50 µm, covering a major part of icing environments encountered during regular flight [13, 16]. These metastable supercooled cloud droplets occur at temperatures between approximately 0 to −40 °C in the absence of ice nuclei and fully or partially freeze upon impact, thereby accreting on the aircraft surfaces [31]. The certification relevant icing envelopes, divided into continuous maximum and intermittent maximum icing intensities and, among others, defined by the cloud variables of air temperature, droplet size and liquid water content (LWC; typically given in $\mathrm{g\,m^{-3}}$), are defined in Appendix C of the European Aviation Safety Agency Certification Specifications 25 (EASA CS-25) [18] and the US Federal Aviation Administration Code of Federal Regulations Title 14 Part 25 (FAA CFR-25) [19]. Aircraft manufacturers need to demonstrate by test and analysis acceptable operation within these icing envelopes. Tests conducted in icing wind tunnels (IWTs) with experimentally simulated icing, typically generated by air-water spray nozzles, is one accepted means of showing compliance [18]. For such IWT facilities involved in the calibration process, it is necessary to repeatably verify adherence to the specified conditions during tests (droplet spectra, LWC and spatial uniformity, etc.) by calibration according to Aerospace Recommended Practices (SAE ARP5905) [18], which define maximum uncertainties and required measurement instrumentation [36]. Regarding Appendix C conditions, the ARP requires an LWC instrumentation combined measurement uncertainty smaller than ±10 % [36].

Research following accidents in environments of freezing precipitation containing supercooled large drops (SLDs; maximum drop diameters greater than 50 µm, up to 3 mm) has led to the detailed characterization [13, 37, 38, 20] and, in 2015, to the uptake of SLD conditions into certification requirements for large airplanes (Appendix O of EASA CS-25 and of CFR-25) [23, 24]. The severe icing risk by SLDs arises due to the larger inertia, which reduces the aerodynamic diversion of large droplets around lifting surfaces and results in accretion behind ice protection systems usually placed at the leading edges [14, 16, 39]. Measurement of liquid water content in such environments (airborne and on ground) with conventional methods and instrumentation has proven difficult [40, 41]. These integral methods, described in the SAE ARP5905 [36], encompass ice accretion blades and cylinders for mere LWC measurement, as well as evaporating hot-wire sensors, typically used in multi-element configurations targeting the simultaneous LWC and total condensed water content (CWC; combined liquid and ice water content). The former are used to infer the LWC from the ice thickness accumulated on a standardized geometry and, thus, do not allow a time-resolved measurement and exhibit splashing losses for larger drops such as SLDs [42, 43]. Similar losses by re-entrainment and inaccuracies are known to exist for hot-wire instruments, which are used to infer the liquid and total condensed water content from evaporation of droplets and ice particles upon impact on differently shaped surfaces [42, 44, 45, 28]. The lack of suitable LWC measurement technology for IWT facility simulating Appendix O SLD environments, together with issues in sufficiently supercooling, secondary break-up, spatial distribution, as well as size distributions of large droplets, has led to the situation that it is hardly possible for such facilities and aircraft manufacturers to comply with current regulations [43, 46–49]. To date, only few facilities capable of simulating SLD environments exist. To address the need of suitable water content measurement technology with adequate temporal resolution and precision, the FFG TAKEOFF project AquaSense [50] was started in 2015, as part of which this thesis has been conducted.

Initiated by aviation industry working groups (Ice Protection and Engine Harmonization Working Groups) [41], international scientific and regulatory focus in the last decade has extended towards high ice water content (IWC) mixed phase (liquid droplets and ice crystals) and fully glaciated ice crystal icing (ICI) conditions with peak CWCs of $9\,\mathrm{g\,m^{-3}}$, found in mesoscale convective cloud systems [51, 21, 18], which have been recognized to cause jet engine power loss and damage, as well as air data probe failures upon ingestion and accumulation at stagnation points [12]. As in SLD environments, evaporating hot-wire instrumentation is considered partly inadequate for IWC environments, as bouncing of ice crystals off of the evaporating elements is well documented [41, 42, 52, 44, 45, 27]. Although only few icing test facilities have been capable of simulating these icing conditions [33], corresponding envelopes and certification specifications of both EASA (CS-25 Appendix P [23]) and FAA (CFR-33 Appendix D [53]) for mixed phase and ice crystal icing have been introduced in 2015 together with the SLD specifications, thus still increasing the demand for appropriate water content measurement equipment.

Water Content and Humidity Instrumentation

The request for reliable and accurate cloud water mass concentration instrumentation for the in-flight characterization and icing test facility replication of SLD and high ice water content conditions triggered the development of new benchmark humidity sensing-based isokinetic evaporator probe (IKP) instruments, one generation of devices by a North American cooperation (NRC Canada, SEA Inc., NASA) [54–58] and a single device in Europe (Cranfield University) [33]. The IKPs are used in combination with hygrometers, non-dispersive infrared (NDIR) H_2O/CO_2 gas analyzers operated at 2.595 µm/4.255 µm (LI-COR Inc. [59]) [39, 58], measuring the total water vapor concentration after evaporation of droplets and/or ice particles entering the isokinetically operated inlet. Isokinetic sampling, i.e., representative sampling of ambient air and hydrometeors, minimizes hydrometeor size dependence of the measurement and eliminates the possibility of re-entrainment into the flow after capture [45]. From the total water content measurement, which includes the water vapor concentration of the (humid) ambient air, the combined cloud liquid and ice water content is calculated by subtraction of the separately determined ambient air water vapor mass concentration. Although much-needed in icing, as well as atmospheric sciences [60], phase discrimination, i.e., separate measurement of LWC and IWC, cannot be achieved with this method.

Current compact and fast-response commercialized realizations of NDIR gas analyzers provide the required water vapor concentration short-term accuracy and the required measurement range of 50 to 20,000 ppm (ppm = $\mu\text{mol}\,\text{mol}^{-1}$) for high ice water content measurement [2], as well as other airborne humidity sensing applications [61]. However, reported baseline drifts [58] and the CO_2 cross-sensitivity characteristic of NDIR sensors raise questions about long-term stability. Apart from the aforementioned IKP instruments, only a handful of similar extractively sampling and evaporating devices with accompanying hygrometers are in operation for TWC measurement and, applying different humidity measurement principles, are mostly tailored to specific atmospheric research needs. Overviews about existing instruments are given by [45, 60] and a comparison of applied state-of-the art hygrometers can be found in [62]. Common hygrometers for atmospheric sensing are based on chilled mirrors (dew-/frost-point hygrometers), UV-absorption/fluorescence (Lyman-α hygrometers) and NIR-absorption (tunable diode laser absorption spectroscopy, TDLAS; cavity ring-down spectroscopy, CRDS). Chilled mirror hygrometers offer accurate humidity measurement combined with a wide dynamic range, but typical response times of several seconds are considered insufficient for atmospheric measurement, as well as sub-optimal for IWT water content control [56]. Implementations of Lyman-α hygrometers designed for aircraft applications achieve response times in the order of 1 s [63–66] with the required accuracy and, in the case of non-fluorescence-based realizations, the dynamic water vapor mixing ratio range needed for IWT total condensed water content measurement [63, 67]. However, required correction for oxygen cross-sensitivity and reported frequent issues with drifts caused by UV source instability and window degradation [68] have resulted in the development of various NIR-absorption based optical hygrometers as alternatives with comparable accuracy at water vapor concentrations greater 10 ppm [62]. TDLAS instruments employing wavelength-modulation with second-harmonic detection in atmospheric sensing have achieved interference-free water vapor detection over four orders of magnitude and accuracies better than 5 % [69–73], covering the required measurement range and necessary accuracy for IWT application. Wavelength-scanning cavity ring-down instruments and related cavity-enhanced absorption spectrometers suited for field-application exhibit performances similar to TDLAS devices [74–77] and can also be considered appropriate for IWT water content measurement.

In AquaSense, photoacoustic spectroscopy (PAS) has been identified as a viable alternative technique for humidity sensing in IWT water content measurement, promising to fulfill the spectroscopic requirements in accuracy, dynamic range, selectivity and robustness. A first realization of a NIR distributed feedback (DFB) laser diode based instrument demonstrated minimum detectable water vapor concentrations below 1 ppm and a dynamic range of four orders of magnitudes [78–82], thus indicating the feasibility of the technique for water content measurement. Primarily applied in trace gas measurement, photoacoustic (PA) gas analyzers employing comparably cheap acoustic resonators and transducers exhibit some significant advantages over purely optical transmission-based techniques. The disappearing need for cost-expensive cooled photodetectors and multi-pass setups combines with the potential for compact or miniaturized implementations, which cannot be achieved with transmission-based methods where the sensitivity intrinsically depends on the absorption path length.

An instrument combining a photoacoustic hygrometer with an isokinetic sampling system has thus been determined to fulfill the requirements of an accurate, robust and cost-effective tool for icing wind tunnel water content measurement in SLD and high IWC conditions. For the development of the hygrometer, the following additional requirements have been determined:

- Response times comparable to purely optical methods, enabling the real-time monitoring of IWT water content.
- Integrated means for frequent recalibration of the hygrometer over the full dynamic range, providing the necessary short- and long-term accuracy and repeatability.
- Acoustic insulation from noise generated by the wind tunnel air flow, as well as spray nozzles, enabling necessary limits of quantification and accuracy.

As PAS is also applied in condensed matter spectroscopy, concepts for combining mass concentration measurements with phase discrimination (vapor, liquid and ice) have been studied in this thesis and the research project AquaSense initially, intending an open photoacoustic cell and multiple laser sources targeting the different thermodynamic phases. This concept was abandoned early on, due to the impracticable application of photoacoustic resonators in the harsh and noise-laden IWT environment.

1.3 Scope of the Thesis

The top-level aim of this thesis was the development of a liquid, ice and total water content measurement device suitable for experimentally simulated cloud or cloud-like environments, as present in icing wind tunnels. Such a system was designed with the requirement of comprising a sampling strategy appropriate for water content assessment in SLD environments. The new instrument in the form of an isokinetic evaporator probe combined with a photoacoustic gas analyzer (hygrometer), was built, evaluated and applied in an icing wind tunnel measurement and instrumentation intercomparison campaign in the course of the research project AquaSense. The results presented in this thesis demonstrate equivalent achievable accuracies as state-of-the-art instrumentation, proving the suitability of the device and the technology to water content measurement in (simulated) atmospheric icing environments as used in aviation certification, thereby providing an additional measuring tool for the characterization of such environments.

The majority of the effort of this thesis was put into the development, theoretical description, as well as laboratory and field characterization of the main component of the water content measurement system, the photoacoustic hygrometer. A considerable part addresses the description of a so far undocumented nonlinear response occurring in the photoacoustic measurement of water vapor in air, which gives rise to increased complexity in the calibration process of photoacoustic hygrometers. The development of a practical and application-oriented theoretical model, describing the thermal energy transfer in photoacoustic signal generation, aims at facilitating the calibration procedure and should be useful not only for the measurement of water vapor in air, but also for other gas sensing applications employing photoacoustic or photothermal spectroscopy.

In the third and last part of this thesis, the application of photothermal spectroscopy using a vibration-insensitive, rigid Fabry-Pérot interferometer-based sensing approach for the measurement of water vapor is investigated on the basis of experiments with nitrogen dioxide as a test gas. This concept targets the performance evaluation of an alternative fast response optical gas sensing technique for water vapor, which can provide the necessary operating range and with the potential for size reduction down to miniaturization.

CHAPTER 2

BACKGROUND TO PHOTOACOUSTIC AND PHOTOTHERMAL WATER VAPOR SPECTROSCOPY

This chapter aims at providing some theoretical background of the spectroscopic methods applied in this thesis. All descriptions and explanations are confined to the spectroscopy of gaseous samples, although, some parts may be applicable to liquid and solid samples as well. Determination of gaseous molecular concentrations using photoacoustic and photothermal spectroscopy is based on the measurement of pressure and refractive index changes that occur upon heating of a gas sample through the absorption of electromagnetic radiation. Figure 2.1 gives a simplified overview of the chain of processes involved in the signal generation and detection in the two methods.

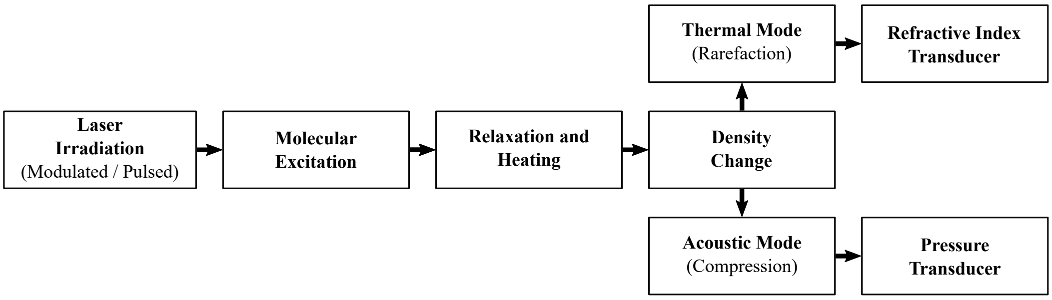

Fig. 2.1 Schematic of the signal generation and detection sequence in PAS and PTS.

The basic sequence is common to both methods. In state of the art implementations, the gas sample is (*I.*) irradiated by laser radiation of a wavelength matching an absorption band of the target gas, which causes (*II.*) excitation of the molecule or atomic constituents upon absorption. Subsequent to excitation, (*III.*) non-radiative, i.e., collisional relaxation converts parts of the absorbed energy to translational motion, resulting in (*IV.*) local density changes. To generate detectable density changes, PAS-based gas analyzers require a modulation of the heat source. This typically is achieved by either wavelength or intensity modulation of the laser radiation. PTS-based sensors may, although this is often unfavorable, be operated with continuous wave (CW) radiation. An initial expansion of the gas upon release of absorbed energy causes (*V.a*) an acoustic (compression) wave which is (*VI.a*) measured by some sort of pressure transducer, typically after resonant amplification of the periodically generated acoustic wave. A remaining, slowly decaying rarefaction of the gas, maintained by (*V.b*) increased thermal energy can, for example, be detected by (*VI.b*) measuring the refractive index of the gas. Extensive treatments about the entire chain of signal generation and detection can be found in the standard references Pao [83] for the field of photoacoustic spectroscopy (PAS) and Bialkowski et al. [84], regarding photothermal spectroscopy (PTS).

In the following, the individual processes are reviewed in view of the application of near-infrared PAS and PTS to the concentration measurement of water vapor in air. Sensing of water vapor is typically conducted with sources of near-infrared (NIR; wavelengths of approx. 780 nm to 3 µm) or mid-infrared (MIR; approx. 3 µm to 14 µm) radiation [71, 79, 59] and the gas analyzers realized in this work also apply a NIR laser source. Therefore, the discussion is confined to rotational and vibrational transitions only, as well as combinations thereof, as the electronic transitions of water vapor, e.g. targeted by Lyman-α instruments, are only relevant in the UV region, at wavelengths below 180 nm [85]. As usable radiation source, modulation scheme, as well as acoustic resonators in PAS are highly specific to the individual application, the following review commences with a treatment of the absorption of radiation. General descriptions of the working principles of typical PAS and PTS setups and quantitative expressions to predict instrument performance are given in Sections 2.3.3 and 2.3.4.

2.1 Infrared Laser Absorption Spectroscopy

Photoacoustic and photothermal spectroscopy are, along with purely optical absorption spectroscopy techniques, based on the absorption of electromagnetic radiation, most commonly in the ultra-violet (UV), visible (VIS), or infrared (IR) regions of the spectrum, where atoms and molecules exhibit characteristic absorption bands, due to transitions between discrete electronic, vibrational and/or rotational energy levels determined by their structure. Transmission based techniques (an extensive and up-to-date review and comparison of notable detection methods, such as the already mentioned TDLAS, NDIR spectroscopy, or CRDS may be found in [77]) build upon measuring the transmission of radiation through the attenuating gas sample and, hence, rely on a thorough description of the attenuation along the optical path. Locally generated PA and PT signals also depend on the absorption of radiation, given by the power of the incident radiation and the amount of absorbers combined with the strength (probability) of the absorption at the laser wavelengths. However, in PA and PT trace gas applications, samples are often assumed optically thin and generated signals are thus assumed constant and independent of the position.

In high contrast to trace gas applications, atmospheric water vapor mole fractions x_{wv} (ppm), including evaporated condensed water contents of some g m^{-3}, may reach up to several 10,000 ppm [1]. At these concentrations NIR radiation is attenuated considerably over the absorption path length of typical gas cells. Hence, the prediction of the power available for PA and PT signal generation requires consideration of the attenuation along the optical path. The following subsection reviews the macroscopic description of attenuation of radiation applied in optical (laser-based) absorption spectroscopy. Thereafter, a description of the optical absorption properties of water vapor is given.

2.1.1 Radiative Transfer (Beer-Lambert Law)

In the absence of interference effects, the irradiance of radiation propagating through an absorbing and scattering gas along a path $\mathbf{s}$ (m) is described without dealing with the specific electromagnetic field. The change of the spectral radiance $I_{\Omega,\lambda}$ (W m^{-2} sr^{-1} nm^{-1}) of electromagnetic radiation at wavelength λ (nm) and in a certain direction, given by a solid angle Ω (sr), is determined by absorption, scattering and emission of radiation, as summarized by the radiative transfer equation [86]

$$\frac{\mathrm{d}I_{\Omega,\lambda}}{\mathrm{d}\mathbf{s}} = -\sigma_{ext}(\lambda)\, n_i\, I_{\Omega,\lambda} + j_\lambda\ . \tag{2.1}$$

Here, $\sigma_{ext}(\lambda) = \sigma_{\mathrm{abs}}(\lambda) + \sigma_{sca}(\lambda)$ is the extinction or attenuation cross section (m^2 molec^{-1}) and is the sum of absorption and scattering cross sections of the gas, σ_{abs} and σ_{sca}, respectively. n_i is the number concentration of an absorbing species i and j_λ is the emitted spectral radiance (W m^{-3} sr^{-1} nm^{-1}) in the direction of Ω, for example, due to scattering or fluorescence, i.e., elastic or inelastic scattering of radiation originating from other directions. The spectral radiance and all following quantities are frequently also written in terms of the frequency ν (Hz) of the radiation, i.e., $I_{\Omega,\nu}$ (W m^{-2} sr^{-1} Hz^{-1}).

Assuming negligible emission along the optical path length z of a collimated beam and propagation in a homogeneous material which negligibly scatters (i.e., $\sigma_{\mathrm{abs}}(z) \approx$ const. and $\sigma_{sca} \approx 0$), the solution to the radiative transfer equation at wavelength λ is an exponential attenuation of the spectral irradiance I_λ (W m^{-2} nm^{-1}), known as the *(Bouguer-) Beer-Lambert* law.

For a collimated laser beam, operated in the fundamental TEM$_{00}$ spatial mode and with a normalized radial Gaussian beam profile $g(r) = \exp(-2r^2/w^2)$, the spectral irradiance along

---

[1] Mole fraction:

$$x_i = \frac{n_i}{n_0} \overset{\text{(ideal gas)}}{=} \frac{n_i k_B T_0}{p_0}$$

the absorption path is given by [84]

$$\begin{aligned} I_\lambda(r,z,t) &= I_{\lambda,0}(z,t)\, g(r) && (2.2)\\ &= I_{\lambda,0}(z{=}0,t)\, g(r)\, e^{-\sigma_\mathrm{abs} n_i z} && (2.3)\\ &= \frac{2P_\lambda(z,t)}{\pi w^2}\, g(r)\;, && (2.4)\\ &= \frac{2P_\lambda(z{=}0,t)}{\pi w^2}\, g(r)\, e^{-\sigma_\mathrm{abs} n_i z}\;, && (2.5) \end{aligned}$$

where w is the beam waist (radius; $1/e^2$ intensity), $P_\lambda(z,t)$ is the instantaneous spectral radiant power of the beam ($\mathrm{W\,nm^{-1}}$) at time t (s) and $I_{\lambda,0} = 2P_\lambda(z,t)/\pi w^2$ is the spectral irradiance at the beam center ($r = 0$). In the PAS and PTS applications discussed in this work, assuming a collimated beam is sufficiently accurate.

The product of absorption cross section and concentration is the *absorption coefficient* $\alpha_\mathrm{abs} = \sigma_\mathrm{abs} n_i$ ($\mathrm{m^{-1}}$) and has to be considered a function of intensity when nonlinear effects, such as optical saturation (depletion of the lower state), are relevant. As laser intensities and powers in the applications discussed herein are sufficiently low, it is assumed throughout this thesis that the beam has negligible effect on the population of the targeted ro-vibrational states. An additional dependence of the cross section on the number concentration arises through self-broadening of the targeted spectral line. This is discussed in section 2.2.2.

The reduction in irradiance at each point along the beam, $\mathrm{d}I_\lambda/\mathrm{d}z$ ($\mathrm{W\,m^{-3}\,nm^{-1}}$), is equal to the power absorbed, which partly leads to the generation of the PA and PT signals. As mentioned before, at trace concentrations it is possible to assume an optically thin sample with $I_\lambda(r,z,t) \approx g(r)\, I_\lambda(r, z{=}0, t)$ and, thus, the power absorbed at each point along the beam is constant:

$$\frac{\mathrm{d}I_\lambda(r,z,t)}{\mathrm{d}z} = -\sigma_\mathrm{abs}\, n_i\, I_\lambda(r,z,t) \approx -\sigma_\mathrm{abs}\, n_i\, I_{\lambda,0}(z{=}0,t)\, g(r)\;. \tag{2.6}$$

For water vapor concentrations of several 10,000 ppm the above approximation does not hold and, as applied in **Paper I**, a somewhat better description of the irradiance along the attenuated beam is obtained with a first order approximation of Eq. (2.3):

$$I_\lambda(r,z,t) = I_{\lambda,0}(z{=}0,t)\, g(r)\, (1 - \sigma_\mathrm{abs}\, n_i\, z)\;. \tag{2.7}$$

2.2 Infrared Spectroscopic Properties of Water Vapor

2.2.1 Rotational-Vibrational Absorption Transitions

Water vapor is a particularly strong absorber in the NIR and MIR (up to ≈8 µm), as radiation is absorbed by resonantly inducing combined vibrational and rotational (ro-vibrational) transitions of H_2O from the most occupied (around room temperature) vibrational ground state $H_2O(\nu_1{=}0, \nu_2{=}0, \nu_3{=}0)$ to the first excited states. Water molecules generally exhibit three fundamental modes of vibration: the symmetric stretch mode (ν_1), the bend mode (ν_2) and the asymmetric stretch mode (ν_3). The three lowest energy states (levels) of these modes are shown in the energy diagram in Fig. 2.2. Superposed rotational energy levels are spaced much closer. Figure 2.3 shows the ro-vibrational absorption spectrum in the range of 0.7 to 3 µm. For a detailed description about the absorption spectrum of water vapor, the reader is referred to Wozniak and Dera [85], Regula [87].

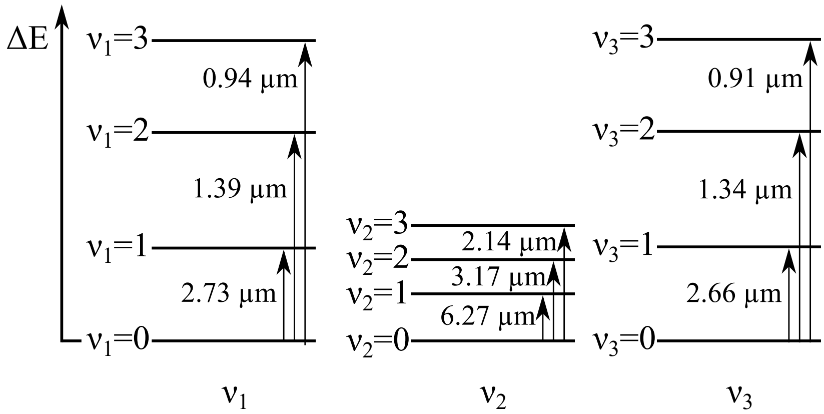

Fig. 2.2 Energy diagram of the H_2O normal modes of vibration up to the third excited state, together with selected vibrational transitions and the corresponding wavelengths. Redrawn according to [85].

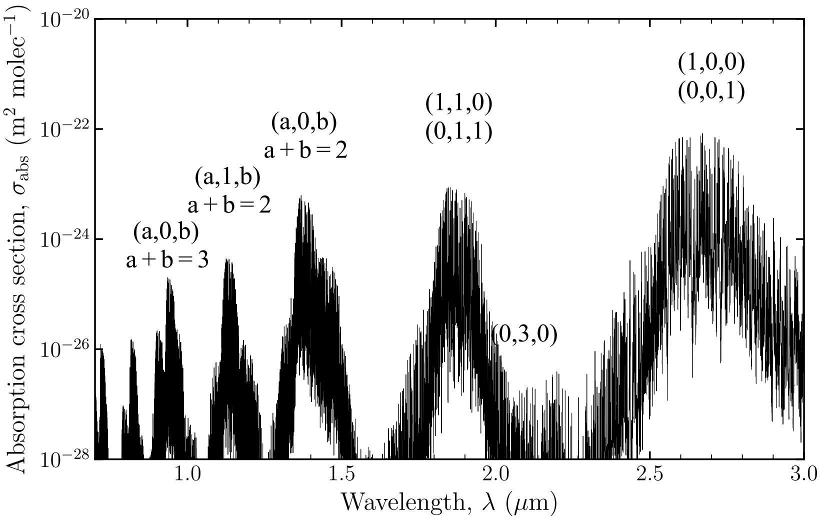

Fig. 2.3 Ro-vibrational absorption cross section of 1 ppm water vapor in air (20 °C, 1013.25 hPa) in the NIR and parts of the visible spectrum. Excited vibrational transitions from the ground state ($\nu_1 = 0, \nu_2 = 0, \nu_3 = 0$) to the state ($\nu_1, \nu_2, \nu_3$) are given in parenthesis.

Highest absorption cross sections in the above range are achieved at approximately 2.7 µm, due to the coinciding of the fundamental transitions ($\nu_i{=}0 \rightarrow \nu_i{=}1$) of the stretch modes. These transitions are targeted by NDIR applications [e.g., 59]. In contrast, due to the availability of relatively low-cost telecommunication-type laser diodes around 1.55 µm, laser-based absorption spectroscopy techniques (TDLAS, CRDS, PAS) usually target absorption lines in the 1.4 µm band [88]. More recent developments, employing quantum cascade lasers (QCLs), have brought forward MIR spectrometers targeting the more than an order of magnitude stronger 6.27 µm absorption band [89]. Due to the abundance of absorption lines and by using narrow-band laser sources, cross-interference from other atmospheric constituents is usually not an issue. In this work, a ro-vibrational transition $(0,0,0) \longrightarrow (1,0,1)$ at $7327.675\,\mathrm{cm}^{-1} \approx 1364.68\,\mathrm{nm}$ is targeted. This line is shown in Fig. 2.4. With a laser diode specified CW spectral linewidth (full width half maximum, FWHM) of $\Delta\nu = 2\,\mathrm{MHz} \approx 1.2 \times 10^{-5}$ nm, the laser linewidth is supposed to be considerably narrower than the absorption line.

The absorption probability of electromagnetic radiation for a given photon energy $\Delta E = h\nu$ is specified in the form of the absorption cross section $\sigma_{\mathrm{abs}}(\bar{\nu})$ as a function of the photon wavenumber $\bar{\nu} = 1/\lambda = \nu/c$ (cm^{-1}). Here, h is the Planck constant and c is the speed of light. At any wavenumber, the cross section is given by the contributions of all possible transitions (lines) $i \longrightarrow j$ from an initial state i with energy E_i to a final state j with energy $E_j > E_i$. Each line itself is characterized by a temperature dependent integrated spectral line intensity $S_{ij}(T)$ ($\mathrm{cm}^2\,\mathrm{molec}^{-1}\,\mathrm{cm}^{-1}$), determined by the quantum mechanical transition probabilities for absorption and stimulated emission (Einstein coefficients), as well as the populations of the initial and final states (Boltzmann-distribution, degeneracy) and isotopic abundance [90]. All lines, centered at photon energies $\Delta E = E_j - E_i = \bar{\nu}_{ij} = h\nu_{ij}$, are broadened due to several effects, resulting in line shapes defined by normalized line profiles $\Phi(\bar{\nu}; \bar{\nu}_{ij}, T, p)$ (in units cm), where $\int \Phi(\bar{\nu}; \bar{\nu}_{ij}, T, p)\mathrm{d}\bar{\nu} = 1$. As a result of the line broadening, the overall absorption cross section at the wavenumber $\bar{\nu}$ is given by [91]:

$$\sigma_{\mathrm{abs}}(\bar{\nu}, T, p) = \sum_{i,j} S_{ij}(T)\Phi(\bar{\nu}; \bar{\nu}_{ij}, T, p) \ . \tag{2.8}$$

In the following subsection the main contributing effects determining ro-vibrational line shapes are reviewed in combination with the parameters introduced for their description. For wavelengths accessible by the chosen or available laser source type, these line parameters have to be considered in the selection of a suitable absorption line for a specific application.

2.2.2 Transition Line Shapes

Effects responsible for the broadening of ro-vibrational lines are typically classified into the three main contributors:

1. **Natural broadening** Finite lifetimes of molecules in some state, before transitioning to another state, are related to uncertainties in the energies of the states by the Heisenberg uncertainty principle and result in a continuum of allowed energies ΔE for the transitions, which are observed as a Lorentzian distributed natural width of the absorption lines when stronger broadening effects are absent. At very low pressures, when interactions and energy transfer due to collisions are negligible, the lifetimes and

line widths are determined by the radiative decay of the (upper) excited state due to spontaneous emission to all lower states [90]. This radiative lifetime τ_r (s) is given by the Einstein coefficients for spontaneous emission A_{ij} (s^{-1})

$$\tau_{\mathrm{r,i}} = \frac{1}{\sum_{j,E_j<E_i} A_{ij}} \,. \tag{2.9}$$

For the water vapor transition of $7327.675\,\mathrm{cm}^{-1}$ targeted in this work, the radiative lifetime is approximately 6 ms, resulting in negligible natural line width (calculated using the HITRAN molecular spectroscopic compilation [92]). Since, at the measurement conditions applied in this work, inelastic collisions induce non-radiative relaxations much faster [**Paper I**], radiative relaxation of excited H_2O is effectively suppressed in the applications discussed.

2. **Collisional broadening** (also pressure or Lorentz broadening) With increasing pressure, the lifetimes are increasingly shortened by inelastic collisional processes, thus leading to an increase of the line width [93]. Additionally, the interactions interfere with the rotational and vibrational motions, affecting the individual molecular potentials in a statistical manner. This further broadens allowed transition energies. Both effects in combination are satisfyingly described by the Lorentzian profile (also Cauchy distribution) [91]:

$$\Phi_\mathrm{L}(\bar{\nu}; \bar{\nu}_{ij}, T, p) = \frac{1}{\pi} \frac{\gamma_{ij}(T,p)}{\gamma_{ij}(T,p)^2 + \left(\bar{\nu} - \bar{\nu}^*_{ij}\right)^2} \,. \tag{2.10}$$

Through the specific nature of the intermolecular interactions, pressure broadening generally depends on the surrounding gas composition and therefore introduces a concentration dependence into the line shape and maximum absorption cross section. The different broadening effects of the environment and the gas under consideration thus have to be taken into account in the Lorentzian halfwidth of each profile,

$$\gamma_{ij}(T,p) = \left(\frac{T_\mathrm{ref}}{T}\right)^{n_T} \left(\gamma^\mathrm{air}_{ij}\, p_\mathrm{air} + \gamma^\mathrm{self}_{ij}\, p_\mathrm{self}\right) \,, \tag{2.11}$$

where γ^air_{ij} and $\gamma^\mathrm{self}_{ij}$ ($\mathrm{cm}^{-1}\,\mathrm{atm}^{-1}$) are the air- and self-broadened (by the absorbing gas itself) line halfwidths at reference conditions (296 K, 1 atm). The concentration dependencies are included in the partial pressures p_air and p_air, respectively. n_T is an empirical coefficient for the temperature dependence of the halfwidth. The above mentioned changes in the molecular potentials of the collision partners also shift the line position to a new center $\bar{\nu}^*_{ij} = \bar{\nu}_{ij} + \delta_{ij}\, p$ with a pressure shift coefficient δ_{ij} ($\mathrm{cm}^{-1}\,\mathrm{atm}^{-1}$), determined at the reference temperature and pressure.

3. **Doppler broadening** The molecular translational (Brownian) motion, with velocities distributed according to a Maxwell-Boltzmann distribution, introduces a Doppler-shift

in the radiation wavelength and thus a photon energy shift encountered by molecules moving along the radiation direction. Although this does not influence the transition energies, a range of photon energies fulfills the transition energy condition for absorption in the gas as a whole. As a consequence of the velocity distribution, this range is mathematically described by a Gaussian profile:

$$\Phi_{\mathrm{G}}(\bar{\nu};\bar{\nu}_{ij},T) = \sqrt{\frac{\ln(2)}{\pi\gamma_{\mathrm{D}}^2}}\exp\left(-\frac{(\bar{\nu}-\bar{\nu}_{ij})^2\ln(2)}{\gamma_{\mathrm{D}}^2}\right) \tag{2.12}$$

with the Doppler width (HWHM)

$$\gamma_{\mathrm{D}}(T) = \frac{\bar{\nu}_{ij}}{c}\sqrt{\frac{2\ln(2)N_A k_B T}{M}}\ , \tag{2.13}$$

where N_A is the Avogadro constant, k_B is the Boltzmann constant and M is the molar mass of the absorbing molecule. Doppler broadening is the width dominating effect at low pressures, e.g., as encountered in the upper terrestrial atmosphere.

At atmospheric pressures, line profiles resulting from the combined effects of Doppler and collisional broadening may be calculated in good approximation by a convolution of both profiles, resulting in the Voigt function:

$$\Phi_{\mathrm{V}}(\bar{\nu};\bar{\nu}_{ij}) = \Phi_{\mathrm{G}}(\bar{\nu};\bar{\nu}_{ij}) * \Phi_{\mathrm{L}}(\bar{\nu};\bar{\nu}_{ij})\ . \tag{2.14}$$

For a large number of atmospheric constituents the Voigt profile has been demonstrated to be less accurate than the achievable precision of current absorption spectrometers (e.g. [94]). One line profile developed to further increase line shape simulation accuracy is the Hartmann-Tran profile, which extends the Voigt profile for various additional collisional contributions, such as velocity changing collisions that lead to a reduction in the line width [95]. Unless otherwise stated, the Hartmann-Tran line profile has been used for the calculation of the theoretical absorption cross sections of water vapor in this work. Line intensities together with all other line-by-line parameters were retrieved from the HITRAN molecular spectroscopic compilation [92] using the HITRAN Application Programming Interface (HAPI) [96].

Figures 2.4a-2.4c show calculated spectra around the line targeted in the realized photoacoustic spectrometer (7327.675 cm^{-1}) to illustrate the temperature, pressure and concentration dependence of the absorption cross section at typical measurement conditions and demonstrate the requirement of either stabilizing temperature and pressure or compensating for any changes occurring between calibration and measurement. Contrary to the picture conveyed by Fig. 2.4b, increasing the absorption cross section by reducing measurement pressure results in no considerable increases in the achieved absorption coefficient, due to a simultaneous decrease in number concentration.

PAS instrument performance specifications are often derived assuming a linear relationship between absorption coefficient and concentration (cf. Section 2.4). In light of the significant

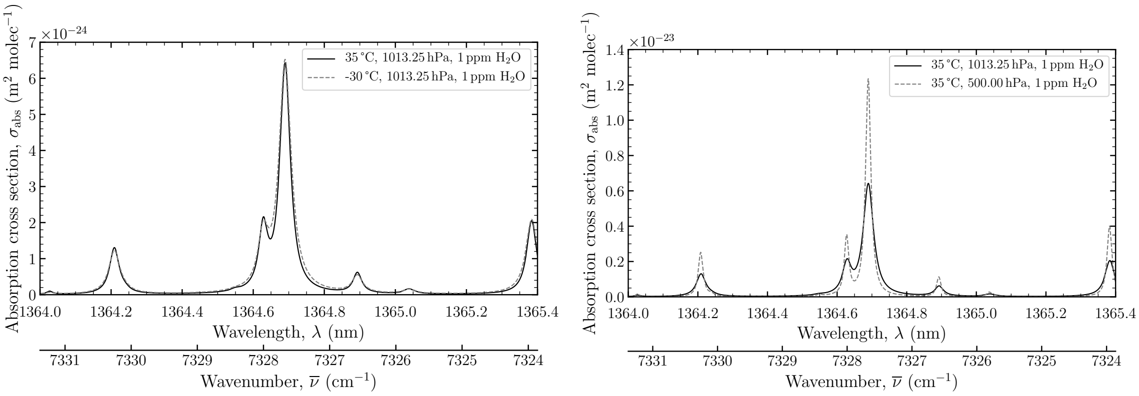

(a) Temperature dependence

(b) Pressure dependence

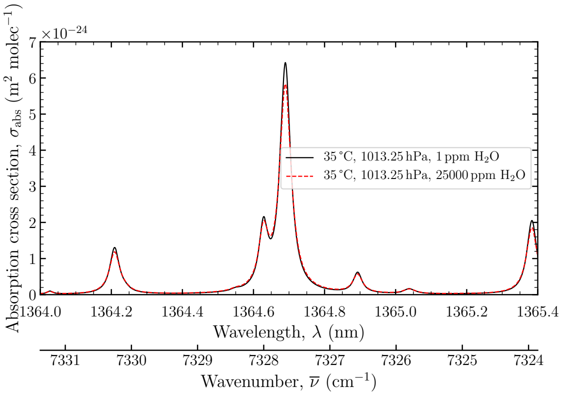

(c) Concentration dependence

Fig. 2.4 Absorption cross section (a) temperature, (b) pressure and (c) concentration dependence of the water vapor absorption line targeted in the realized photoacoustic spectrometer (7327.675 cm^{-1}).

self-broadening effect of water vapor, this may lead to an overestimation of the instrument performance. Figure 2.5 illustrates the importance of considering the effect of self-broadening with rising concentrations on the absorbed power. The absorbed power is given in terms of the transmittance $Tr(x_{\mathrm{wv}}) = P_\lambda(z)/P_\lambda(z{=}0)$ using different approximations to the Beer-Lambert law (cf. Eq. (2.7)). Calculations were made for the AquaSense PA cell operating conditions.

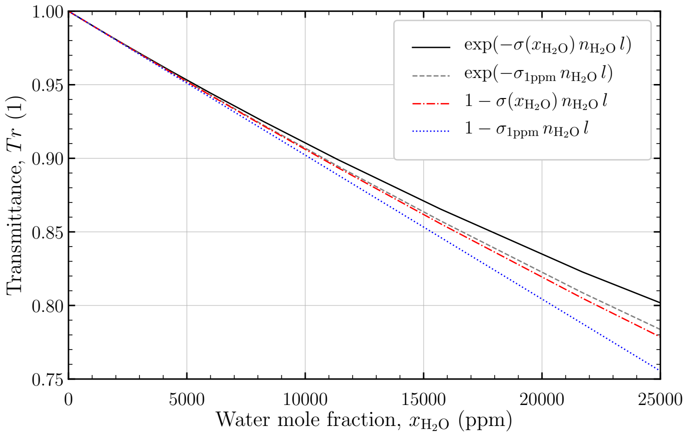

Fig. 2.5 Transmittance through $z = 6.5$ cm humid air as a function of the water vapor mole fraction (7327.675 $\mathrm{cm^{-1}}$, 35 °C, 800 hPa), calculated by the Beer-Lambert law and the linear approximation.

2.3 Photoacoustic and Photothermal Spectroscopy in Gases

Photoacoustic and photothermal spectroscopy differ from transmission sensing techniques by the method of detection of the absorption. In the latter, absorption is measured indirectly by a comparison (difference) of incident and transmitted power, whereas PAS and PTS detect physical changes of the gas following absorption. In the linear regime, where absorption saturation is negligible, this implicates the great advantage of the PA and PT signals being directly proportional to the incident power, rather than to the ratio of incident to transmitted, explaining the improved relative intensity noise characteristics of PAS and PTS [77]. Dependence of the PA and PT signals on the number concentration and gas composition in general, however, is not as straightforward as in transmission-based techniques, making the correct prediction and interpretation of generated signals difficult. The sensitivity of PAS and PTS instruments is known to highly depend on the gas matrix [83, 84], causing a nonlinear signal-over-concentration response for many gas monitoring applications [e.g. 97–101] as well as aerosol monitoring applications [102, 103]. This particularly affects applications, such as the application of this work, where large ranges and absolute values of concentrations have to be detected and, as a result, the gas matrix changes considerably over the range of detectable concentrations. Therefore, a knowledge about the signal generation process is necessary to reliably predict and understand PAS and PTS instrument performance. The following subsections aim at providing a principle understanding of the processes involved in the conversion of the absorbed power in the gas into thermal energy and to measurable acoustic pressure or refractive index changes.

2.3.1 Molecular Kinetics and Energy Transfer

Excitation by photon absorption increases the internal energy of the targeted molecule, which subsequently has to be transferred to thermal energy of the gas to produce PA and PT signals. Thermodynamic equilibrium can be restored by several different processes. Excited molecules non-instantaneously relax to the ground state through radiative processes, such as stimulated or spontaneous emission (photoluminescence), chemical reactions or inelastic collisions [83]. The individual processes are usually described by lifetimes with time constants τ (s) or relaxation rates $k = \tau^{-1}$ (s^{-1}) [84]. For the applications under study, chemical reactions can be neglected, as excitation energies are too low to induce molecular dissociation or other chemical reactions. For most gases at typical – close to standard atmospheric – operating conditions, also spontaneous emission can be neglected since the radiative lifetime τ_R of excited ro-vibrational states is much longer than the average timescale τ_C of non-radiative collisional transfer (cf. Section 2.2.2, natural line broadening) [104]. At lower pressures, collisional transfer is less probable and spontaneous emission may have to be considered. Neglecting chemical reactions, the lifetime or time constant of an excited state is given by [104]:

$$\frac{1}{\tau_\mathrm{E}} = \frac{1}{\tau_\mathrm{C}} + \frac{1}{\tau_\mathrm{R}} \tag{2.15}$$

Only collisional deactivation with transfer of internal ro-vibrational energy to thermal energy (sensible heat) ultimately contributes to PA and PT signal generation. In gases, rates of collisional energy transfer depend on the collision partners of the mainly bimolecular collisions, the pressure dependent collision frequency, transferred energy, as well as temperature and, in general, follow an Arrhenius-type relation [84]. A detailed discussion of collisional energy transfer mechanisms goes beyond the scope of the present chapter and the reader is referred to [105]. Due to the low energies of rotational states, collisional equilibration of the rotation in gases at typical instrument measurement conditions is much faster than equilibration of the vibrational state ($\tau \approx 1 \times 10^{-8}$ s, 300 K, 1 bar) [84] and excess rotational energy may be assumed to be released instantaneously. Timescales for vibrational thermalization vary over many orders of magnitude [106] and no general assumption can be made about the vibrational relaxation time for PAS and PTS applications. Thermalization of excited ro-vibrational states is commonly referred to as ro-vibrational-translational (V,R–T), or simply vibrational-translational (V–T) relaxation when rotational relaxation is considered fast [106]. Non-thermal processes are analogously referred to as V,R–V,R or simply V–V processes.

Fast V–T is the preferred path in many PAS and PTS applications targeting the measurement of gas concentrations, as for modulated irradiation the generated signals then are directly proportional to the number concentration of the absorbing molecule [88]. When τ_C is significant compared to the timescale of modulation τ_{mod} of the radiation source, the heat transfer rate is reduced, which often occurs when the collisional relaxation involves intermediate vibrational excitation of metastable (regarding the excited state) gas species, such as O_2 [100] or N_2 [97]. In PAS and PTS sensing applications with initially large τ_C, water vapor is sometimes added to the sample gas to prevent such non-thermal processes and to increase collisional relaxation rates, as H_2O is known to be an effective promoter for thermal collisional relaxation [e.g., 100, 101, 107, 108].

When collisional relaxation times are much faster than modulation timescales, the temporal acoustic and thermal response is mostly governed by the temporal characteristics of the radiation source, i.e., the modulation of the laser power. The source heat transfer or production rate $q_H(\mathbf{r}, t)$ ($\mathrm{W\,m^{-3}}$) then is simply given by

$$\begin{aligned} q_H(\mathbf{r}, t) &= \int_{-\infty}^{+\infty} \left(-\frac{\mathrm{d}I_\nu(\mathbf{r}, t)}{\mathrm{d}z} \right) \mathrm{d}\nu \\ &= n(\mathbf{r}, t) \int_{-\infty}^{+\infty} \sigma_{\mathrm{abs}}(\nu)\, I_\nu(\mathbf{r}, t) \mathrm{d}\nu \\ &= n(\mathbf{r}, t) \overline{\sigma}_{\mathrm{abs}}\, I(\mathbf{r}, t) \,, \end{aligned} \tag{2.16}$$

where n is the number concentration of the absorbing molecule, $\overline{\sigma}_{\mathrm{abs}}$ is a spectral irradiance weighted absorption cross section of this molecule and I is the spectrally integrated irradiance ($\mathrm{W\,m^{-2}}$). In the more general case, however, a complex relaxation chain from the excited ro-vibrational state back to the ground state follows after excitation, possibly involving excitation of other molecular species [84].

For some systems, the relaxation process may be modeled by a discrete number of selected, rate-determining relaxation steps in multiple, simultaneously proceeding relaxation paths [109]. Other relaxation processes can often be assumed much faster than these limiting steps, which determine the overall kinetics and thus the heat production rate within the sample. As applied in **Paper I**, this approach can be used when metastable vibrational states are involved in the relaxation process. The corresponding theoretical framework is introduced in a general form in the following, considering radiative excitation and possible radiative relaxation.

Radiative Relaxation

Absorption, stimulated emission, as well as spontaneous emission rates can be summarized by the local radiative transition rate l_{ij} ($\mathrm{s^{-1}}$) between states i and j. For spectral photon irradiances $\varphi_\nu(\mathbf{r}, t) = I_\nu / h\nu$ (in units photon $\mathrm{m^{-2}\,s^{-1}\,Hz^{-1}}$) the radiative transition rate is given by [90, 83, 84]

$$\begin{aligned} l_{ij} &= \int_{-\infty}^{+\infty} \sigma_{\mathrm{abs}}(\nu; \nu_{ij})\, \varphi_\nu \mathrm{d}\nu + A_{ij} \\ &= \overline{\sigma}_{\mathrm{abs}}(\nu_{ij})\, \varphi(\nu_{ij}) + A_{ij} \;. \end{aligned} \tag{2.17}$$

Here, the integration is carried out over the transition line centered at ν_{ij} and $\varphi(\nu_{ij})$ is the line integrated photon irradiance (photon $\mathrm{m^{-2}\,s^{-1}}$). The Einstein A-coefficient for spontaneous emission is zero for transitions $i \rightarrow j$ to energetically higher levels ($E_i < E_j$). The radiative transition rate can also be written in terms of the Einstein B-coefficients, B_{ij} and B_{ji}, which are related to the absorption cross section by the speed of light, with $B_{ij} = B_{ji} = \sigma_{\text{abs}}(\nu_{ij})c$ [84].

Non-Radiative Relaxation

V–T relaxation reactions and V–V transfer processes between two collisional partners (molecules) $\mathrm{A}(i)$ in state i and $\mathrm{B}(p)$ in state p, and with number concentrations $n_i(\mathbf{r}, t)$ and $n_p(\mathbf{r}, t)$, respectively, may be assumed of the general form

$$\mathrm{A}(i) + \mathrm{B}(p) \underset{k}{\overset{k'}{\leftrightarrows}} \mathrm{A}(j) + \mathrm{B}(q) + \Delta E \,, \tag{2.18}$$

where $j{\neq}i$ and q are the final states after the collision (thermal: $q{=}p$; non-thermal: $q{\neq}p$) and $\Delta E = (E_j - E_i) + (E_q - E_p)$ is the thermal energy released (or absorbed) by the two molecules during the process. The coefficients k and k' ($\mathrm{cm^3\,molec^{-1}\,s^{-1}}$) are the forward and backward rate coefficients (or constants) of the reaction and are the product of the collision frequency between the collision partners and the probability of energy transfer [105]. Rates of production $v_r(\mathbf{r}, t)$ ($\mathrm{molec\,cm^{-3}\,s^{-1}}$) in the forward or backward direction can be approximated by products of the rate coefficients and the individual number concentrations, $v_r = k_{ij,pq} n_j n_p = k_{ij} n_p$. Here, $k_{ij,pq}$ is a second-order rate coefficient ($\mathrm{cm^3\,molec^{-1}\,s^{-1}}$). Alternatively, so-called pseudo-first-order rate coefficients $k_{ij} = k_{ij,pq} n_p$ ($\mathrm{s^{-1}}$) are often used. This is more convenient when the number concentration n_p of the collisional partner is large and remains approximately constant during the reaction [84, 106], for example, when collisions with molecules of the gas matrix are considered. When multiple collisional partners contribute in the relaxation $A(i) \longrightarrow A(j)$, pseudo-first-order rates can be taken as the sum of all contributing reactions, $k_{ij} = \sum_p k_{ij,pq} n_p$. The backward rate can be described analogously. A collection and visualization of typical literature values for the rate coefficients of the main V–T and V–V processes of excited water vapor in air is given in **Paper I**.

Each relaxation step liberates a certain amount of energy and in the final description of the total heat production rate, the heat released by all individual relaxation steps and paths, including processes considered fast, have to be accounted for. This is accomplished by formulating rate equations for the state populations, considering the reaction rates and the time-dependent irradiation [110]. For simple forms of irradiation (harmonic, pulsed, CW) analytical solutions then may be found, describing the temporal behavior of the heat released in the sample.

Rate Equations

The time dependence of the number of molecules per volume in state or level $i = 1, \ldots, N$ is determined by the rates of change of the individual populations. These rates of change are given by the number of molecules going out of each level per unit time by radiative and collisional processes and the number of molecules going in [83]:

$$\frac{\partial n_i}{\partial t} = -\left[\sum_{j,\, j\neq i}^{N} (k_{ij} + l_{ij})\right] n_i + \left[\sum_{j,\, j\neq i}^{N} (k_{ji} + l_{ji}) n_j\right] . \tag{2.19}$$

Above and in the following, i and j are used to simultaneously designate the type and state of a molecule. Therefore, no particular distinction is made between the different molecular species involved in the transitions and collisions. The states of each component can be assumed as a subset of the total N levels. The rate coefficients in Eq. (2.19) are pseudo-first-order coefficients and implicitly include the number concentrations of the collisional partners.

For given irradiation conditions and gas mixtures with corresponding transition rates and relaxation coefficients, the time dependent number concentration of molecules in all relevant states can be determined from the system of rate equations. A general solution for the number concentrations of an N-level system can be found in [83]. For simple systems analytical approximations can be obtained. The solution to the often quoted two-level system is reviewed at the end of this subsection.

Mass Diffusion

Mass diffusion is the concentration gradient driven flux of molecules or particles to regions of lower concentrations [111]. For excited molecular species carrying substantial fractions of the overall excitation energy, a diffusion driven spatial redistribution may have to be considered when the relaxation time is long [109, 84]. Relevant diffusion of excited molecules has the practical implication that the region of heat production is distributed to a larger area than the area irradiated by the laser beam and, consequently, the signal is reduced at the center point of excitation. Additionally, deexcitation by collision with gas cell walls may reduce signal generation [104].

The additional rate of change of the number density of each molecule type and state i at position $\mathbf{r}$ due to the diffusional spatial redistribution (in the absence of additional advection) is described by the mass diffusion equation [111]

$$\frac{\partial n_i}{\partial t} = \nabla \cdot \left(D_{m,i} \nabla n_i\right) . \tag{2.20}$$

$D_{m,i}$ ($\propto T^{3/2}/p$) is the mass diffusivity (m^2 s^{-1}) of species i in the gas mixture, which often can be assumed constant and equal to the diffusivity of the ground state molecule. To determine the importance of considering mass diffusion in a specific PAS or PTS application and measurement geometry, the characteristic mass diffusion time $\tau_m = w^2/4D_m$ (s) for a Gaussian beam of width w can be used. During this time, diffusion decreases the peak concentration to one third of the initial value and the width of the initial distribution has tripled. Characteristic mass diffusion times for water vapor in air are shown in Fig. 2.7 (page 35) and compared to characteristic excitational time scales.

In the absence of excitational relaxation and for optically thin samples, the solution to the mass diffusion equation for a collimated Gaussian beam impulse excitation with unit centerline excited molecule number concentration is [112]

$$n_i'(r,t) = \frac{1}{1+2t/\tau_{m,i}}\, e^{-2r^2/w^2(1+2t/\tau_{m,i})} \; . \tag{2.21}$$

In many applications, number concentrations of excited molecules are low and local differences in these concentrations do not significantly affect collisional relaxation rates. In this case, convolution of the diffusion impulse response with the number of molecules transitioning into each state (second term on the RHS of Eq. (2.19)) can be used to calculate the number concentration for an arbitrary excitation source time dependence. Simultaneously, one has to consider that the resulting concentration is steadily decreased at each point by radiative transitions and collisional relaxation (first term on the RHS of Eq. (2.19)). This method is applied in the next chapter, where general expressions for the source rate of heat production in the irradiated sample are derived from the rate equation.

Heat Production

The already introduced source rate of heat production $q_H(\mathbf{r},t)$, eventually responsible for PA and PT signal generation, is the rate of change of translational energy $U_T(\mathbf{r},t)$ (J m^{-3}). As a consequence of energy conservation, this rate of change can be obtained from the absorbed radiant power $q_R(\mathbf{r},t)$ (W m^{-3}) and the rate of change of vibrational and rotational energy in the system $U_{V,R}(\mathbf{r},t)$ (J m^{-3}) [83]:

$$\begin{aligned} \frac{\partial U_T}{\partial t} &= q_R - \frac{\partial U_{V,R}}{\partial t} && (2.22)\\ &= \sum_{i,j,i\neq j}^{N} l_{ij} n_i \left(E_j - E_i\right) - \sum_{i}^{N} \frac{\partial n_i}{\partial t} E_i && (2.23)\\ &= q_H \; , && (2.24) \end{aligned}$$

where E_i is the excess energy per molecule relative to the ground state (J molec^{-1}). Thus, recalling the general expression for the rate of change of the number concentration, Eq. (2.19), the source rate of heat production is the sum of excess energy released by all collisional transitions per unit volume and time [83]:

$$q_H(\mathbf{r},t) = \sum_{i,j,i\neq j}^{N} \left(k_{ij} n_i - k_{ji} n_j\right) E_i \; . \tag{2.25}$$

Collisional excitation from lower to higher energetic states may be disregarded, as long as $\Delta E \gg k_B T$ [83]. The above result is the starting point in **Paper I** for the calculation of the time dependence of the source rate of heat production for excitation of $H_2O(1,0,1)$ in air.

In the following, a general expression for the calculation of the source heat generation for a Gaussian excitation beam is derived. This expression is used in Section 2.3.4 in the calculation of the theoretical photothermal signal produced by a Gaussian excitation beam under harmonic modulation.

Thinking of the above result for the heat release, Eq. (2.25), as the sum of energy-weighted, thermal relaxation impulse responses $R'_i(t')$ (W s^{-1} molec^{-1}) of each state/species i, excited at $t' = 0$, it is straightforward that, for a source with arbitrary time dependence and in the linear regime where saturation effects are negligible, the heat production can be approximated by the temporal convolution of the excitation source with this relaxation impulse response function:

$$q_H(\mathbf{r}, t) = \left(n(\mathbf{r}, t)\, \overline{\sigma}_{\text{abs}}\, \varphi(\mathbf{r}, t) \right) * \left(\sum_i^N R'_i(t) \right) . \tag{2.26}$$

Here, n again is the number concentration of the absorbing molecule. As described in the previous subsection, mass diffusion can be considered in the heat source rate by multiplying the relaxation response by the local diffusion impulse response $n'_i(\mathbf{r}, t)$ for each species i and additionally conducting a spatial convolution:

$$q_H(\mathbf{r}, t) = \left(n(\mathbf{r}, t)\, \overline{\sigma}_{\text{abs}}\, \varphi(\mathbf{r}, t) \right) \circledast \left(\sum_i^N R'_i(t)\, n'_i(\mathbf{r}, t) \right) . \tag{2.27}$$

Here, the symbol $\circledast$ denotes the convolution in space and time.

For a Gaussian excitation source, the spatial convolution of the excitation source and the diffusion impulse response is given by Eq. (2.21), which, for a sufficiently constant number concentration of absorbing molecules, results in a heat source of:

$$q_{H,Gaussian}(r, t) = \left(n\, \overline{\sigma}_{\text{abs}}\, \varphi_0(t) \right) * \left(\sum_i^N \frac{R'_i(t)}{1 + 2t/\tau_{m,i}}\, e^{-2r^2/w^2(1+2t/\tau_{m,i})} \right) . \tag{2.28}$$

When collisional relaxation progresses much faster than the excitation source varies in time ($\sum_i R'_i(t) \longrightarrow \delta(t)\Delta E$) and mass diffusion does not play a role, the heat source rate reduces to the result given at the beginning of this section, Eq. (2.16).

Heat Production for a Harmonically Excited Two-Level System

In certain idealized conditions and with assumptions about the radiation source and the transition rates, a simplified analytical relation for the source rate of heat production can be obtained for a two-level system with upper and lower state populations n_u and n_l, respectively.

As a more complex system can often be interpreted as a two-level system with an effective relaxation time, this result is often quoted for PA and PT measurements in gas mixtures with non-negligible collisional relaxation times [e.g., 88].

The photon irradiance of a harmonic radiation source with modulation frequency f (Hz) and modulation depth b/a (or only the stationary component and a single Fourier component) can be written as

$$\boldsymbol{\varphi}(\mathbf{r},t) = \frac{I(\mathbf{r})}{h\nu}\left(a + b\,e^{i\omega t}\right) \ , \tag{2.29}$$

where $\omega = 2\pi f$ is the angular frequency. A bold italicized font is used to indicate complex quantities.

Without accounting for mass diffusion (or when the irradiation is uniform in the region of interest), the time dependent upper state number concentration, the solution to Eq. (2.19), takes the steady state form [83]

$$\boldsymbol{n_u}(\mathbf{r},t) = n\tau_E\left[k_{lu} + \overline{\sigma}_{\text{abs}}\frac{aI}{h\nu} + \overline{\sigma}_{\text{abs}}\frac{bI}{h\nu}\frac{\tau_E(k_{ul} - k_{lu} + A_{ul})}{\sqrt{1 + (\omega\tau_E)^2}}\,e^{i(\omega t - \phi)}\right] \ . \tag{2.30}$$

Here, $n = n_l + n_u$ is the overall number density of the considered absorbing molecule and τ_E is the effective excitation relaxation time,

$$\tau_E = \left(k_{ul} + k_{lu} + 2\overline{\sigma}_{\text{abs}}\frac{aI}{h\nu} + A_{ul}\right)^{-1} \ . \tag{2.31}$$

The introduced phase ϕ (rad) is the effective phase lag betsween excitation and deexcitation,

$$\phi = \arctan(\omega\tau_E) \ . \tag{2.32}$$

For the (idealized) conditions of

1. negligible spontaneous emission ($A_{ul} \ll k_{ul}$),
2. a low fraction of molecules in the upper state ($n_u/n_l \approx k_{lu}/k_{ul} \ll 1$; by detailed balance – RHS holds around room temperature [84]),
3. low excitation rates, i.e., negligible stimulated emission ($\overline{\sigma}_{\text{abs}}\varphi \ll k_{ul}$),

the upper state number density Eq. (2.30) reduces to

$$\boldsymbol{n_u} \approx n\tau_E\left[k_{lu} + \frac{\overline{\sigma}_{\text{abs}}I}{h\nu}\left(a + \frac{b}{\sqrt{1 + (\omega\tau_E)^2}}\,e^{i(\omega t - \phi)}\right)\right] \ , \tag{2.33}$$

with $\tau_E \approx k_{ul}^{-1}$. Setting $E_l = 0$ and using the fact that the upper state energy equals the photon excitation energy, $E_u = h\nu$, the heat source rate according to Eq. (2.25) is

$$\boldsymbol{q_H}(\mathbf{r},t) = n\,\overline{\sigma}_{\text{abs}}\boldsymbol{I}(\mathbf{r})\left(a + \frac{b}{\sqrt{1+(\omega\tau_E)^2}}\,e^{i(\omega t-\phi)}\right) \tag{2.34}$$

$$= q_{H,0} + \boldsymbol{\delta q_H}\,e^{i\omega t} \tag{2.35}$$

The stationary heating $q_{H,0}$ described by the first term results in a continuous temperature rise in the sample until an equilibrium with the surrounding is reached. This is usually neglected in photoacoustic considerations, as only the time varying part significantly contributes to the acoustic pressure signal generation (cf. Eq. (2.67)). The photoacoustically relevant amplitude $\boldsymbol{\delta q_H}$ of the harmonic heating thus is directly proportional to the number concentration of the absorbing species and the modulated component of the irradiance,

$$\boldsymbol{\delta q_H}(\mathbf{r},t) = n\,\overline{\sigma}_{\text{abs}}\boldsymbol{I}(\mathbf{r})b\boldsymbol{\eta} \tag{2.36}$$

$$= \overline{\alpha}_{\text{abs}}\boldsymbol{I}(\mathbf{r})b\boldsymbol{\eta}\ , \tag{2.37}$$

where effects introduced by the finite relaxation time τ_E are collected in the so-called *conversion efficiency* (or heat yield)

$$\eta = |\boldsymbol{\eta}| = \left|\frac{1}{\sqrt{1+(\omega\tau_E)^2}}\,e^{-i\phi}\right| < 1\ . \tag{2.38}$$

This efficiency eventually determines the instrument sensitivity, as it is directly proportional to the generated photoacoustic or photothermal signal when harmonic modulation is applied. Thus it can be used to quantify collisional relaxation times in the order of the modulation period by studying the photoacoustic signal. Figure 2.6 shows the effects of a variation of the modulation frequency or the relaxation time on the heat conversion efficiency and phase lag.

With increasing frequency (or relaxation time) a gradual transition from full conversion efficiency below $\omega\tau_E = 0.1$ to a practically fully suppression of the relevant/usable heat rate above $\omega\tau_E = 100$ can be observed. For $\omega\tau_E = 1$, the signal amplitude already decreases to $1/\sqrt{2}$ times its initial value. When effective collisional relaxation rates at chosen modulation frequencies result in an $\omega\tau_E$ in the above range, small variations in the gas composition may result in a considerable variation of the setup sensitivity. In addition to the effects on signal amplitude, an increasing phase lag is introduced with increasing $\omega\tau_E$, which is detectable by common phase-sensitive detection techniques (i.e., lock-in amplifiers) and may also be used to detect possible variations of the excitational relaxation time with gas composition. Analogous expressions can also be derived for the excitation (heating) of absorbing colloidal particles, where the thermal relaxation time of the particle limits and delays the generated photoacoustic response in the dispersion medium [e.g., 113].

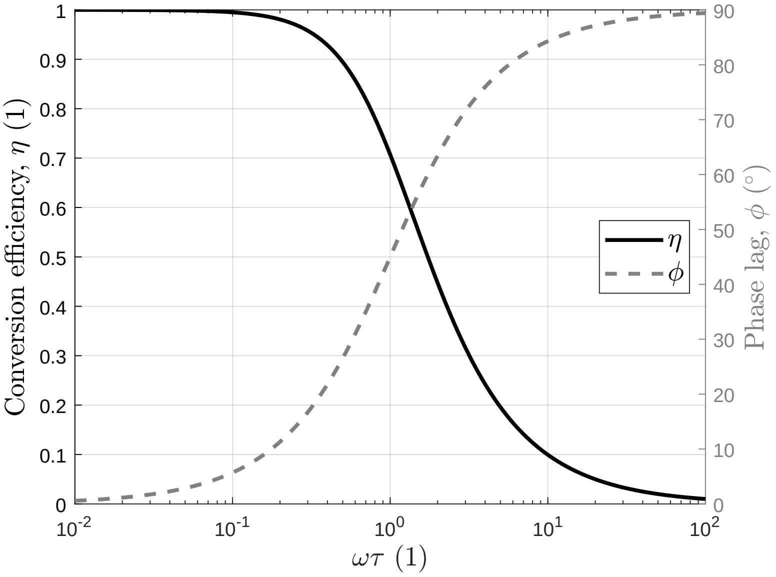

Fig. 2.6 Heat conversion efficiency and phase lag for a modulated radiation source calculated as a function of the product of modulation frequency and effective relaxation time, $\omega\tau_E$.

2.3.2 Acoustic and Thermal Mode Gas Dynamics

The heat released by excitational relaxation increases the thermal energy (temperature) of the gas, which itself is converted to either radiation, phase transition or density and pressure variation [109]. Generation of thermal radiation is the preferred pathway in laser-induced incandescence (LII) techniques for the detection and characterization of aerosols [114]. Typical PAS and PTS CW laser powers of up to 1 W and corresponding irradiances only induce small (acoustic) thermal disturbances, which do not increase temperature enough to produce significant thermal radiation. Conversion to latent heat by phase transition is usually not an issue for gas samples, but may significantly impact the measurement of liquids or aerosols by evaporation of liquid components [e.g., 113]. PAS and PTS applications are based on the measurement of the pressure and density variation after (modulated) heating of the gas. The pressure and temperature perturbations generated in dependence of the heat production rate are most commonly used for the description of the generated acoustic and thermal waves (modes) and can be derived from gas dynamics.

This subsection is a review of the governing relations describing the similarities and differences between photoacoustic and photothermal signal generation. Since solutions to (almost) arbitrary geometries may nowadays "easily" be found numerically, primary focus is put on the description of the physical processes relevant to the particular applications. Solutions to the final equations, applicable to PAS and PTS for simple geometries are given in Sections 2.3.3 and 2.3.4. The reader more interested in the final equations used to obtain these solutions is referred to the subsection *Linear Gas Dynamics* on page 31.

Starting point of this review are the fluid conservation equations and the equation of state. A full derivation of the equations of motion and energy for fluids with application to small (acoustic) motion can, for example, be found in Chapter 6 of Morse et al. [115]. Mathematical definitions of the applied tensor notation can be found in Panton [116]. Vector quantities are written in bold, tensor quantities in capitalized or greek letters with bold typeface.

Equation of State

The equation of state, providing the relation between density ρ ($\mathrm{kg\,m^{-3}}$), pressure p (Pa) and temperature T (K), in a differential form is given by [116]:

$$\begin{aligned} \mathrm{d}\rho &= \left(\frac{\partial\rho}{\partial p}\right)_T \mathrm{d}p + \left(\frac{\partial\rho}{\partial T}\right)_p \mathrm{d}T && (2.39)\\ &= \rho\left(\kappa_T \mathrm{d}p - \beta \mathrm{d}T\right) \ . && (2.40) \end{aligned}$$

Here, κ_T ($\mathrm{Pa^{-1}}$) is the isothermal compressibility defined by

$$\kappa_T = 1/\rho\ (\partial\rho/\partial p)_T\ , \tag{2.41}$$

and β ($\mathrm{K^{-1}}$) is the thermal expansion coefficient given by

$$\beta = -1/\rho\ (\partial\rho/\partial T)_p\ . \tag{2.42}$$

Conservation of Mass

The mass continuity equation for a gas is given by [116]:

$$\begin{aligned} \frac{\partial\rho}{\partial t} + \nabla\cdot\mathbf{j}_m &= 0 && (2.43)\\ &= \frac{\partial\rho}{\partial t} + \rho\nabla\cdot\mathbf{u} + \mathbf{u}\cdot\nabla\rho\ , && (2.44) \end{aligned}$$

where $\nabla\cdot\mathbf{j}_m = \rho\mathbf{u}$ ($\mathrm{kg\,m^{-2}\,s^{-1}}$) is the divergence of the mass flux or momentum density vector, and $\mathbf{u} = (u_x, u_y, u_z)^T$ is the fluid velocity.

Conservation of Momentum

The three equations for the conservation of momentum may be written as [116]

$$\frac{\partial\mathbf{j}_m}{\partial t} + \nabla\cdot\mathbf{T} = \mathbf{f} \quad (= 0)\ , \tag{2.45}$$

where the symmetrical tensor $\mathbf{T} = \rho\mathbf{u} \otimes \mathbf{u} - \boldsymbol{\sigma}$ is the sum of the momentum flux and the stress tensor $\boldsymbol{\sigma}$ ($\mathrm{N\,m^{-2}}$), with $\otimes$ denoting the outer or tensor product of two vectors ($\mathbf{u} \otimes \mathbf{u} = \mathbf{u}\mathbf{u}^T$). The vector $\mathbf{f}$ ($\mathrm{N\,m^{-3}}$) contains all external body forces, such as gravity or electromagnetic forces, which typically can be neglected in the analysis of PA and PT applications.

The stress tensor may be split up in normal and (viscous) shear stresses,

$$\boldsymbol{\sigma} = -p\mathbf{I} + \boldsymbol{\tau} \tag{2.46}$$

where $\mathbf{I} = \delta_{ij}$ is the identity tensor. The latter contribute to the dissipational losses, reducing PA and PT signals. For Newtonian fluids, the shear stress is a function of the rate-of-strain tensor $\boldsymbol{\varepsilon} = \frac{1}{2}[\nabla \otimes \mathbf{u} + (\nabla \otimes \mathbf{u})^T]$ ($\mathrm{s^{-1}}$) [109]:

$$\begin{gathered}
\boldsymbol{\tau} = 2\eta_s\left(\boldsymbol{\varepsilon} - \frac{1}{3}(\nabla\cdot\mathbf{u})\mathbf{I}\right) + \eta_b(\nabla\cdot\mathbf{u})\mathbf{I}\,, \\
\tau_{ij} = \begin{cases} 2\eta_s\left(\frac{\partial u_i}{\partial x_i} - \frac{1}{3}\nabla\cdot\mathbf{u}\right) + \eta_b\nabla\cdot\mathbf{u} & i = j \\ \eta_s\frac{\partial u_i}{\partial x_j} + \eta_s\frac{\partial u_j}{\partial x_i} & i \neq j \end{cases}
\end{gathered} \tag{2.47}$$

where η_s and η_b are the shear and bulk viscosities (Pa s), respectively. The second term within the brackets corrects for an isotropic dilation included in the rate-of-strain $\boldsymbol{\varepsilon}$ of the considered volume and the last term is the compressional resistance, which accounts for a partly irreversible transfer of translational energy to molecular ro-vibrational energy for poly-atomic gases. This resistance opposes the compression and expansion and results in energy being dissipated and lost as heat, contributing to the attenuation of sound when traveling through the gas.

Separating momentum flux and stress tensor and using the mass continuity equation (2.44), one arrives at a form of the nonlinear partial differential Navier-Stokes equation of motion for an isotropic, viscous, compressible fluid:

$$\begin{gathered}
\frac{\partial(\rho\mathbf{u})}{\partial t} + \nabla\cdot(\rho\mathbf{u}\otimes\mathbf{u}) = \nabla\cdot\boldsymbol{\sigma} \\
\rho\frac{\partial\mathbf{u}}{\partial t} + \mathbf{u}\frac{\partial\rho}{\partial t} + \mathbf{u}\nabla\cdot(\rho\mathbf{u}) + \rho(\mathbf{u}\cdot\nabla)\mathbf{u} = -\nabla p + \nabla\cdot\boldsymbol{\tau} \\
\rho\left[\frac{\partial\mathbf{u}}{\partial t} + (\mathbf{u}\cdot\nabla)\,\mathbf{u}\right] = -\nabla p + \left(\frac{1}{3}\eta_s + \eta_b\right)\nabla(\nabla\cdot\mathbf{u}) + \eta_s\nabla^2\mathbf{u}\,.
\end{gathered} \tag{2.48}$$

where $2\eta_s\nabla\cdot\boldsymbol{\varepsilon} = 2\eta_s\nabla(\nabla\cdot\mathbf{u}) - \eta_s\nabla\times(\nabla\times\mathbf{u}) = \eta_s\nabla(\nabla\cdot\mathbf{u}) + \eta_s\nabla^2\mathbf{u}$ has been used [109].

By separating the vector fluid velocity into $\mathbf{u} = \mathbf{u}_l + \mathbf{u}_t$ with a longitudinal part $\mathbf{u}_l$, for which $\nabla\times\mathbf{u}_l = 0$, and a rotational (or transverse) part $\mathbf{u}_t$, for which $\nabla\cdot\mathbf{u}_t = 0$, and recognizing that the gradient of pressure only contributes to the longitudinal part, the momentum equations for small (acoustic) perturbations may be solved separately for each component [115]. The longitudinal part then is given by

$$\rho\left[\frac{\partial \mathbf{u}_l}{\partial t}+(\mathbf{u}\cdot\nabla)\,\mathbf{u}\right]=-\nabla p+\left(\frac{4}{3}\eta_s+\eta_b\right)\nabla(\nabla\cdot\mathbf{u}_l)\;, \tag{2.49}$$

where the second term in the brackets on the LHS vanishes in the linear approximation, as is shown below. The rotational part only is of importance close to boundaries [115, 109], i.e., gas cell or resonator walls in PAS and PTS applications.

Conservation of Energy

Conservation of the specific total energy $E_{tot} = U + E_{kin}$ ($\mathrm{J\,kg^{-1}}$) may be written as [116]

$$\frac{\partial(\rho E_{tot})}{\partial t}+\nabla\cdot\mathbf{j}_E=q_E\;, \tag{2.50}$$

where ρU and $\rho E_{kin}=\frac{1}{2}\rho|\mathbf{u}|^2$ are the internal and kinetic energy density, respectively, and $q_E(\mathbf{r},t)$ is the energy source (or sink) rate ($\mathrm{W\,m^{-3}}$), which in photoacoustic and photothermal spectroscopy is the source heat production rate $q_H(\mathbf{r},t)$. The total energy density flux $\mathbf{j}_E=\rho E_{tot}\mathbf{u}-\boldsymbol{\sigma}\cdot\mathbf{u}-K\nabla T$ ($\mathrm{W\,m^{-3}}$) is composed of convected energy, work done on the fluid and heat conduction. The material parameter K is the thermal conductivity ($\mathrm{W\,m^{-1}\,K^{-1}}$).

Separating the work term into four terms by applying $\nabla\cdot(\boldsymbol{\sigma}\cdot\mathbf{u})=(\nabla\cdot\boldsymbol{\sigma})\cdot\mathbf{u}+\boldsymbol{\sigma}:(\nabla\otimes\mathbf{u})$ and the definition of $\boldsymbol{\sigma}$, Eq. (2.46), the total energy equation is usually split into a mechanical and a thermal energy equation [116]. The double dot in the last equation indicates the scalar tensor product, such that the last term, exploiting the symmetry of $\boldsymbol{\sigma}$, is equal to $\sigma_{ij}(\partial u_i/\partial x_j)=\sigma_{ji}(\partial u_i/\partial x_j)$ in index notation. The mechanical or kinetic energy part contains all terms resulting in acceleration and increase of kinetic energy of the fluid and the remaining thermal or internal energy part is given by

$$\frac{\partial(\rho U)}{\partial t}+\nabla\cdot(\rho U\mathbf{u})=-p\nabla\cdot\mathbf{u}+\boldsymbol{\tau}:(\nabla\otimes\mathbf{u})+K\nabla^2T+q_H \tag{2.51}$$

or

$$\rho\left(\frac{\partial U}{\partial t}+\mathbf{u}\nabla\cdot U\right)=-p\nabla\cdot\mathbf{u}+\Phi+K\nabla^2T+q_H\;. \tag{2.52}$$

In the last step the continuity equation has been applied and the dissipation function $\Phi=\boldsymbol{\tau}:(\nabla\otimes\mathbf{u})$ [116] has been introduced, which is positive everywhere and results in the irreversible transformation of mechanical to internal energy as a result of the viscosity of the fluid.

For many applications, such as photoacoustic and -thermal spectroscopy, it is more appropriate to consider internal energy in terms of temperature. Writing the internal energy change as a function of temperature and density, $dU=c_V dT+1/\rho^2\,\left(p-T(\partial p/\partial T)_\rho\right)d\rho$, and applying the definitions of the isothermal compressibility κ_T (Eq. (2.41)) and the thermal expansion coefficient β (Eq. (2.42)), one arrives at the energy equation in terms of temperature [117]:

$$\rho c_V \left(\frac{\partial T}{\partial t} + \mathbf{u}\nabla \cdot T \right) = \frac{\beta T}{\rho \kappa_T} \frac{\partial \rho}{\partial t} + \Phi + K\nabla^2 T + q_H \ . \tag{2.53}$$

Here, $c_V = (\partial U / \partial T)_V$ is the specific heat capacity (per unit mass; $\mathrm{J\,kg^{-1}\,K^{-1}}$) at constant volume. The heat capacity includes a time or frequency dependence, due to the before mentioned delay during redistribution of translational energy to ro-vibrational energy by molecular collisions (thermalization) or, conversely, the time required for the relaxation of the excited states when the translational energy has been reduced [115]. For sound waves, this behavior of the gas introduces increasing attenuation with higher frequencies, which may be considered by a complex valued specific heat capacity or ratio of specific heats. In air, mainly the already discussed metastable first excited vibrational states of O_2 and N_2 contribute to this delay [118].

The coupled equations for conservation of mass (Eq. (2.44)), momentum (Eq. (2.48)) and energy (Eq. (2.53)) together with the boundary conditions have to be solved to calculate the pressure and temperature response to an external heat source q_H. To arrive at analytical solutions for the description of PA and PT effects, as well as acoustics in general, these equation can be further simplified by only considering small perturbations.

Linear Gas Dynamics

In applications of photoacoustic and photothermal spectroscopy changes in the thermodynamic and fluid variables due to the heat deposited by the radiation are usually small and may be assumed equal to small perturbations of the equilibrium values. The parameters are thus split into the equilibrium values ξ_0, plus the small (acoustic) perturbations $\delta\xi$, where ξ is used to denote any of the thermodynamic variables:

$$p(\mathbf{r},t) = p_0 + \delta p(\mathbf{r},t) \tag{2.54}$$

$$T(\mathbf{r},t) = T_0 + \delta T(\mathbf{r},t) \tag{2.55}$$

$$\rho(\mathbf{r},t) = \rho_0 + \delta\rho(\mathbf{r},t) \tag{2.56}$$

When the mean fluid velocity is assumed zero or small compared to the speed of sound, i.e., $\mathbf{u}_l(\mathbf{r},t) = \delta\mathbf{u}_l(\mathbf{r},t)$, which is a valid assumption for many (but not all) applications, the continuity, momentum and energy equations may be further simplified. For (photo-)acoustic applications, negligible mean velocity refers to velocities much smaller than the speed of sound [115]. In PTS setups, even low fluid velocities may change the local thermal response. A treatment of photothermal spectroscopy considering mean flow can be found in Sell [119].

For zero mean flow, the first-order approximations of the derived conservation equations are

$$\frac{\partial \delta\rho}{\partial t} = -\rho_0 \nabla \cdot \delta\mathbf{u}_l \tag{2.57}$$

$$\rho_0 \frac{\partial \delta\mathbf{u}_l}{\partial t} = -\nabla\delta p + \left(\frac{4}{3}\eta_s + \eta_b\right) \nabla(\nabla \cdot \delta\mathbf{u}_l) \tag{2.58}$$

$$\rho_0 c_V \frac{\partial \delta T}{\partial t} = \frac{\beta T_0}{\rho_0 \kappa_T} \frac{\partial \delta\rho}{\partial t} + K\nabla^2 \delta T + q_H \,. \tag{2.59}$$

In this approximation viscous dissipation (Φ) is neglected. The solution to this system of partial differential equations, showing the theoretical splitting into photoacoustic and photothermal effects, may be found by solving for the density change [84]. However, in PTS the thermal mode is, for historic reasons, most often described in terms of temperature, although primarily density changes are responsible for the measured refractive index changes and a density description delivers more accurate results [84]. To obtain the pressure wave and the temperature diffusion equations in the form they are most often used to describe and approximate both effects individually, the change in density may also be eliminated in Eqs. (2.58) and (2.59) by taking the divergence of Eq. (2.58) and inserting the continuity equation and the equation of state. With the thermodynamic relations [115]

$$c_0 = \frac{1}{\sqrt{\rho_0 \kappa_S}} = \sqrt{\frac{\gamma}{\rho_0 \kappa_T}} \qquad (2.60) \qquad \text{and} \qquad \gamma - 1 = \frac{T_0 \beta^2}{\kappa_T \rho_0 c_V} \,, \qquad (2.61)$$

together with the definitions of the (longitudinal) momentum and thermal diffusivity ($\mathrm{m^2\,s^{-1}}$),

$$D_v = \frac{\frac{4}{3}\eta_s + \eta_b}{\rho_0} = l_v' c_0 \qquad (2.62) \qquad \text{and} \qquad D_T = \frac{K}{\rho_0 c_p} = l_h c_0 \,, \qquad (2.63)$$

respectively, one arrives at the coupled equations which describe the propagation and diffusion of pressure and temperature in a fluid when disturbed by a heat source $q_H(\mathbf{r}, t)$ [115]:

$$\nabla^2 \delta p = \frac{\gamma}{c_0^2} \left(\frac{\partial^2}{\partial t^2} - D_v \frac{\partial}{\partial t} \nabla^2\right) \left(\delta p - \frac{\beta}{\kappa_T} \delta T\right) \tag{2.64}$$

$$D_T \nabla^2 \delta T = \frac{\partial}{\partial t} \left(\delta T - \frac{(\gamma - 1)\kappa_T}{\gamma\beta} \delta p\right) - \frac{q_H}{\rho_0 c_p} \,. \tag{2.65}$$

Here, the constant c_0 ($\mathrm{m\,s^{-1}}$) is the isentropic (adiabatic and reversible) speed of sound, $\gamma = c_p/c_V = \kappa_T/\kappa_S$ is the ratio of specific heats and l_v' and l_h are the two characteristic lengths (m) of viscosity and heat conductivity, which are in the order of the mean molecular free path.

Acoustic and Thermal Modes

The solution to the system of equations (2.64)-(2.65) is a superposition of two solutions, usually called modes [84, 115]. An approximation of the first solution, the *propagating* or *acoustic mode* (actually two modes; the second is for propagation in opposite direction) may formally be obtained by assuming negligible acoustic attenuation through thermal conduction or momentum diffusion, usually summarized by the diffusive constant ($\mathrm{m}^2\,\mathrm{s}^{-1}$) [84]

$$\Gamma = \frac{1}{2}\left[D_\nu + (\gamma - 1)D_T\right] \ . \tag{2.66}$$

With the temporal change of the temperature obtained from Eq. (2.65), Eq. (2.64) then reduces to the inhomogeneous wave equation, describing the generation and propagation of an adiabatic pressure wave as a result of the temporal change of a heat source q_H [84]:

$$\nabla^2 \delta p - \frac{1}{c_0^2}\frac{\partial^2 \delta p}{\partial t^2} = -\frac{\beta}{c_p}\frac{\partial q_H}{\partial t} \ . \tag{2.67}$$

The solutions to this acoustic wave equation are the starting point for optimizing PAS gas cells and amplification by acoustic or mechanical resonators. Considering appropriate boundary conditions, the solution delivers acceptable results for photoacoustic cells where the pressure transducer (microphone, quartz tuning fork, etc.) is placed outside the region affected by the heat source. Thermal and viscous losses (Eq. (2.66)), assumed negligible in the derivation of the wave equation, are typically re-introduced together with other acoustic losses (e.g., acoustic radiation through gas in- and outlets) by introducing a perturbation to the solution of the loss-free Eq. (2.67) [83].

The *thermal mode*, i.e., the response measured in PTS, may be approximated by solutions to the heat/diffusion equation, which arises from Eq. (2.65) when assuming heat dissipation at constant pressure, i.e., when $\delta p \approx 0$ [115]:

$$\frac{\partial \delta T}{\partial t} = D_T \nabla^2 \delta T + \frac{q_H}{\rho_0 c_p} \ . \tag{2.68}$$

Relaxation Time Scales

Before discussing generated acoustic and thermal signals from laser heating in the context of typical PAS and PTS setups, a comparison of the relevant time scales of processes in the two separately considered mode solutions is given in the following.

The thermal (diffusion) mode approximation only describes the sample gas density and temperature around the laser-heated region when considering time scales much longer than the pressure wave relaxation time τ_p, which is the characteristic time for a generated pressure pulse to traverse (or leave) the heat source region [109]:

$$\tau_p = \frac{w}{c_0} , \tag{2.69}$$

where w again is the (Gaussian) beam waist (cf. Eq. (2.4)). For high frequency modulation, both modes need to be accounted for in the description of the sample properties within the heated region. Other relevant timescales include the V–T relaxation of excited molecules, proceeding with the effective excitation relaxation time τ_E, which is the inverse of the overall pseudo-first-order relaxation rate $k = 1/\tau_E$. As already elaborated in Section 2.3.1, the region affected by the heat source does not only include the sample region directly irradiated by the light source, but may also be increased by thermal diffusion and mass diffusion of excited molecules. The spatial redistribution of excited molecules by mass diffusion prior to local V–T relaxation has to be considered when the excitational relaxation time of some component, carrying a considerable fraction of the excitation energy, is significant compared to the characteristic time constant τ_m of mass diffusion (Eq. (2.20)). An similar thermal diffusion time constant τ_T exists with respect to Eq. (2.68). These characteristic diffusion time constants are given by [109]

$$\tau_m = w^2/4D_m \tag{2.70}$$

and

$$\tau_T = w^2/4D_T , \tag{2.71}$$

respectively. Also considering the modulation period $\tau_{mod} = 1/f$ of the radiation for intensity modulated laser excitation, a comparison of relaxation time constants allows to identify the applicability of propagating and thermal mode approximations for specific applications.

Fig. 2.7 shows the characteristic time constants for water vapor in air as a function of the sample pressure. The shadowed area indicates the large range of the V–T relaxation times of the reactions occurring in the relaxation chain of water vapor in air and is bounded by the values of two relaxation processes with particularly short and long relaxation times. For laser-based and modulated vibrational excitation of water vapor in air including V–V-transfer to slowly relaxing components (O_2), two distinct regions may be identified:

$\underline{\tau_E, \tau_p \ll \tau_m \approx \tau_T}$: (E.g., V–T relaxation of excited H_2O by H_2O) Absorbed energy is transferred to heat immediately. The pressure response thus follows the modulation of the irradiation without any significant phase delay and the response is solely determined by the absorbing gas number concentration. Mass diffusion is practically absent and does not influence the acoustic and thermal mode signals.

$\underline{\tau_p \ll \tau_m \approx \tau_T < \tau_E}$: (E.g., V–T relaxation of excited O_2 by O_2 or N_2) Slow V–T relaxation results in reduced amplitudes of the source heat rate amplitude (cf. Eq. (2.38)). The long lifetime excited molecular species is subject to considerable mass diffusion, additionally lowering the local acoustic pressure and temperature response. When the gas cell volume is small, relaxation of excited molecules at the cell walls may have to be considered (heterogeneous relaxation). Increasing gas pressure decreases the excitational lifetime and simultaneously increases thermal and mass diffusion

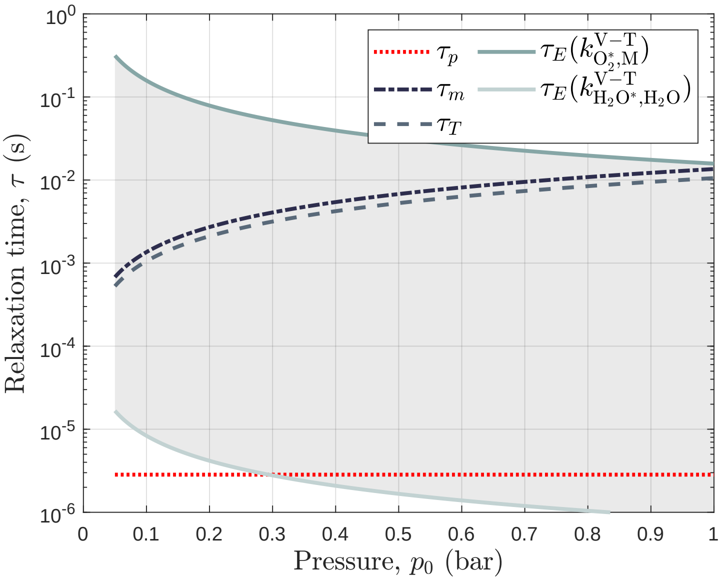

Fig. 2.7 Relaxation time scales of propagating and thermal mode relaxation in humid air for modulated excitation of water vapor and molecular oxygen (O_2) as a function of ambient pressure and at a temperature of 35 °C. Symbols are explained in the text. The beam waist w is assumed 1 mm and the water vapor mole fraction x_{H2O} is 1000 ppm. V–T relaxation is calculated for deexcitation of $H_2O(0,1,0)$ by H_2O and $O_2(1)$ by M = $\{O_2, N_2\}$ ($k_i = n_j\ k_{ij}^{\mathrm{V-T}}$ with $k^{\mathrm{V-T}}_{\mathrm{O}_2^*,\mathrm{M}} = 2.7 \times 10^{-18}\,\mathrm{cm^3\,molec^{-1}\,s^{-1}}$ and $k^{\mathrm{V-T}}_{\mathrm{H_2O^*,H_2O}} = 5.1 \times 10^{-11}\,\mathrm{cm^3\,molec^{-1}\,s^{-1}}$ [120]. $n_j = x_j\,p_0/(k_B\,T_0)$). The mass diffusivity is taken for O_2 in air as $D_m = 0.176\,\mathrm{cm^2\,s^{-1}} \times (T_0/T_{ref})(p_{ref}/p_0)$ [111]. Humid air thermal diffusivity has been calculated using the Coolprop library [121].

timescales. Hence, improved conversion efficiency is achieved by increasing the measurement pressure [122].

2.3.3 Photoacoustic Spectroscopy

A multitude of PAS techniques and setups has been developed to measure the acoustic wave generated in response to the heating. The generated electronic signal magnitude (and solutions to the wave equation), therefore, heavily depends on the geometry and setup applied. Components common to basic PAS setups are indicated in Fig. 2.8.

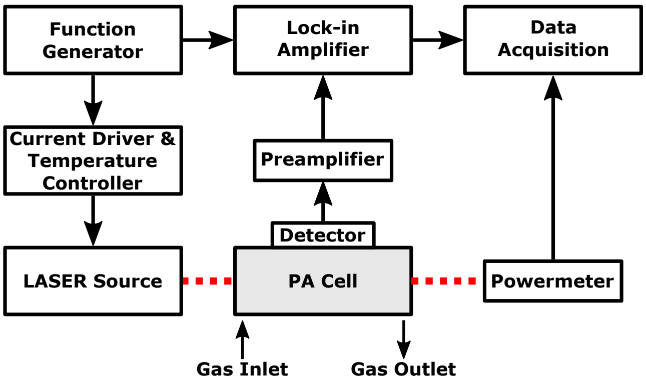

Fig. 2.8 Schematic of a basic PAS setup.

The radiation source (laser, LED [123, 124], etc.) is modulated either in amplitude (AM), i.e., power, or wavelength (WM) [125] by modulating the source current at the modulation frequency f (Hz) with a function generator, or as is the case for WM, applying a more sophisticated current modulation. AM may also be achieved by other means (chopper wheel, acousto-optic modulator, etc.). WM generates higher harmonic signals ($2f$, etc.) at frequencies less affected by laser and ambient noise [126] and is usually combined with a slower sweep of the wavelength over an absorption line. Due to the superior achievable signal-to-noise ratios (SNRs), partly from a decreased background signal of the gas cell windows at the modulation frequency, and the potential for calibration-free measurement [127], WM is state-of-the-art in PA trace gas sensing [77]. Reduced window or cell wall background signal results from the wavelength-continuous absorption of most solids in typical laser wavelength-tuning ranges. However, for the same reason, only AM can be applied for the measurement of aerosols [114]. In most cases, modulation at high frequencies desirable, as the magnitude of electronic and ambient acoustic noise generally shows a $1/f$ dependence [128]. The modulation frequency is typically set equivalent or close to the resonance frequency of an acoustical or mechanical resonator used to resonantly amplify the acoustic wave signal. Heating of the sample gas by the absorbed modulated radiation generates the resonantly enhanced acoustic wave in an appropriately designed gas cell (PA cell), which then is sensed by a pressure transducer. In addition to single-pass configurations, optical multi-pass cell design may also be realized, increasing the deposited amount of heat. Monitoring of the radiation power is used to ensure steady operating conditions and/or to correct the signal for power variations. For the enhancement and the measurement of the pressure of the signal, *conventional PAS*, *quartz-enhanced photoacoustic spectroscopy* (QEPAS) and optical detection (e.g., *cantilever-enhanced photoacoustic spectroscopy*; CEPAS) are most commonly applied. Conventional PAS instruments, e.g. the AquaSense PAS hygrometer, use acoustic resonance chambers (acoustic resonators) to amplify the acoustic wave during measurement with miniaturized, typically high-sensitivity electret condenser or MEMS [129] microphones. Due to the relative ease of implementation, PAS using acoustic resonance chambers and commercial microphones has brought forward a great number of different realizations. Such configurations and associated key aspects are discussed in more detail in the following subsection. However, a more extensive and general review about the application of acoustic resonators can be found in [83, 109, 128]. QEPAS-setups apply millimeter- to centimeter-sized piezoelectric quartz tuning forks at a flexural resonance mode frequency of about 32.8 kHz, often in combination with acoustic (micro-) resonators, to amplify the pressure wave before a measurement of the piezoelectric current, achieving amplifications (Q factors) above 10,000 at atmospheric pressures [130]. Detailed reviews about the operating principle and the variety of applied detection schemes can be found in [131] and [130]. QEPAS-based gas measurement bears the advantage of high miniaturization potential, due to the small size required for the detection module. In CEPAS and similar optical detection techniques [132] the pressure level in the gas cell is measured from the deflection of a micro-mechanical cantilever or diaphragm, sensed either interferometrically or by the deflection of a leaser beam [133]. Detection of the electronic signal generated by the transducer is accomplished (typically after preamplification) by phase-sensitive detection, i.e., with a lock-in amplifier, at the frequency of modulation ($1f$) or some higher harmonic thereof ($2f$, etc.) in the case of WM.

Photoacoustic Signal of Acoustic Resonators

Although non-resonantly operated PA cells are sometimes used, the majority of applications is based on setups where the radiation source is modulated at a frequency matching a resonance frequency of the PA cell. Due to the superior performance with Q factors above 500 [134], acoustic resonators employed are usually either cylindrical resonators (azimuthal [81], radial [134], longitudinal mode [82, 135]) or Helmoltz resonators [136, 137]. However, also rectangular cavities with Q factors above 100 have been presented [138]. In the optimization of PA cells (achieving maximum SNR), multiple cell design constraints have to be considered. These can be partially derived from the theoretical expression of the PAS signal obtained for a specific configuration.

The analytical (pressure) solution to the inhomogeneous acoustic wave equation Eq. (2.67) for an arbitrary resonator is usually given in terms of a Fourier transform and expansion of the (complex valued) lossless eigenmodes $\boldsymbol{p}_j(\mathbf{r})$ (normal modes) of the specific resonator

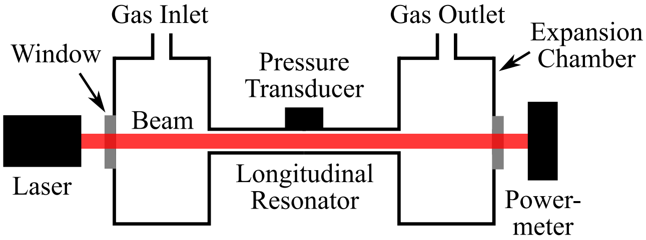

Fig. 2.9 Schematic of a basic photoacoustic cell with a longitudinal resonator operated at the fundamental resonance frequency.

with eigenfrequency ω_j and complex valued amplitudes $\boldsymbol{A}_j(\omega)$ (Pa), i.e., [83]

$$\delta \boldsymbol{p}(\mathbf{r},\omega) = \sum_j \boldsymbol{A}_j(\omega)\boldsymbol{p}_j(\mathbf{r}) \tag{2.72}$$

with

$$\boldsymbol{A}_j(\omega) = -\frac{i\omega\,[(\gamma-1)/V_c]\int_{V_c}\boldsymbol{p}_j^*\boldsymbol{q}_H\mathrm{d}V}{\omega_j^2-\omega^2-i\omega\omega_j/Q_j}\,, \tag{2.73}$$

where V_c (m^3) is the volume of the sample gas cell, Q_j (1) denotes the Q factor of mode j and $\boldsymbol{p}_j^*$ is the complex conjugate of the eigenmode. The Q factor corresponds to the amplification at the resonance frequency and is determined by all loss mechanisms contributing to dampening of the resonant mode. The integral in A_j is termed the overlap integral [128] and determines the coupling of the source heat production rate with the eigenmode [83]. To maximize the resulting pressure amplitude and, thus, the signal, this integral has to be maximized by a suitable resonator mode choice or resonator design and the alignment of the laser beam. Together with the practical losses given by the Q factor, this narrows the choice of reasonable cell designs to rather simple resonator geometries operated at the fundamental resonance frequency or low harmonics. The above expression also holds for the non-resonant mode $\omega_j = 0$ [83].

For a resonantly operated PA cell, the resulting pressure signal amplitude at the resonance frequency and the position $\mathbf{r}_M$ of the pressure transducer can be given by assuming a heat production rate $\boldsymbol{q}_H$ with the conversion efficiency $\boldsymbol{\eta}(\omega)$ of a two level-system, Eq. (2.37), and irradiation by a collimated Gaussian laser beam, Eq. (2.5):

$$\delta \boldsymbol{p}_j(\mathbf{r}_M,\omega_j) = \frac{(\gamma-1)\,\boldsymbol{F}_j\,Q_j}{V_c\omega_j}\,bP_0\,\overline{\sigma}_{\mathrm{abs}}\,n\,\boldsymbol{\eta}\,, \tag{2.74}$$

where $\boldsymbol{F}_j = \int_{V_c} 2/(\pi w^2)\,\boldsymbol{p}_j^*\,g(r)\,e^{-\overline{\sigma}_{\mathrm{abs}}n_i z}\mathrm{d}V$. The fraction is usually termed the cell constant $\boldsymbol{c}_j$ (Pa m W^{-1}) and characterizes the complete interaction of the heat source and the acoustic resonator for a given measurement arrangement [128]. Also including the pressure transducer (microphone) sensitivity $\boldsymbol{s}(\omega)$ (V Pa^{-1}) and a possible background source pressure $\boldsymbol{p}_B(\omega)$ (e.g., windows, flow, external) [88], one arrives at the photoacoustic signal amplitude $\boldsymbol{S}_j$ (V) at the resonance frequency ω_j

$$\boldsymbol{S}_j = bP_0\,\boldsymbol{s}\,\left(\boldsymbol{c}_j\,\overline{\sigma}_{\text{abs}}\,n\,\boldsymbol{\eta} + \boldsymbol{p}_B\right)\ . \tag{2.75}$$

For gases containing multiple radiation absorbing species, the above expression has to be adapted accordingly [88].

PA Setup Optimization

For a modulated laser radiation source, the absolute value of the microphone signal amplitude, loosely called PA signal, can be seen to linearly depend on the modulated power, as long as background signal and the signal generated in the gas are linear in the the modulated power. Therefore, the SNR of the PA signal can typically be improved by decreasing the relative intensity noise of the laser, and the signal-to-background-noise ratio (excluding laser power noise) can be improved by increasing the modulated part of the laser power. In the special case or concentration range where the conversion efficiency, the cell constant (through $\boldsymbol{F}_j$) and the absorption cross section only negligibly depend on the absorbing gas species concentration, the PA signal will be linear in the absorbing species concentration as well. Due to the inverse dependence on ω_j, the signal decreases with $1/f$, which counterbalances the benefit of choosing high modulation frequencies to decrease noise from sources with $1/f$ dependence. Additionally, it can be shown that the integral $\boldsymbol{F}_j$, for optically thin and short absorption path lengths L (m) overlapping with the resonance mode, is directly proportional to L [128]. This results in an overall L/V_c-dependence (i.e., inverse effective resonator cross section dependence) of the signal, which can be exploited to increase the cell constant by decreasing the cell cross section. This results in an improvement until, at typical diameters of a few mm [128], increasing surface/wall losses decreasing the Q factor counterbalance the improvements. This additional dependence arises from the direct proportionality to the Q factor included in the cell constant.

The Q factor in Eq. (2.73) corrects for the acoustic mode damping/attenuation by all loss mechanisms neglected during the derivation (cf. Section 2.3.2). Such losses include heat conduction and viscosity driven dissipation within the bulk and at the cell walls or the microphone, as well as acoustic radiation through cell openings [83]. Although often considered negligible, bulk losses resulting from frequency dependent attenuation of sound by heat conduction, viscosity and the finite time for thermalization of rotational and vibrational energy may contribute humidity dependent losses in air. This is mainly due to humidity dependent relaxation time constant of vibrationally excited O_2 and N_2 (cf. Section 2.3.1). The resulting bulk attenuation, particularly affecting high Q and high frequency acoustic resonators, is shown in Fig. 2.10.

Acoustic radiation losses through gas in- and outlets are typically minimized by placing the openings close to the pressure nodes of the chosen resonance mode [139] or by designing appropriate high impedance acoustic terminations at the openings that confine the resonance mode [128]. The latter can be achieved by acoustic band-stop (quarter-wavelength resonators)

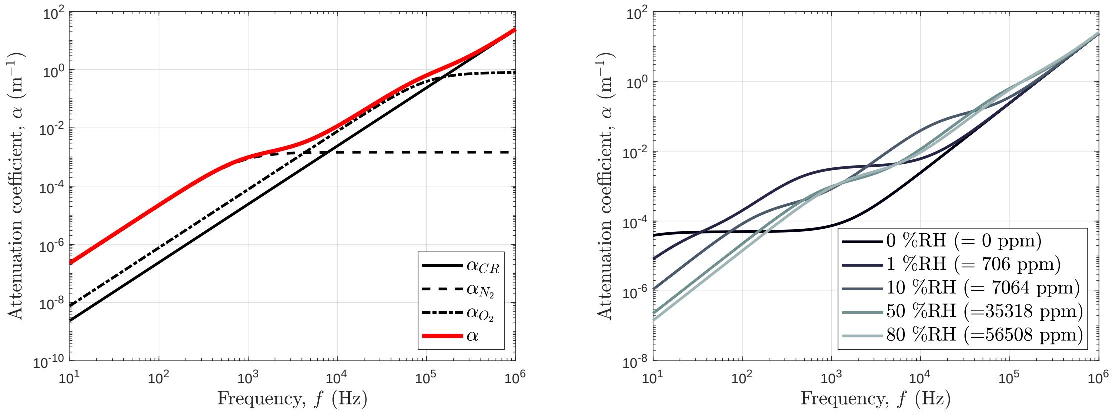

(**a**) Attenuation coefficient components

(**b**) Total attenuation coefficient

Fig. 2.10 Attenuation coefficient of sound in humid air, calculated for 35 °C and 800 hPa [118]. α_{CR}, α_{N_2} and α_{O_2} indicate contributions from heat conduction / viscosity / rotational thermalization, vibrational thermalization of N_2 and O_2, respectively. (**a**) Components of attenuation coefficient at 50 %RH. (**b**) Total sound attenuation coefficient at varying relative humidities.

[134] or low-pass filters (expansion chambers) [140]. Placing openings at the nodes also decreases the effectiveness of noise (ambient of flow noise) entering and exciting the resonator [83]. Acoustic filters are used to suppress external acoustic noise, otherwise entering and exciting the resonator or reaching the microphone. However, care must be taken in the design of acoustic filters and the placement of windows to avoid the generation and measurement of background signals from absorption and photoacoustic effects at the windows [128]. Significant reductions of the background signal can also be achieved with the above mentioned wavelength modulation of the source.

Response Time and Flow Noise

Two further essential points in the design of acoustic filters, and PA cells in general, are the response time and generation of flow noise. To some extent, increasing expansion chamber volume (actually cross section ratio) lower acoustic cut-off frequencies can be achieved for broadband noise [141], however, at the same flow rate gas exchange times and resulting response/recovery times can be increased considerably, if there are poorly flushed volumes. One focus in the design of the PA cell of this work has been put on decreasing measurement response and recovery times to transients in the concentration, as adequate response times are of relevance to many practical gas or aerosol monitoring application, including IWT water content measurement. Especially in the monitoring of polar molecules, such as water vapor, adsorption-desorption processes at the cell walls are known to considerably decrease response times, which can only be shortened by appropriate cell materials, heating and increased gas exchange rates, i.e., flow rates [88, 142, 143]. However, with increasing flow rates expansion chambers (buffer volumes) or other type of changes in PA cell cross section also contribute to the generation of noise, mainly arising from interactions of the flow with the cell walls [144, 145]. Excluding possible excitation of PA cell resonances, this flow noise exhibits a $1/f$-dependence [146]. The high susceptibility to noise in general, and flow noise in particular, is known to be a major disadvantage of PA instruments compared to optical analyzers, limiting achievable response times without a trade-off in minimum detectable concentrations. Flow noise limits mass flow rates in PA cells to typical maximum values of 0.5 to 1.5 slpm [e.g., 88, 147–150]. A nonlinear increase in noise with the flow rate abruptly deteriorates the SNR of PA instruments above these rates [e.g., 88]. A general requirement put forward to maintain minimum noise is a laminar flow through the cell [83]. This theoretically requires Reynolds numbers below the critical transition value of approximately $Re_c = 2300$ [151]. However, most applications are limited to flow rates much lower than given by the critical Reynolds number [142] and achieved response times are typically above 10 s [e.g., 147, 148, 152]. Similar values apply to QEPAS gas sensors [153]. To increase flow rates, Rück et al. [147] have applied rounded edges in their 3D-printed PA cell design, thereby successfully increasing possible flow rates by a factor of 4. Szakáll et al. [140] have applied a differential measurement between two resonators, where only one is actively excited by a laser source, to partially eliminate the effects of flow and external noise sources.

Resonance Frequency Stabilization

In air, the same effect responsible for the humidity dependent attenuation of sound also contributes to the speed of sound being humidity dependent [154]. This dependence results in a shift of the resonance frequency of a resonantly operated photoacoustic sensor with changing water vapor concentration, which increases at higher frequencies. A similar dependence for the speed of sound can be observed for variations in CO_2 [154]. Changes in temperature likewise alter the speed of sound in the PA cell and contribute to the detuning of the resonance frequency from the modulation frequency, which reduces the amplification of the pressure wave according to Eq. (2.73). Therefore, either stabilization of the operating conditions by temperature controlling the PA cell (and sample gas) or active tracking of the resonance frequency is required to maintain constant instrument sensitivity, especially at high Q factors. Resonance characterization and tracking may either be achieved by measuring the frequency dependent response after excitation with a loudspeaker [88], a radiation pulse [155], or a chirped modulation frequency [156]. Characterization by laser excitation, however, requires a sufficiently high analyte concentration to generate a measurable signal when background signals have been efficiently eliminated. Resonance frequency changes from water vapor concentration changes can also be adjusted/corrected from calibration, or estimation according to Eq. (2.73) (cf. **Paper I**).

In addition to the consequences on the resonant amplification, temperature, humidity, as well as pressure may impact microphone sensitivity [103, 88]. Therefore, pressure and temperature calibration or stabilization [82], combined with a calibration for the dependence on humidity are required for the stable operation of a photoacoustic hygrometer.

2.3.4 Photothermal Spectroscopy

In photothermal spectroscopy analyte detection is performed similar to the basic scheme described for photoacoustic spectroscopy (Fig. 2.8), however, sensing of the thermal mode in the gas sample (PT cell) is performed. In PTS either refractive index changes or deformations of surfaces, induced by a change in density through photothermal heating by an excitation beam are utilized to indirectly determine the concentration or other sample properties of interest. Methods targeting the deformation of surfaces are limited to liquid and solid samples. The measurement of gas phase refractive index changes can be accomplished with various detection techniques. In *photothermal lens*, *deflection* and *diffraction spectroscopy*, gradients in the refractive index are detected by the deflection of a probe beam traversing the heated area [157, 119]. Gradients are induced by inhomogeneously heating the sample with a single or multiple excitation beams. Detection or monitoring of the deflection is accomplished using a photodetector.

Refractive index changes may also be detected and measured interferometrically [158]. In *photothermal interferometry* the heated sample is only present in one arm of a (monochromatic) double-path interferometer. The change of refractive index in the sample induces a phase shift in the beam of the measurement arm, which causes a change in the interference pattern after superposition with the reference arm beam. Changes in the intensity measured by the detector of the interferometer can thus be related to refractive index changes of the sample. Typically, only relative measurements of the refractive index are conducted by measuring the difference in the optical path lengths through the photothermally heated and the unheated sample [119]. This can be achieved by either pulsed or modulated operation of the excitation source [112], which may assist in gaining some immunity from low frequency $1/f$-noise [84].

Photothermal interferometry has been demonstrated and applied with a variety of interferometers. Among others, Mach-Zehnder- [e.g., 112, 159], Jamin- [e.g., 160, 161] and Fabry-Pérot-interferometers [e.g., 162, 163] have been applied for gas and aerosol measurement. Figure 2.11 shows the basic setup of a Fabry-Pérot-etalon used for photothermal gas sensing, as applied in this work (right hand side).

Fabry-Pérot Etalon (FPE) Sensor

Campillo et al. [162] have first studied the use of Fabry-Pérot interferometers for photothermal trace detection in gases. The FP cavity is used to amplify the detection sensitivity by a factor depending on the cavity finesse F, compared to the sensitivity achieved in a Mach-Zehnder interferometer. In **Paper III** a commercialized, all-optical FP etalon-based sensor for the measurement of refractive index changes was used. The sensor has been designed for (ultra-)sound pressure measurement [164]. The sensor measures the reflected power of a narrow-linewidth, wavelength-stabilized and monochromatic detection beam from the fiber-coupled FP etalon. The etalon is an open, air-filled cavity and is constructed with rigid spacers between the mirror faces to minimize vibration-induced variations in the cavity

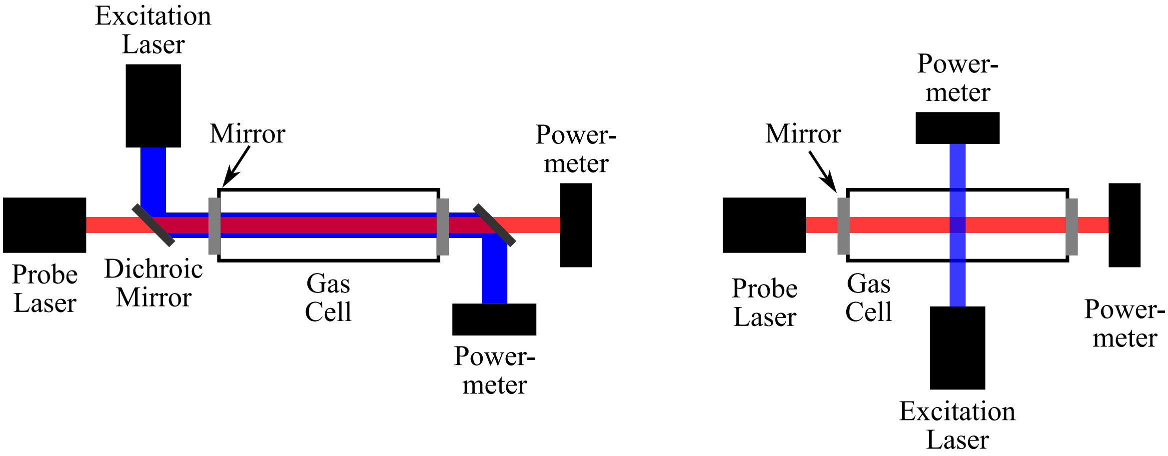

Fig. 2.11 Schematic of a basic photothermal Fabry-Pérot etalon-based PT setup. (**left**) Collinear excitation and probe beam alignment. (**right**) Crossed-beam alignment.

length, which can drastically increase noise in free-spaced FP designs. The reflected power is a function of the beam wave front phase difference $\Delta\phi$ (rad) accumulated per round trip in the cavity. For an idealized plane parallel etalon, the reflectance $R_{\mathrm{FP}}(\phi)$ (1) can be expressed in terms of a transfer function $\mathrm{f}(\Delta\phi)$ (1), relating reflected irradiance I_R and incident irradiance I_0 [165]:

$$R_{\mathrm{FP}}(\Delta\phi) = \frac{I_R(\Delta\phi)}{I_0} = R_{\mathrm{FP,max}}\, \mathrm{f}(\Delta\phi)\ . \tag{2.76}$$

Here, $R_{\mathrm{FP,max}}$ (1) is the maximum achievable reflectance, which is determined by non-ideal losses. The transfer function itself is a function of the optical phase difference and the individual cavity surface (mirror) reflectivity R_{M} (1). Writing the mirror reflectivity in terms of the cavity finesse $F = \pi\sqrt{R_{\mathrm{M}}}/(1 - R_{\mathrm{M}})$ and assuming identical reflectivity for both mirror surfaces, the transfer function can be given as [165]

$$\mathrm{f}(\Delta\phi) = \frac{(2F/\pi)^2 \sin^2(\Delta\phi/2)}{1 + (2F/\pi)^2 \sin^2(\Delta\phi/2)}\ , \tag{2.77}$$

which is the Airy function's complement to one. For the rigid etalon with cavity length l (m) and normal incidence, the round trip phase difference of a partial beam through the open cavity only depends on the wavelength and the refractive index [165, 164]:

$$\Delta\phi(t) = \frac{4\pi\, l\, \mathrm{n}(t)}{\lambda}\ . \tag{2.78}$$

Figure 2.12 shows the theoretical FPE sensor response in dependence of the round trip phase difference. The wavelength of the typically narrow-linewidth detection laser (1550 nm center-wavelength telecommunication laser-diode in this work) is stabilized to a point of maximum sensitivity to refractive index changes for a given average refractive index n_0 [164]. This point corresponds to one of the inflection (or quadrature) points of the periodic transfer function and depends on the cavity air density, temperature, etalon length, etc., along the

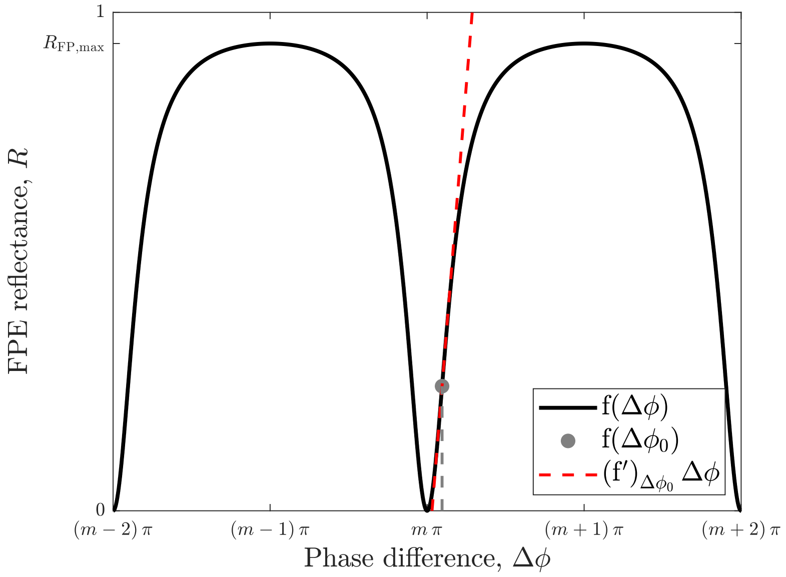

Fig. 2.12 Schematic of the FPE reflectance response to the round trip phase difference ($R_{\mathrm{M}} \approx 0.6$). The gray dot marks one of the inflection points and the red dotted line shows the linear approximation to the small signal response at the inflection point.

detection beam path. Compensation of slow environmental drifts can be accomplished by tracking the wavelength to maintain the low-pass filtered reflected power at a constant value corresponding to the initially determined point of maximum sensitivity. Campillo et al. [162] calculated the inflection points $\Delta\phi_m$, from which the reflectance for small amplitude harmonic excitation $\delta\phi_{\mathrm{osc}}$ in the limit of a high finesse ($(2F/\pi)^2 = \gamma \gg 1$) can be determined:

$$\Delta\phi_m = \pm \arccos\left(1 - 2/(3\gamma)\right) + 2\pi m \ , \tag{2.79}$$

$$\Delta R_{\mathrm{osc}} = \left[\frac{3}{16}\sqrt{3\gamma}R_{\mathrm{FP,max}}\right]\delta\phi_{\mathrm{osc}} \ , \tag{2.80}$$

where $\delta\phi_{\mathrm{osc}}$ and ΔR_{osc} are the (small signal) amplitudes of phase difference and reflectance, respectively. This shows that at the inflection point, to first order, the sensitivity is directly proportional to the finesse. Hence, increasing the FPE finesse allows to increase sensitivity and to balance (within certain limits) sensitivity losses from a design reduction of the cavity length, which is the advantage of an FPE over other interferometer configurations (Mach-Zehnder, etc.) with regard to miniaturization potential.

In the following, a short description of the photothermal mode generation for a collimated Gaussian beam, the refractive index generated and the sensing using interferometers is given.

Collimated Gaussian Beam Thermal Mode

Solutions to the heat/diffusion equation, Eq. (2.68), can be found using a Green's function formalism [119]. Due to the linear nature of the diffusion equation, the radial temperature distribution resulting from a collimated Gaussian excitation source with negligible axial (z-direction) gradient of the deposited heat is the spatial and temporal convolution of the heat source and the point-impulse temperature response (Green's function) $\delta T_{\text{point}}(r,t)$ [84]:

$$\delta T(\mathbf{r},t) = q_H(\mathbf{r},t) \circledast \delta T_{\text{point}}(r,t) \ , \tag{2.81}$$

where the point impulse temperature response to a unit heat impulse at a point $r' = 0$ is given by

$$\delta T'_{\text{point}}(r,t) = \frac{1}{\rho_0 c_p} \frac{1}{4\pi D_T t} \, e^{-r^2/4D_T t} \ . \tag{2.82}$$

Performing the radial spatial convolution for a Gaussian beam profile (Eq. (2.4)) gives the Gaussian beam temperature impulse response [84]:

$$\delta T'(r,t) = \frac{1}{\rho_0 c_p} \frac{1}{(1 + 2t/\tau_T)} \, e^{-2r^2/w^2(1+2t/\tau_T)} \ , \tag{2.83}$$

where τ_T is the characteristic time for thermal diffusion (Eq. (2.71)). This result assumes negligible advection by the possibly moving fluid. Solutions including the effects of a non-zero gas velocity can be found in Sell [119]. Non-radiative relaxation time scales and mass diffusion can be included in the impulse response, if relevant [112]. In this case, the temperature response for an arbitrary excitation source time dependence, including mass diffusion of excited gas components i, is obtained by combining Eq. (2.83) with the general description of a heat source including mass diffusion, Eq. (2.28):

$$\delta T(r,z,t) = \left(\frac{n\,\overline{\sigma}_{\text{abs}}}{\rho_0 c_p} \, \varphi_0(z,t) \right) * \left(\int_0^t \sum_i^N \frac{R'_i(t')\, e^{-2r^2/w^2(1+2t'/\tau_{m,i}+2(t-t')/\tau_T)}}{1 + 2t'/\tau_{m,i} + 2(t-t')/\tau_T} \mathrm{d}t' \right) \ . \tag{2.84}$$

This result assumes simultaneous excitation of all excited components i, but is nevertheless is applicable for situations where only the excitation of one species with long lifetime can be expected (such as excited O_2 or N_2 in air). Solutions for the temperature response to photothermal heating including the effects of mass diffusion can be obtained numerically and can be used to optimize PT cells and setups.

Above approximations assume infinite sample cell dimensions. When excitation times are long enough, thermal conduction at the sample cell walls will conduct away heat much faster than the gas, limiting the maximum sample wall temperature rise to a steady-state value determined by the heat flux through the cell walls [112]. As this temperature for practical materials and temperature-controlled cells is negligibly small, the cell walls can be assumed to be kept at the surrounding/cell temperature. The time up to which the sample temperature can be assumed unaffected by the cell is given by the thermal diffusion time constant for the cell radius r_{cell} (m): $(r_{\text{cell}}^2/w^2)\tau_T$ [84]. Temperature distributions including the effects of thermal conduction for collinear alignment of the excitation beam with a cylindrical sample cell are given by [112].

Refractive Index Change with Temperature

As with the acoustic variables, the refractive index $\mathrm{n}(T, \rho; \mathbf{r}, t)$ can, for small perturbations, be approximated by a mean value n_0 (1) plus a fluctuating part $\delta\mathrm{n}(\mathbf{r}, t)$, caused by the photothermal heating:

$$\begin{aligned} \mathrm{n}(\mathbf{r}, t) &= \mathrm{n}_0 + \delta\mathrm{n}(\mathbf{r}, t) \\ &= \mathrm{n}_0 + \left(\frac{\mathrm{dn}}{\mathrm{d}T}\right)\delta T(\mathbf{r}, t) \; . \end{aligned} \tag{2.85}$$

(An upright n is used for the refractive index to distinguish it from the number concentration n.) The change in refractive index with temperature can, for non-polar gases such as dry air, be approximated using the Lorenz-Lorentz equation, which relates refractive index and density [166]:

$$\begin{aligned} \left(\frac{\mathrm{dn}}{\mathrm{d}T}\right) &= \overbrace{\left(\frac{\partial \mathrm{n}}{\partial T}\right)_{\rho_0}}^{\approx 0} + \left(\frac{\partial \mathrm{n}}{\partial \rho}\right)_{T_0} \left(\frac{\partial \rho}{\partial T}\right)_{p_0} \\ &= -\frac{1}{\rho_0}\left(\frac{\partial \rho}{\partial T}\right)_{p_0} \frac{(\mathrm{n}_0^2 - 1)(\mathrm{n}_0^2 + 2)}{6\,\mathrm{n}_0} \\ &= \beta\, \frac{(\mathrm{n}_0^2 - 1)(\mathrm{n}_0^2 + 2)}{6\,\mathrm{n}_0} \qquad (2.86) \\ &\approx -\frac{\mathrm{n}_0 - 1}{T_0} \; . \qquad (2.87) \end{aligned}$$

The first derivative in the first line is negligible due to the small temperature dependence of the molar refractivity at typical conditions of PTS [84]. The last line results from an ideal gas law approximation for β, together with a first order Taylor series expansion around $\mathrm{n}_0 = 1$. This is the so-called Clausius-Mossotti equation [112, 162]. The series expansion is a valid approximation for gases at atmospheric pressures, as air, for example, has a refractive index of $\mathrm{n}_0 \approx 1.0003$ around standard conditions and a wavelength of 1.550 µm, which is the probe laser wavelength applied in this work. More precise equations for the calculation of the temperature dependence of the refractive index in humid and CO_2 containing air in the visible and near infrared wavelength range are for example given by Ciddor [167].

Photothermal Interferometry

The wavelength-dependent phase change $\delta\phi(r,t)$ (rad) introduced by the photothermal refractive index change $\delta\mathrm{n}(\mathbf{r},t)$ in a constant path length sample cell placed in the single-pass measurement arm of an interferometer and heated by a collinear, collimated Gaussian laser beam is given by [119]

$$\begin{aligned}\delta\phi(r,t) &= \frac{2\pi}{\lambda}\int_{cell}\delta\mathrm{n}(\mathbf{r},t)\mathrm{d}\mathbf{s} && (2.88)\\ &= \frac{2\pi}{\lambda}\left(\frac{\mathrm{dn}}{\mathrm{d}T}\right)\int_{cell}\delta T(\mathbf{r},t)\mathrm{d}\mathbf{s}\,, && (2.89)\end{aligned}$$

where λ (m) is the wavelength of the interferometer (probe) beam. In a configuration with a collinear alignment of detection and excitation beams along the sample path length l (m), where the temperature can be assumed constant along the path (optically thin with regard to the excitation beam), Eq. (2.89) together with the Clausius-Mossotti relation (Eq. (2.87)) may be simplified to [84]

$$\delta\phi(r,t) = -\frac{2\pi\, l}{\lambda}\frac{(\mathrm{n}_0-1)}{T_0}\delta T(r,t)\;. \tag{2.90}$$

Collinear Geometry Harmonic Excitation

Using a modulated excitation/heat source of the form given in Eq. (2.29) induces a continuous temperature increase until heat conduction to the surrounding PT cell walls establishes an equilibrium temperature distribution. On top of this steady-state temperature distribution, an oscillating temperature component,

$$\delta T(\mathbf{r},t) = \delta T_{cw}(\mathbf{r},t) + \delta T_{\mathrm{osc}}(\mathbf{r})\, e^{i(\omega t+\phi)}\;, \tag{2.91}$$

is observed, for which an analytic expression can only be derived for the centerline amplitude of the oscillating part and in the case of negligible mass diffusion [84]. In this case, the temperature amplitude then is given by [84]:

$$\delta T_{\mathrm{C,osc}}(r{=}0) = \frac{n\,\overline{\sigma}_{\mathrm{abs}}\,P_0\,b\,\tau_T}{\pi\,w^2\,\rho_0 c_p}\,|E_1(i\omega\tau_T/2)|\;, \tag{2.92}$$

where $E_1(z)$ is the exponential integral. For $\omega\tau_T \gg 1$, the exponential integral can be approximated by $1/z$. Around standard air conditions and for a beam width above $w = 0.5$ mm, the error lies below 5 % for modulation frequencies above 500 Hz (cf. Fig. 2.13).

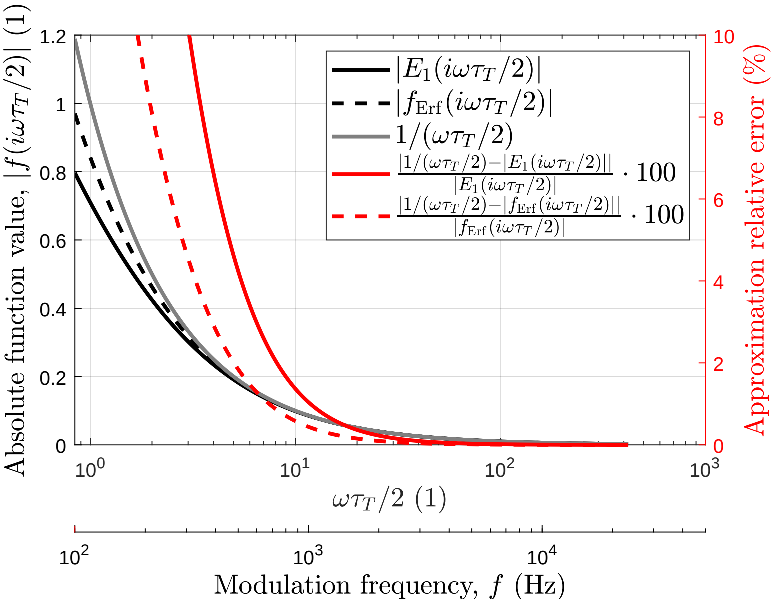

Fig. 2.13 Left hand y-axis shows absolute values of the evaluated exponential integral, the function f_{Erf} and the approximation $1/(\omega\tau_T/2)$ as a function of the product $\omega\tau_T/2$, as well as a function of modulation frequency calculated for air with a beam width of $w = 0.5$ mm and a thermal diffusivity of $D_T = 2.3 \times 10^{-1}\,\text{cm}^2\,\text{s}^{-1}$ (35 °C, 1013.25 hPa). The right hand y-axis shows the relative error of the approximation.

Thus, using Eq. (2.63), the centerline amplitude of the oscillating temperature component may be approximated by

$$\delta T_{\text{C,osc}}(r{=}0) \approx \frac{2\,n\,\overline{\sigma}_{\text{abs}}\,P_0\,b}{\pi\,w^2\,\rho_0 c_p}\,\frac{1}{\omega} \qquad (\omega\tau_T \gg 1)\,, \tag{2.93}$$

which, for a interferometer sample length of l, results in an interferometer centerline phase shift amplitude (cf. Eq. (2.90)) of

$$\delta\phi_{\text{C,osc}} \approx \frac{2\pi\,l}{\lambda}\,\frac{(\text{n}_0-1)}{T_0}\,\frac{2\,n\,\overline{\sigma}_{\text{abs}}\,P_0\,b}{\pi\,w^2\,\rho_0 c_p}\,\frac{1}{\omega} \qquad (\omega\tau_T \gg 1)\,. \tag{2.94}$$

Hence, as in photoacoustic spectroscopy, a general $1/f$ dependence of the temperature and phase shift amplitude can be observed in modulated PT spectroscopy/interferometry. This result has been derived without an axial dependence of the laser power and deposited heat. However, for the small absorption path lengths of the photothermal sensor applied in this work, this does not limit applicability (cf. Section 3.1). As a result, the obtainable PT signal is linear in the excitation beam modulated power. Additionally, the PT signal may be increased by reducing the excitation beam width w.

Crossed-Beam Geometry Harmonic Excitation

As for amplitude modulated excitation in a collinear alignment, the transmission of the (high power) excitation beam through the interferometric optics may considerably increase window background signals, a crossed-beam geometry provides some advantages, although considerably decreasing the interaction length. An analytical expression for fast excitational relaxation can be obtained from Eq.(2.89) by using the fact that

$$\int_{-\infty}^{+\infty} e^{-2(x^2+y^2)/w^2} \mathrm{d}x = \sqrt{\frac{\pi}{2}}\, w\, e^{-y^2/w^2} \,. \tag{2.95}$$

Assuming a probe beam width considerably smaller than the excitation beam width w, the oscillating part of the thermal response then is

$$\delta\phi_{\mathrm{CB}}(t) = -\frac{2\pi}{\lambda}\frac{(\mathrm{n}_0-1)}{T_0}\left[\int_{-\infty}^{+\infty} \delta T_{\mathrm{Gauss}}(x,y,t)\mathrm{d}x\bigg|_{y=0}\right] \tag{2.96}$$

$$= -\frac{2\pi}{\lambda}\frac{(\mathrm{n}_0-1)}{T_0}\left(\frac{n\,\overline{\sigma}_{\mathrm{abs}}}{\rho_0 c_p}\,\varphi_0(t)\right) * \left(\int_0^t \sum_i^N \frac{\sqrt{\pi/2}\, w\, R_i'(t')}{\sqrt{1+2t'/\tau_{m,i}+2(t-t')/\tau_T}}\mathrm{d}t'\right) , \tag{2.97}$$

which for harmonic excitation and a single relaxation path with a collisional relaxational time constant much shorter than the thermal time constant, can be evaluated for the oscillating part of the phase shift $\delta\phi_{\mathrm{CB,osc}}$:

$$\delta\phi_{\mathrm{CB,osc}} = -\frac{2\pi}{\lambda}\frac{(\mathrm{n}_0-1)}{T_0}\frac{n\,\overline{\sigma}_{\mathrm{abs}}\, I_0\, b}{\rho_0 c_p}\frac{\sqrt{\pi}w\,\tau_T}{2}\left|\frac{\sqrt{\pi}\left[1-\mathrm{Erf}(\sqrt{i\omega\tau_T/2})\right]}{\sqrt{i\omega\tau_T/2}}\right|$$

$$= -\frac{2\pi}{\lambda}\frac{(\mathrm{n}_0-1)}{T_0}\frac{n\,\overline{\sigma}_{\mathrm{abs}}\, P_0\, b\,\tau_T}{\sqrt{\pi}\,w\,\rho_0 c_p}\left|\underbrace{\frac{\sqrt{\pi}\left[1-\mathrm{Erf}(\sqrt{i\omega\tau_T/2})\right]}{\sqrt{i\omega\tau_T/2}}}_{f_{\mathrm{Erf}}(i\omega\tau_T/2)}\right| , \tag{2.98}$$

where Erf(z) is the error function. For $\omega\tau_T \gg 1$, the function $f_{\mathrm{Erf}}(i\omega\tau_T/2)$ of the error function can again be approximated by $1/(\omega\tau_T/2)$. Around standard air conditions and a similar excitation beam width as considered for the collinear case ($w = 0.5$ mm), the error is below the approximation for the exponential integral (cf. Fig. 2.13). Thus the anticipated phase shift for an interferometer with transverse alignment of excitation and detection beam is

$$\delta\phi_{\mathrm{CB,osc}} \approx \frac{2\pi}{\lambda}\frac{(\mathrm{n}_0-1)}{T_0}\frac{2\,n\,\overline{\sigma}_{\mathrm{abs}}\, P_0\, b}{\sqrt{\pi}\,w\,\rho_0 c_p}\frac{1}{\omega} \qquad (\omega\tau_T \gg 1) \,, \tag{2.99}$$

Comparing this result to the collinear beam alignment signal (Eq. (2.94)) for comparable sample lengths $l = 2w$, shows that in the crossed-beam configuration the signal is reduced by a factor of $\sqrt{\pi}/2 \approx 0.89$. It can also be seen that by reducing the excitation beam width w for a fixed interferometer path length ($l = const.$), the signal of the collinear aligned interferometer to first order increases with $1/w^2$, while the crossed-beam signal only increases with $1/w$.

2.4 Performance Characterization

In both, photoacoustic and photothermal spectroscopy, several figures of merit based on the signal noise are applied to characterize the performance of a given setup. As in both techniques a setup can, with modifications to the cell and by exchanging the radiation source and optical elements, be used to detect another target gas, these values are often normalized to the effective absorption cross section of the gas, the effective laser power used, as well as the averaging (also integration) time. This, in theory, allows the comparison of different setups and techniques, without the direct need of referring to the specific target gas. Practical limitations, for example, arise from a differing relative power noise of the radiation sources or a differing background signal with accompanying noise. Figures of merit used in this work are introduced in the following.

Signal-To-Noise Ratio

The signal-to-noise ratio (SNR) is the ratio of the signal determined at some nonzero concentration n_S to an estimate of the noise, which is usually determined at zero concentration but otherwise unaltered measurement conditions (regarding flow rate, laser irradiation, integration time constant, etc.):

$$\mathrm{SNR}(3\sigma) = \frac{\overline{S}(n_S)}{3 s_N}\,, \tag{2.100}$$

where $\overline{S}$ (V) is the average background-corrected signal amplitude determined at the nonzero concentration, and s_N is the noise sample standard deviation, often loosely referred to as standard deviation σ. Alternatively, the root-mean-square (RMS) value of the noise is applied in SNR calculation. This, however, is equal to the sample standard deviation when the estimator can be taken as the mean of the noise, which is the case for PA and PT background signals. A threefold of the sample standard deviation is used in the definition of the SNR or the detection limit (see below), as this corresponds to a boundary encompassing roughly 99.7 % of values for a Gaussian noise distribution and, hence, gives a more realistic limit for the discrimination (detection) of a signal from noise than a single standard deviation. At times, the more practically relevant *limit of quantification* is used, referring to $\mathrm{SNR}(10\sigma)$. It is possible to calculate the noise from a nonzero concentration signal, this, however, may lead to increased noise originating from concentration variations created by the sample source (e.g., the humidity generator).

Noise Equivalent Concentration (NEC) and Absorption Coefficient (NEA)

From the SNR, as defined by Eq. (2.100), the minimum detectable concentration or absorption coefficient, equivalent to the defined noise level, are determined by

$$n_{\min} = \frac{n_S}{\mathrm{SNR}} \qquad \text{and} \tag{2.101}$$

$$\alpha_{\min} = \frac{\alpha_S}{\mathrm{SNR}} = \frac{n_S\,\overline{\sigma}_{\mathrm{abs}}}{\mathrm{SNR}} = \overline{\sigma}_{\mathrm{abs}}\,n_{\min}\ . \tag{2.102}$$

These values are also termed *limit of detection* (LOD; n_{LOD} and α_{LOD}, respectively) or *minimum detectable concentration* (MDC). The method of calculation implies a linear dependence of the signal on the target gas concentration. This approximation may not be applicable when concentration-dependent nonlinear effects have to be considered, e.g., originating from a concentration dependence of the collisional relaxation kinetics. In this case, the NEC and NEA can be determined from an appropriate (approximate) function relating the concentration to the signal [e.g., **Paper I**].

Normalized Noise Equivalent Absorption (NNEA)

As the photoacoustic and photothermal signals both are directly proportional to the radiation source power, the NEA may further be normalized with respect to effective power P_{eff} ($P_{\mathrm{eff}} = bP$ for amplitude modulation) to obtain a figure theoretically independent of the specific radiation source. Additionally, for short averaging/integration times τ_{avg} (s), a $1/\sqrt{\tau_{\mathrm{avg}}}$ decrease in noise can be achieved in many instruments since the dominating noise component often is white noise [cf. Allan deviation below; 168]. A decrease in noise and, hence, detection limit achieved by averaging over longer periods of time is normalized by the square root of the measurement equivalent noise bandwidth $\Delta f(\tau_{\mathrm{avg}})$ (ENBW; Hz). The NNEA is therefore calculated from [169]

$$\mathrm{NNEA} = \frac{\alpha_{\min} P_{\mathrm{eff}}}{\sqrt{\Delta f}}\ . \tag{2.103}$$

Generally, the ENBW depends on the specific lock-in amplifier low-pass filter design and order [170]. In good approximation for higher order filters, the −3 dB cut-off frequency $f_{-3\,\mathrm{dB}} = 1/(2\pi\tau_{\mathrm{avg}})$ is sometimes used [e.g., 171].

Allan Deviation

After zeroing and calibration, PA and PT devices are, as any real world system, only stable for a limited amount of time. Temperature drift, laser wavelength or power drift, etc., at some point are larger than the noise for a chosen averaging time. Determination of the Allan deviation (or variance) allows to determine optimum averaging times and precision (minimum detection limits) of gas analyzers, taking into account system drifts [172]. Such analyses are frequently used in PAS and PTS [e.g., 173, 174]. A rigorous description of the application to atmospheric trace-gas monitoring by spectroscopy is given by Werle et al. [168].

The Allan variance $\sigma_{\mathrm{A}}^2(\tau_{\mathrm{avg}})$ of a signal time series S_i is the two-sample variance in dependence of the averaging time τ_{avg}, which is given by the time average of the sample variance of consecutive subgroup averages $A_{s+1}(\tau_{\mathrm{avg}})$ and $A_s(\tau_{\mathrm{avg}})$ [169]:

$$\sigma_{\mathrm{A}}^2(\tau_{\mathrm{avg}}) = \frac{1}{2(m-1)} \sum_{s=1}^{M-1} \left[A_{s+1}(\tau_{\mathrm{avg}}) - A_s(\tau_{\mathrm{avg}})\right]^2 , \qquad \text{with} \tag{2.104}$$

$$A_s(\tau_{\mathrm{avg}}) = \frac{1}{k} \sum_{l=1}^{k} S_{(s-1)k+l} \, . \tag{2.105}$$

Here, M is the number of subgroups ($s = 1 \ldots M$) for the averaging time $\tau_{\mathrm{avg}} = k\Delta t$ in the total measurement time $T = M\tau_{\mathrm{avg}}$ and k is the number of samples per subgroup. As PA and PT signals determined by phase-sensitive detection can be considered as vector signals composed of the in-phase and quadrature components, it is important to perform the above operations on the vector signals instead of the signal magnitudes. Otherwise, the variance will be overestimated.

The square root of the variance, the *Allan deviation* σ_{A}, therefore is an estimate for the standard deviation of the mean signal, examined in dependence of the averaging time at stationary concentrations. Example time series from the zeroing of the PA demonstrator built within this work, together with the Allan deviation plot are shown in Figs. 2.14a and 2.14b, exhibiting a visible drift in the in-phase component of the signal.

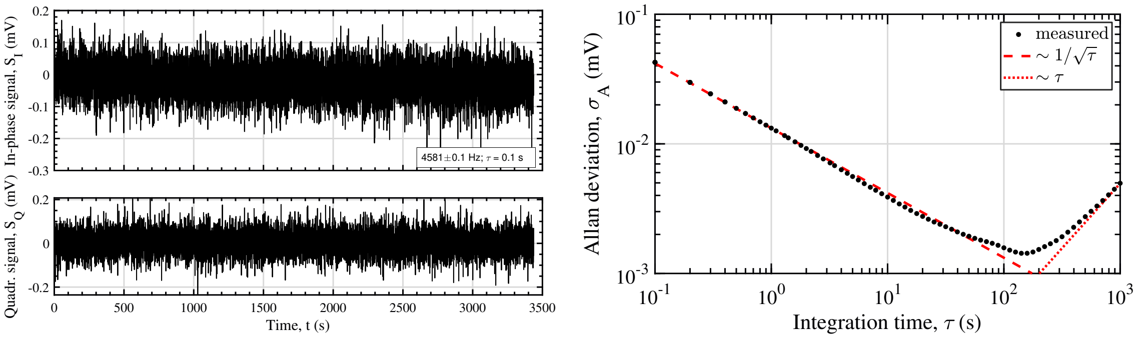

(a) **(b)**

Fig. 2.14 (**a**) In-phase and quadrature signal time series of a measurement with the PAS demonstrator and with zero gas, used in the Allan deviation analysis of **Paper II** to determine optimum averaging times and short-term system stability. (**b**) Allan deviation calculated from the time series of (a), exhibiting typical $\sigma_{\mathrm{A}} \propto 1/\sqrt{\tau_{\mathrm{avg}}}$ noise and $\sigma_{\mathrm{A}} \propto \tau_{\mathrm{avg}}$ drift behavior for shorter and longer than optimum averaging times, respectively.

In the case of Gaussian white noise with standard deviation σ_{N} being the dominant source of the deviations of adjacent subgroup means, the Allan deviation reduces to the standard deviation of the mean of the white noise, i.e., $\sigma_A = \sigma_N/\sqrt{k} \propto 1/\sqrt{\tau_{avg}}$ [168]. This is the case for short averaging times, when the consequences of drift are minor, and results in achievable SNR improvements proportional to $1/\sqrt{\tau_{avg}}$, until drift between larger sample subgroups becomes relevant. At these longer averaging times, dominating linear drift results in an increase of the Allan deviation proportional to τ_{avg} and to the slope of the drift [169]. Thus, by the method of elimination (e.g., measurements with/without flow or irradiation), the Allan deviation analysis allows to determine the source of the dominating drift.

The optimum averaging time, which corresponds to the lowest noise and detection limit achievable by signal averaging, is found at the minimum of the Allan deviation plot. This is the maximum time available for zeroing, performing a measurement and purging the device in between, before drift affects the measurement. The maximum possible measurement and averaging time, hence, is less than half of the optimum averaging time.

2.5 Calibration

In PAS, instrument sensitivity depends on the power of radiation, the resonant acoustic amplification of the PA cell (including radiation source alignment), as well as the pressure transducer sensitivity (cf. Section 2.3.3). As these parameters are subject to short and long term variations and resonant amplification also is a function of the gas temperature and composition, calibration of a water vapor PA gas analyzer with known concentrations of water vapor is necessary [88]. This section is a short review of available methods and the calibration unit implemented in this work.

In light of the nonlinear PA and PT signal obtained for water vapor [**Paper I**] and many other target gases [e.g., 100], calibration over the full target concentration range is preferred over single point calibrations, which cannot capture deviations from the linear signal behavior assumed for quasi-instantaneous collisional relaxation. Additionally, the considerable dependence of the signal generation on the specific buffer gas [107, 175, 153, 1, 100], requires high similarity of the calibration gas to the measurement gas. Ideally, ambient zero air, containing all impurities and scrubbed from water vapor before humidification, should be used for calibration [126]. In practice, contamination and degradation of the humidity source, however, would result from such a method.

Lowest measurement uncertainties can be provided by frequent recalibration of the gas analyzer. Therefore, measurement systems are frequently combined with the calibration unit, to provide a repeatable, automated method of calibration [e.g., 82, 176] or are used in combination with a dedicated calibration bench [e.g., 66]. First PA calibration-free methods, similar to the methods applied in TDLAS [73], have recently been demonstrated for a resonant cell with methane and a QCL [127]. These methods, however, rely on wavelength modulation spectroscopy and, hence, are not applicable to the current version of the PA gas analyzer built in the scope of this work.

2.5.1 Humidity Generators

Various techniques currently are applied for calibration of spectroscopic (trace) water vapor sensors. Overviews of methods in use are given by Wiederhold [177] and Wernecke and Wernecke [178]. Although, gas cylinders with small amounts of water vapor in nitrogen do exist [179], which allow calibration by dilution of the standard gas mixture, saturation type humidity generators are most often used [180]. As a saturation type humidity generator has also been implemented in this work, a detailed discussion is given in the following subsection. A short review of alternative methods applied in the calibration of (atmospheric) water vapor sensors is given in the following. Some calibration benches apply permeation sources, which are solid membranes (e.g., PTFE tubes) immersed in a temperature controlled liquid water bath, where dry synthetic air is passed along the membrane or through the tube to humidify the zero air [66]. Adjustment of the water bath temperature, as well as the dry air flow rate can be used to vary the mixing ratio. As with gas cylinders, permeation sources typically only provide concentrations in the trace gas range [62]. The calibration unit of Thornberry et al. [176] uses the Pt-catalyst based oxidation of variable amounts of hydrogen (H_2) in dry air, a method which is also used as a national primary standard for humidity generation [180]. In principle, concentrations in the range of 1 to 20,000 ppm with an accuracy close to the used H_2 standard accuracy can be achieved [181]. However, these humidity generators are primarily used for trace concentration generation [178] and similar implementations for atmospheric applications only provide concentrations up to 2500 ppm [176].

The basic principle of saturation type humidity generators (HGs) and the generator used in this work, is to saturate synthetic air flowing over a sealed liquid or ice water reservoir (saturator; spiraling/meandering saturation chamber or a gas wash bottle) held at constant temperature, usually by a surrounding termostated bath. Assuring near-equilibrium conditions for saturation, the water vapor partial pressure (saturation pressure) in the air flow may be varied and determined by changing and measuring the saturator temperature. The gas may be saturated first at a higher temperature and cooled to a lower target temperature, condensing excess water in a heat exchanger (condenser).

Precise correlations between saturation vapor pressure $e(T)$ over liquid water and temperature have been established by Saul and Wagner [182] and Wagner and Pruss [183], with validity within the temperature range of 273.16 to 647.096 K and with deviations to experimental data below ±0.1 % [184]. Wexler [185] established formulations for the vapor pressure over ice in the range of −100 to 0 °C. The mentioned correlations do not consider departures of the vapor pressure in mixtures with air and from non-ideal gas-effects [186]. These effects are considered by an *enhancement factor* $f_e(T, p)$, which depends on temperature as well as pressure [187]. In summary, the saturator water vapor mole fraction x_s may be calculated from [177]:

$$x_s = \frac{e_s(T_s)}{p_s} f_e(T_s, p_s) \; , \tag{2.106}$$

where the subscript s is used to denote saturator conditions. In atmospheric sciences, provided humidities are also often given in terms of the (ideal gas) volume mixing ratio VMR = $p_{wv}/(p_s - p_{wv})$ (ppmV) of water vapor with partial pressure $p_{wv} = e(T_s)f_e(T_s, p_s)$ (Pa) to dry air [177].

Saturation type HGs are further divided into three sub-types. In two-temperature HGs, saturation is performed at a temperature lower than the test device measurement temperature and typically at comparable pressures [178]. Eliminating all moisture sinks and sources between saturator and gas analyzer, the output humidity is then controlled by controlling the saturator temperature. The drawback lies in the slow process of changing the saturator temperature, which is limited by the thermal inertia of the saturator and bath. Therefore, calibration over a wide range of concentrations is time expensive and is limited to infrequent repetition. Tátrai et al. [82] have built a two-temperature HG for the calibration of their PA hygrometer *WaSul-Hygro*, operated close to atmospheric pressure. The saturator is cooled to 120 to 140 K with liquid nitrogen and subsequently warmed to room temperature. Calibration measurements at different PA cell pressures are conducted continuously in the volume mixing ratio range of 1 to 25,000 ppmV with a repeatability better than ±0.5 % or ±0.3 ppmV below 60 ppmV. One calibration cycle, however, takes approximately 1.5 days [82], making this technique impractical for frequent recalibration.

The two-pressure humidity generation technique refers to the saturation of an air stream at a higher pressure and, subsequently, expansion of the humidified gas to a lower ambient or measurement pressure [177]. As the pressure dependence of f_e is small, the water vapor saturation pressure, i.e., the product $e_s f_e$ remains approximately constant when the saturation chamber pressure is increased. However, the water vapor mole fraction decreases inversely proportional to the total chamber pressure (cf. Eq. (2.106)), which allows control and variation of the generated humidity by changing the pressure at the location of saturation. When expanding the humidified air to the measurement pressure, the water vapor and air mole fractions remain constant. Accurate temperature and pressure measurement again allows a precise determination of the saturation mole fraction. The capability to precisely control pressure with short response-times via a pressure controller (valves) enables faster variation of the humidity, than with the two-temperature method. Nevertheless, the two-pressure principle is usually combined with a two-temperature operation to further extend the operational range of the HG. It has to be noted that saturation at higher pressures requires the removal of CO_2 from the air prior to saturation, as otherwise carbonic acid would form within the saturator [188].

Humidity variation by diluting or mixing saturated air with dry air is a third possibility of providing different water vapor concentrations for calibration, which may be combined with a two-temperature or -pressure operation [hybrid type; 186, 177]. Mixing additionally requires accurate and precise mass flow measurement and control to minimize concentration uncertainty. Gas diluters with critical orifices offer a method of precise dilution in the ppm range and below [189, 190].

In **Paper I** and **Paper II**, as well as in the PT measurements with the setup of **Paper III**, a two-pressure humidity generator, custom built and integrated into the AquaSense PA measurement system [**Paper II**], was used. For laboratory calibrations, the humidity generator was combined with the gas diluter of Breitegger and Bergmann [190].

A rigorous treatment of the uncertainties in the provided mole fractions of the two-pressure humidity generator according to the *ISO Guide to the Expression of Uncertainty in Measurement* [GUM; 191] as a result of the uncertainties in the saturation chamber temperature and pressure, as well as the correlations for water vapor saturation pressure and enhancement factor, is given by Meyer et al. [188]. As for a (single) chosen pressure transducer, the accuracy is typically highest near the maximum of the full scale operating range, concentration uncertainty is typically highest at low pressures.

For the humidity generator integrated into the AquaSense instrument, Fig. 2.15a shows the provided water vapor mole fraction according to Eq. (2.106) (upper panel), as well as the combined relative and expanded water vapor uncertainty (lower panel) in dependence of the saturator pressure and for two different saturator temperatures most often used in calibration. The uncertainties of the input quantities (temperature and pressure) are summarized in [**Paper II**] and the resulting individual uncertainty contributions to the provided water vapor mole fraction are shown in Fig. 2.15b in dependence of the water vapor mole fraction, again for both temperatures. This illustrates the possibility of generating water vapor mole fractions in the range of 800 to 20,000 ppm with expanded uncertainties below 1 % by only two temperature setpoints and by varying the saturator pressure in the range of 1 to 10 bar. Additionally, Fig. 2.15b shows the current limitation of the humidity generator by the temperature measurement uncertainty of $u(T_s) = 0.16\,\mathrm{K}$. Hence, as mentioned in

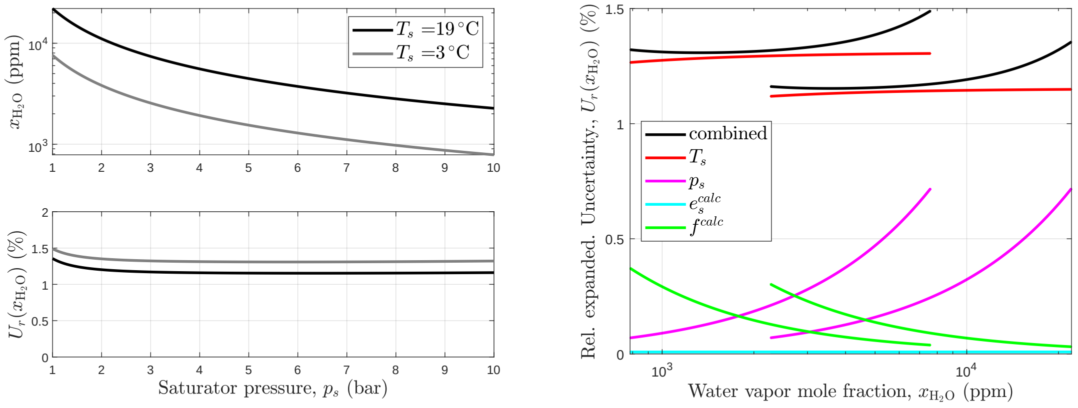

(a) **(b)**

Fig. 2.15 Two-pressure humidity generator operating range of the AquaSense instrument calibration unit. (**a**) Provided Water vapor mole fraction in dependence of saturator pressure for two different saturator temperature setpoints (upper panel) and corresponding combined expanded uncertainty (95 %) in the provided mole fraction (lower panel). (**b**) Expanded combined uncertainty and individual contributions to the water vapor mole fraction uncertainty at the two saturator temperature setpoints in (b). For each color, the right-hand line corresponds to the higher saturator temperature. Calculation according to [188]. Uncertainties of the input quantities (temperature and pressure) are summarized in [**Paper II**].

Paper II, further improvement of the temperature measurement will significantly contribute to increasing the accuracy of hygrometers calibrated by the humidity generator.

Diluting the humidified air with the gas diluter by a dilution factor D_{GD} reduces the water vapor mole fraction to

$$x_{\mathrm{GD}} = D_{\mathrm{GD}} x_{\mathrm{HG}} + (1 - D_{\mathrm{GD}}) x_0 \,, \tag{2.107}$$

where x_{HG} is the humid air water vapor mole fraction provided by the humidity generator and x_0 is the zero air, i.e., the synthetic air water vapor mole fraction, which typically is in the low ppm range. The combined uncertainty in the resulting mole fraction $u(x_{\mathrm{GD}})$ of the humidity generator in combination with the gas diluter is then given by:

$$u^2(x_{\mathrm{GD}}) = D_{\mathrm{GD}}^2 u^2(x_{\mathrm{HG}}) + (1 - D_{\mathrm{GD}})^2\, u^2(x_0) + x_{\mathrm{HG}}^2 u^2(D_{\mathrm{GD}}) \,. \tag{2.108}$$

In this work, the uncertainties introduced by mixing with the gas diluter are taken from Breitegger and Bergmann [190]. It should be noted that the uncertainty in the zero air water mole fraction x_0 is asymmetric with nonzero mean [4.3.8 in 191].

CHAPTER 3

RESULTS AND DISCUSSION

This section contains a concise summary and discussion of the results of this thesis, presented in the form of the three peer-reviewed publications appended in Part II. The discussion, except for the first subsection, is organized according to the order of the articles and, where relevant, contains some additional selected results not contained in the publications. Section 3.1 presents results and a discussion of the response time characterization of the AquaSense PAS hygrometer.

3.1 AquaSense PAS Hygrometer Transient Response

The PA hygrometer described in **Paper I** and **Paper II** was built for icing wind tunnel (IWT) water content measurement in combination with the isokinetic sampling unit of **Paper II**. The PA cell has been designed with the target of achieving high rejection of external noise entering the sampling probe inlets and noise generated within the tubing. Nozzles used to synthesize water droplet distributions to achieve defined icing conditions are some of the high power external noise sources encountered in IWTs. The discharge of air and water through the nozzles is known to create severe noise over a broad band of frequencies [192]. Furthermore, at wind speeds encountered in IWTs, noise arising from turbulent flow is considerable. In addition to the noise rejection requirement, the cell was designed to minimize sources of internal flow noise, targeting short response times by raising the limit of permissible flow rates through the cell. By chamfering the edges at the transitions between the main PA cell duct and the acoustic filters, reduced interactions of separated shear layers with the downstream edges have been anticipated.

To determine the efficacy of the realized cell design with regard to achievable response times, experimental characterizations of the PA cell at varying gas flow rates are shown in Figs. 3.1 and 3.2. Dotted lines in Fig. 3.1a and Fig. 3.1b show the measured signal noise (1σ) in zero air in dependence of the flow rate through the PA cell and a second cell of similar design, respectively. At the lower end of flow rates, signal noise is attributed to electronic noise, ambient acoustic noise and intensity noise of the laser power. Only at flow rates above 3.5 slpm the noise level starts to increase appreciably. This equals a Reynolds number of ≈1000, close to the theoretical critical Reynolds number of $Re_c = 2300$, and demonstrates the advantage of the implemented flow-through PA cell design in combination with chamfered edges of the acoustically short concentric resonators (SCRs), compared to conventional PA cell designs. To further evaluate the benefits of chamfered edges, the cell has been operated with the direction of flow applied opposite to the intended direction (red line in Fig. 3.1b). This revealed an approximately 30 % decrease in the permissible flow rate and confirms a significant impact of the transition edges on the occurring flow noise. From these investigations it is, however, inconclusive, if the same flow-through design with right-angled transitions from the piping elements to the SCRs will achieve similar performance. Omitting the chamfered edges would certainly improve manufacturability of the PA cell.

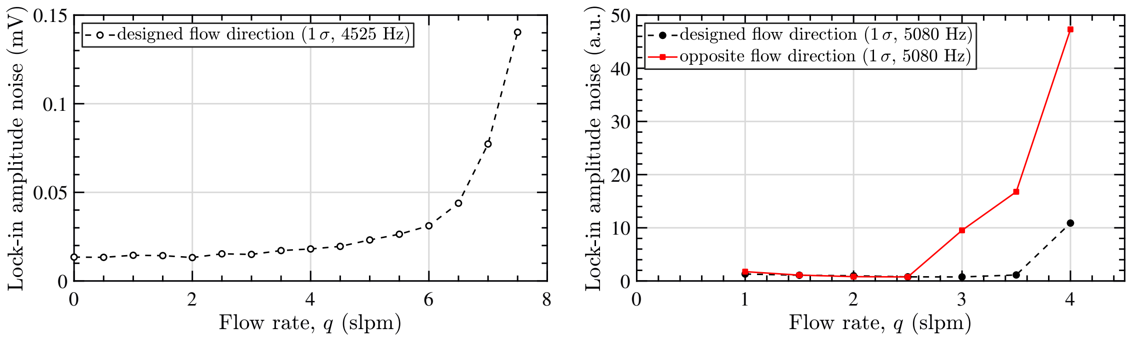

(a) **(b)**

Fig. 3.1 Measured signal noise (1σ) in dependence of the applied gas flow rate. (**a**) Original PA cell design. (**b**) Modified cell with dissimilar resonance frequency, but equivalent internal design. For (b) flow noise was measured with gas flow applied in the design direction and subsequently was applied in the opposite direction (red line). (Measurements of (b) conducted by Markus Knoll.)

To assess the response time of the system, gradients in concentration have been applied to the cell during operation by switching from humidified air to zero air. Figures 3.2a and 3.2b show PA signals obtained for measurements conducted with the unheated cell at flow rates of 1 slpm and 5 slpm, respectively, which correspond to cell volume gas exchange rates of 0.6 s^{-1} and 3.3 s^{-1}. At the lower flow rate, recovery and response times (0 to 63 % relative signal) have been determined to $\tau_{63} = (2.9 \pm 0.2)$ s and $\tau_{63} = (6.2 \pm 0.2)$ s, respectively. The difference in recovery and response time illustrates the consequences of wall adsorption-desorption effects of water vapor at low concentrations when the PA cell is unheated. For cell temperatures above 35 °C, this effect has been shown to be negligible. At the higher flow rate recovery and response times are $\tau_{63} = (0.8 \pm 0.1)$ s and $\tau_{63} = (1.0 \pm 0.1)$ s, respectively, accompanied by a flow noise increase of less than two-fold compared to the 1 slpm case.

The presented response times demonstrate an fair improvement by the flow-through design compared to conventional PAS cells and QEPAS implementations, opening up new possibilities for fast response photoacoustic gas monitoring applications. However,

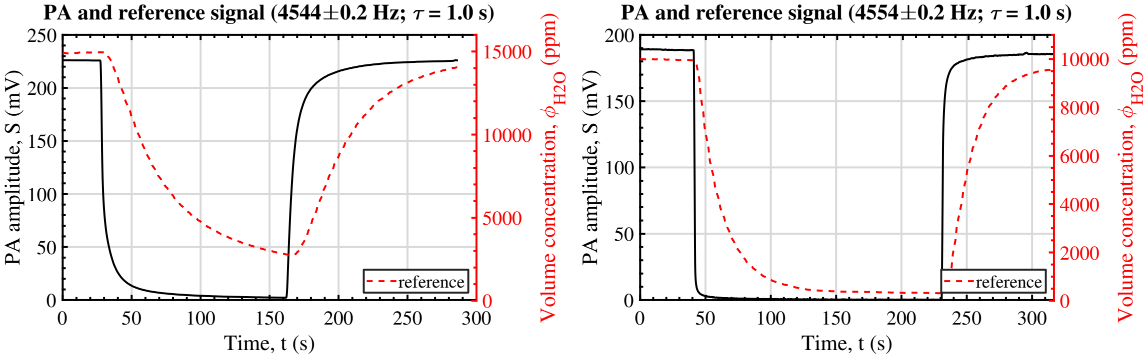

(a) **(b)**

Fig. 3.2 Transient signal response to steps in water vapor concentration between zero and humidified air. Dotted lines show the response of a capacitive humidity sensor (Vaisala Humicap, HMT337) mounted downstream of the PA cell. (**a**) Gas flow rate of 1 slpm. (**b**) Gas flow rate of 5 slpm.

as the normalized noise equivalent absorption coefficient achieved by the present system is approximately an order of magnitude higher than achieved by comparable systems (cf. Section 3.3), minor increases in terms of limit of detection have to be admitted at high flow rate measurement. A comparison to a capacitive humidity sensor (dotted line in Fig. 3.2; Vaisala Humicap, HMT337) additionally shows the benefit of the PA gas analyzer over conventional humidity sensors in terms of response time.

3.2 Vibrational Photoacoustic Spectroscopy of Water Vapor in Air

Paper I addresses the process of photoacoustic signal generation by the thermalization of vibrationally excited water vapor in air. Although some realizations of NIR PA hygrometers with large dynamic ranges are known [78, 81, 82] and a nonlinear relationship between water vapor concentration and generated photoacoustic signal has been mentioned before [193], a linear response has been adopted throughout literature [81, 108, 194, 195]. In the only high-precision and high dynamic range application, a 10th-order polynomial had to be used as a calibration function to include apparent sensitivity changes with water vapor concentration [82]. Using the AquaSense PAS hygrometer, it was demonstrated experimentally that, for typical atmospheric compositions and conditions, the presence of oxygen reduces the sensitivity of a photoacoustic hygrometer up to 80 % at low water vapor concentrations. The gradual reduction in sensitivity towards lower fractions of H_2O was shown to manifest itself in a nonlinear correlation between the generated signal and the amount of water vapor present. This gradual reduction occurs over the full operational concentration range required for IWT water content or atmospheric water vapor level measurement and, hence, was determined to adversely affect the accuracy of photoacoustic and photothermal instruments when using lower or higher order polynomial functions for calibration in combination with a low number of calibration points. The observable nonlinear correlation has now been confirmed by Szakáll et al. [196].

To reduce calibration complexity, a simplifying analytical model describing the excitational relaxation path of $H_2O(1,0,1)$ in air, was set up and used to derive the photoacoustic response and microphone signal for a harmonic excitation source. Similar three-state models have first been used for the description of electronic relaxation of aromatic molecules [110]. The model builds on literature evidence that the thermalization of vibrationally excited water vapor (bending mode) is inhibited by a resonant V–V energy transfer to oxygen, which in air around standard conditions has an average lifetime longer than typical PA modulation periods and, thus, reduces the generated photoacoustic signal. Increasing fractions of water vapor are thought to contribute to the direct thermal V–T relaxation of excited H_2O and the collisional quenching of the metastable oxygen state, thereby speeding up the conversion to translational energy and increasing the signal generation efficiency.

The model has been formulated so to separate setup-specific parameters, i.e., microphone sensitivity, resonator Q-factor, etc., from physical constants (kinetic coefficients and carrier gas composition) into two cell parameters. This aims at facilitating the calibration of future PA or PT hygrometers, requiring only the determination of two setup parameters after a one-time characterization of the physical constants. In the model, physical constants are combined in a separate function describing the modulation frequency dependent signal conversion efficiency, which also allows to generally estimate PA and PT signal generation efficiency in dependence of the water vapor concentration and gas composition for the design and optimization of novel and innovative PA- and PT-based humidity sensing concepts. Section 3.4 presents the satisfying applicability of the conversion efficiency determined during the calibration of the AquaSense PA hygrometer (cf. **Paper I** and **Paper II**) to the signal amplitude provided by a Fabry-Pérot etalon-based photothermal hygrometer. The model is considered valid including modulation frequencies typical for QEPAS (32.8 kHz) down to frequencies used in non-resonant photoacoustic and photothermal applications (e.g., **Paper III**).

The derived calibration function was applied in the calibration of the AquaSense PAS instrument in **Paper II** and enabled calibration over a concentration range of two orders of magnitude (250 to 21.200 ppm) with only 16 calibration points. The resulting measurement accuracy of the PA hygrometer was then determined to be better than 5 % within this range and better than 3.3 % within the range of 510 to 12.360 ppm. Gained confidence in the function describing the conversion efficiency is expected to allow a further reduction in calibration points providing equivalent accuracy, thereby substantially reducing the time necessary for instrument calibration. In addition to the application to water vapor in air, the model proposed by Hunter et al. [110] and applied in **Paper I** is assumed to be adaptable to other gas compositions, where metastable vibrational states reduce conversion efficiency. Systems with observed molecular relaxation effects include mixtures with hydrogen chloride [101], methane [100], carbon monoxide [197] and carbon dioxide [97–99]. For carbon dioxide in a nitrogen-water gas mixture, a similar approach as presented in **Paper I** has been applied by Wysocki et al. [99].

Finally, the evaluation of the physical model constants also provided the opportunity to estimate the forward rate coefficient of the V–T relaxation reaction

$$O_2(1) + H_2O \rightarrow O_2(0) + H_2O \,, \tag{3.1}$$

which is the reason for the increasing conversion efficiency with increasing fractions of H_2O and is of central importance to the description of absorption of sound in air [198, 199] and to atmospheric radiative transfer calculations [106, 200, 201]. The determined rate coefficient of $k = (3.1 \pm 1.7) \times 10^{-13}\,\mathrm{cm^3\,molec^{-1}\,s^{-1}}$ is an order of magnitude higher than estimated by Bass et al. [202] in 1976, which, however, is associated with an order of magnitude uncertainty [199].

3.3 Water Content Measurement with the AquaSense Instrument

Paper II presents the design, operation, calibration and excerpts of the performance evaluation of the assembled AquaSense instrument during a water content probe intercomparison in the Rail Tech Arsenal (RTA) closed-circuit icing wind tunnel.

A major focus in this work has been put on the estimation of the instrument measurement uncertainty, which combines the individual uncertainties of the PA hygrometer and the sampling system, including the IKP. The hygrometer accuracy is given by the uncertainties of the integrated two-pressure humidity generator, the calibration function determined in **Paper I**, as well as measurement precision ($\leq$10 ppm or 0.7 %, where the higher value in absolute terms applies). The latter also determines the minimum detectable water vapor concentration of $\approx$23 ppm (3σ, NNEA = $8.6 \times 10^{-7}\,\mathrm{cm^{-1}\,W\,Hz^{-1/2}}$) for a practical averaging time of 1 s, which is equivalent to $14\,\mathrm{mg\,m^{-3}}$ (standard temperature and pressure) and can be considered sufficient for IWT water content measurement. Nevertheless, this is considerably higher than achieved by other PAS instruments (e.g., $\approx$1 ppm [196]) and has been traced to the sub-optimal choice of the pressure-controlling valve of the PA cell, which at the chosen flow rate is operated at small opening positions, resulting in increased levels of noise. Therefore, replacement of this valve is assumed to further decrease noise and limit of detection.

The calculated combined measurement uncertainty (95 % coverage) of the hygrometer of less than 2.5 to 3.3 % within the range of 512 to 12.361 ppm (cf. Fig. 7 in **Paper II**) is higher than the accuracy specified by commercial NDIR systems (e.g., 1.5 % [59]). However, this figure is considered to have large potential for improvement by minor improvements to the PA hygrometer and the humidity generator, such as improved temperature and laser power control, as well as an independent calibration. The aforementioned concentration range covers cloud-free saturated air at −30 °C up to CWCs of $5\,\mathrm{g\,m^{-3}}$ in fully saturated air at 0 °C and, thus, covers the primarily targeted EASA CS-25 and FAA CFR-25 Appendix C and O conditions.

CFD analysis of the thick-walled total water inlet of the IKP was used to estimate droplet/particle size dependent collection losses for isokinetic sampling, but revealed only marginal impact from assuming ideal efficiency for the Appendix O conditions present during the probe intercomparison. This highlights one of the advantages of using IKP instruments for water content measurement in supercooled large drop icing conditions over conventional instrumentation. However, with a minimum collection efficiency of 88 % at particle Stokes numbers around 1, collection efficiency is shown to be relevant for measurements with the current probe in Appendix C or ice crystal icing conditions and, similar to other probes [203], corrections to the measured CWC need to be applied. During the evaluation, two additional major drawbacks of the current IKP have been determined. First, insufficient power of the evaporator or the total water inlet heating with associated accumulation of condensed water limits operation at below condensed water mass fluxes of $\approx 90\,\mathrm{g\,m^{-2}\,s^{-1}}$ (equivalent to $1.5\,\mathrm{g\,m^{-3}}$ at wind speeds of $60\,\mathrm{m\,s^{-1}}$). Hence, at $60\,\mathrm{m\,s^{-1}}$ only Appendix C continuous maximum and Appendix O water contents currently are within the operating range of the system. Additionally, the choice of the total water inlet inner diameter of only 3.3 mm, mainly constrained by the low-noise vacuum pump used in the sampling system, has been determined to limit the achievable instrument uncertainty to above 10 %.

For the combined instrument, CWC measurement uncertainty has been estimated from an analytical expression specifically derived for the AquaSense system. The expression is used in the estimation of the actual CWC from hygrometer, flow rate and icing wind tunnel wind speed readings. Ambient (icing wind tunnel) static air temperature and pressure uncertainties have been shown to not contribute to the measurement uncertainty of the instrument at hand and similar IKP-based instruments. Despite limitations by the inlet design, the AquaSense instrument is shown to achieve an accuracy better than 20 % above CWCs of $14\,\mathrm{g\,m^{-3}}$ in cold air (−30 °C) in combination with suitable background humidity measurement. This does not fulfill current requirements given by the SAE ARP5905 [36] defined for Appendix C conditions (max. ±10 %), but with modifications of the total water inlet is considered adequate to future instrumentation requirements for Appendix O SLD icing conditions, which currently are in preparation (SAE AIR6341 [204]).

During the probe intercomparison campaign conducted at RTA the assessment of the measurement uncertainty in SLD conditions could be partially confirmed by the agreement of the AquaSense instrument with the Cranfield-University reference IKP [39] to within ±20 % in a CWC range of approximately 0.2 to $0.9\,\mathrm{g\,m^{-3}}$ (cf. Fig. 13 in **Paper II**). However, two essential and necessary modifications to the AquaSense instrument have been determined, indispensable for future deployment of the measurement system:

1. The AquaSense instrument at this point in time only features a single PA hygrometer used for total water measurement. Therefore, CWC calculation relies on background humidity values supplied by the icing wind tunnel facility. For the measurement campaign, this meant that large parts of the gathered total water content data could not be used for CWC estimation, as the ingestion of excess water into the background humidity inlet of the AquaSense instrument prohibited background humidity measurement and

a necessary drift correction. This applied to a considerable part of the measurements conducted in Appendix C conditions. Hence, a dedicated means of background humidity measurement, i.e., a second hygrometer featuring an inlet in the vicinity of the total water inlet, is required.

2. Ingestion of excess water into the background water vapor inlet of the instrument (initially oriented perpendicular to the flow and designed similar to [176]) has been determined to stem from either sampling of runback water flowing along the heated probe, sampling from the heated thermal and humidified concentration boundary layer flow around the probe, or a combination thereof. Combined with findings of incomplete evaporation at the total water inlet for condensed water mass fluxes above 90 $\mathrm{g\,m^{-2}\,s^{-1}}$, improvable collection efficiency characteristics by changing to a thin-walled inlet nozzle design, accuracy limitations given by the small inlet diameter and issues with maintaining the probe pylon free from ice accretion, a redesign of the IKP incorporating these changes is deemed necessary. To mitigate background humidity enhancement from sampling of the boundary layer, runback water and stagnation temperature rises, an unheated and expanding rearward facing inlet design as implemented in [205–207] is suggested for background humidity sampling.

3.4 Photothermal Spectroscopy of Nitrogen Dioxide and Water Vapor with a Fabry-Pérot Etalon

Paper III shows a first realization and characterization of a PTS gas analyzer, using a commercially available, rigid and fiber-coupled Fabry-Pérot etalon (FPE) refractive index sensor [164]. The presented photothermal sensor was realized using a 450 nm diode laser for excitation in a crossed-beam alignment with the probe beam and nitrogen dioxide in (dry) synthetic air as a test gas. This proof-of-principle setup, sketched in Figure 2 of **Paper III**, was intended to demonstrate the achievable sensitivity/accuracy and miniaturization potential of small-size FPE-based photothermal spectroscopy for various gas detection and concentration measurement applications.

The initial sensor characterization included the determination of the frequency response of the signal, combined with the analysis of different noise sources, such as flow noise and mechanical vibrations. Although the non-optimized 9 $\mathrm{cm^3}$ volume gas cell was not designed for fast response, the response time of the setup was shown to lie below 3 s, with an achievable NNEA (3σ) of $2.3 \times 10^{-7}\,\mathrm{cm^{-1}\,W\,Hz^{-1/2}}$ at the optimum modulation frequency (optimum SNR) of 1.4 kHz. The demonstrated 1 s integration time detection limit, equivalent to 1 ppm NO_2 (3σ), is higher than achieved by QEPAS [208], CEPAS [209] and conventional PAS [147] implementations, but supports further improvement by collinear excitation and probe beam alignment, combined with wavelength-modulation of the excitation source for other gases (e.g., water vapor). For averaging times appropriate for environmental monitoring

(100 s), signal averaging has shown to permit LODs (3σ) below 80 ppb NO_2. On of the most noteworthy features of the Fabry-Pérot interferometric setup is the demonstrated insensitivity to mechanical vibrations due to the rigid build of the used etalon. This insensitivity resulted in marginal increases in noise, well within the 3σ background noise level, for broadband and peak accelerations above 1.7 g applied to the gas cell, hence showing the possibility of robust gas sensing in field applications.

Since in **Paper III** the frequency dependence of the signal (Fig. 5(a)) has not been compared to the theoretically predicted response for the photothermal signal in a crossed-beam geometry (Eq. (2.98)), Fig. 3.3 shows this comparison together with the $1/f$ approximation, (Eq. (2.99)), which holds for $\omega\tau_T \gg 1$. This comparison shows a generally good agreement between measured and predicted response, which, thus, may be used in the design and dimensioning of an optimized gas analyzer based on PTS in a crossed-beam interferometric setup.

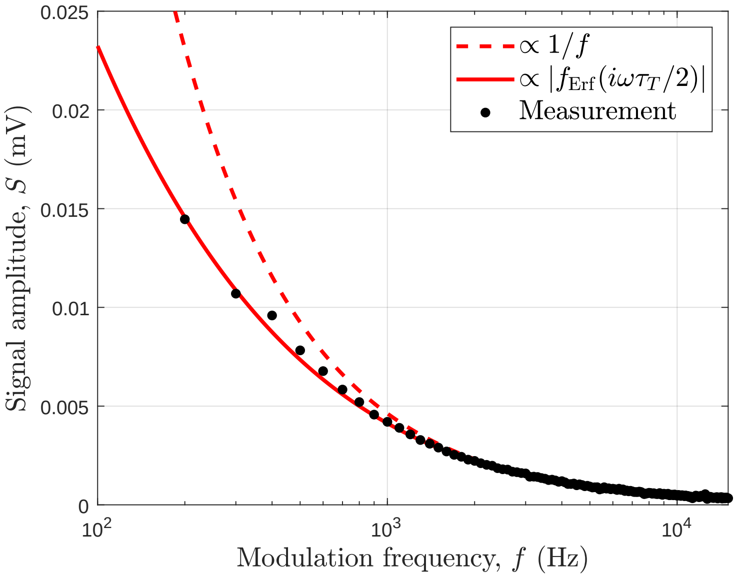

Fig. 3.3 Measured and theoretical (Eq. (2.98)) photothermal signal over the modulation frequency for NO_2 in dry synthetic air (20 °C, 1000 hPa, w=200 µm), together with the $1/f$ approximation, which holds for $\omega\tau_T \gg 1$ ($\omega\tau_T = 10$ at $f \approx 600$ Hz).

To further investigate the performance of the photothermal setup for applications in humidity measurement, the determined NNEA of **Paper III** may be used to calculate the minimum detectable water vapor concentration assuming similar noise characteristics for the laser and, in a first approximation, linear signal response to concentration changes. Using the setup parameters of the AquaSense PAS hygrometer, i.e., an effective modulation amplitude of 10 mW, a detection bandwidth of 0.16 Hz and an average absorption cross section for H_2O of 6.3×10^{-24} m^2 molec^{-1} (7327.67 cm^{-1}, 20 °C, 1000 hPa), the minimum detectable concentration (or mole fraction) according to Eqs. (2.102) and (2.103) amounts to approximately

$$x_{\mathrm{min}} = \frac{n_{\mathrm{min}}}{n_0} = \mathrm{NNEA}\,\frac{\sqrt{\Delta f}}{P_{\mathrm{eff}}\,\overline{\sigma}_{\mathrm{abs}}\,n_0} = 5.8\,\mathrm{ppm}\;. \tag{3.2}$$

It should be noted that the expected actual LOD for water vapor in air using PTS is approximately 5 times this figure, as the sensitivity is expected to decrease to approximately 20 % at low concentrations (cf. **Paper I**). This is approximately equivalent to the LOD of 29 ppm determined for the PAS gas analyzer in **Paper I** (converted to 20 °C, 1000 hPa). As the photothermal gas cell width and, hence, the optical path length of the excitation beam within the gas can be reduced down to the size of the etalon length of 2 mm, an optimized gas cell design is expected to result in signal linearity up to concentrations of 32,000 ppm (attenuation less than 1 %; 20 °C, 1000 hPa), providing the high dynamic range in concentration required for atmospheric and IWT water content measurement. For the PA cell used in **Paper I** and **Paper II**, the same attenuation is obtained at the center of the resonator at a concentration of 1000 ppm, significantly decreasing the sensitivity of the setup (cf. Fig. 12 of **Paper I**).

A first experimental characterization of the described FPE-based sensor using water vapor in synthetic air, together with the AquaSense PAS instrument laser diode (7327.67 cm^{-1}) and data acquisition and signal processing hardware, are shown in Fig. 3.4. The PT signal amplitude and phase can be seen to exhibit the expected nonlinear dependence on the water vapor concentration, allowing to employ the same calibration function as determined in **Paper I**, which drastically reduces the number of calibration points required. Observable issues in Fig. 3.4 with repeatability during the calibration are attributed to a PT gas cell flow rate instability caused by a manually operated mass flow controller.

Overall, the presented results demonstrate the potential of applying photothermal spectroscopy in an etalon-based configuration to robust and fast response humidity measurement in water content instrumentation and in a manifold of other, possibly miniaturized, gas sensing applications. Especially the (acoustically) non-resonant mode of operation removes restraints on the modulation frequency, which can be set to the value exhibiting highest SNR within a specific measurement environment. With some modifications to the gas cell design and beam alignment (collinear excitation and probe beam alignment) significant improvements of the minimum detectable concentration, down to the ppb level can be expected.

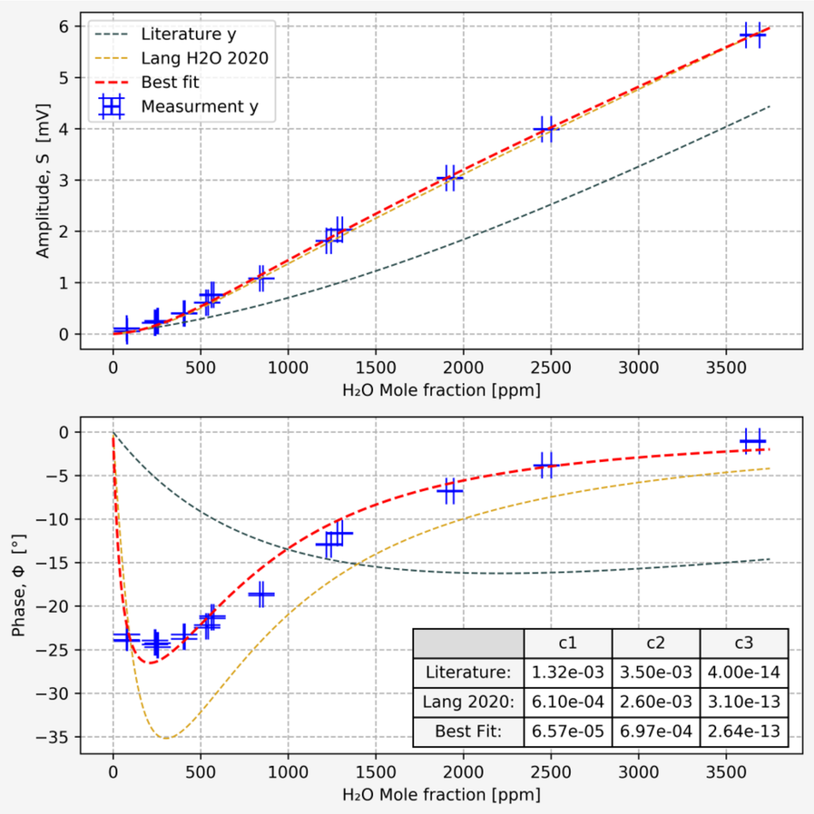

	c1	c2	c3
Literature:	1.32e-03	3.50e-03	4.00e-14
Lang 2020:	6.10e-04	2.60e-03	3.10e-13
Best Fit:	6.57e-05	6.97e-04	2.64e-13

Fig. 3.4 Photothermal signal amplitude and phase for water vapor in synthetic air at the modulation frequency of 1000 Hz, together with curve fits of the predicted response according to **Paper I** with a set of parameters. The fit parameters, excluding the setup sensitivity, are summarized in the table shown in the lower sub-plot. The (arbitrary) signal phase offset has only been corrected for the *Best Fit*. (Measurements and evaluation conducted by Ulrich Radeschnig.)

CHAPTER 4

CONCLUSIONS AND OUTLOOK

This thesis has been carried out with the underlying goal of contributing to the development of accurate reference measurement instrumentation required in the aviation sector after legislation amendments regarding in-flight icing. The specific need addressed in this work, as part of the FFG TAKEOFF project AquaSense, concerned the characterization of experimentally simulated icing conditions used in the development, testing and certification of aircraft and ice protection and detection systems. More specifically, the requirement for condensed water content measurement in icing wind tunnel-generated cloud and precipitation conditions, containing significant fractions of supercooled drops greater than 50 µm in diameter (supercooled large drops; SLDs), has been addressed by the development and characterization of instrumentation based on an isokinetic evaporator probe and humidity measurement.

To fulfill high dynamic range requirements and particularly challenging accuracy requirements at the low end of liquid and ice water contents demanded by certification specifications and icing wind tunnel calibration practices, a considerable effort has been put in the development, description and characterization of a customized hygrometer employing near-infrared diode laser-based photoacoustic spectroscopy. Precise calibration of photoacoustic hygrometers has been determined to be complicated by previously unsatisfactorily described collisional relaxation phenomena of water vapor in air during the signal generation process, contributing to varying instrument sensitivities that are highly dependent on the operating condition. In this work calibration complexity has been successfully reduced by introducing a theoretical description of these processes, allowing to reproducibly predict the sensitivity of photoacoustic, as well as future photothermal water vapor gas analyzers. These efforts enabled to achieve accuracies and precision comparable to commercial optical hygrometers. By combination of the photoacoustic gas analyzer with a compact, portable calibration unit, a two-pressure humidity generator, the realized device offers the benefit of increased confidence in measurements from a readily available and practicable recalibration. Concluding from the experimental investigations, it is expected that gained confidence in the values of the physical constants underlying the relaxation processes and the theoretical description, as well as further effort put in the improvement of the present photoacoustic device and the calibration unit will allow to attain reliable instrument measurement performance at par with all-optical atmospheric water vapor and total water instruments.

The theoretical description of the signal generation has been carried out without restriction to the specific realization, thus allowing and targeting the transferability to quartz-enhanced photoacoustic and photothermal gas analyzers. Advantages and measurement capabilities provided by these methods with ongoing developments, such as miniaturization and, possibly, large volume production, can therefore also be applied in accurate water vapor sensing. Realization and characterization of a Fabry-Pérot etalon-based photothermal sensor confirmed these expectations with promising performance, suggesting achievable sensitivities at the level of sophisticated state-of-the-art photoacoustic instruments with modest modifications, as well as fast response. With the maturing of stable and high-power mid-infrared optical sources, such as quantum cascade and interband cascade lasers, further progress for photothermal sensors can be expected with regard to combinations of degree of miniaturization and achieved limits of detection.

In addition to the research and development related to the photoacoustic hygrometer and calibration unit, development of a sampling system suitable for SLD condition icing wind tunnel condensed water content measurement and the integration of all components into a single device, the AquaSense instrument, has been carried out during this work. Detailed evaluation of the condensed water content measurement uncertainty of the final instrument and the individual components, partly based on laboratory characterizations and CFD analysis, led to the conclusion of partial fulfillment of the accuracy requirements of the targeted certification conditions and recommended icing wind tunnel calibration practices. During an intercomparison campaign with state-of-the-art isokinetic evaporator and hot-wire-based water content instrumentation, performed in the Rail Tech Arsenal icing wind tunnel, these estimations could be confirmed, however, demonstrating the superiority to conventional instrumentation and the potential for accurate determination of condensed water content in experimentally simulated SLD conditions. From the laboratory characterization and probe intercomparison, several operating limitations and considerable uncertainty contributions have been traced to the realization of the isokinetic evaporator probe, for which a redesign has been proposed. Improvements in the hygrometer and calibration unit, combined with the proposed modifications of the isokinetic evaporator probe and the extension of the instrument by a dedicated means for icing wind tunnel background humidity measurement is expected to further reduce the water content measurement uncertainty to provide the high level of accuracy required in aviation testing and certification combined with real-time monitoring capabilities. The experience and knowledge gained in the design and development of the AquaSense instrument are currently incorporated into the development of a follow-up isokinetic evaporator probe instrument within the scope of a research and industry cooperation.

Part II

Journal Articles

PAPER I. MOLECULAR RELAXATION EFFECTS ON VIBRATIONAL WATER VAPOR PHOTOACOUSTIC SPECTROSCOPY IN AIR

Author contributions: The author of this thesis led the development, design and construction of the PA measurement hardware and control used in the experiments, developed the presented analytical model of PA signal generation, contributed to the conceptualization of the work and determined the methodology. The author wrote the original draft of the manuscript and handled the submission, as well as editing after review.

Publication status: This article is an accepted and published version of [1]: Lang, B., Breitegger, P., Brunnhofer, G. et al.: Molecular relaxation effects on vibrational water vapor photoacoustic spectroscopy in air. Appl. Phys. B 126, 64, doi.org/10.1007/s00340-020-7409-3, 2020.

Paper I

Applied Physics B (2020) 126:64
https://doi.org/10.1007/s00340-020-7409-3

Applied Physics B
Lasers and Optics

Molecular relaxation effects on vibrational water vapor photoacoustic spectroscopy in air

Benjamin Lang[1] · Philipp Breitegger[1] · Georg Brunnhofer[2] · Jordi Prats Valero[2] · Simon Schweighart[3] · Andreas Klug[2] · Wolfgang Hassler[3] · Alexander Bergmann[1]

Received: 27 November 2019 / Accepted: 26 February 2020

Abstract

Photoacoustic spectroscopy is a highly sensitive technique, well suited for and used in applications targeting the accurate measurement of water vapor in a wide range of concentrations. This work demonstrates the nonlinear photoacoustic response obtained for water vapor in air at typical atmospheric concentration levels, which is a result of the resonant vibrational coupling of water and oxygen. Relevant processes in the relaxation path of water in a mixture with air, excited with near-infrared radiation, are identified and a physical model for the acoustic signal measured with a resonant photoacoustic cell is presented. The model is valid for modulation frequencies typical for conventional and quartz-enhanced photoacoustic spectroscopy and provides a simplified means of calibration for photoacoustic water vapor sensors. Estimated values for comprised model coefficients are evaluated from photoacoustic measurements of water vapor in synthetic air. Furthermore, it is shown experimentally that the process of vibrational excitation of nitrogen is of negligible importance in the relaxation path of water vapor and thus insignificant in the photoacoustic heat production in atmospheric measurement environments.

1 Introduction

The amount of published research on photoacoustic spectroscopy and the number of commercially available sensor systems based on this method are rising steadily, as technical advances allowed substantial progress in the limits of detection (LOD) and reduction of size and cost (e.g., [1, 2]). While the technical advances lead to increased sensitivities and allow for detection at trace levels, the upper limits remain more or less unaltered, yielding increased dynamic ranges of the methods.

Water vapor in atmospheric measurement environments can vary over a wide range of concentrations, which therefore makes photoacoustic (PA) spectroscopy an ideal detection and measurement technique. Water vapor mole fractions can fall below 10 ppm in the upper troposphere as well as lower stratosphere, and rise above 40,000 ppm for dew points around 30 °C at standard pressure [3]. A large number of applications for the PA measurement of water vapor already exists, mostly measuring at wavelengths in the near infrared [4–14]. In the overwhelming majority of literature, the measured PA signal is interpreted in terms of a linear response. Quite often, validation or calibration measurements are conducted for a narrow range of concentrations and the response is linearly extrapolated to lower or higher concentrations. Linear extrapolation is also used for the determination of the LOD. In the case of an incorrect linear assumption, extrapolation inevitably leads to large errors in the predicted concentrations and also in the predicted theoretical LOD.

Tátrai et al. [11] have calibrated a photoacoustic hygrometer for a large range of water vapor concentrations and determined a nonlinear relationship between the measured microphone response and the water vapor mixing ratio. A tenth-order polynomial fit had to be applied to calibrate the device. High absorption and a resulting nonlinear power

---

Electronic supplementary material The online version of this article (https://doi.org/10.1007/s00340-020-7409-3) contains supplementary material, which is available to authorized users.

✉ Benjamin Lang
benjamin.lang@tugraz.at

[1] Institute of Electrical Measurement and Sensor Systems, Graz University of Technology, 8010 Graz, Austria

[2] Nanophysics & Sensor Technologies, AVL List GmbH, 8020 Graz, Austria

[3] Institute of Aviation, University of Applied Sciences FH JOANNEUM Graz, 8020 Graz, Austria

loss, given by the Beer–Lambert law, explain sensitivity losses at high concentrations, and it is also known that a background signal not or incorrectly subtracted can cause a nonlinear behavior at low concentrations [15]. These effects, however, do not explain pronounced increases in sensitivity at intermediate concentrations as observed by Tátrai et al. and which are also reproduced in this work. Other drawbacks of using polynomial functions of high order are the generally poor results achieved for extrapolations of the PA signal to concentrations outside of the calibration range.

Nonlinear relationships between PA response and concentration have previously been reported when molecular relaxation times of molecules involved in the relaxation path are comparable to the time variation of the incident radiation and relaxation times change with varying concentration. Several well-known practical examples of combinations of absorbing species and buffer gases exist, where the overall relaxation time is in the order of the modulation period. For example, the first vibrationally excited, asymmetric stretching mode of carbon dioxide, $CO_2(0,0,1)$ (2349 cm^{-1}), is long known to exhibit a near-resonant, vibrational–vibrational (V–V) coupling with N_2, which leads to a long relaxation time at atmospheric conditions, due to the long lifetime of the first excited state of the nitrogen molecule, $N_2(1)$ (2331 cm^{-1}) [16]. Another example for near-resonant coupling of practical relevance is known to exist between the bending modes of methane (1311 cm^{-1} and 1533 cm^{-1}) and vibrationally excited molecular oxygen, as $O_2(1)$ (1556 cm^{-1}) again has a long lifetime [17].

Water vapor is utilized as a highly efficient promoter for vibrational–translational (V–T or thermal) collisional relaxation [18], also acting as a promoter in the V–T relaxation of $O_2(1)$ [17]. Water is either added to maximize the photoacoustic response [4, 17, 19], or measured simultaneously, to correct for changing overall relaxation times [5]. However, the H_2O molecule itself has a near-resonant V–V coupling of the first bending mode, $H_2O(v_1 = 0, v_2 = 1, v_3 = 0)$ (1595 cm^{-1}), with $O_2(1)$, with an energy transfer more efficient than the thermal relaxation by the major atmospheric constituents O_2 and N_2 [20, 21]. This suggests a corresponding PA signal loss, when measuring water vapor at low concentrations in atmospheric environments at typical modulation frequencies and when the relaxation path involves the $H_2O(0,1,0)$ state. Combined with the properties of H_2O as an efficient promoter of V–T relaxations at increasing concentrations, a variable relaxation time and hence a nonlinear PA response when measuring water vapor in air are to be expected.

In this work, a simplified model of the relaxation process of water vapor in atmospheric environments, applicable to vibrational photoacoustic spectroscopy, is postulated and validated experimentally. Model parameters derived from relaxation rates and setup parameters are evaluated from photoacoustic measurements of water vapor at varying concentrations in air by comparison of the predicted PA amplitude and phase shifts with the experimentally measured amplitude and phase. Measurements of the PA response of water vapor in a nitrogen-buffered environment are presented to affirm assumptions about the relaxation process. Finally, a simplified model of the photoacoustic response, valid for modulation frequencies typical for conventional and quartz-enhanced photoacoustic spectroscopy, is provided as a means of calibrating PA water vapor sensors.

2 Theory

2.1 Linear photoacoustic response

The often applied theoretical result of a linear dependence of the background-corrected photoacoustic signal amplitude (at the frequency of modulation), S (in V), on the number concentration of a single absorbing gas species, n_g (in molecules/m^3), is given by [1]

$$S = C_{\text{cell}}\,\sigma\,P\,n_g\,\eta, \tag{1}$$

with average radiation power P (in W), cell constant C_{cell} (including microphone sensitivity, in Vm/W), absorption cross section σ (in m^2/molecule) and efficiency of conversion of the radiation into heat η. This expression assumes negligible power loss along the optical path and absorption cross sections and applied intensities also have to be low to prevent significant depletion of the ground state of the targeted transition [22]. This conditions are fulfilled for most near-infrared laser photoacoustic sensor applications, as absorbance usually is sufficiently low and mostly diode lasers with powers up to only several tens of milliwatts are applied. For water vapor at high concentrations and typical absorption path lengths, however, significant absorbance has to be expected.

In addition to the above assumptions, the energy-weighted, average vibrational relaxation time from the excited vibrational state back to the initial state, τ, is usually assumed shorter than the time variation of the incident radiation ($\omega\tau \ll 1$, with the angular frequency of modulation $\omega = 2\pi f$) [22]. Therefore, the photoacoustic conversion efficiency,

$$\eta = \frac{1}{\sqrt{1 + (\omega\tau)^2}}, \tag{2}$$

is implicitly assumed to be unity, which results in a linear PA response. A linear behavior may also be observed when the condition $\omega\tau \ll 1$ is not fulfilled. The relaxation time may be in the order of the modulation period or longer, but constant for a given combination of absorbing species and buffer gas. The signal amplitude given by Eq. (1) then still is a linear function of the concentration.

Currently, no assessment of the conversion efficiency for PA measurements of water vapor in air exists. For this reason, the photoacoustic conversion efficiency is investigated theoretically and experimentally in the following. Conversion efficiencies different from unity are only measurable in the amplitude of the PA signal by varying the modulation frequency, gas temperature or pressure, while correcting for a change in microphone sensitivity and frequency response, radiation waveform and corresponding dependencies of the cell constant. Otherwise, deviations from an efficiency of unity are indiscernible from a changing cell constant. However, it is often overlooked that the phase shift, ϕ, of the PA response, which is not only a function of the average lifetime of the excited vibrational state, but may be a complicated function of a number of different relaxation times of states involved in the relaxation process, contains valuable information about the relaxation time and thus also the conversion efficiency, as

$$\phi = \arctan(\omega\tau) \tag{3}$$

[23]. This relationship is used in the present work to experimentally verify the PA response and conversion efficiency for water vapor in air derived in the following.

2.2 Model for the photoacoustic response of water vapor in air

The near-infrared is also favored in most PA water vapor sensing applications, due to the high absorption line strengths and the availability of relatively cheap distributed feedback laser diodes in this region. Mainly, ro-vibrational transitions from the vibrational ground state $H_2O(v_1=0,\ v_2=0,\ v_3=0)$, to the vibrational $H_2O(1,0,1)$ (7250 cm^{-1}) state of the main H_2O isotope are targeted, where the variables v_1, v_2 and v_3 denote the state of the symmetric stretch, bending, and asymmetric stretch vibrational mode, respectively. For this reason, the following derivation addresses relaxation from the vibrational $H_2O(1,0,1)$ state. However, as will be shown below, the relaxation path can be approximated by a three-level system of the $H_2O(v_1, v_2, v_3)$, $H_2O(v_1, v_2-1, v_3)$, $O_2(1)$ and $O_2(0)$ levels, which reduces the complexity of the relaxation process. This implies that the model should extend to situations where lower vibrational states are excited by radiation and may also be applicable at higher excitation energies.

At typical PA measurement temperatures and pressures, rotational relaxation rates are much higher than typical modulation frequencies, so that the rotational temperature can be assumed equal to the translational temperature of the gas for all steps in the relaxation path [32]. For this reason, only relaxation of vibrationally excited levels needs to be considered. Nevertheless, to accurately model the relaxation process from the excited $H_2O(1,0,1)$ level in air, one would need to model at least 13 H_2O vibrational energy levels, as well as 2 levels each for the main constituents O_2 and N_2 (e.g., [24, 33]) and all possible reactions among the participating molecular levels (cf. Fig. 1). Although relaxation through and by trace constituents may occur in atmospheric environments (mainly Ar and CO_2), only reactions between water, molecular oxygen and nitrogen are considered in the following kinetic analysis. The possible consequences of this restriction are discussed in the supplementary material, Sec. S1. Relevant relaxation reactions and literature values for the corresponding reaction rate coefficients with references are given in Table 1.

As modeling the full system is impractical, it is shown in the following sections that the system can be approximated by the three-level system, describing the rate-determining steps of the relaxation process and the heat released in dependence of the gas composition. The assumptions leading to the three-level model are discussed in the next section by reference to the relaxation processes in Table 1. Typical time constants for these reactions in air at 35 °C, 800 hPa and different water vapor concentrations are given in Fig. 2. Time constants are calculated from $\tau = 1/k[B]$, where [B] is the concentration of the second reactant, which is assumed to remain constant. For brevity, molecules excited to the lowest vibrational level above the ground level are denoted by an asterisk in the following (e.g., O_2^* instead of $O_2(1)$). M denotes either O_2 or N_2. Relaxation processes are denoted by (Ri), with the reaction number i given in Table 1.

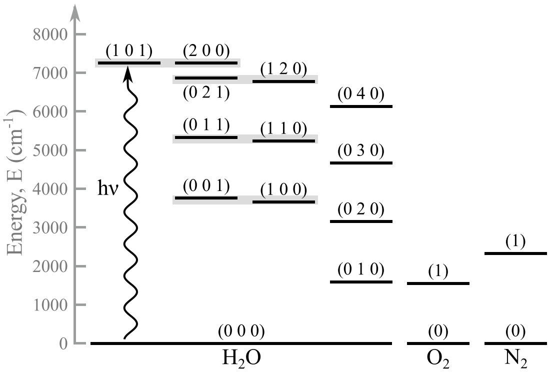

Fig. 1 Energy diagram of the vibrational levels of the considered constituents. H_2O levels considered in reservoirs are connected by gray rectangular boxes. The radiative excitation is indicated by a wavy line

Table 1 Main processes of vibrational energy exchange of H_2O in atmospheric environments. M is either O_2 or N_2. T is the temperature in Kelvin and T_r the reference temperature of 300 K. Values for the rate coefficients have to be taken with care, as uncertainties and discrepancies between measured rates are generally high

No.	Reaction	Model rate symbol	Forward rate ($cm^3/(molec.s)$)	References
(R1)	$H_2O(\nu_1,\nu_2,\nu_3)+O_2 \overset{k_1^{V-V}}{\longleftrightarrow} H_2O(\nu_1+1,\nu_2,\nu_3-1)+O_2$		$\approx 1.1\times10^{-11}\times\sqrt{T}$	[21]
(R2)	$H_2O(\nu_1,\nu_2,\nu_3)+O_2 \overset{k_2^{V-V}}{\longleftrightarrow} H_2O(\nu_1-1,\nu_2+2,\nu_3)+O_2$		$\approx \nu_1\times3.3\times10^{-13}\times\sqrt{T/T_r}$	[21, 24]
(R3)	$H_2O(\nu_1,\nu_2,\nu_3)+O_2 \overset{k_3^{V-V}}{\longleftrightarrow} H_2O(\nu_1,\nu_2+2,\nu_3-1)+O_2$		$\approx \nu_3\times3.3\times10^{-13}\times\sqrt{T/T_r}$	[21, 24]
(R4)	$H_2O(\nu_1,\nu_2,\nu_3)+N_2 \overset{k_4^{V-V}}{\longleftrightarrow} H_2O(\nu_1+1,\nu_2,\nu_3-1)+N_2$		$\approx 1.2\times10^{-11}\times\sqrt{T}$	[21]
(R5)	$H_2O(\nu_1,\nu_2,\nu_3)+N_2 \overset{k_5^{V-V}}{\longleftrightarrow} H_2O(\nu_1-1,\nu_2+2,\nu_3)+N_2$		$\approx \nu_1\times4.6\times10^{-13}\times\sqrt{T/T_r}$	[21, 24]
(R6)	$H_2O(\nu_1,\nu_2,\nu_3)+N_2 \overset{k_6^{V-V}}{\longleftrightarrow} H_2O(\nu_1,\nu_2+2,\nu_3-1)+N_2$		$\approx \nu_3\times4.6\times10^{-13}\times\sqrt{T/T_r}$	[21, 24]
(R7)	$H_2O(\nu_1,\nu_2,\nu_3)+H_2O \overset{k_7^{V-T}}{\longleftrightarrow} H_2O(\nu_1,\nu_2-1,\nu_3)+H_2O$	$k^{V-T}_{H_2O^*,H_2O}$	$\nu_2\times(5.1\pm0.5)\times10^{-11}$	[25]
(R8)	$H_2O(\nu_1,\nu_2,\nu_3)+M \overset{k_8^{V-T}}{\longleftrightarrow} H_2O(\nu_1,\nu_2-1,\nu_3)+M$	$k^{V-T}_{H_2O^*,M}$	$\nu_2\times(4.1\pm2)\times10^{-14}\times\sqrt{T/T_r}$	[21, 26]
(R9)	$H_2O(\nu_1,\nu_2,\nu_3)+O_2 \overset{k_9^{V-V}}{\longleftrightarrow} H_2O(\nu_1,\nu_2-1,\nu_3)+O_2^*$	$k^{V-V}_{H_2O^*,O_2}$	$\approx \nu_2\times10^{-12}$	[20, 21, 27]
(R10)	$H_2O(\nu_1,\nu_2,\nu_3)+N_2 \overset{k_{10}^{V-V}}{\longleftrightarrow} H_2O(\nu_1,\nu_2-1,\nu_3)+N_2^*$		$\approx \nu_2\times1.2\times10^{-14}\times\sqrt{T/T_r}$	[28]
(R11)	$O_2^*+M \overset{k_{11}^{V-T}}{\longleftrightarrow} O_2+M$	$k^{V-T}_{O_2^*,M}$	$(2.7\pm0.4)\times10^{-18}$	[25]
(R12)	$N_2^*+M \overset{k_{12}^{V-T}}{\longleftrightarrow} N_2+M$		$\approx 3.3\times10^{-21}$	[29]
(R13)	$O_2^*+H_2O \overset{k_{13}^{V-T}}{\longleftrightarrow} O_2+H_2O$	$k^{V-T}_{O_2^*,H_2O}$	$\approx 4\times10^{-14}$	[26, 27, 30]
(R14)	$N_2^*+H_2O \overset{k_{14}^{V-T}}{\longleftrightarrow} N_2+H_2O$		$\approx 4.1\times10^{-15}$	[30]
(R15)	$N_2^*+O_2 \overset{k_{15}^{V-V}}{\longleftrightarrow} N_2+O_2^*$		$\approx 6\times10^{-18}$	[31]

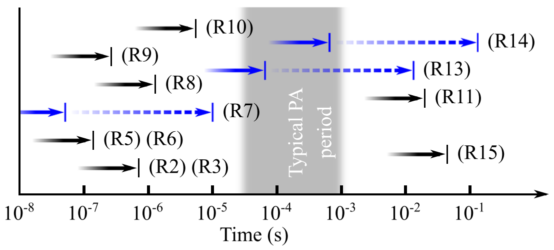

Fig. 2 Approximate time constants for reactions in Table 1 with $\nu_2 = 1$ at 35 °C and 800 hPa in air together with typical PA modulation periods (frequencies of 1 kHz to 33 kHz). Time constants of (R7), (R13) and (R14) are indicated for H_2O mole fractions of 100 ppm (dashed arrow) and 20,000 ppm (solid arrow). Values for time constants of reactions (R1) and (R4) are smaller, (R12) larger than the drawn scale

2.2.1 Assessment of relaxation path

The low energy differences between the pairs of H_2O levels $(1,0,1)\leftrightarrow(2,0,0)$, $(1,2,0)\leftrightarrow(0,2,1)$, $(1,1,0)\leftrightarrow(0,1,1)$ and $(1,0,0)\leftrightarrow(0,1,1)$ is the reason for the fast relaxation rate coefficient of k_1^{V-V} and k_4^{V-V} in reactions (R1) and (R4) (in both directions). So after initial excitation into the H_2O (1,0,1) state and after further steps in the relaxation process, this leads to a fast and efficient equilibration of the corresponding level pairs. As a result, each pair can be viewed as a single reservoir [24, 34, 35].

From these reservoirs ν_1 and ν_3, stretching quanta are quickly converted to two ν_2 quanta via processes (R2), (R3), (R5) and (R6). The energies released by these transitions of H_2O and of the above reactions, (R1) and (R4), are considered to be transferred to kinetic energy instantaneously. Justifications of this assumption are the high relaxation rates and short corresponding lifetimes of these reactions near atmospheric conditions ($\tau = 1/(k[M]) \leq 1\,\mu s$; cf. Fig. 2) in comparison to conventional and also quartz-enhanced PA spectroscopy (QEPAS, modulation frequencies typically up to 33 kHz).

It is difficult to evaluate theoretically if the vibrational excitation of N_2 plays a role in the reduction of the PA signal at low concentrations of H_2O. A similar relaxation delay as with oxygen can be expected when nitrogen is vibrationally excited in relevant numbers, since the lifetime of N_2^* in air is even longer than that of O_2^* (see (R12)). The large energy difference of 736 cm^{-1} between the levels of H_2O and N_2^* in the V–V process (R10) makes this process unlikely, which is why it has mainly been measured in the backward sense, with various values collected by Whitson et al. [28]. However, Feofilov et al. [33] cite a forward reaction rate, repeated in Table 1, in the same order as the backward rate from Whitson et al., possibly calculated by the principle of detailed balance. This relaxation process would compete with reactions (R7), (R8) and (R9). The rate of reaction (R15) suggests that the coupling of the vibrationally excited N_2 and O_2 levels and excitation of N_2 through this process can be neglected. Therefore, N_2^* and O_2^* populations can be studied independently and the effect of excitation of nitrogen can be experimentally measured by measuring the PA response at varying H_2O fractions in a purely nitrogen-buffered environment. Measurement results at the modulation frequency of 4.6 kHz for such an environment proving negligible excitation of N_2 are presented in Sect. 4.1.

At low fractions of water in air, the most probable relaxation process from the levels $H_2O(\nu_1,\nu_2\neq0,\nu_3)$, which includes in total six H_2O levels, is the V–V transfer to O_2^* (R9). This process is much faster than typical PA modulation periods ($1/\{k_9^{V-V}[O_2]\} \leq 1\ \mu s$; cf. Fig. 2). As the sequential conversion of up to all four ν_2 quanta is still fast in comparison to one PA modulation period, it is possible to regard each $H_2O(\nu_1,\nu_2\neq0,\nu_3)$ molecule as ν_2 molecules in a reservoir with $\nu_2 = 1$ and an average lifetime of $\tau_{H_2O^*}$. H_2O^* denotes this single reservoir. Increasing water vapor fractions lead to a competing relaxation of molecules in the reservoir by collision with H_2O (R7). As mentioned in the introduction, this process is even more efficient than the coupling to O_2, only decreasing the relaxation time of the reservoir. Hence, on the timescale of the modulation period, there is negligible difference in considering the total number of available ν_2 quanta instead of the number of excited H_2O molecules at a given point in time. The viewpoint of a single reservoir, H_2O^*, with an equivalent number of excited molecules with $\nu_2 = 1$, thus can be maintained from low to high water vapor mole fractions.

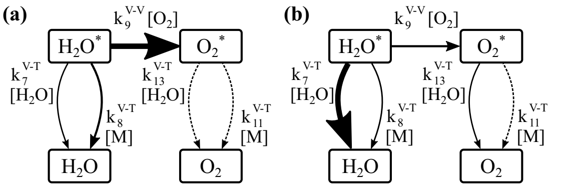

Fig. 3 Relaxation path diagram for the relaxation from the H_2O^* reservoir. Arrow widths are scaled with the magnitude of the labeled pseudo-first-order reaction rates, calculated for **a** 100 ppm and **b** 20,000 ppm water vapor mole fraction in air. Paths drawn with dashed arrows indicate rates much lower than can be indicated on the chosen scale

Taken together, the overall rate of relaxation of H_2O (1,0,1) in air is mainly determined by the following competing relaxation processes, for which the relaxation path is schematically drawn in Fig. 3:

1. V–T relaxation of the bending mode of $H_2O(\nu_1,\nu_2\neq0,\nu_3)$ by one through collisions with O_2, N_2 or H_2O, i.e., processes (R7) and (R8).
2. V–V energy transfer to O_2, with relaxation of the bending mode of $H_2O(\nu_1,\nu_2\neq0,\nu_3)$ by one and excitation of O_2 to O_2^*, i.e., process (R9).
3. V–T relaxation of O_2^* to the ground state, through collisions with O_2, N_2 or H_2O, i.e., processes (R11) and (R13).

In the following analysis of the relaxation path, the forward rate coefficients of the total five involved reactions have been renamed for easier identification. The rate coefficient symbols used in the model and the corresponding reactions are given in Table 1. Subscripts of the rates have been renamed according to the initial reactants. Superscripts of these rates again specify whether the reaction is of V–T or V–V type.

2.2.2 Three-level relaxation model

The above five remaining processes can be described by a simplified three-level model, similar to the one described by Hunter [36], drawn schematically in Fig. 4.

This system is described by the rates of change of the number concentrations of vibrationally excited water molecules in

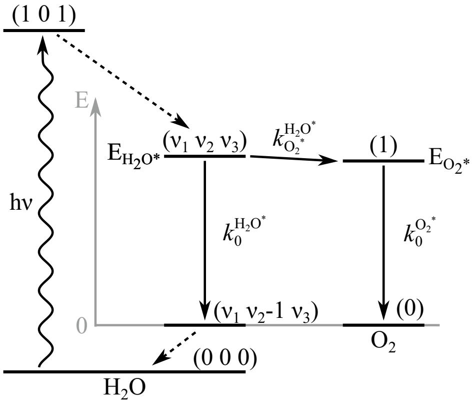

Fig. 4 Energy and relaxation path diagram for the proposed three-level model, describing the relaxation from the H_2O^* reservoir with coupling to the first vibrationally excited state of O_2. Energies of the H_2O ground state and the $H_2O(1,0,1)$ level are not to scale

the reservoir, $[\mathrm{H_2O^*}]$, and vibrationally singly excited molecular oxygen, $[\mathrm{O_2^*}]$:

$$\frac{\mathrm{d}[\mathrm{H_2O^*}]}{\mathrm{d}t} = 4\sigma\varphi(\mathbf{r},t)[\mathrm{H_2O}] - \frac{[\mathrm{H_2O^*}]}{\tau_{\mathrm{H_2O^*}}}, \tag{4}$$

$$\frac{\mathrm{d}[\mathrm{O_2^*}]}{\mathrm{d}t} = k_{\mathrm{O_2^*}}^{\mathrm{H_2O^*}}[\mathrm{H_2O^*}] - \frac{[\mathrm{O_2^*}]}{\tau_{\mathrm{O_2^*}}}. \tag{5}$$

The first term on the right hand side of Eq. (4) describes the excitation of water molecules from the ground state, by absorption of photons with energy $h\nu$, in a radiation photon flux, $\varphi(t)$, harmonically modulated at the angular frequency ω:

$$\varphi(\mathbf{r},t) = \frac{I(\mathbf{r})}{h\nu}(a + b\,\mathrm{e}^{i\omega t}). \tag{6}$$

$I(\mathbf{r})$, a and b describe the irradiance at position $\mathbf{r}$. σ is the absorption cross section of $\mathrm{H_2O}$ at the radiation frequency ν, also depending on gas composition, pressure and temperature. A prefactor of 4 is included to describe the conversion of the radiatively excited $\mathrm{H_2O(1,0,1)}$ to four vibrationally excited molecules in the reservoir $\mathrm{H_2O^*}$. The second term gives the combined de-excitation rate by V–T relaxation to the ground state and the resonant V–V transfer to $\mathrm{O_2^*}$, described by the $\mathrm{H_2O}$-concentration dependent, average lifetime of the $\mathrm{H_2O^*}$ state, $\tau_{\mathrm{H_2O^*}}$. It is implicitly assumed that the number of excited molecules is small in comparison to the number of molecules in the ground state, hence $[\mathrm{H_2O}]$ can be assumed constant and stimulated emission can be neglected.

The $\mathrm{O_2^*}$ level is populated by the aforementioned V–V energy transfer and relaxes to the ground state after an $\mathrm{H_2O}$-concentration dependent average lifetime $\tau_{\mathrm{O_2^*}}$. The italicized letter k is used for average pseudo-first-order reaction rate coefficients, with superscripts and subscripts specifying initial and final states in the relaxation path, respectively. Inverse average lifetimes of the excited states are given by

$$\begin{aligned}\tau^{-1}_{\mathrm{H_2O^*}} &= k_0^{\mathrm{H_2O^*}} + k_{\mathrm{O_2^*}}^{\mathrm{H_2O^*}}\\ &= \mathrm{k}^{V-T}_{\mathrm{H_2O^*,M}}[\mathrm{M}] + \mathrm{k}^{V-T}_{\mathrm{H_2O^*,H_2O}}[\mathrm{H_2O}]\\ &\quad + \mathrm{k}^{V-V}_{\mathrm{H_2O^*,O_2}}[\mathrm{O_2}]\end{aligned} \tag{7}$$

$$\tau^{-1}_{\mathrm{O_2^*}} = k_0^{\mathrm{O_2^*}} = \mathrm{k}^{V-T}_{\mathrm{O_2^*,M}}[\mathrm{M}] + \mathrm{k}^{V-T}_{\mathrm{O_2^*,H_2O}}[\mathrm{H_2O}]\,, \tag{8}$$

where as above, the roman type k is used for second-order reaction rate coefficients. [M] stands for the sum of $\mathrm{O_2}$ and $\mathrm{N_2}$ concentrations, and the associated collisional relaxation rates, $\mathrm{k}^{V-T}_{\mathrm{H_2O^*,M}}$ and $\mathrm{k}^{V-T}_{\mathrm{O_2^*,M}}$, are weighted averages for the two constituents.

As summed up in the previous section, $\tau_{\mathrm{H_2O^*}}$ is governed by processes (R7), (R8) and (R9), and $\tau_{\mathrm{O_2^*}}$ by processes (R11) and (R13). In accordance with Hunter [36], the solutions to the system of Eqs. (4)-(5) are given by

$$[\mathrm{H_2O^*}] = \frac{4\sigma bI}{h\nu}\frac{\tau_{\mathrm{H_2O^*}}[\mathrm{H_2O}]\,\mathrm{e}^{i(\omega t-\phi_{\mathrm{H_2O^*}})}}{\sqrt{1+\omega^2\tau^2_{\mathrm{H_2O^*}}}}, \tag{9}$$

$$[\mathrm{O_2^*}] = \frac{4\sigma bI}{h\nu}\frac{\tau_{\mathrm{H_2O^*}}\,\tau_{\mathrm{O_2^*}}\,k_{\mathrm{O_2^*}}^{\mathrm{H_2O^*}}\,[\mathrm{H_2O}]\,\mathrm{e}^{i(\omega t-\phi_{\mathrm{H_2O^*}}-\phi_{\mathrm{O_2^*}})}}{\sqrt{1+\omega^2\tau^2_{\mathrm{H_2O^*}}}\sqrt{1+\omega^2\tau^2_{\mathrm{O_2^*}}}}\,, \tag{10}$$

where explicit spatial and temporal dependencies have been omitted for brevity. Constant terms and terms with decaying factors $\exp(-t/\tau_{\mathrm{H_2O^*}})$ and $\exp(-t/\tau_{\mathrm{O_2^*}})$ have been neglected, as they do not contribute to the resonant photoacoustic signal after a few multiples of the relaxation times. The phase delay of the signals is given by

$$\tan(\phi_{\mathrm{H_2O^*}}) = \omega\,\tau_{\mathrm{H_2O^*}}, \tag{11}$$

$$\tan(\phi_{\mathrm{O_2^*}}) = \frac{\omega\left(\tau_{\mathrm{O_2^*}} + \tau_{\mathrm{H_2O^*}}\right)}{1-\omega^2\tau_{\mathrm{O_2^*}}\tau_{\mathrm{H_2O^*}}} \approx \omega\,\tau_{\mathrm{O_2^*}}, \tag{12}$$

where the last approximation holds because of the short lifetime of the $\mathrm{H_2O^*}$ reservoir.

2.2.3 Photoacoustic heat source rate

The photoacoustic source rate of heat production per unit volume and time is then given by the sum of heat released by the three transitions drawn in Fig. 4 and the heat assumed to be released instantaneously after excitation by rotational relaxation and the conversion of ν_1 and ν_3 to ν_2 quanta, i.e., reactions (R1) to (R6):

$$\begin{aligned}\mathbf{H}(\mathbf{r},t) = {}&\left(k_0^{\mathrm{H_2O^*}}E_{\mathrm{H_2O^*}} + k_{\mathrm{O_2^*}}^{\mathrm{H_2O^*}}\left(E_{\mathrm{H_2O^*}}-E_{\mathrm{O_2^*}}\right)\right)[\mathrm{H_2O^*}]\\ &+ k_0^{\mathrm{O_2^*}}E_{\mathrm{O_2^*}}[\mathrm{O_2^*}] + \sigma\varphi(t)E_{\mathrm{inst}}[\mathrm{H_2O}].\end{aligned} \tag{13}$$

Here, E_{inst} is the average energy per excited molecule, released by the mentioned rotational relaxation and the vibrational conversion. Since the energies of the $\mathrm{O_2(1)}$ level and the $\mathrm{H_2O^*}$ reservoir are approximately equal ($-89\,\mathrm{cm^{-1}}$ to $19\,\mathrm{cm^{-1}}$ difference for $\nu_2 = \{1,2,3,4\}$), we can set

$$E_{\mathrm{H_2O^*}} = E_{\mathrm{O_2^*}}, \tag{14}$$

without greater losses in the energy balance. With the literature values for the relevant relaxation rate coefficients stated in Table 1, the following approximations are used in finding a simplified solution for the photoacoustic response as a function of the H_2O concentration:

$$\mathrm{k}^{V-T}_{\mathrm{O}_2^*,\mathrm{M}}[\mathrm{M}] \ll \omega \ll \mathrm{k}^{V-V}_{\mathrm{H_2O^*},\mathrm{O}_2}[\mathrm{O}_2]. \tag{15}$$

The left-hand-side of Eq. (15) results in the model being independent of reaction (R11), which is reasonable considering the low rate coefficient.

Writing the photoacoustic source rate in a form with harmonic time dependence,

$$\mathbf{H}(\mathbf{r}, t) = \boldsymbol{\mathcal{H}}(\mathbf{r}, \omega) \cdot \mathrm{e}^{i\omega t}, \tag{16}$$

and using the assumptions of Eq. (15) together with the solutions for $[\mathrm{H_2O^*}]$ and $[\mathrm{O}_2^*]$ (Eqs. (9) and (10)) in the equation for the time-dependent photoacoustic source rate, Eq. (13), the complex amplitude at the frequency of modulation can be written as a function of the mole fraction of water, $x_{\mathrm{H_2O}}$ (see supplementary material):

$$\boldsymbol{\mathcal{H}}(\mathbf{r}, \omega) \approx \sigma\, b\, I\, n_0\, x_{\mathrm{H_2O}}\, \boldsymbol{\eta}(x_{\mathrm{H_2O}}), \tag{17}$$

with

$$\boldsymbol{\eta}(x_{\mathrm{H_2O}}) = \frac{1}{c_1 + x_{\mathrm{H_2O}} + c_2\left(1 - x_{\mathrm{H_2O}}\right)} \cdot \left(c_1 + x_{\mathrm{H_2O}} + \frac{c_2\left(1 - x_{\mathrm{H_2O}}\right) \mathrm{e}^{-i \arctan\left(\frac{\omega}{c_3\, n_0\, x_{\mathrm{H_2O}}}\right)}}{\sqrt{1 + \omega^2 / \left(c_3\, n_0\, x_{\mathrm{H_2O}}\right)^2}} \right), \tag{18}$$

where

$$c_1 = \frac{\mathrm{k}^{V-T}_{\mathrm{H_2O^*},\mathrm{M}} + \frac{E_{\mathrm{inst}}}{h\,\nu}\, \mathrm{k}^{V-V}_{\mathrm{H_2O^*},\mathrm{O}_2}\, x_{\mathrm{O}_2,\mathrm{dry}}}{\mathrm{k}^{V-T}_{\mathrm{H_2O^*},\mathrm{H_2O}} - \mathrm{k}^{V-T}_{\mathrm{H_2O^*},\mathrm{M}} - \frac{E_{\mathrm{inst}}}{h\,\nu}\, \mathrm{k}^{V-V}_{\mathrm{H_2O^*},\mathrm{O}_2}\, x_{\mathrm{O}_2,\mathrm{dry}}}, \tag{19}$$

$$c_2 = \frac{\frac{4E_{\mathrm{H_2O^*}}}{h\,\nu}\, \mathrm{k}^{V-V}_{\mathrm{H_2O^*},\mathrm{O}_2}\, x_{\mathrm{O}_2,\mathrm{dry}}}{\mathrm{k}^{V-T}_{\mathrm{H_2O^*},\mathrm{H_2O}} - \mathrm{k}^{V-T}_{\mathrm{H_2O^*},\mathrm{M}} - \frac{E_{\mathrm{inst}}}{h\,\nu}\, \mathrm{k}^{V-V}_{\mathrm{H_2O^*},\mathrm{O}_2}\, x_{\mathrm{O}_2,\mathrm{dry}}}, \tag{20}$$

$$c_3 = \mathrm{k}^{V-T}_{\mathrm{O}_2^*}, \mathrm{H_2O}. \tag{21}$$

Here, n_0 (in molecules/m^3) is the overall number concentration or density at the measurement temperature, T, and pressure, p, calculated for an ideal gas in the remainder of this work. Slight improvements in the prediction of the PA response should be possible, when also considering the real gas effects. $x_{\mathrm{O}_2,\mathrm{dry}}$ is the molecular oxygen mole fraction in dry air. Finally, the absolute value of $\boldsymbol{\eta}$ is the overall conversion efficiency, η (cf. Eq. (1)), which is a measure of the average relaxation time. The conversion efficiency is lower than one, when the relaxation time is in the order or longer than the modulation period. $\boldsymbol{\eta}$ also describes the average phase delay of the PA heat source rate relative to the excitation:

$$\phi\left(x_{H_2O}\right) = Arg(\boldsymbol{\eta}). \tag{22}$$

By equating Eqs. (3) and (22), the average relaxation time, τ, can be calculated. Explicit dependencies of $\boldsymbol{\eta}$ on n_0, $x_{\mathrm{O}_2,\mathrm{dry}}$ and ω have been dropped for clarity.

The absorption cross section intrinsically depends on the water vapor mole fraction, as the self-broadening of the chosen absorption line will lead to a non-negligible decrease in the absorption cross section with rising water mole fractions. This can either be taken into account by defining σ as a function of water mole fraction, or, approximating the absorption cross section with an average, lower value, which is sufficient for the purposes of this work. The introduced parameters c_1 to c_3 are practically constant in environments with constant dry air mole fractions for O_2 and N_2, which is reasonable for most atmospheric measurement applications.

2.2.4 Microphone signal for a resonant cell

In a resonant PA cell, the complex pressure amplitude, $\boldsymbol{\mathcal{A}}_{\mathbf{j}}$, of mode j, at the angular frequency of resonance, ω_j, is proportional to the overlap of the heat source with the complex conjugate of the normal mode of the acoustic resonator, $\mathbf{p}^*_{\mathbf{j}}$ [22]:

$$\boldsymbol{\mathcal{A}}_j \propto \int \mathbf{p}^*_j(\mathbf{r})\, \boldsymbol{\mathcal{H}}(\mathbf{r}, \omega_j)\, \mathrm{d}V. \tag{23}$$

Here, the ratio of specific heats was assumed independent of water vapor concentration and the volume integral extends over every point where the integrand does not vanish. Because of the spatial distribution of the (laser) irradiance, a spatial dependence of the rate of heat production remains. As pointed out in the introduction, large absorption at large mole fractions of water vapor will lead to a decrease in sensitivity and in the PA signal generated, due to the decreased irradiance along the beam path. However, for absorptions or path lengths not too large, the Beer–Lambert law and hence the irradiance of a sufficiently collimated laser beam at point l along the PA cell can be approximated linearly by

$$I(l, r) = I_0\, g(r)\, (1 - \sigma'\, [\mathrm{H_2O}]\, l), \tag{24}$$

with a normalized radial beam profile $g(r)$ and a reduced absorption cross section σ'. With the assumptions that the water vapor is uniformly distributed along the laser beam and the acoustic normal mode is symmetric about the center of the cell along the laser beam (as it is the case for the fundamental longitudinal mode in a resonator with open ends), the complex pressure amplitude together with Eqs. (17) and (24) reduces to

$$\mathcal{A}_j \propto \sigma P n_0 x_{\mathrm{H_2O}} (1-\sigma' n_0 x_{\mathrm{H_2O}} l_0)\, \boldsymbol{\eta}(x_{\mathrm{H_2O}}), \tag{25}$$

where $P = b P_0$ is the alternating component radiant flux (i.e., average power). The length l_0 is the absorption path length to the center of the resonator. Combining all mentioned and other setup constants affecting the measured signal, including microphone sensitivity, microphone positional dependence and electronic amplification, the complex amplitude of the microphone signal (in V) will be of the form

$$\mathbf{S}(x_{\mathrm{H_2O}}) = C_{\mathrm{cell}}\, \sigma P n_0 x_{\mathrm{H_2O}} (1-B_{\mathrm{cell}}\, n_0 x_{\mathrm{H_2O}})\, \boldsymbol{\eta}(x_{\mathrm{H_2O}}). \tag{26}$$

The introduced cell constants, C_{cell} and B_{cell}, will be functions of the variables temperature, pressure and modulation frequency. Thus, determined and stated values for these constants (in the following referred to as 'setup parameters') are only valid for a given combination of these variables.

In addition to the explicitly included second-order term in the microphone signal, arising from the linearly approximated laser power attenuation, several more effects will introduce deviations from a linear PA signal. For example, electret condenser microphones as used in this work exhibit a dependency of the microphone sensitivity, s_{mic}, on humidity, i.e., $s_{\mathrm{mic}}(T,p,f) = c_{\mathrm{mic}}(T,p,f) + b_{\mathrm{mic}}(T,p,f)\, n_0 x_{\mathrm{H_2O}} + \mathcal{O}(x^2_{\mathrm{H_2O}})$, which has to be accounted for [37].

First-order coefficients of these effects in the cell constant C_{cell}, such as the microphone humidity sensitivity coefficient b_{mic}, result in additional second-order terms in the PA signal and thus can be included in the parameter B_{cell}, which in the following is referred to as first-order correction of the cell constant (see supplementary material, Sec. S3). The resulting third- and higher-order terms in the microphone signal are neglected.

In the special case, where the microphone sensitivity is independent of humidity and the optical path length is short, the amplitude (absolute value) of the derived theoretical microphone signal reduces to the same form as in Eq. (1).

The resulting function $\mathbf{S}(x_{\mathrm{H_2O}})$, describing the amplitude and phase of the generated and measured photoacoustic signal, is a function of the two setup parameters C_{cell} and B_{cell}, the three coefficients c_1, c_2 and c_3, the known or measurable values of ω_j, P and n_0, and the unknown water vapor mole fraction, $x_{\mathrm{H_2O}}$. When calibration over a large range of water vapor concentrations has to be performed, this function cannot be approximated by a lower degree polynomial, due to the intricate nonlinearity of $\boldsymbol{\eta}(x_{\mathrm{H_2O}})$. However, a conventional nonlinear curve fit to measurement data in a limited range can be used to determine the two parameters and three coefficients of $\mathbf{S}(x_{\mathrm{H_2O}})$. It can be seen that for a given excitation energy, the parameters c_1 to c_3 do not depend on the measurement apparatus and thus should be universal for atmospheric measurement applications at similar conditions. A slight temperature dependence should be observable, due to the temperature dependence of the reaction rate coefficients.

In general, it will be advisable to only use the amplitude of the measured PA signal in the curve fit, as at resonance the measurement uncertainty of the amplitude will be much lower than the uncertainty of the measured phase. Additionally, the phase given by the model goes to zero in the limit of small and large mole fractions. In practice, however, some offset of the model phase from the measured phase will be observable, as the measured signal will not reach zero phase, due to time delays in the electronics and signal processing. One possibility to make use of all information available is to include an additional model parameter for the constant phase offset and to include uncertainties for the phase in a nonlinear curve fit of the complex signal.

In most applications, a calibration curve returning the water vapor mole fraction corresponding to a measured PA signal is of interest. Although no closed-form expression for the water vapor mole fraction can be given, $x_{\mathrm{H_2O}}$ can be efficiently determined for a measured PA signal amplitude, S_i, by numerically finding the root of $f(x_{\mathrm{H_2O}}) = S_i - \|\mathbf{S}(x_{\mathrm{H_2O}})\|$.

3 Experimental setup and methods

To investigate the described effects on the relaxation time of water vapor in air, a single resonant photoacoustic cell is used for measuring the PA amplitude and phase at water vapor mole fractions in the range of 120–22,000 ppm in pure nitrogen and in synthetic air. An overview of the measurement system used for the validation of the relaxation model is shown in Fig. 5. Humidities are set with a humidity generator and further diluted with a gas diluter. In the following, the individual components and methods applied are described in detail.

3.1 Photoacoustic cell

The photoacoustic cell is a custom-built cell designed to handle increased flow rates. A 6 mm diameter cylindrical duct, milled into a stainless steel block, guides the gas flow axially through an acoustic resonator and acoustic filters (see Fig. 6).

The resonator has a length of 34 mm and is excited at the fundamental longitudinal mode at a frequency around 4580 Hz (35 °C) and with the pressure antinode in the middle of the resonator, where a microphone is connected in a noise- and gas-tight enclosure to measure the photoacoustic signal. Acoustically short concentric-tube resonators (SCRs), which are small volume, reactive acoustic bandstop filters similar to quarter-wavelength tubes [38], are connected at both ends

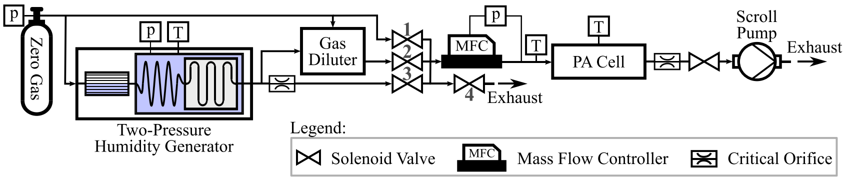

Fig. 5 Schematic drawing of the experimental setup with zero gas, humidity generator and gas diluter on the left hand side and photoacoustic (PA) cell, together with sampling and conditioning components on the right hand side. Rectangles with *p* and *T* mark locations where pressure and temperature, respectively, are controlled within the ranges stated in the text

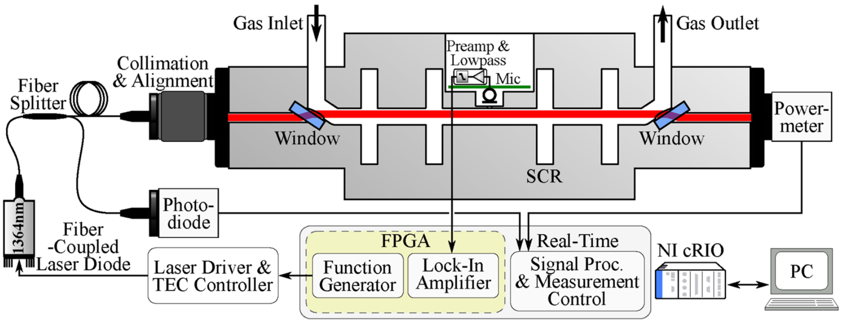

Fig. 6 Schematic drawing of the photoacoustic cell and measurement setup. System control and data acquisition are performed on the real-time embedded controller (NI cRIO)

of the resonator (i.e., at the pressure nodes). The SCRs are 6 mm in length and have diameters of 34 mm, tuned to the same resonance frequency as the resonator using finite element method based optimization. This maximizes acoustic reflection at the resonator ends for the resonant mode and for unwanted external noise reaching the resonator. To further decrease outside noise transmission at the measurement frequency into the resonator, one additional SCR is placed upstream as well as downstream of the resonance section. The distance between the SCRs is numerically optimized to maximize overall transmission loss. An additional measure to minimize measurement noise is the vibrational decoupling of the cell from the device rack by short sections of PTFE tubing and a vibration absorbing mounting.

The laser source is a fiber-coupled distributed feedback laser diode (NEL, NLK1E5GAAA), temperature controlled to the 7327.7 cm^{-1} (296 K) absorption line, which corresponds to a ro-vibrational transition from the vibrational ground state to the vibrational $H_2O(1,0,1)$ state. This specific line was chosen because of the minimal line shift with pressure, high line intensity and low interference from other anticipated atmospheric constituents. The laser is square wave intensity modulated down to just below the lasing threshold at the resonance frequency with a benchtop laser driver (Thorlabs, ITC4001), maintaining an average power of 9.9 ± 0.1 mW. The laser beam is collimated to 2 mm diameter, entering and exiting the cell at two flush-mounted N-BK7 Brewster-windows (angle of 56.4°), which allows to maximize transmitted laser power. A thermal powermeter (Thorlabs, PM16-401) is used to measure the average laser power when no water vapor is present in the cell, i.e., during background measurements, when the cell is flushed with synthetic air. During measurements a fiber splitter with 99:1 split ratio (Thorlabs, TW1300R1A1) is used to monitor the laser power with an InAsSb photodetector (Thorlabs, PDA10PT-EC). Due to the stability of the laser diode in use over typical time periods between calibrations, no wavelength locking or power correction of the photoacoustic signal had to be applied.

The microphone in use is an electret condenser microphone (Knowles, EK-23028) with a specified humidity sensitivity of 0.02 dB/% RH. Signals are preamplified with a tenfold gain, before sampling at 51.2 kHz with a 24 bit ADC (National Instruments, NI 9234) and processing with a real-time embedded controller (National Instruments, NI cRIO-9031) is carried out. This controller features a function generator for generating the laser modulation signal and a digital lock-in amplifier for phase-sensitive detection, implemented on a reconfigurable field programmable gate array (FPGA). All signals are acquired with an integration time of 1 s. Background signal correction is carried out on the real-time processor of the controller.

The PA cell temperature and the gas temperature approximately 100 mm upstream of the cell are controlled to 35.0 ± 0.2 °C by two heating cartridges (125 W each) integrated into the stainless steel cell and heating tape around the upstream piping. The heating elements are controlled by a PID-controller implemented on the real-time embedded controller, which is supplied with the cell temperature and the gas temperature upstream of the cell measured with resistance temperature detectors (PT100, 1/3 DIN). A scroll pump in combination with a critical orifice with 350 µm nominal diameter is used to maintain a constant volumetric flow rate of 0.75 slpm through the cell. The critical orifice has the additional benefit of inhibiting noise from the downstream pump reaching the cell. Directly upstream of the PA cell, a pressure controller maintains a constant pressure of 800(5) hPa inside the cell.

3.2 Humidity generation

Synthetic air or molecular nitrogen (Messer, for properties see Table 2) is either directly routed to the photoacoustic cell for the measurement of the background signal and noise, or humidified with a custom-made two-pressure humidity generator. The humidity generator consists of a pre-saturator, a heat exchanger and a saturator, where the latter two components are placed in a temperature-controlled water bath. Supplied zero gas is humidified in the presaturator to approximately 95% relative humidity at room temperature by passing the gas through a porous ceramics with honeycomb structure (IBIDEN Ceram) in a bath of distilled water. After pre-saturation, the gas is cooled and saturated to the desired saturation vapor pressure in a coiled tube heat exchanger combined with a saturator, which is formed by a milled channel in a stainless steel block, halfway filled with distilled water. The temperature of the water bath can be controlled to values between 1 and 20 °C with an uncertainty of 0.16 °C. Setting the pressure in the saturator with a pressure controller in the range of 1–8 bar (±2 hPa) allows to calculate the set saturation water vapor pressure or mole fraction [39, 40]. Uncertainties for the water vapor mole fractions in the two-pressure humidity generator have been calculated according to Meyer et al. [41]. The humidified air can then either be passed directly to the PA cell, or passed through the temperature controlled gas diluter [42], where the zero gas is mixed with the humidified gas based on binary weighted critical flows. This way, dilution ratios down to 1 : 31 have been used to further lower the water vapor mole fraction.

Table 2 Supplier specification for composition and relevant trace levels of synthetic air and nitrogen used in measurements

	Synthetic air	Nitrogen
$x_{N_2,\mathrm{dry}}$	79.5 vol%	99.99 vol%
$x_{O_2,\mathrm{dry}}$	20.5 vol%	≤2 ppmV
x_{H_2O}	≤2 ppmV	≤3 ppmV

3.3 Correction of the photoacoustic phase

The speed of sound in the PA cell and hence the resonance frequency of the resonator is a function of the gas temperature and pressure, as well as the water vapor mole fraction [43]. To accurately determine the PA signal at varying water vapor mole fractions, a change in the resonance frequency either has to be actively tracked with the modulation frequency or corrected for. The measurement system in use is only capable of reliably tracking the resonance frequency at water vapor mole fractions above 1000 ppm and exhibits phase errors too large for the targeted accuracy. Therefore, the modulation frequency is held constant for all measurements with one carrier gas and the phase of the measured signal is then corrected according to the procedure described in the following. A correction of the PA amplitude was not carried out, because signal losses in the amplitude are low for the given Q-factor and the anticipated resonance frequency shifts (see Sects. 4.1 and 4.2).

In the proximity of the resonance peak, the phase of the photoacoustic signal can be approximated by a linear function of the frequency shift with slope a_ϕ. Using this function, the phase measured at frequency f_0 and water vapor mole fraction x_{H_2O} can then be corrected to give the phase at the actual resonance frequency, f_{res}:

$$\phi(f_{\mathrm{res}}, x_{H_2O}) = \phi(f_0, x_{H_2O}) + a_\phi \cdot (f_{\mathrm{res}} - f_0). \tag{27}$$

The slope a_ϕ can be determined from a measurement of the PA response around the resonance and the unknown f_{res} is calculated by using the fact that for a longitudinal resonator the resonance frequency is given by

$$f = m_j \frac{c}{2\,L_{\mathrm{res}}}, \tag{28}$$

where c is the speed of sound, m_j is a non-negative integer, characteristic for the chosen resonance mode, and L_{res} is the effective length of the resonator. When the resonance frequency and speed of sound are known at a reference point (denoted by the subscript 0), the actual resonance frequency can be approximated by

$$f_{\mathrm{res}}(x_{H_2O}) = f_0 \frac{c(f_0, x_{H_2O})}{c_0}. \tag{29}$$

The speed of sound in the gas mixtures was calculated according to Zuckerwar [43], as it can be described to great accuracy by theory at various temperatures and pressures. For the nitrogen mixture, however, no virial correction of the speed of sound was carried out.

3.4 Measurement

First, photoacoustically excited resonance curves were recorded at steady water vapor mole fractions of 4900 ppm in synthetic air and 11821 ppm in nitrogen, to determine the reference speed of sound and the reference resonance frequency for later correction of the phase according to Eq. (27). High water mole fractions were used to ensure a high signal to noise ratio (SNR). Resonance frequency and quality factor (Q-factor) were determined from a nonlinear curve fit of a Lorentzian function to the microphone signal power, which was measured at modulation frequencies in a ±400 Hz range of the resonance frequency with a resolution of 25 Hz. The resonance frequency is the frequency with maximum power and the Q-factor is the ratio of the resonance frequency to the full frequency width at half the maximum (FWHM) of the measured resonance curve. All following measurements were then conducted with the laser modulated at the determined resonance frequency.

Before each measurement series with synthetic air or nitrogen, the background signal, $\mathbf{S}_{BG} = (S_{BG,I}, S_{BG,Q})^T$, was acquired for 60 s, after flushing the PA cell with the respective zero gas for approximately 20 minutes. Here, I and Q denote the in-phase and quadrature components of the lock-in amplifier signal, respectively. Subsequently, the photoacoustic signal in the humidified gas, $\mathbf{S}_m = (S_{m,I}, S_{m,Q})^T$, was measured and the actual signal amplitude, S, and phase, ϕ, were calculated after phase-correct background correction. This was achieved by subtracting the mean of the background signal of the corresponding buffer gas before calculating amplitude or phase:

$$\begin{aligned} S &= \|\mathbf{S}_m - \overline{\mathbf{S}}_{BG}\| \\ &= \sqrt{(S_{m,I} - \overline{S}_{BG,I})^2 + (S_{m,Q} - \overline{S}_{BG,Q})^2}, \end{aligned} \tag{30}$$

$$\phi = \arctan\left(\frac{S_{m,Q} - \overline{S}_{BG,Q}}{S_{m,I} - \overline{S}_{BG,I}}\right). \tag{31}$$

An Allan deviation analysis of the PA background signal for pure synthetic air showed that deviations in the background signal due to drift over the time necessary for each measurement series are below the noise level at 1 s integration time. For this reason and the fact that the overall uncertainty is dominated by the uncertainty in the provided humidity, fluctuations of the background signal are not considered in the evaluation.

Starting from initial water vapor mole fractions (11435 ppm in synth. air and 11821 ppm in N_2), the water concentration was incrementally decreased. After reaching the minimum concentration (124 ppm and 132 ppm, respectively) the water vapor concentration was increased again until reaching the maximum measured concentration (22154 ppm and 20278 ppm, respectively). This way, each measurement at a specific water vapor concentration is only taken once, but the interleaved measurements give a measure of repeatability. For each mole fraction set, the PA signal was recorded for 30 s after attaining a steady signal level. Mole fractions below 3900 ppm were generated in combination with the gas diluter.

3.5 Data analysis

The amplitude of the postulated nonlinear function for the PA response of water vapor in air, Eq. (26), was fit to the measured PA amplitude in a weighted least-squares sense, using a commercial curve fitting software [44]. Mole fraction weighted signal amplitudes were used to force minimization of the relative error, as otherwise large relative errors are tolerated for low signal levels in favor of small absolute errors at high amplitudes. The iterative trust region reflective solver was used to determine the best-fit values of the five parameters and coefficients C_{cell}, B_{cell}, c_1, c_2 and c_3. Starting values for the coefficients c_1 to c_3 were calculated using the rate coefficients given in Table 1 and setting $E_{\text{H}_2\text{O}^*} = 1595\ \text{cm}^{-1}$ (i.e., equal to the energy of the H_2O (0,1,0) level) and

$$E_{\text{inst}} = h\,\nu - 4\,E_{\text{H}_2\text{O}^*}. \tag{32}$$

For measurements in humidified nitrogen, the oxygen mole fraction of the carrier gas, $x_{\text{O}_2,\text{dry}}$, in c_1 and c_2 (Eqs. (19) and (20)) is set to zero. The conversion efficiency then is equal to unity (cf. Eq. (18)) and, as a result, the PA response of water vapor, Eq. (26), in nitrogen reduces to a simple second-degree polynomial with the fit parameters C_{cell} and B_{cell}. Therefore, the coefficients c_1 to c_3 cannot be determined from measurements in humidified nitrogen.

In all of the presented figures, error bars for the PA amplitude mark the standard deviations calculated for the measured signal during the measurement time. Error bars for the phase indicate the uncertainty in the measured phase, calculated according to the GUM [45] using Eq. (27), while error bars for the mole fraction mark the uncertainty (95%) in the mole fraction (see Sect. 3.2).

4 Results and discussion

4.1 Nitrogen

In humidified nitrogen, a resonance frequency of 4658 Hz was determined at the reference water vapor mole fraction of 11821 ppm. As explained before, the modulation frequency was held constant at this value for all subsequent measurements in nitrogen and the phase was corrected using Eq. (27). However, additional resonance curves at higher and lower water mole fractions were acquired. The determined resonance frequencies showed good agreement with the theoretical values calculated from Eq. (29). For the maximum and minimum water vapor mole fractions measured, the resonance frequencies calculated are 4664 Hz and 4650 Hz, respectively. The largest resulting resonance shift, which occurs for the smallest H_2O concentration, is estimated to cause amplitude errors less than 0.4% for the evaluated Q-factor of the PA cell of 17.

The measured and background-corrected PA amplitude and phase for nitrogen is shown in Fig. 7, together with the determined polynomial fit. Figure 8 is a plot of the amplitude with logarithmic scales, better displaying a linear response at low mole fractions.

A nonlinear PA response and phase shift with increasing H_2O concentration as is shown below for air would be measurable, if N_2 would be excited in similar quantities as O_2, because of the similar rate coefficients of (R13) and (R14).

For the evaluated range of water concentrations, it can be seen that the response is presumably linear for a large range of water fractions and a polynomial of second degree is sufficient to adequately capture and predict the PA amplitude response in nitrogen. In this range, the error in the humidity sensitivity of the electret microphone by a linear approximation is lower than 0.4% for the specified sensitivity of 0.02 dB/%RH. The best-fit values and 95% confidence intervals for C_{cell}, and B_{cell} in Eq. (26) are given in Table 3 in terms of sensitivity and first-order sensitivity correction, respectively.

The initial offset of approximately 22° of the corrected phase, shown in the lower part of Fig. 7, is arbitrary and is a result of the time delays in the electronics and signal processing for the given modulation frequency, affecting the measured phase. The phase, however, exhibits a small dip below 2000 ppm and a decreasing trend above. At low water fractions, the small measured decrease and recovery of less than 1° may be the result of the competing V–T relaxation processes (R12) and (R14).

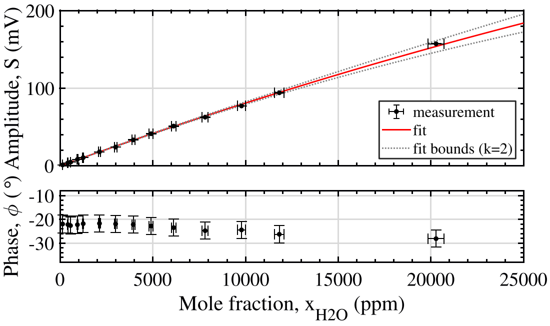

Fig. 7 Measured and background-corrected amplitude and phase of the photoacoustic signal of water vapor in nitrogen at 35 °C and 800 hPa, together with the polynomial fit to the amplitude response. Dotted lines give the 95% (i.e., coverage factor $k = 2$) functional bounds of the fit. Error bars are described in the text

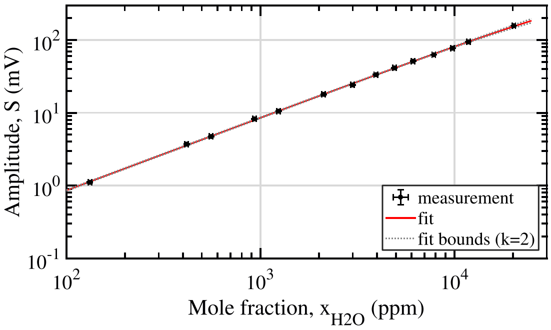

Fig. 8 Logarithmic plot of the measured and background corrected amplitude of the photoacoustic signal of water vapor in nitrogen. For an explanation of the lines, see Fig. 7

H_2O is much more efficient in the thermalization of vibrationally excited nitrogen than N_2 itself or O_2 and thus a phase shift and increase in sensitivity should be observable, if nitrogen is excited in substantial numbers. The small magnitude of the observed shift in phase, however, indicates the marginal contribution of the V–T relaxation of N_2^* to the PA source rate of heat production. Because the measured amplitude also remains practically linear over the full range of concentrations (to the extent measurable with the accuracy of the given setup), we conclude that the vibrational excitation of molecular nitrogen is of negligible importance in the PA signal generation process of water vapor in nitrogen, as well as in air. This justifies neglecting the V–V transfer process (R10) in the derivation of the three-state model. We would like to note at this point that it is still necessary to experimentally validate this assumption for higher modulation frequencies.

The values for the cell constant and the first-order correction differ from the values in air, mainly because of the modulation frequency and composition-dependent microphone sensitivity. As mentioned in Sect. 3.5, the coefficients c_1 to c_3 cannot be determined for the carrier gas

Table 3 Best-fit values and confidence interval (95%) of the parameters of the model, Eq. (26), determined from the curve fit to the measured and background-corrected PA amplitude of water vapor in nitrogen at 35 °C and 800 hPa

Coefficient	Value	Confidence interval
$C_{\text{cell}}\,\sigma\,P\,n_0$	8.566 μV/ppm	± 0.17 μV/ppm
$B_{\text{cell}}\,n_0$	5.649 ppm/ppm	±2.5 ppm/ppm

nitrogen, the reason being the fast relaxation of H_2O^* by N_2, i.e., the rate k_8^{V-T} (or equivalently $k_{H_2O^*,M}^{V-T}$) in reaction (R8). Without the possibility of vibrational coupling of H_2O^* and O_2^*, this reaction on its own induces full relaxation of $H_2O(1,0,1)$ within typical PA modulation periods. For the N_2 environment, this fast relaxation time results in a constant zero phase shift with respect to the excitation predicted by the model.

Due to the small magnitude of the observed phase shift, it cannot be fully ruled out that the measured variations are caused by minor temperature variations of the PA cell, inducing a shift of the resonance frequency. The reasons for the observable, superimposed trend with increasing water mole fractions are still unclear, but changing microphone sensitivity could be one possible source of origin. An error in the correction of the resonance frequency could be ruled out, as the calculated phase at resonance was verified at several water vapor mole fractions with additionally acquired resonance curves.

4.2 Synthetic air

The resonance frequency at the measurement temperature and pressure, determined for humidified synthetic air at the reference water vapor mole fraction of 4900 ppm, is 4586 Hz. Background measurement and measurements of the PA signal in humidified synthetic air were conducted at this modulation frequency. For the maximum and minimum water vapor mole fractions measured, the resonance frequencies calculated according to Eq. (29) are 4598 and 4584 Hz, respectively. Experimental determination of the resonance frequency at several water vapor mole fractions confirmed the theoretical calculation. The largest resulting resonance shift, which occurs for the largest H_2O concentration, is estimated to cause amplitude errors less than 0.8% for the evaluated Q-factor.

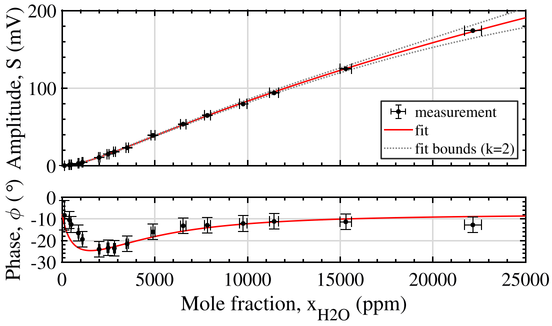

Fig. 9 Measured and background-corrected amplitude and phase of the photoacoustic signal of water vapor in synthetic air at 35 °C and 800 hPa. Solid lines are evaluated from the fit of the three-level model to the measured and background-corrected PA amplitude. The phase evaluated from the model fit is offset by −7.7°. Dotted lines give the 95% (i.e., coverage factor $k = 2$) functional bounds of the fit. Error bars are described in the text

4.2.1 PA amplitude and phase

Figure 9 shows the measured and background-corrected PA response for water vapor in synthetic air. The solid line in the upper panel is the fit of the PA amplitude response, calculated by fitting the amplitude of the model function (absolute value of Eq. (26)) to the measured PA amplitude data with the given starting values for the model parameters and coefficients. Dashed lines again show the 95% confidence bounds for the fit and a plot of the PA amplitude with logarithmic scales is shown in Fig. 10.

The lower panel of Fig. 9 shows the measured and corrected phase of the PA signal, together with the phase calculated from Eq. (22) with the coefficients estimated from the amplitude fit. Because of the different modulation frequency, the absolute value of the phase in synthetic air cannot be directly compared to the phase measured in nitrogen. The measured phase again includes a constant arbitrary phase

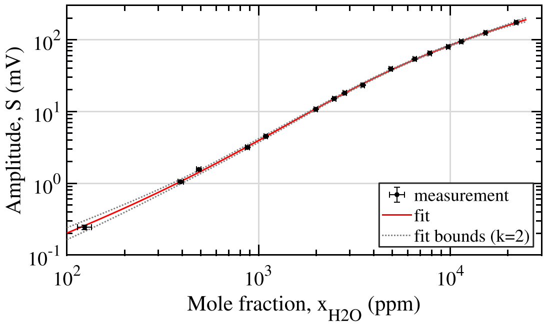

Fig. 10 Logarithmic plot of the measured and background-corrected amplitude of the photoacoustic signal of water vapor in synthetic air. For an explanation of the lines, see Fig. 9

Table 4 Best-fit values and uncertainties of the parameters and coefficients of the model, Eq. (26), determined from the nonlinear curve fit to the measured and background-corrected PA amplitude of water vapor in synthetic air at 35 °C and 800 hPa

Coefficient	Value	Confidence interval (95%)
$C_{cell}\,\sigma\,P\,n_0$	9.285 µV/ppm	±0.82 µV/ppm
$B_{cell}\,n_0$	7.023 ppm/ppm	±4.6 ppm/ppm
c_1	6.112×10^{-4}	$\pm 5.5 \times 10^{-4}$
c_2	2.565×10^{-3}	$\pm 1.4 \times 10^{-3}$
c_3	3.101×10^{-13} cm^3/(molec.s)	$\pm 1.7 \times 10^{-13}$ cm^3/(molec.s)

shift from the specific time delays at the given modulation frequency. For the purpose of an easier comparison of measured and modeled phase, the model phase is offset by −7.7°.

Estimated best-fit parameters and coefficients are given in Table 4, where C_{cell}, and B_{cell} again have been given in terms of sensitivity and first-order sensitivity correction, respectively. The calculated sensitivity of 9.28 µV/ppm is approximately the maximum achievable sensitivity, which is reached when the conversion efficiency $\eta \rightarrow 1$ in the limit of large water vapor mole fractions. In this limit, H_2O^* is thermalized by H_2O, before V–V transfer to O_2 can occur. One may notice the high uncertainty in the value of the first-order sensitivity correction, which comes from the limited range of water vapor concentrations used for calibration. To decrease the uncertainty, a larger range would be necessary, but measuring at even higher concentrations may require higher-order terms, as the linear approximation of the Beer–Lambert law is invalidated.

Figure 11 shows the relative residual of the model response, which is, for a given microphone signal, the difference of the water vapor mole fraction predicted by the model and the mole fraction set by the humidity generator. With the estimated parameters and coefficients, residual mole fractions are below 4% above 500 ppm water vapor mole fraction. At lower fractions, the decreasing relative accuracy of the combination of humidity generation and PA measurement setup results in increasing deviations of the model from the measured response. Therefore, it is inconclusive whether the model is capable of returning satisfying predictions for the PA response for mole fractions down to the ppm level with the assumptions made in the derivation. Validation with a larger range of concentrations, especially below 1000 ppm, and a setup of combined higher accuracy would allow a much preciser determination of the model coefficients.

Overall, the derived model shows excellent capability of reproducing the functional relationship between the water vapor mole fraction in air and the measured PA amplitude response. The additional close agreement between measured and predicted phase response reassures that the model describes the main processes involved in release of kinetic energy by relaxation of H_2O from low lying vibrational states. Also, considering the trend of decreasing phase observed in the nitrogen buffer gas, which presumably is independent of the relaxation process, further decreases the differences in the measured and predicted PA phase response for water vapor in air. Measured and trend-adjusted phase values in Fig. 9 below the reference point concentration of 4900 ppm should be decreased, whereas values above should be increased.

An idea briefly discussed in Sect. 2.2.2 is the use of the complex signal for finding the best-fit parameters. Fitting the complex PA signal gives parameter values in close agreement to the values determined by only fitting the amplitude response. However, the large uncertainty in the measured phase may introduce large systematic errors, deteriorating the estimated values. For devices with an accurate resonance frequency tracking functionality implemented, a precise relative measurement of the signal phase may be possible and allow enhancing the parameter estimation by the simultaneous use of the entire information available, i.e., measured amplitude and phase.

4.2.2 Sensitivity and PA conversion efficiency

Figure 12 shows the sensitivity of the measurement setup and the overall PA conversion efficiency calculated from Eq. (18) with the determined fit parameters. The sensitivity equals the derivative of the signal amplitude with respect to the water vapor mole fraction. It is calculated numerically from the determined best-fit model function.

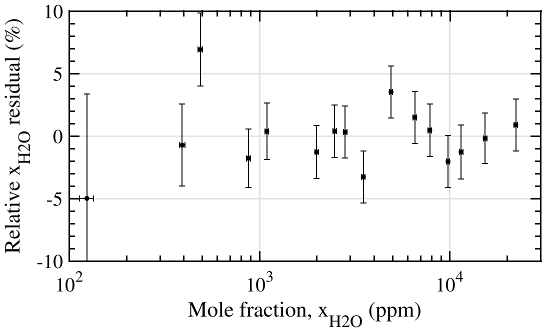

Fig. 11 Relative residual of water vapor mole fraction for the model fit. Both, vertical and horizontal error bars mark the uncertainty (95%) of the humidity generation

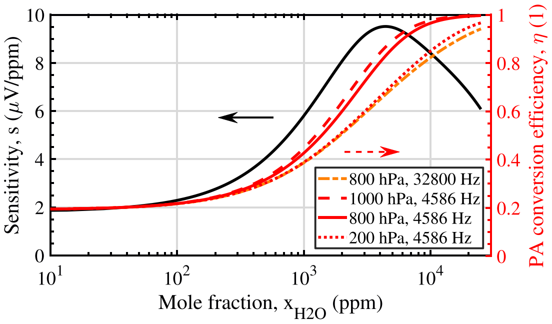

Fig. 12 Sensitivity of the PA measurement setup calculated numerically from the determined best-fit model function (800 hPa and 35 °C), together with the determined overall PA conversion efficiency at various pressures and modulation frequencies (all at 35 °C)

The PA conversion efficiency asymptotically approaches approximately 19.2% in the limit of small mole fractions of water vapor. As a consequence, the sensitivity also reaches only about 19% of the maximum sensitivity (cf. Table 4) in this region, where the attenuation of irradiated power is negligible. In the process of heat production, this value corresponds to the energy released instantaneously after radiative excitation, i.e., E_{inst}, plus the energy released by the V–T relaxation of H_2O^* or O_2^* by collision with either O_2 or N_2. For an excitation energy equal to 7327 cm^{-1}, the photoacoustically available energy is approximately equal to 1400 cm^{-1} per exited molecule at the conditions of measurement. The large residual energy, in the low concentration limit, is lost in vibrationally excited oxygen, due to its long relaxation time. Increasing the water vapor mole fraction up to 16,000 ppm increases the PA conversion efficiency and the heat production rate up to the point, where the full energy (99%) is released within the period of modulation. However, before this point is reached, decreased irradiance due to absorption deteriorates the sensitivity for the presented setup. The attenuation, calculated from B_{cell}, rises above 1% at approximately 1400 ppm and initiates a transition to decreasing sensitivity. Maximum sensitivity for the given cell is reached at 4400 ppm. For PA spectroscopy setups where absorption path lengths are much shorter (e.g., in QEPAS), attenuation effects may be delayed to higher water vapor concentrations. Increasing modulation frequency, however, also delays reaching the full conversion efficiency to higher concentrations (cf. Fig. 12).

With the value of the sensitivity in the limit of low concentrations, s_0, the theoretical 3σ limit of detection can be estimated:

$$\mathrm{LOD}_{\mathrm{H_2O}} = \frac{3\,\sigma_{\mathrm{noise}}}{s_0} = 38\ \mathrm{ppm}, \tag{33}$$

where σ_{noise} is the standard deviation of the measured PA amplitude in the background measurement at an integration time of 1 s. Neglecting the nonlinear nature of the PA response and taking a value of the sensitivity close to the maximum observed would result in underestimating the LOD by approximately a factor of five.

The model may also be used to explain the sensitivity characteristics of the photoacoustic hygrometer of Tátrai et al. [11] (their Fig. 4). In their work, the measured sensitivity at a pressure of 800 hPa roughly remains constant below 250 ppmV, from where it steadily increases up to approximately 5000 ppmV. Above, the sensitivity starts to decrease again. This behavior closely matches the sensitivity demonstrated in this work.

The PA conversion efficiency given in Eq. (18) and shown in Fig. 12 is a function of the number density, which itself is a function of measurement pressure and temperature according to the ideal gas law. In a typical pressure and temperature-controlled photoacoustic setup, these two variables can be varied to some extent; therefore, it is beneficial to identify favorable magnitudes for the state variables, which maximize the conversion efficiency. In Eq. (18) the number density, n_0, only appears in combination with c_3, which is the rate coefficient for the V–T relaxation of O_2^* by collision with H_2O, i.e., $\mathrm{k}^{V-T}_{\mathrm{O_2^*,H_2O}}$ (cf. Eq. (21)). Increasing pressure can thus be viewed as proportionally increasing the V–T relaxation rate $\mathrm{k}^{V-T}_{\mathrm{O_2^*,H_2O}}$, which results in accelerated deexcitation of O_2^* and consequently in an increased PA conversion efficiency when relevant amounts of water vapor are present. It follows that the conversion efficiency can be maximized by maximizing the measurement pressure. This behavior is shown in Fig. 12 for the measurement pressure of 800 hPa, as well as higher and lower pressures. Contrary to the pressure dependence, the conversion efficiency is maximized by minimizing temperature. When the modulation frequency is increased, less heat is released in phase with the modulation and therefore the conversion efficiency is decreased (cf. Fig. 12). In general the PA signal, given by Eq. (26), will also depend on pressure and temperature through the characteristics of the microphone, hence the overall dependence of the PA signal on pressure and temperature can only be calculated for a specific setup.

The best-fit values for the coefficients c_1 and c_2 are slightly lower than the starting values calculated from literature values. Due to the convoluted dependencies of these coefficients on the rate coefficient and energies, it is difficult to draw direct conclusions about the involved processes. To assess relevant physical constants in these model coefficients, Figs. 13 and 14 show the local relative sensitivity of the PA conversion efficiency and the phase shift on the four

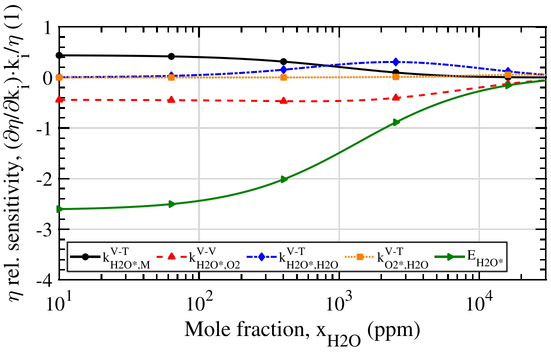

Fig. 13 Relative local sensitivity of the PA conversion efficiency on rate coefficients, k_i, and on the energy of the H_2O^* reservoir, $E_{\mathrm{H_2O^*}}$. The sensitivity is calculated with literature rate coefficients and for the conditions of measurement (800 hPa, 35 °C, 4586 Hz and 20.5% O_2 fraction)

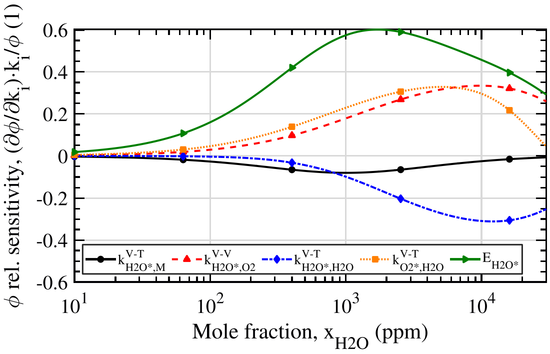

Fig. 14 Relative local sensitivity of the PA phase shift on rate coefficients, k_i, and on the energy of the H_2O^* reservoir, $E_{H_2O^*}$. The sensitivity is calculated with literature rate coefficients and for the conditions of measurement (800 hPa, 35 °C, 4586 Hz and 20.5% O_2 fraction)

remaining rate coefficients of the model and on the energy of the H_2O^* reservoir, $E_{H_2O^*}$, at the conditions of measurement. The shown sensitivity gives the local relative change in η or ϕ per relative change in the rate coefficient or energy at the given water concentration. The relative sensitivity of η is equal to the relative sensitivity of the signal amplitude. It can be seen that the magnitude of the conversion efficiency as well as the phase shift is most sensitive to $E_{H_2O^*}$. The value for the energy of the reservoir determines the energy released instantaneously after radiative excitation (cf. Eq. (32)), which at low water vapor concentrations is the main contribution to the PA heat source rate and therefore also to η and the signal amplitude. This explains the large sensitivity of η to $E_{H_2O^*}$ at low concentrations. Figures 13 and 14 also show that directly applying literature values for rate constants and the energy of the reservoir in the model, instead of the fit parameters c_1 and c_2, requires the accurate determination of all of the rate constants of the involved reactions to accurately predict the amplitude and phase response of a PA hygrometer over the range of mole fractions studied in this work. As uncertainties and therefore probably also errors in the literature rate coefficients are generally large (e.g., Huestis [25]), this inevitably will lead to large deviations between model prediction and experimental measurements. However, this underlines the benefit of the proposed model function of summarizing four coefficients: ($k^{V-T}_{H_2O^*,M}$, $k^{V-V}_{H_2O^*,O_2}$, $k^{V-T}_{H_2O^*,H_2O}$ and $E_{H_2O^*}$) in the two coefficients c_1 and c_2, which can be determined from calibration.

Only at large concentrations, where η approaches unity, the conversion efficiency and therefore also the PA signal amplitude become insensitive to the constants and a simple second-order polynomial suffices to describe the signal amplitude. At low water concentrations, the signal amplitude only depends on $k^{V-T}_{H_2O^*,M}$, $k^{V-V}_{H_2O^*,O_2}$, and $E_{H_2O^*}$. Therefore, the PA response for low water concentrations can be fully described by the coefficients c_1 and c_2 in addition to the cell parameters. This also opens up the possibility of determining the ratio of $k^{V-T}_{H_2O^*,M}$ and $k^{V-V}_{H_2O^*,O_2}$ by measuring the PA response at low concentrations for excitation into the H_2O (0,1,0) state, where $E_{H_2O^*}$ is accurately known. Additionally, in such an experiment the model describes the full relaxation path, and uncertainties introduced by model assumptions are negligible.

The third coefficient, c_3, is equivalent to the rate coefficient of the V–T relaxation of O_2^* by collision with H_2O, i.e., $k^{V-T}_{O_2^*,H_2O}$ in reaction (R13). The determined value is about an order of magnitude higher than the rate measured by Bass et al. [26, 27, 30]. Unfortunately, the latter, much-cited rate coefficient is, to our knowledge, the only literature value available for this process. When constraining the value of c_3 (and thus $k^{V-T}_{O_2^*,H_2O}$) to the reaction rate coefficient stated by Bass et al., it is not possible to reproduce the measured PA response with the derived model function, Eq. (26). This is the result of an underestimation of the phase-delayed PA heat source rate component due to reaction (R13) (cf. last term in brackets in Eq. (S2)). For this reason we suspect that the value stated for $k^{V-T}_{O_2^*,H_2O}$ by Bass et al. may be underestimated. Figure 14 shows the high sensitivity of the phase shift to the rate coefficient in question. This implies that $k^{V-T}_{O_2^*,H_2O}$ may be directly and accurately determined from a fit of the model to PA measurements of excitation into the H_2O (0,1,0) state considering the measured phase. The sensitivity of η and the signal amplitude to the rate coefficient are shown to be negligible (cf. Fig. 13). However, this changes when $k^{V-T}_{O_2^*,H_2O}$ is set to the value determined by the fit parameter c_3. In this case, the reaction coefficient strongly contributes to η in the range of 1000–10,000 ppm. This also explains the inability of the model to reproduce the measured amplitude when $k^{V-T}_{O_2^*,H_2O}$ is constrained to the literature value.

5 Conclusions

In the present work, we demonstrated the significant and unfavorable effects of relaxation processes involving molecular oxygen, on the vibrational photoacoustic measurement of water vapor in air. The strong resonant coupling of the first vibrationally excited state of water vapor, H_2O (0,1,0), with the long-living, first vibrationally excited state of molecular oxygen, $O_2(1)$, leads to a relaxation time that is large in comparison to typical modulation periods in photoacoustic spectroscopy. This results in a nonlinear photoacoustic signal response which has to be taken into account in measurements of water vapor in atmospheric environments. Neglecting relaxation losses and assuming a linear functional relationship between the number of absorbing molecules and the measured PA signal as it is commonly done may lead to indeterminate errors when extrapolating the signal outside the measurement range.

We propose a simplified model in the form of Eq. (26), physically approximating the main relaxation processes involved. The derived model describes the microphone signal measured in a resonant photoacoustic cell and a mixture of air and water vapor, after radiative excitation from the ground state into vibrational $H_2O(1,0,1)$ state. Furthermore, the suggested model may easily be adapted to lower and possibly also higher excitation energies. Additionally, adaption of the model to predict the PA response for other systems of measured species and carrier gas, where the vibrational coupling to oxygen is of importance, seems feasible (e.g., CH_4 in air [17]). Validation of the model was performed for the range of approximately 100–22,000 ppm water vapor mole fraction in synthetic air.

The presented PA measurement results of water vapor in nitrogen show that the process of excitation of nitrogen by V–V energy transfer does not contribute significantly to the decrease of the signal for water vapor mole fractions greater than 100 ppm and at typical modulation frequencies. Hence, sensitivity losses in air are fully attributable to oxygen, and no losses are to be expected in nitrogen environments. Thus, applying corrections based on photoacoustic water vapor measurements in nitrogen to measurements made in air (e.g., [5]) can lead to significant errors. Contributions arising from minor air constituents (e.g., Ar, CO_2) have been neglected in the current analysis. Consideration of relevant relaxation processes of these constituents may lead to a more accurate, but possibly more complicated model.

The derived model contains three coefficients, c_1 to c_3, which summarize kinetic coefficients and are universal for a given excitation energy and carrier gas composition. The three coefficients should be practically independent of the measurement setup. Only minor temperature dependence should be observable, caused by the temperature dependence of the rate coefficients. Thus, determining c_1 to c_3 once allows to predict the response of a PA hygrometer outside the calibration range. Best-fit results for the two device parameters, C_{cell} and B_{cell}, and the three coefficients, determined from measurement data are given in Table 4.

The two device parameters, C_{cell} and B_{cell}, correlate to measurement sensitivity and first-order correction of the cell constant C_{cell}. In environments of sufficiently low water vapor concentrations, where a decrease of irradiance due to absorption and other second-order effects in the microphone signal may be neglected, the sensitivity is the only setup specific parameter. When the coefficients of the kinetic model, c_1 to c_3, are accurately determined, the calibration of a photoacoustic hygrometer (i.e., the determination of C_{cell}) in this region may be accomplished by a background measurement combined with a single, accurate reference concentration measurement. The presented findings suggest that the derived model should then allow extrapolation within the region of low water vapor concentrations. When measurements have to be accomplished at high water vapor concentrations, where second-order effects cannot be neglected, the two device parameters, C_{cell} and B_{cell}, can be determined solely from calibration at high water vapor concentrations. Accurately determined coefficients of the PA conversion efficiency may allow accurate extrapolation to lower water vapor fractions.

Evaluation of the model coefficient c_3 opens up the possibility of estimating the V–T relaxation rate coefficient of $O_2(1)$ by H_2O, i.e., of reaction (R13). The estimated value determined in this work is an order of magnitude larger than the value measured by Bass et al. [26, 27, 30], which apparently is the only literature source available for this rate. As this value is also of relevance to the atmospheric radiative transfer community, the discrepancy will be further investigated.

Acknowledgements Open access funding provided by Graz University of Technology.

Author Contributions Conceptualization: Benjamin Lang, Alexander Bergmann. Methodology and investigation: Benjamin Lang, Philipp Breitegger. Software and material preparation: Benjamin Lang, Georg Brunnhofer, Jordi Prats Valero, Simon Schweighart. Writing—original draft preparation: Benjamin Lang. Writing—review and editing: all authors. Funding acquisition: Andreas Tramposch, Alexander Bergmann, Wolfgang Hassler. Resources: Alexander Bergmann, Andreas Klug, Wolfgang Hassler. Supervision: Alexander Bergmann, Wolfgang Hassler. Project administration: Alexander Bergmann, Andreas Klug, Wolfgang Hassler.

Funding This work has been partly funded by the Austrian Aeronautics Programme TAKE OFF of the Federal Ministry of Transport, Innovation and Technology (BMVIT), managed by the FFG (Project number: 850457).

Compliance with ethical standards

Conflict of interest The authors declare that they have no conflict of interest.

References

1. Z. Bozóki, A. Pogány, G. Szabó, Appl. Spectrosc. Rev. **46**(1), 1 (2011). https://doi.org/10.1080/05704928.2010.520178
2. P. Patimisco, A. Sampaolo, L. Dong, F.K. Tittel, V. Spagnolo, Recent advances in quartz enhanced photoacoustic sensing. Appl. Phys. Rev. (2018). https://doi.org/10.1063/1.5013612
3. J. Seinfeld, S. Pandis, *Atmospheric Chemistry and Physics: From Air Pollution to Climate Change*, 3rd edn. (Wiley, New York, 2016). https://doi.org/10.1080/00139157.1999.10544295
4. X. Yin, L. Dong, H. Zheng, X. Liu, H. Wu, Y. Yang, W. Ma, L. Zhang, W. Yin, L. Xiao, S. Jia, Sensors **16**(2), 162 (2016). https://doi.org/10.3390/s16020162
5. H. Wu, L. Dong, X. Yin, A. Sampaolo, P. Patimisco, W. Ma, L. Zhang, W. Yin, L. Xiao, V. Spagnolo, S. Jia, Sens. Actuators B Chem. **297**, 126753 (2019). https://doi.org/10.1016/j.snb.2019.126753
6. J.M. Rey, M.W. Sigrist, Sens. Actuators B Chem. **135**(1), 161 (2008). https://doi.org/10.1016/j.snb.2008.08.002
7. Z. Bozóki, J. Sneider, Z. Gingl, Á. Mohácsi, M. Szakáll, Z. Bor, G. Szabó, Meas. Sci. Technol. **10**(11), 999 (1999). https://doi.org/10.1088/0957-0233/10/11/304
8. M. Szakáll, Z. Bozóki, M. Kraemer, N. Spelten, O. Moehler, U. Schurath, Environ. Sci. Technol. **35**(24), 4881 (2001). https://doi.org/10.1021/es015564x
9. M. Szakáll, J. Csikós, Z. Bozóki, G. Szabó, Infrared Phys. Technol. **51**(2), 113 (2007). https://doi.org/10.1016/j.infrared.2007.04.001
10. H. Yi, W. Chen, S. Sun, K. Liu, T. Tan, X. Gao, Opt. Express **20**(8), 9187 (2012). https://doi.org/10.1364/oe.20.009187
11. D. Tátrai, Z. Bozóki, H. Smit, C. Rolf, N. Spelten, M. Krämer, A. Filges, C. Gerbig, G. Gulyás, G. Szabó, Atmos. Meas. Tech. **8**(1), 33 (2015). https://doi.org/10.5194/amt-8-33-2015
12. Z. Bozóki, A. Szabó, Á. Mohácsi, G. Szabó, Sens. Actuators B Chem. **147**(1), 206 (2010). https://doi.org/10.1016/j.snb.2010.02.060
13. A. Beenen, R. Niessner, Analyst **123**(4), 543 (1998). https://doi.org/10.1039/a707113b
14. A. Elefante, M. Giglio, A. Sampaolo, G. Menduni, P. Patimisco, V.M. Passaro, H. Wu, H. Rossmadl, V. MacKowiak, A. Cable, F.K. Tittel, L. Dong, V. Spagnolo, Anal. Chem. **91**, 12866 (2019). https://doi.org/10.1021/acs.analchem.9b02709
15. R.D. Kamm, J. Appl. Phys. **47**(8), 3550 (1976). https://doi.org/10.1063/1.323153
16. M.S. Shumate, R.T. Menzies, J.S. Margolis, L.G. Rosengren, Appl. Opt. **15**(10), 2480 (1976). https://doi.org/10.1364/ao.15.002480
17. S. Schilt, J.P. Besson, L. Thévenaz, Appl. Phys. B Lasers Opt. **82**(2 SPEC. ISS.), 319 (2006). https://doi.org/10.1007/s00340-005-2076-y
18. P.L. Meyer, M.W. Sigrist, Atmospheric pollution monitoring using CO2-laser photoacoustic spectroscopy and other techniques (1990). https://doi.org/10.1063/1.1141097
19. N. Barreiro, A. Peuriot, G. Santiago, V. Slezak, Appl. Phys. B Lasers Opt. **108**(2), 369 (2012). https://doi.org/10.1007/s00340-012-5018-5
20. M. Lopez-Puertas, F.W. Taylor, *NON-LTE Radiative Transfer in the Atmosphere* (World Scientific, Singapore, 2001)
21. B. Funke, M. López-Puertas, M. García-Comas, M. Kaufmann, M. Höpfner, G.P. Stiller, J. Quantum Spectrosc. Radiat. Transfer **113**(14), 1771 (2012). https://doi.org/10.1016/j.jqsrt.2012.05.001
22. Y.H. Pao, *Optoacoustic Spectroscopy and Detection* (Academic Press Inc, New York, 1977)
23. T.L. Cottrell, I.M. Macfarlane, A.W. Read, A.H. Young, Trans. Faraday Soc. **62**, 2655 (1966). https://doi.org/10.1039/tf9666202655
24. R.O. Manuilova, A.G. Feofilov, A.A. Kutepov, V.A. Yankovsky, Adv. Space Res. **56**(9), 1806 (2015). https://doi.org/10.1016/j.asr.2014.12.002
25. D.L. Huestis, J. Phys. Chem. A **110**(21), 6638 (2006). https://doi.org/10.1021/jp054889n
26. H.E. Bass, R.G. Keeton, D. Williams, J. Acoust. Soc. Am. **60**(1), 74 (1976). https://doi.org/10.1121/1.381050
27. H.E. Bass, F.D. Shields, J. Acoust. Soc. Am. **56**(3), 856 (1974). https://doi.org/10.1121/1.1903337
28. M.E. Whitson, R.J. McNeal, Temperature dependence of the quenching of vibrationally excited N2 by NO and H2O (1977). https://doi.org/10.1063/1.435443
29. A.J. Zuckerwar, K.W. Miller, J. Acoust. Soc. Am. **84**(3), 970 (1988). https://doi.org/10.1121/1.396612
30. H.E. Bass, A microscopic description of sound absorption in the atmosphere (1976)
31. H.E. Bass, J. Acoust. Soc. Am. **69**(1), 124 (1981). https://doi.org/10.1121/1.385356
32. L.B. Kreuzer, J. Appl. Phys. **42**(7), 2934 (1971). https://doi.org/10.1063/1.1660651
33. A.G. Feofilov, A.A. Kutepov, W.D. Pesnell, R.A. Goldberg, B.T. Marshall, L.L. Gordley, M. García-Comas, M. López-Puertas, R.O. Manuilova, V.A. Yankovsky, S.V. Petelina, J.M. Russell, Atmos. Chem. Phys. **9**(21), 8139 (2009). https://doi.org/10.5194/acp-9-8139-2009
34. J. Finzi, F.E. Hovis, V.N. Panfilov, P. Hess, C.B. Moore, J. Chem. Phys. **67**(9), 4053 (1977). https://doi.org/10.1063/1.435379
35. P.F. Zittel, D.E. Masturzo, J. Chem. Phys. **90**(2), 977 (1989). https://doi.org/10.1063/1.456122
36. T.F. Hunter, D. Rumbles, M.G. Stock, J. Chem. Soc. Faraday Trans. 2 Mol. Chem. Phys. **70**, 1010 (1974). https://doi.org/10.1039/F29747001010
37. J.M. Langridge, M.S. Richardson, D.A. Lack, C.A. Brock, D.M. Murphy, Aerosol Sci. Technol. **47**(11), 1163 (2013). https://doi.org/10.1080/02786826.2013.827324
38. A. Selamet, P.M. Radavich, J. Sound Vib. **201**(4), 407 (1997). https://doi.org/10.1006/jsvi.1996.0720
39. L. Greenspan, J. Res. Natl. Bureau Stand. A Phys. Chem. **80A**(1), 41 (1976)
40. A. Saul, W. Wagner, J. Phys. Chem. Ref. Data **16**(4), 893 (1987). https://doi.org/10.1063/1.555787
41. C.W. Meyer, J.T. Hodges, P.H. Huang, W.W. Miller, D.C. Ripple, G.E. Scace, C.M. Gutierrez, P. Gallagher, NIST Spec. Publ. **250**, 83 (2008). https://doi.org/10.6028/NIST.SP.250-83
42. P. Breitegger, A. Bergmann, Proceedings **2**(13), 998 (2018). https://doi.org/10.3390/proceedings2130998
43. A.J. Zuckerwar, *Handbook of the Speed of Sound in Real Gases* (Academic Press Inc, New York, 2002)
44. M.C.F. Toolbox, *The MathWorks* (Natick, 2019)
45. JCGM, Evaluation of measurement data - Guide to the expression of uncertainty in measurement (2008)

Paper I

Applied Physics B
https://doi.org/10.1007/s00340-020-7409-3

Supplementary Material: Molecular relaxation effects on vibrational water vapor photoacoustic spectroscopy in air

Benjamin Lang[1], Philipp Breitegger[1], Georg Brunnhofer[2], Jordi Prats Valero[2], Simon Schweighart[3], Andreas Klug[2], Wolfgang Hassler[3], Alexander Bergmann[1]

[1] Institute of Electrical Measurement and Sensor Systems, Graz University of Technology, 8010 Graz, Austria
[2] Nanophysics & Sensor Technologies, AVL List GmbH, 8020 Graz, Austria
[3] Institute of Aviation, University of Applied Sciences FH JOANNEUM Graz, 8020 Graz, Austria

Received: 27. November 2019 / Accepted: 26 February 2020

In this supplementary material a discussion of the effects of trace constituents on the relaxation path and the derivation of the complex amplitude of the PA heat source rate are presented.

S1 Relaxation by trace constituents in atmospheric environments

The restriction to only model reactions of H_2O with the major atmospheric constituents N_2 and O_2 should only have minor ramifications for practical atmospheric measurement applications, as discussed in the following. In specific applications, however, where substantial amounts of other constituents are present (e.g. CO_2 in exhaust gas measurements), relevant relaxation processes of these constituents will have to be included in the analysis of the relaxation path.

S1.1 Argon

In atmospheric environments the rate coefficient for V-T relaxation of H_2O^* by Argon is of the same order as the rate coefficient for V-T relaxation by N_2 or O_2 [1]. For the population of the O_2^* state, the V-T relaxation by Ar is also insignificant, as it is even slower than the self relaxation, i.e. the relaxation by O_2 [2]. Hence, the presence of Ar will not change the presented relaxation path.

S1.2 Carbon dioxide

At large concentrations of water vapor, carbon dioxide also is a negligible collision partner due to the low atmospheric concentrations, currently in the order of 400 ppmV [3]. In the limit of low concentrations of H_2O, the strong V-V coupling of H_2O^* and O_2^* will lead to an efficient and fast excitation of O_2^* irrespective of the presence of CO_2, with only a minor increase in the PA conversion efficiency caused by the additional V-T relaxation of H_2O^* by CO_2. For this rate literature values are only available for high temperatures [4], but it can be assumed lower than the self relaxation rate of H_2O. V-T relaxation of O_2^* by CO_2 is negligible as $k^{V\text{-}T}_{O_2^*,CO_2} \approx k^{V\text{-}T}_{O_2^*,O_2}$ [5]. The rate coefficient for the V-V transfer from O_2^* to CO_2 is an order of magnitude lower than the V-T relaxation rate by H_2O, i.e. $k^{V\text{-}T}_{O_2^*,H_2O}$. Thus if all vibrational energy transferred to CO_2 were released instantaneously, 400 ppmV CO_2 are approximately equivalent to 40 ppmV H_2O. However, from the sensitivity of the conversion efficiency on $k^{\mathrm{V-T}}_{O_2^*,H_2O}$, shown in Fig. 13, it can be seen that 40 ppmV of water vapor do not significantly contribute to the relaxation of O_2^*.
Altogether only minor increases in the PA conversion efficiency at low water vapor concentrations have to be expected in the presence of CO_2 in air, due to the additional V-T relaxation of H_2O^* by CO_2.

Correspondence to: benjamin.lang@tugraz.at

S2 Three-coefficient form of photoacoustic source rate of heat production

Writing the photoacoustic source rate in a form with harmonic time dependence,

$$\mathbf{H}(\mathbf{r},t) = \boldsymbol{\mathcal{H}}(\mathbf{r},\omega) \cdot e^{i\omega t} \quad , \tag{S1}$$

and using the assumptions of Eq. (15) together with the solutions for $[\mathrm{H_2O^*}]$ and $[\mathrm{O_2^*}]$ (Eq. (9) and Eq. (10)) in the equation for the time dependent photoacoustic source rate, Eq. (13), the complex amplitude at the frequency of modulation is given by

$$\begin{aligned}\boldsymbol{\mathcal{H}}(\mathbf{r},\omega) \approx{}& \frac{\sigma b I}{h\nu} \frac{4E_{\mathrm{H_2O^*}}[\mathrm{H_2O}]\ e^{-i\phi_{\mathrm{H_2O^*}}}}{\mathrm{k}^{V\text{-}T}_{\mathrm{H_2O^*,M}}[\mathrm{M}] + \mathrm{k}^{V\text{-}T}_{\mathrm{H_2O^*,H_2O}}[\mathrm{H_2O}] + \mathrm{k}^{V\text{-}V}_{\mathrm{H_2O^*,O_2}}[\mathrm{O_2}]} \\ & \cdot \left(\mathrm{k}^{V\text{-}T}_{\mathrm{H_2O^*,M}}[\mathrm{M}] + \mathrm{k}^{V\text{-}T}_{\mathrm{H_2O^*,H_2O}}[\mathrm{H_2O}] \right. \\ & \left. + \frac{\mathrm{k}^{V\text{-}V}_{\mathrm{H_2O^*,O_2}}[\mathrm{O_2}]\ e^{-i\phi_{\mathrm{O_2^*}}}}{\sqrt{1+\omega^2/\left(\mathrm{k}^{V\text{-}T}_{\mathrm{O_2^*,H_2O}}[\mathrm{H_2O}]\right)^2}} \right) + \frac{\sigma I b}{h\nu} E_{inst}[\mathrm{H_2O}] \ .\end{aligned} \tag{S2}$$

The first two terms in the brackets in Eq. (S2) give the share of the heat released by V-T relaxation from the reservoir to the next state of lower energy. The third term in the brackets gives the share of heat released by the relaxation of the $\mathrm{O_2^*}$ state after the V-V transfer from the reservoir. This contribution to the photoacoustic signal has an additional phase delay, $\phi_{\mathrm{O_2^*}}$, which depends on the amount of water vapor present. When $\mathrm{H_2O}$ is increased, the V-T relaxation rate increases and $\phi_{\mathrm{O_2^*}}$ will approach zero. Because of the short relaxation time of the reservoir compared to the modulation period (even at low $\mathrm{H_2O}$ concentrations; see RHS of assumption (15)), the phase $\phi_{\mathrm{H_2O^*}}$, given by Eq. (11), in general can be assumed zero for all concentrations and therefore, $e^{-i\phi_{\mathrm{H_2O^*}}}$ is approximately unity. For large concentrations the three terms in the brackets cancel out with the denominator, which means that in total the full amount of heat, equal to the excitation energy, will be recovered without any relevant phase delays. This implies that the terms in the brackets together with the denominator correspond to a part of the conversion efficiency. The full conversion efficiency can be identified more clearly after some further steps in the derivation.

With the assumption of $\phi_{\mathrm{H_2O^*}} \approx 0$, the complex amplitude of the photoacoustic source rate of heat production, Eq. (S2), can be reduced to a function only depending on three coefficients. Expanding the last term in Eq. (S2), i.e. the instantaneously released fraction of the energy, with the denominator of the first term, the source rate can be rewritten in the following form:

$$\begin{aligned}\boldsymbol{\mathcal{H}}(\mathbf{r},\omega) \approx{}& \frac{\sigma b I}{h\nu} \frac{[\mathrm{H_2O}]}{\mathrm{k}^{V\text{-}T}_{\mathrm{H_2O^*,M}}[\mathrm{M}] + \mathrm{k}^{V\text{-}T}_{\mathrm{H_2O^*,H_2O}}[\mathrm{H_2O}] + \mathrm{k}^{V\text{-}V}_{\mathrm{H_2O^*,O_2}}[\mathrm{O_2}]} \\ & \cdot \left\{ \left(4E_{\mathrm{H_2O^*}} + E_{inst}\right)\left(\mathrm{k}^{V\text{-}T}_{\mathrm{H_2O^*,M}}[\mathrm{M}] + \mathrm{k}^{V\text{-}T}_{\mathrm{H_2O^*,H_2O}}[\mathrm{H_2O}]\right) \right. \\ & \left. + \left(\frac{4E_{\mathrm{H_2O^*}}\ e^{-i\phi_{\mathrm{O_2^*}}}}{\sqrt{1+\omega^2/\left(\mathrm{k}^{V\text{-}T}_{\mathrm{O_2^*,H_2O}}[\mathrm{H_2O}]\right)^2}} + E_{inst} \right) \mathrm{k}^{V\text{-}V}_{\mathrm{H_2O^*,O_2}}[\mathrm{O_2}] \right\} .\end{aligned} \tag{S3}$$

Pulling $h\nu = 4E_{\mathrm{H_2O^*}} + E_{inst}$ out of the brackets, expanding the term with $\mathrm{k}^{V\text{-}V}_{\mathrm{H_2O^*,O_2}}$ in the denominator by $h\nu$ and rearranging leads to

$$\begin{aligned}\boldsymbol{\mathcal{H}}(\mathbf{r},\omega) \approx\ & \frac{\sigma b I[\mathrm{H_2O}]}{\mathrm{k}^{V\text{-}T}_{\mathrm{H_2O^*,M}}[\mathrm{M}]+\frac{E_{inst}}{h\nu}\mathrm{k}^{V\text{-}V}_{\mathrm{H_2O^*,O_2}}[\mathrm{O_2}]+\mathrm{k}^{V\text{-}T}_{\mathrm{H_2O^*,H_2O}}[\mathrm{H_2O}]+\frac{4E_{\mathrm{H_2O^*}}}{h\nu}\mathrm{k}^{V\text{-}V}_{\mathrm{H_2O^*,O_2}}[\mathrm{O_2}]} \\ & \cdot\left\{\mathrm{k}^{V\text{-}T}_{\mathrm{H_2O^*,M}}[\mathrm{M}] + \frac{E_{inst}}{h\nu}\mathrm{k}^{V\text{-}V}_{\mathrm{H_2O^*,O_2}}[\mathrm{O_2}] + \mathrm{k}^{V\text{-}T}_{\mathrm{H_2O^*,H_2O}}[\mathrm{H_2O}]\right. \\ & \left. + \frac{4E_{\mathrm{H_2O^*}}}{h\nu}\frac{e^{-i\phi_{\mathrm{O_2^*}}}}{\sqrt{1+\omega^2/\left(\mathrm{k}^{V\text{-}T}_{\mathrm{O_2^*,H_2O}}[\mathrm{H_2O}]\right)^2}}\mathrm{k}^{V\text{-}V}_{\mathrm{H_2O^*,O_2}}[\mathrm{O_2}]\right\} \ . \end{aligned} \tag{S4}$$

Assuming an ideal gas, the concentrations of $\mathrm{N_2}$ and $\mathrm{O_2}$ can be written as a function of the water vapor mole fraction:

$$[\mathrm{O_2}] = n_0(1 - x_{\mathrm{H_2O}})x_{\mathrm{O_2,dry}} \tag{S5}$$

$$[\mathrm{N_2}] = n_0(1 - x_{\mathrm{H_2O}})x_{\mathrm{N_2,dry}} \tag{S6}$$

$$[\mathrm{M}] = n_0(1 - x_{\mathrm{H_2O}}) \quad , \tag{S7}$$

where n_0 is the overall number concentration at the given temperature and pressure. $x_{\mathrm{O_2,dry}}$ and $x_{\mathrm{N_2,dry}}$ are the molecular oxygen and nitrogen mole fractions in dry air, respectively. Inserting Eqs. (S5) and (S7) into (S4), rearranging and making the substitutions

$$c_1 = \frac{\mathrm{k}^{V\text{-}T}_{\mathrm{H_2O^*,M}} + \frac{E_{inst}}{h\nu}\,\mathrm{k}^{V\text{-}V}_{\mathrm{H_2O^*,O_2}}\,x_{\mathrm{O_2,dry}}}{\mathrm{k}^{V\text{-}T}_{\mathrm{H_2O^*,H_2O}} - \mathrm{k}^{V\text{-}T}_{\mathrm{H_2O^*,M}} - \frac{E_{inst}}{h\nu}\,\mathrm{k}^{V\text{-}V}_{\mathrm{H_2O^*,O_2}}\,x_{\mathrm{O_2,dry}}} \tag{S8}$$

$$c_2 = \frac{\frac{4E_{\mathrm{H_2O^*}}}{h\nu}\,\mathrm{k}^{V\text{-}V}_{\mathrm{H_2O^*,O_2}}\,x_{\mathrm{O_2,dry}}}{\mathrm{k}^{V\text{-}T}_{\mathrm{H_2O^*,H_2O}} - \mathrm{k}^{V\text{-}T}_{\mathrm{H_2O^*,M}} - \frac{E_{inst}}{h\nu}\,\mathrm{k}^{V\text{-}V}_{\mathrm{H_2O^*,O_2}}\,x_{\mathrm{O_2,dry}}} \tag{S9}$$

$$c_3 = \mathrm{k}^{V\text{-}T}_{\mathrm{O_2^*,H_2O}} \quad , \tag{S10}$$

gives the final result for the heat rate:

$$\boldsymbol{\mathcal{H}}(\mathbf{r},\omega) \approx \sigma\, b\, I\, n_0\, x_{\mathrm{H_2O}}\, \boldsymbol{\eta}(x_{\mathrm{H_2O}}) \ , \tag{S11}$$

with the photoacoustic conversion efficiency $\boldsymbol{\eta}$ given by

$$\begin{aligned}\boldsymbol{\eta}(x_{\mathrm{H_2O}}) = & \frac{1}{c_1 + x_{\mathrm{H_2O}} + c_2\,(1 - x_{\mathrm{H_2O}})} \cdot \left(c_1 + x_{\mathrm{H_2O}} \right. \\ & \left. + \frac{c_2\,(1 - x_{\mathrm{H_2O}})\; e^{-i \arctan\left(\frac{\omega}{c_3\, n_0\, x_{\mathrm{H_2O}}}\right)}}{\sqrt{1 + \omega^2/\left(c_3\, n_0\, x_{\mathrm{H_2O}}\right)^2}} \right) \ . \end{aligned} \tag{S12}$$

S3 Microphone humidity sensitivity

When writing the microphone signal without including the microphone sensitivity, $s_{mic}(T, p, f, x_{\mathrm{H_2O}})$, in the cell constant one obtains

$$\mathbf{S}(x_{\mathrm{H_2O}}) = c_{cell}\, s_{mic}(T, p, f, x_{\mathrm{H_2O}})\, \sigma\, P\, n_0\, x_{\mathrm{H_2O}}\, (1 - b_{cell}\, n_0\, x_{\mathrm{H_2O}})\, \boldsymbol{\eta}(x_{\mathrm{H_2O}}) \quad , \tag{S13}$$

where the additional explicit temperature, pressure and frequency dependence of the microphone sensitivity has been included, to emphasize the strong dependence on these variables. Assuming a linear relationship for the humidity dependence of the microphone sensitivity of the form

$$s_{mic}(T, p, f) = c_{mic}(T, p, f) + b_{mic}(T, p, f)\, n_0\, x_{\mathrm{H_2O}} \quad , \tag{S14}$$

the microphone signal can be rewritten to give

$$\begin{aligned}
\mathbf{S}(x_{\mathrm{H_2O}}) &\approx c_{cell}(c_{mic} + b_{mic}\, n_0\, x_{\mathrm{H_2O}})\, \sigma\, P\, n_0\, x_{\mathrm{H_2O}} \\
&\qquad\qquad\qquad \cdot (1 - b_{cell}\, n_0\, x_{\mathrm{H_2O}})\, \boldsymbol{\eta}(x_{\mathrm{H_2O}}) && \text{(S15)}\\
&\approx c_{cell}\, c_{mic}\, \sigma\, P\, n_0\, x_{\mathrm{H_2O}} \left(1 + \frac{b_{mic}\, n_0}{c_{mic}}\, x_{\mathrm{H_2O}}\right) \\
&\qquad\qquad\qquad \cdot (1 - b_{cell}\, n_0\, x_{\mathrm{H_2O}})\; \boldsymbol{\eta}(x_{\mathrm{H_2O}}) && \text{(S16)}\\
&\approx c_{cell}\, c_{mic}\, \sigma\, P\, n_0\, x_{\mathrm{H_2O}} \left(1 + \frac{b_{mic}\, n_0}{c_{mic}}\, x_{\mathrm{H_2O}} - b_{cell}\, n_0\, x_{\mathrm{H_2O}}\right. \\
&\qquad\qquad\qquad \left. - \frac{b_{mic}\, b_{cell}\, n_0^2}{c_{mic}}\, x_{\mathrm{H_2O}}^2\right) \boldsymbol{\eta}(x_{\mathrm{H_2O}}) && \text{(S17)}\\
&\approx c_{cell}\, c_{mic}\, \sigma\, P\, n_0\, x_{\mathrm{H_2O}} \left(1 - \left(b_{cell} - \frac{b_{mic}}{c_{mic}}\right) n_0\, x_{\mathrm{H_2O}}\right. \\
&\qquad\qquad\qquad \left. - \frac{b_{mic}\, b_{cell}\, n_0^2}{c_{mic}}\, x_{\mathrm{H_2O}}^2\right) \boldsymbol{\eta}(x_{\mathrm{H_2O}}) \quad . && \text{(S18)}
\end{aligned}$$

Defining the new constants

$$C_{cell} = c_{cell}\, c_{mic} \quad , \tag{S19}$$

$$B_{cell} = b_{cell} - \frac{b_{mic}}{c_{mic}} \quad , \tag{S20}$$

$$D_{cell} = \frac{b_{mic}\, b_{cell}}{c_{mic}} \quad , \tag{S21}$$

and dropping the microphone signal third- and higher-order dependence on $x_{\mathrm{H_2O}}$, i.e. also the term including D_{cell}, the photoacoustic microphone signal can be approximated by

$$\mathbf{S}(x_{\mathrm{H_2O}}) = C_{cell}\, \sigma\, P\, n_0\, x_{\mathrm{H_2O}}\, (1 - B_{cell}\, n_0\, x_{\mathrm{H_2O}})\, \boldsymbol{\eta}(x_{\mathrm{H_2O}}) \quad , \tag{S22}$$

where C_{cell} and B_{cell} are constants and the latter includes the first-order coefficient of the microphone humidity sensitivity, $b_{mic}(T, p, f)$.

References

1. J. Finzi, F.E. Hovis, V.N. Panfilov, P. Hess, C. Bradley Moore, The Journal of Chemical Physics **67**(9), 4053 (1977). DOI 10.1063/1.435379
2. D.R. White, R.C. Millikan, The Journal of Chemical Physics **39**(7), 1807 (1963). DOI 10.1063/1.1734533
3. P.Y. Foucher, A. Chédin, R. Armante, C. Boone, C. Crevoisier, P. Bernath, Atmospheric Chemistry and Physics **11**(6), 2455 (2011). DOI 10.5194/acp-11-2455-2011
4. J. Blauer, G. Nickerson, (American Institute of Aeronautics and Astronautics (AIAA), 1974). DOI 10.2514/6.1974-536
5. H.E. Bass, The Journal of Chemical Physics **58**(11), 4783 (1973). DOI 10.1063/1.1679059

PAPER II. PHOTOACOUSTIC HYGROMETER FOR ICING WIND TUNNEL WATER CONTENT MEASUREMENT: DESIGN, ANALYSIS AND INTERCOMPARISON

Author contributions: The author of this thesis led the development and design of the PA hygrometer and the isokinetic sampling system used in the probe intercomparison, except for the evaporator probe (Wolfgang Breitfuss). The author developed the adapted model for condensed water content estimation, performed the hygrometer evaluation and conducted the uncertainty analysis. He also contributed to the conceptualization of the work and the methodology, operated the PA instrument during the intercomparison and performed the evaluation of the measurement data. The hot-wire and CU-IKP data have been provided by Wolfgang Breitfuss and Hugo Pervier, respectively. The author wrote the original draft of the manuscript and handled the submission.

Publication status: The appended publication is a pre-print version of the submitted article [2], currently in review: Lang, B., Breitfuss, W., Schweighart, S. et al.: Photoacoustic hygrometer for icing wind tunnel water content measurement: Design, analysis and intercomparison, Atmos. Meas. Tech. Discuss., doi.org/10.5194/amt-2020-295, in review, 2020.

https://doi.org/10.5194/amt-2020-295
Preprint. Discussion started: 8 September 2020

Atmospheric Measurement Techniques
Discussions
Open Access

Photoacoustic hygrometer for icing wind tunnel water content measurement: Design, analysis and intercomparison

Benjamin Lang[1,2,3], Wolfgang Breitfuss[4], Simon Schweighart[2], Philipp Breitegger[1], Hugo Pervier[5], Andreas Tramposch[2], Andreas Klug[3], Wolfgang Hassler[2], and Alexander Bergmann[1]
[1]Graz University of Technology, Institute of Electrical Measurement and Sensor Systems, Graz, Austria
[2]FH JOANNEUM GmbH, Institute of Aviation, Graz, Austria
[3]AVL List GmbH, Nanophysics & Sensor Technologies, Graz, Austria
[4]RTA Rail Tec Arsenal Fahrzeugversuchsanlage GmbH, Vienna, Austria
[5]Cranfield University, School of Aerospace, Transport and Manufacturing, Cranfield, United Kingdom
Correspondence: B. Lang (benjamin.lang@tugraz.at)

Abstract. This work describes the latest design, calibration and application of a near-infrared laser diode-based photoacoustic (PA) hygrometer, developed for total water content measurement in simulated atmospheric freezing precipitation and high ice water content conditions with relevance in fundamental icing research, as well as aviation testing and certification. The single-wavelength and single-pass PA absorption cell is calibrated for molar water vapor fractions with a two-pressure humidity generator integrated into the instrument. Laboratory calibration showed an estimated measurement accuracy better than $3.3\,\%$ in the water vapor mole fraction range of $510-12,360\,\mathrm{ppm}$ ($5\,\%$ from $250-21,200\,\mathrm{ppm}$) with a theoretical limit of detection (3σ) of $3.2\,\mathrm{ppm}$. The hygrometer is examined in combination with a basic isokinetic evaporator probe (IKP) and sampling system designed for icing wind tunnel application, for which a general description of total condensed water content (CWC) measurement and uncertainties are presented. Despite the current limitation of the IKP to a hydrometeor mass flux below $90\,\mathrm{g\,m^{-2}\,s^{-1}}$, a CWC measurement accuracy better than $20\,\%$ is achieved by the instrument above a CWC of $0.14\,\mathrm{g\,m^{-3}}$ in cold air ($-30\,^{\circ}\mathrm{C}$) with suitable background humidity measurement. Results of a comparison to the Cranfield University IKP instrument in freezing drizzle and rain show a CWC agreement of the two instruments within $20\,\%$, which demonstrates the potential of PA hygrometers for water content measurement in atmospheric icing conditions.

1 Introduction

Atmospheric water in the form of clouds and precipitation is of particular concern to aviation at temperatures below freezing, as supercooled liquid water and ice crystal environments present potentially hazardous conditions to aircraft, leading to airframe and air data probe icing (Vukits, 2002; Gent et al., 2000) or in-flight engine power loss (Mason et al., 2006).

Freezing precipitation containing supercooled large drops (SLDs), with drop diameters in excess of $50\,\mu\mathrm{m}$, as well as convective mixed-phase and glaciated clouds with high mass concentrations of ice crystals, i.e., ice water contents (IWCs) up to several grams per cubic meter, constitute two particular meteorological environments associated with severe icing events (Politovich, 1989; Bernstein et al., 2000; Cober et al., 2001b; Riley, 1998).

https://doi.org/10.5194/amt-2020-295
Preprint. Discussion started: 8 September 2020

SLD icing environments of freezing drizzle (maximum drop diameters from 100 µm to 500 µm) or freezing rain (max. diameters greater than 500 µm), as classified for the certification of large transport aircraft, are comprehensively characterized by envelopes of liquid water content (LWC), temperature, pressure altitude, drop size distributions and horizontal extent in Appendix O of the European Aviation Safety Agency Certification Specifications 25 (EASA CS-25, 2020) and the Code of Federal Regulations Title 14 Part 25 (FAA CFR-25, 2019). Mixed-phase and ice crystal environments are likewise covered with a total condensed water content envelope by Appendix P and D of the two documents, respectively.

Replication of the full SLD, mixed-phase or high IWC condition envelopes in icing wind tunnels (IWTs) has been largely accomplished by organizations devoted to the experimental simulation of icing environments for the purpose of fundamental icing research and certification of aeronautical components, but is associated with a lack of appropriate instrumentation and is still a work in progress for some conditions (Orchard et al., 2018; Van Zante et al., 2018; Bansmer et al., 2018; Breitfuss et al., 2019; Chalmers et al., 2019).

The accuracy and reliability of conventional water content instrumentation in the conditions encompassed by Appendix O and P/D is an issue frequently addressed for in-flight and IWT characterization (Strapp et al., 2003; Korolev et al., 2013; Orchard et al., 2019). Conventional instrumentation in this context refers to ice accretion blades or cylinders for LWC measurement and evaporating (multi-element) hot-wire sensors used for simultaneous LWC and total condensed water content (CWC[1]; combined LWC and IWC) measurement. Both methods are either known or suspected to suffer from size and water content dependent inaccuracies in large drop or ice crystal icing environments due to uncertainties in collection efficiency and mass losses before accretion or evaporation (Cober et al., 2001a; Strapp et al., 2003; Emery et al., 2004; Isaac et al., 2006; Korolev et al., 2013; Steen et al., 2016).

This situation has led to the development of new benchmark isokinetic evaporator probe (IKP) instruments for CWC measurement (Davison et al., 2008; Strapp et al., 2016), regarded as closest to a first principles measurement and primarily designed for and deployed in the characterization of high IWC mixed-phase/glaciated conditions (e.g. Ratvasky et al., 2019). IKPs are used to extractively sample droplets and ice crystals in the icing environment with a forward facing, isokinetically operated inlet. After sampling, hydrometeors are evaporated to measure the combined condensed and ambient air water content with a suitable hygrometer. Ambient air background water vapor (BWV) is measured separately and subtracted from the total water content (TWC) to derive the condensed water content. Measurement of the BWV concentration is usually accomplished via a second, backward facing inlet connected to another hygrometer. Due to the isokinetic sampling, losses of droplets or particles by re-entrainment into the flow after entering a sufficiently long inlet are improbable. Hence, IKP particle size distribution dependence is in theory only governed by the aspiration efficiency of the inlet.

Collectively, only few such reference instruments for CWC measurement in icing conditions similar to Appendix O and P/D currently exist. This lack of instrumentation has motivated the development of the hygrometer and sampling system described in this work.

Hygrometers in devices specifically designed for IWT operation typically apply commercially available optical absorption spectroscopy based non-dispersive infrared (NDIR) gas analyzers (e.g. Strapp et al., 2016; Bansmer et al., 2018, sec. 4.3). The

---

[1] Often abbreviated as *TWC*. To provide a clear distinction to total water content, we adhere to the nomenclature and reasoning given by Dorsi et al. (2014).

https://doi.org/10.5194/amt-2020-295
Preprint. Discussion started: 8 September 2020

Atmospheric Measurement Techniques Discussions
Open Access

upper end of water contents that have to be within the range of suitable hygrometers is given by the combined background and condensed water content in the measurement environment. The former is approximately limited to fully saturated air at a static air temperature (SAT) of $0\,^{\circ}\mathrm{C}$ and the latter may be taken as an upper bound of $10\,\mathrm{g\,m^{-3}}$ to the peak CWC of $9\,\mathrm{g\,m^{-3}}$ in high IWC conditions (EASA CS-25, 2020). This may add up to molar water vapor fractions of $18,500\,\mathrm{ppm}$ at standard pressure ($1000\,\mathrm{hPa}$). Accuracy requirements are primarily determined by high BWV concentrations that have to be subtracted from high total water concentrations at low CWC and high ambient temperatures (Davison et al., 2016). The necessary hygrometer limit of detection highly depends on the specific measurement conditions but may be estimated from the fact that detection of a CWC of $0.05\,\mathrm{g\,m^{-3}}$ in dry air at standard pressure requires an accuracy and limit of detection better than $48\,\mathrm{ppm}$.

With the measurement system described in detail by Szakáll et al. (2001), Tátrai et al. (2015) have first demonstrated the suitable accuracy of photoacoustic (PA) hygrometers in and beyond the above measurement range. Compared to NDIR sensors, photoacoustic spectroscopy offers the potential of achieving higher signal to noise ratios (SNRs) with equal response time, while providing high selectivity and high robustness, due to the possibility of optical single-pass arrangements and an instrument response that is invariant to the total absorption path length (Hodgkinson and Tatam, 2013).

In this work we describe the latest design, preliminary calibration and basic properties of a new PA hygrometer and two-pressure humidity generator, developed with the goal of providing the total water measurement and calibration ranges typical for simulated atmospheric icing conditions applied in aviation testing and certification. The hygrometer is examined in combination with a basic IKP and sampling system, designed for IWT application in Appendix O conditions, for which a description of CWC measurement and associated uncertainties are presented. Finally, results of water content measurements in freezing drizzle and rain conditions in a closed circuit IWT, calibrated according to SAE Aerospace Recommended Practices (SAE ARP-5905, 2015), are presented and compared to measurements with a reference IKP and a hot-wire instrument.

2 Instrument design

A schematic overview of the entire instrument is shown in Fig. 1(a). The system consists of a sampling probe positioned inside the icing wind tunnel and a measurement and sampling unit integrated into a 19-inch rack, positioned outside the tunnel and connected by $7\,\mathrm{m}$ long heated and thermally insulated PTFE tubing, temperature-controlled to the measurement temperature of $35\,^{\circ}\mathrm{C}$ to prohibit condensation. The probe is a total water (TW) sampling probe operated isoaxially and near isokinetic conditions, also featuring a second inlet port intended for BWV measurement. Hydrometeors entering the forward facing TW inlet are evaporated inside the probe, enriching simultaneously sampled ambient air by the evaporated condensed water.

The sampling system is designed to provide five main operating modes:

1. TW measurement (Path 1 in Fig. 1(a)),
2. BWV measurement (Path 2),
3. Zeroing (PA background signal measurement; Path 3),
4. Calibration (Path 4),

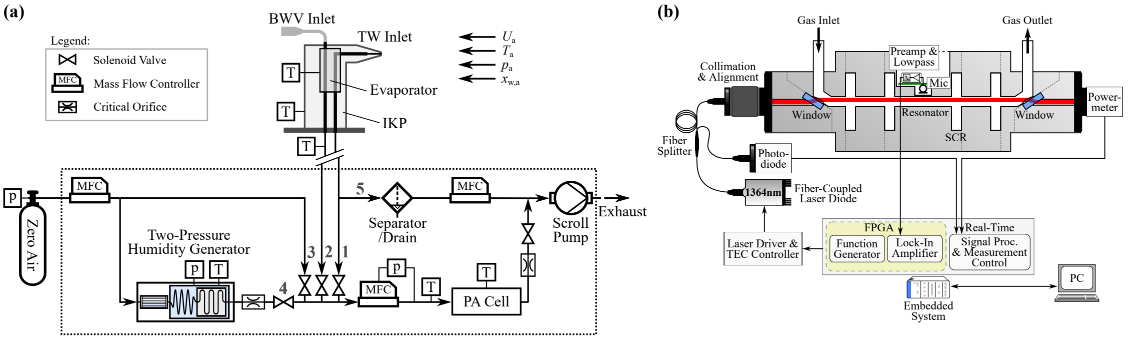

Figure 1. (a) Schematic of the instrument showing the isokinetic evaporator probe (IKP) and the measurement (PA cell), sampling and calibration system (two-pressure humidity generator and zero air). Locations of temperature and pressure control are indicated by (T) and (p), respectively. Indicated numbers enumerate the individual flow paths. The rearward facing BWV probe indicates the extension of the BWV inlet port not applied in this work. **(b)** Schematic of the photoacoustic cell together with the optical and the electronic setup, showing the control, data acquisition and signal processing performed on the real-time embedded system.

5. Inlet purging (Path 3 combined with Path 1 or 2).

For TW and BWV measurement, air sampled through the respective inlet is continuously pumped to the measurement unit, where the PA hygrometer (PA cell) is used to measure the water vapor mole fraction in parts of the TW or the full BWV inlet air flow. Currently, only a single hygrometer has been implemented, and humidity measurement may only be alternated between TW and BWV measurement.

During isokinetic TW sampling the majority of the flow is bypassed the hygrometer (path 5 in Fig. 1(a)) to the scroll pump (Edwards, nXDS10iC). The hygrometer is supplied by a constant standard volumetric flow rate of 0.75(4) standard $\mathrm{l\,min^{-1}}$ (slpm; reference conditions: $273.15\,\mathrm{K}$ and $1013.25\,\mathrm{hPa}$), set by a pressure controller (Vögtlin Instruments, GSP-B9SA-BF26) upstream the cell and a critical orifice of $350\,\mathrm{\mu m}$ nominal diameter downstream the cell. A calibrated mass flow controller (MFC; Vögtlin Instruments, GSC-C9SA-FF12) is used to control the bypass flow rate, and a calibrated flow meter included in the pressure controller measures the actual hygrometer flow rate. Isokinetic sampling at the TW inlet is set by adjusting the MFC flow rate to a combined flow rate matching isokinetic conditions, which are calculated using IWT test section operating and TW inlet geometry parameters (cf. Section 4).

The instrument features a two-pressure humidity generator also integrated into the rack, which in combination with zero air is used for calibration and zeroing of the hygrometer. Control of flow, temperature and pressure together with signal processing and data logging for the sampling system and humidity generator is performed with a dedicated embedded system (National Instruments, NI cRIO 9063).

In the following subsections, the major components of the instrument are described in further detail.

https://doi.org/10.5194/amt-2020-295
Preprint. Discussion started: 8 September 2020

Atmospheric Measurement Techniques Discussions

2.1 Photoacoustic hygrometer

The hygrometer is a custom built single-cell photoacoustic absorption spectrometer, providing a signal proportional to the water vapor number concentration in the total water or background water air stream. Figure 1(b) presents a schematic of the PA cell together with the optic configuration and electronic setup.

A fiber-coupled distributed feedback laser diode (NEL, NLK1E5GAAA) is intensity modulated at approximately $4584\,\mathrm{Hz}$ (at $35\,^\circ\mathrm{C}$) to excite the fundamental acoustic resonance mode of the PA cell when water vapor is present. The diode is temperature-controlled to the peak of a ro-vibrational water vapor transition at $1364.68\,\mathrm{nm}$ ($7327.7\,\mathrm{cm}^{-1}$; $296\,\mathrm{K}$), which was chosen based on HITRAN simulations (Gordon et al., 2017) as it exhibits minimal line shift with pressure, high absorption cross section and low interference from other anticipated atmospheric constituents. Intensity modulation is performed by square wave modulating the applied laser current at the resonance frequency from the maximum permissible laser diode current down to just below the lasing threshold with a benchtop laser driver (Thorlabs, ITC4001), maintaining an average optical power of $9.9(1)\,\mathrm{mW}$. The laser beam is collimated to a diameter of $2\,\mathrm{mm}$ and directed through the resonator via two N-BK7 Brewster windows angled at $56.4\,^\circ$. A thermal powermeter (Thorlabs, PM16-401) is used to measure average optical power when the cell is flushed with zero air during PA background signal measurements. Monitoring of the laser power during measurements is accomplished by a fiber splitter with a $99:1$ split ratio (Thorlabs, TW1300R1A1) in combination with a temperature-controlled InAsSb photodetector (Thorlabs, PDA10PT-EC). However, the high wavelength and output power stability of the laser diode allows stable operation over the duration of typical measurement series, thus no wavelength locking on the absorption line or power correction is applied on measured signals in between calibration cycles.

Measurement air is pumped through the stainless steel PA cell via milled $6\,\mathrm{mm}$ inner diameter (ID) cylindrical ducts. At the center of the modularly designed cell a $34\,\mathrm{mm}$ long cylindrical resonator is formed by a termination on either side with two acoustically short concentric resonators (Selamet and Radavich, 1997). Short concentric resonators are used instead of larger expansion chambers (buffer volumes) to decrease gas exchange and measurement response time. The diameters and distances in between the small volume acoustic band-stop filters are tuned to maximize resonator quality factor (Q=17), while minimizing transmission of external noise into the cell. At the center of the resonator and the location of the antinode of the fundamental longitudinal resonance mode, an electret condenser microphone (Knowles, EK-23028) is connected in a small volume gas- and noise-tight enclosure to measure the PA pressure signal.

The PA cell is operated at constant temperature, pressure and flow to maintain a microphone sensitivity and resonance frequency independent of ambient and IWT conditions.

The temperature of the thermally insulated PA cell is controlled to $35.0(3)\,^\circ\mathrm{C}$ by two integrated heating cartridges to stabilize resonance frequency and microphone sensitivity[2]. An additional resistance temperature detector (RTD), installed in the sampling gas stream approximately $100\,\mathrm{mm}$ upstream of the cell, is used to control the gas temperature to $35.0(3)\,^\circ\mathrm{C}$ inside the PA cell by controlling the heating of the upstream tubing in the measurement unit. This temperature also sets the theoretical

---

[2] The number in parenthesis gives the half-width of the rectangular confidence interval in terms of the last digit.

https://doi.org/10.5194/amt-2020-295
Preprint. Discussion started: 8 September 2020

upper water vapor mole fraction measurement limit of $58,600\,\mathrm{ppm}$ before condensation of water vapor in the sampling lines and the PA cell occurs.

Although the sampling system and the IKP are designed to operate around standard pressure, the PA cell pressure may be set with the pressure controller upstream of the hygrometer within the limits given by the pressure loss of the upstream flow elements down to $100\,\mathrm{hPa}$. For IWT measurement, cell pressure is set to $800(8)\,\mathrm{hPa}$, close to the pressure of optimal signal-to-noise ratio (SNR). Optimum measurement pressure is primarily defined by the valve position of the pressure controller, due to flow noise generated at the valve. To further decrease signal noise, the PA cell is vibrationally decoupled from the scroll pump mounted in the rack by a vibration absorbing mount and short sections of PTFE-tubing at the gas in- and outlet of the cell.

Laser current control, signal processing and data logging of microphone and power monitoring signals is carried out with a second dedicated embedded system (National Instruments, NI cRIO 9031), a real-time processor combined with a reconfigurable field programmable gate array (FPGA). The laser current modulation signal is generated by a function generator implemented on the FPGA Data acquisition of the microphone signal after analog amplification with a transimpedance amplifier (10-fold gain), together with the photodetector signal is carried out with a $24\,\mathrm{bit}$ ADC (National Instruments, NI 9234) at a sampling rate of $52.1\,\mathrm{kHz}$. A digital dual-phase lock-in amplifier implemented on the FPGA is used to determine in-phase and quadrature components of the microphone signal at the frequency of modulation. The lock-in signal amplitude (referred to as PA signal), used to derive the water vapor mole fraction, is calculated and logged on the real-time operating system with a $10\,\mathrm{Hz}$ rate after phase-correct background signal correction (cf. Appendix A).

Despite operation at controlled measurement conditions, the hygrometer sensitivity is a function of the measured water content due to several reasons. Increasing water contents cause decreasing irradiance along the absorption path (Beer-Lambert law) and therefore reduce sensitivity. In addition, the electret microphone sensitivity is a function of humidity (specified $0.02\,\mathrm{dB}\,\%\mathrm{RH}^{-1}$; Langridge et al., 2013). Furthermore, speed of sound and therefore also resonator resonance frequency is a function of humidity (Zuckerwar, 2002). Shifts in resonance frequency may reduce effective resonator amplification and sensitivity according to the approximately Lorentzian resonator frequency response, if the frequency of modulation is not shifted accordingly (Szakáll et al., 2009). Finally, photoacoustic conversion efficiency (i.e., conversion of absorbed laser radiation to a detectable pressure signal) for water vapor in air is concentration dependent and over the range of typical atmospheric concentrations and pressures varies by a factor of five (Lang et al., 2020).

All above effects are to a great extent accounted for by calibrating the hygrometer over the range of expected water vapor concentrations and by applying a suitable nonlinear calibration function, which is described in greater detail in Lang et al. (2020). The PA signal reduction associated with resonance frequency humidity dependence ($0.5\,\%$ for the $14\,\mathrm{Hz}$ shift from $0\,\mathrm{ppm}$ to $20\,000\,\mathrm{ppm}$) is taken into account by maintaining the laser modulation frequency at the dry air resonance frequency ($4584\,\mathrm{Hz}$ at $35\,^{\circ}\mathrm{C}$) for calibration and measurements. This method results in maximum amplification and PA signal at low concentrations. The approximately quadratic sensitivity loss for higher concentrations is considered in the second order term of the calibration function.

https://doi.org/10.5194/amt-2020-295
Preprint. Discussion started: 8 September 2020

Atmospheric Measurement Techniques
Discussions

2.2 Calibration unit

Determination of the water vapor concentration from the hygrometer signal requires background signal correction (zeroing) and calibration with known concentrations of water vapor. The system is calibrated by generating and providing a stable flow of humidified air with known molar fractions of water vapor to the inlet of the hygrometer (e.g., Dorsi et al., 2014; Tátrai et al., 2015). This approach is preferred to the method of introducing a continuous stream of liquid water or ice into the TW inlet and calibrating for CWC (e.g., Strapp et al., 2016), as calibration may be performed during IWT operation without removing the sampling probe. With the goal of performing calibration over a major part of the necessary water content range within a short time, a compact custom-made two-pressure humidity generator (HG) has been integrated into the instrument. Two-pressure humidity generation offers the benefit of enabling rapid and accurate setting of a wide range of humidity levels in a saturation chamber at a convenient and constant temperature by varying the pressure and thus the molar water vapor fraction (Wernecke and Wernecke, 2013).

Zeroing of the instrument is performed by acquiring a PA background signal after continuously flushing the PA cell with zero air from an external gas cylinder (Messer, scientific grade synthetic air; residual water volume fraction below $2\,\mathrm{ppmv}$) until a stable reading is attained (approx. $20\,\mathrm{min}$).

For calibration zero air is initially humidified in a pre-saturation stage, a porous ceramics with honeycomb structure (IBIDEN Ceram) in a room temperature water bath, to a dew point well above the main saturation chamber dew point. The humidified air is subsequently passed through a lower temperature and pressure-controlled $1\,\mathrm{m}$ long coiled tube heat exchanger and the main saturator, where the air is saturated with respect to the local temperature and pressure.

The saturator is a $(6\times25\times600)\,\mathrm{mm}$ (width×height×length) channel milled into a stainless steel block, hermetically sealed and partially filled with distilled water. Both, heat exchanger and saturator are placed in a stirred and thermally insulated water bath, temperature-controlled by thermoelectric coolers within the range of $1\,^\circ\mathrm{C}$ and ambient temperature. Saturator air pressure is controlled within the range of $1000\,\mathrm{hPa}$ to $8000\,\mathrm{hPa}$ with an MFC (Vögtlin Instruments, GSC-C9SA-FF12) upstream of the HG. By increasing the saturator pressure to its maximum value, the $1000\,\mathrm{hPa}$ water vapor saturation fraction may be reduced by a ratio of 1 : 7.8.

Bath temperature and saturator air pressure are measured with a high precision four-wire Pt100 (Omega Engineering, P-M-1/10-1/8-6-0-PS-3) combined with a calibrated 24-Bit ADC (National Instruments, NI 9217) and a calibrated pressure transducer (KELLER AG, PAA 33X), traceable to NIST and Swiss national standards, respectively. Associated measurement uncertainties are given in Table C1. The molar water vapor saturation fraction, which remains constant during expansion to the lower pressure level of the hygrometer, is calculated from the measured saturation temperature and pressure according to Wagner and Pruss (1993) and Greenspan (1976).

In the described configuration the operational range of the HG extends from $845\,\mathrm{ppm}$ to approximately $22,000\,\mathrm{ppm}$ (maximum saturator temperature of $19\,^\circ\mathrm{C}$). Two saturator temperature setpoints are used for calibration, covering the full humidity range by varying the saturator pressure. The settling time to a stationary hygrometer signal after changes in the HG settings is

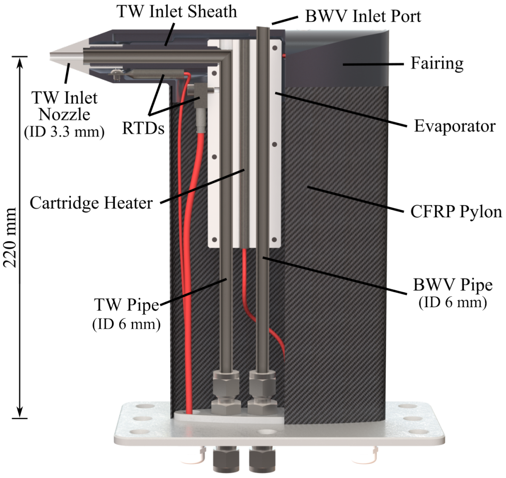

Figure 2. Schematic of the isokinetic evaporator probe assembly showing a partial cut through the main components: TW and BWV inlet lines with TW inlet nozzle, the carbon fiber reinforced polymer (CFRP) pylon, aluminum fairing and evaporator. Fairing cartridge heaters extending alongside the TW inlet sheath are not indicated.

below 7 min. This figure is mainly determined by the relatively low signal noise of the PA hygrometer compared to the slow water vapor adsorption-desorption processes at the piping and cell walls.

An independent calibration of the humidity generator is still pending, which in particular is necessary to verify full saturation at high loads (high saturator temperature). To asses the HG and thus also hygrometer accuracy, the uncertainty in the generated humidity is calculated from first principles, i.e., the measured saturator temperature and pressure and the associated uncertainties, according to Meyer et al. (2008). The resulting uncertainty (95 %) is below $\pm 2.1\,\%$ over the entire range of humidities provided by the HG and is dominated by the saturator temperature measurement uncertainty (cf. Table C1).

2.3 Isokinetic evaporator probe

The inlet system has been designed around the three requirements of enabling reasonably representative isokinetic TW sampling while providing the necessary heating power for hydrometeor evaporation and maintaining the probe free from ice accretion at high water contents. The probe inlets are housed in an airfoil-shaped (32×132) mm (width×length) carbon fiber reinforced polymer (CFRP) pylon capped by an additively manufactured aluminum fairing, with the TW centerline extending 220 mm perpendicular to the free-stream flow from a (100×195) mm base flange. A CAD drawing of the IKP is shown in Fig. 2.

The fairing is controlled to a TW inlet nozzle temperature of approximately 50 °C by maintaining constant 80 °C at the RTD (Pt100) inside the fairing front tip. To this end, integrated cartridge heaters in the aluminum enclosure provide a maximum combined heating power of 390 W.

https://doi.org/10.5194/amt-2020-295
Preprint. Discussion started: 8 September 2020

Atmospheric Measurement Techniques Discussions

2.3.1 Total water inlet

TW is sampled through a screw-on aluminum nozzle with a sharp leading edge and a tapering half angle of $20\,°$. For the measurements presented, a nozzle with an inlet inner diameter of $3.30(15)\,\mathrm{mm}$, measured with a standard caliper, was used. The particular choice of the comparatively small inlet diameter is based on the maximum continuous flow rate attainable with the low-noise vacuum pump in use, which in combination with the TW inlet area determines the maximum wind tunnel airspeed for which isokinetic sampling may be maintained. The ID of $3.3\,\mathrm{mm}$ corresponds to a maximum airspeed slightly above the main targeted wind tunnel airspeed of $60\,\mathrm{m\,s^{-1}}$. The stated nozzle inner diameter uncertainty is attributed to the measurement method and measurable inlet deformations caused by the machining process.

As the TW inlet is considered a thick-walled inlet with an aspiration efficiency expected to deviate from an ideal sampling behavior (Belyaev and Levin, 1974), the collection efficiency of the inlet was determined from combined computational fluid dynamics (CFD) and Lagrangian particle tracking simulations. Definitions of aspiration and collection efficiency, as well as the particle Stokes number St_p used in the evaluation, are given in Appendix B. Simulations were carried out in COMSOL Multiphysics software with a workflow similar to the one described by Krämer and Afchine (2004) and showed good agreement with simulations carried out in ANSYS CFX for the same probe with an inlet diameter of $4.6\,\mathrm{mm}$. However, instead of determining the limiting freestream area A_lim comprising all particle trajectories entering the inlet, collection efficiencies $E(d_\mathrm{p})$ for each droplet diameter d_p considered were calculated from the ratio of the number N_s of droplets sampled to the number N_inlet of droplets passing through the probe TW inlet equivalent area A_inlet in freestream (cf. Appendix B):

$$E(d_\mathrm{p}) = \frac{A_\mathrm{lim}}{A_\mathrm{inlet}} \approx \frac{N_\mathrm{s}}{N_\mathrm{inlet}}\ . \tag{1}$$

Figure 3 shows the determined collection efficiencies for two IWT freestream airspeeds U_a and different isokinetic factors $\mathrm{IKF} = \overline{U}_\mathrm{s}/U_\mathrm{a}$, i.e., velocity ratios of mean inlet sampling velocity $\overline{U}_\mathrm{s}$ to freestream airspeed. Low collection efficiencies at Stokes numbers around one are the result of the thick-walled inlet design (Rader and Marple, 1988). At the conditions of the measurements presented herein ($U_\mathrm{a} = 60\,\mathrm{m\,s^{-1}}$ and $\mathrm{IKF} \approx 1$), the simulated collection efficiency reaches a minimum of $88\,\%$ for particles of $3\,\mathrm{\mu m}$ diameter and is practically independent of the IKF in the range of 0.95 to 1.05 for diameters above $10\,\mathrm{\mu m}$ ($St_\mathrm{p} \approx 7$). For $St_\mathrm{p} \ll 1$, the collection efficiency tends towards the value of the isokinetic factor. Consequences of the non-representative sampling on cloud CWC measurement depend on the individual particle size distribution and are discussed in further detail in Section 4.3.

Hydrometeors aspirated through the TW inlet are transported down a $6\,\mathrm{mm}$ inner diameter stainless steel tubing to the evaporator, a $(125{\times}44{\times}16)\,\mathrm{mm}$ aluminum block controlled to $180\,°\mathrm{C}$ by a $400\,\mathrm{W}$ cartridge heater. An aluminum sheath connects the evaporator and the nozzle and ensures additional heat transfer from the evaporator to the inlet. A sharp $90\,°$ bend of the tubing approximately $100\,\mathrm{mm}$ downstream the inlet forms an impactor, where larger droplets and particles are impacted on the heated wall to increase heat transfer and promote droplet or particle break-up. At the bend the piping is enclosed and in good thermal contact with the evaporator.

For the airspeed of $60\,\mathrm{m\,s^{-1}}$ and the conditions of the measurements presented, calculated particle stopping distances S_p (cf. Appendix B) predict impaction at the bend for particles with diameters larger than approximately $15\,\mathrm{\mu m}$. This is in close

https://doi.org/10.5194/amt-2020-295
Preprint. Discussion started: 8 September 2020

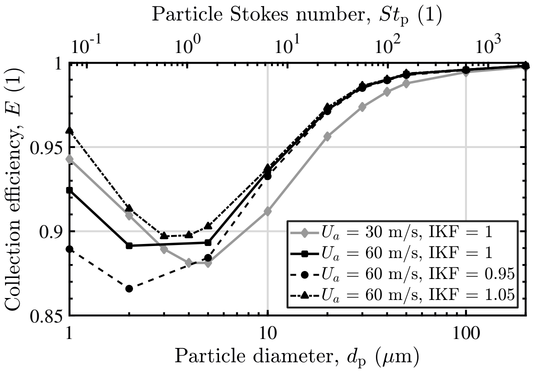

Figure 3. Isoaxial TW inlet collection efficiency as a function of particle diameter determined from combined CFD and Lagrangian particle tracking simulations at different freestream airspeeds U_a and isokinetic factors (IKFs), assuming an ambient air temperature and pressure of $-5\,^\circ\mathrm{C}$ and $1013.25\,\mathrm{hPa}$, respectively. Particle Stokes numbers given in the upper x-axis are only valid for $60\,\mathrm{m\,s^{-1}}$ data. The lines between the evaluation points are used to guide the eye.

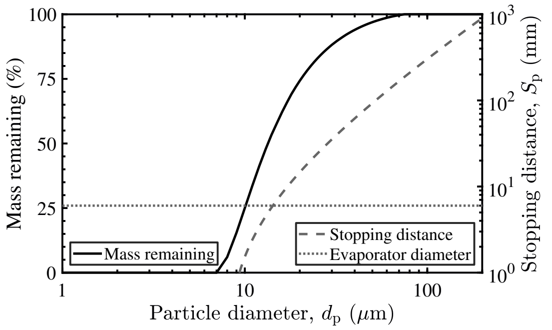

Figure 4. Calculated droplet mass remaining after traversing the probe TW pipe following the evaporator bend and stopping distance as a function of the initial droplet diameter, assuming an ambient air temperature, pressure and freestream airspeed of $-5\,^\circ\mathrm{C}$, $1013.25\,\mathrm{hPa}$ and $60\,\mathrm{m\,s^{-1}}$, respectively. The indicated evaporator diameter marks the stopping distance equal to the inlet pipe diameter of $6\,\mathrm{mm}$.

agreement with the CFD and Lagrangian particle tracking calculations. The calculated stopping distance in dependence of the particle diameter is shown in Fig. 4 together with the stopping distance equal to the evaporator pipe diameter (dotted line).

Also shown is a theoretical calculation of the evaporative mass loss of supercooled spherical droplets when passing the heated probe pipe section following the 90° bend. Droplet evaporation was calculated with the two-parameter model (droplet mass and temperature) summarized by Davis et al. (2007), which includes diffusion of water vapor from the droplet to the humid inlet air, associated latent heat losses and conductive heating of the droplet by the heated inlet air. For the computations

https://doi.org/10.5194/amt-2020-295
Preprint. Discussion started: 8 September 2020

Atmospheric Measurement Techniques Discussions

a minimum (centerline) air temperature of $50\,^{\circ}\mathrm{C}$ was assumed, which was determined from the CFD and heat transfer analysis. Inlet ambient air was assumed fully saturated at $-5\,^{\circ}\mathrm{C}$, with an additional worst case evaporated cloud CWC of $10\,\mathrm{g\,m^{-3}}$.

Droplets with diameters above $15\,\mu\mathrm{m}$ impact the $180\,^{\circ}\mathrm{C}$ evaporator walls and are assumed to evaporate due to the increased heat transfer or break up into smaller, more easily evaporated droplets. Minimum residence times of $1\,\mathrm{s}$ in the attached $7\,\mathrm{m}$ long tubes heated to $35\,^{\circ}\mathrm{C}$ are considered sufficient to achieve full evaporation of smaller droplets. However, observable TW signal oscillations for inlet condensed water mass flow rates above $0.8\,\mathrm{mg/s}$ (hydrometeor mass flux of approx. $90\,\mathrm{g\,m^{-2}\,s^{-1}}$) suggest temporary accumulation of water or ice in the small diameter nozzle or at the evaporator and are the reason for further investigation into the process of droplet and particle evaporation for the chosen inlet diameter and evaporator geometry.

2.3.2 Background water vapor inlet

The BWV inlet port is used for sampling of ambient air with the PA cell mass flow rate of $0.75\,\mathrm{slpm}$ and may be extended by a rearward facing probe with a $16\,\mathrm{mm}$ ID connected to a $4\,\mathrm{mm}$ ID tubing. The connection between the rearward facing probe and the port has been thermally insulated to reduce heating of the inlet, as the port pipe is in direct contact with the evaporator. For the measurements presented, only a single hygrometer used for TW measurement was available, thus the IKP was used without the rearward facing probe and BWV was estimated from IWT humidity sensors. The method of BWV estimation is described in further detail in Section 5.

3 Hygrometer characterization and calibration

3.1 Noise and limit of detection

To quantify measurement noise, expectable system drift and the limit of detection (LOD) of the hygrometer an Allan deviation analysis (Werle et al., 1993) was performed on a background measurement with zero air, acquired at $10\,\mathrm{Hz}$ with an integration time of $0.1\,\mathrm{s}$. Figure 5 shows the Allan deviation σ_{A}, i.e., an estimate for the standard deviation of the mean of the background signal, in dependence of the averaging or integration time τ.

The system exhibits a $1/\sqrt{\tau}$ decrease in noise, typical for white noise averaging, up to a maximum useful averaging time of $150\,\mathrm{s}$, where drift starts to deteriorate system performance. The effectiveness of increasing integration time is limited by a slow drift of the measurement gas temperature. For half the maximum useful averaging time an LOD ($3\sigma_{\mathrm{A}}$), calculated from the calibration curve (see Section 3.2), of $3.2\,\mathrm{ppm}$ water vapor mole fraction or $2.0\,\mathrm{mg\,kg^{-1}}$ in terms of humid air mass mixing ratio at standard temperature and pressure (STP; $273.15\,\mathrm{K}$ and $1000\,\mathrm{hPa}$) can be achieved. More practical averaging times of $1\,\mathrm{s}$ and $10\,\mathrm{s}$ result in noise equivalent concentrations of $23\,\mathrm{ppm}$ and $7\,\mathrm{ppm}$, respectively.

As the $1\,\mathrm{s}$ averaging time precision — equivalent to $14\,\mathrm{mg\,kg^{-1}}$ mass mixing ratio at STP — is sufficient for IWT water content measurement and results in favorable response time, this lock-in integration time is applied in calibration and water content measurements.

https://doi.org/10.5194/amt-2020-295
Preprint. Discussion started: 8 September 2020

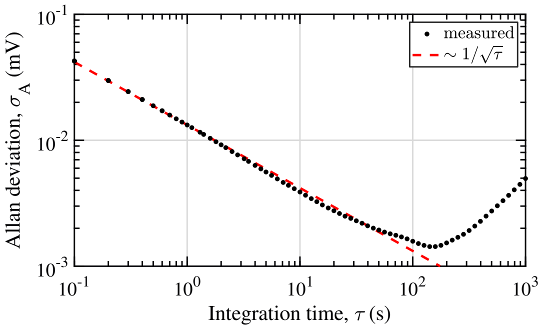

Figure 5. Allan deviation σ_A calculated from the measured signal amplitude of a one hour background measurement with zero air as a function of the lock-in integration time τ. The dotted line indicates a $1/\sqrt{\tau}$ decrease in noise, typical for white noise averaging.

3.2 Hygrometer calibration

The hygrometer is calibrated at constant PA cell temperature and pressure ($800\,\mathrm{hPa}$, $35\,°\mathrm{C}$) with the built-in two-pressure HG. To quantify measurement uncertainties at dew points lower than provided by the HG, a gas diluter (Breitegger and Bergmann, 2018) was used for an initial laboratory calibration. Using the gas diluter, humidified air provided by the humidity generator was further diluted with zero air, down to a minimum water vapor mole fraction of $124\,\mathrm{ppm}$. Background corrected calibration data recorded at concentrations in the range of $124\,\mathrm{ppm}$ to $22,150\,\mathrm{ppm}$ and the inverse calibration curve used to determine the water vapor mole fraction during water content measurement is shown in Fig. 6. Signal amplitude noise of the hygrometer during calibration is typically below water vapor mole fractions of $10\,\mathrm{ppm}$ or $0.7\,\%$ (the higher value in absolute terms applies). The former value, applicable at low concentrations, is in the order of the background signal noise ($1\,\sigma$) determined by the Allan deviation analysis for the integration time of $1\,\mathrm{s}$.

For the determination of the water vapor mole fraction during water content measurement, the calibration data is approximated by the inverse of the theoretically motivated nonlinear 5-parameter calibration function given by Lang et al. (2020), which accounts for the humidity-dependent hygrometer sensitivity. As opposed to higher-order polynomials, which are necessary to reproduce the nonlinear functional relationship, this calibration function adds the benefit of a well-defined behavior for inter- and extrapolation when faced with a reduced number of calibration points. The parameters $\boldsymbol{b}$ of the calibration curve are determined with the weighted nonlinear least-squares method, minimizing

$$\chi^2 = \sum_{i=1}^{N} w_{x,i}\left[x_{\mathrm{w},i} - f^{-1}(S_i,\boldsymbol{b})\right]^2 \tag{2}$$

over the N calibration measurements, where $f^{-1}(S_i,\boldsymbol{b})$ is the inverse calibration function evaluated at the measured PA signal amplitude S_i and for the parameter set $\boldsymbol{b}$. The inverse of the calibration function has been used in order to include the uncertainty of the calibration water vapor mole fraction $u(x_{\mathrm{w},i})$ in the determination of the parameters and parameter confidence intervals.

https://doi.org/10.5194/amt-2020-295
Preprint. Discussion started: 8 September 2020

Atmospheric Measurement Techniques Discussions
Open Access

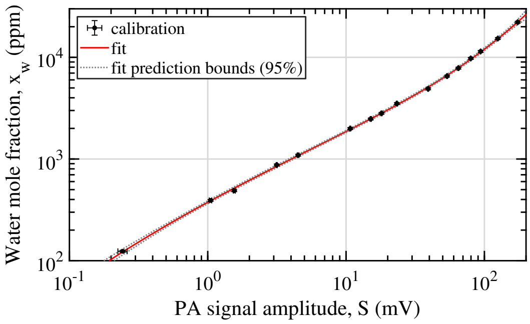

Figure 6. Laboratory calibration data of the PA hygrometer operated at 35 °C, 800 hPa and an integration time of 1 s. Calibration humidities were set with the internal humidity generator and in combination with the gas diluter. The fit indicates the best-fit calibration curve with the parameters obtained by the weighted nonlinear least-squares method. Error bars of the measurements indicate the 95 % uncertainty of the humidity generation and standard deviation of the lock-in signal for the y- and x-axes, respectively.

To this end, each calibration point i is weighted by $w_{x,i} = 1/\sigma^2_{x,i} = 1/u^2(x_{\mathrm{w},i})$, i.e., according to the combined uncertainty in the humidity provided by the humidity generator and gas diluter. The uncertainty in the mean of the measured PA signal amplitude is negligible in comparison to the uncertainty in the mole fraction and therefore is disregarded in the least-squares fit. Residuals, i.e., the differences between calibration data and calibration curve, are typically below $3\,\%$. This remaining variability is largely explained by the error in the generated humidity and changes in microphone sensitivity from temperature oscillations of the PA cell.

3.3 Estimation of hygrometer measurement uncertainty

The measurement uncertainty of the PA hygrometer is the result of uncertainties originating from the calibration and from noise during measurement. Calibration uncertainty itself includes uncertainties from humidity generation and from the approximation by the calibration function. These uncertainties have been jointly estimated from the parameter uncertainties obtained with the nonlinear least-squares method. Instrument signal noise ($1\,\sigma$) is taken equivalent to the calibration noise ($10\,\mathrm{ppm}$ or $0.7\,\%$, whichever is higher). Details to the determination of the combined hygrometer uncertainty are given in Appendix D of this work.

The calculated relative measurement uncertainty of the hygrometer ($95\,\%$ coverage) as a function of the measured water vapor mole fraction is shown in Fig. 7. Measurement uncertainty can be seen to increase rapidly for mole fractions below $200\,\mathrm{ppm}$ and above $23,000\,\mathrm{ppm}$, due to the lack of calibration points at lower and higher water vapor concentrations. Nevertheless, in the range of expected condensed water contents and background humidities encountered during typical IWT evaluation, the hygrometer exhibits an accuracy better than $2.5\,\%$ to $3.3\,\%$. This target water content range is defined by the lower limit of cloud-free, but fully saturated air (with respect to supercooled liquid) at $-30\,°\mathrm{C}$ and the upper limit of $5\,\mathrm{g\,m^{-3}}$ in fully satu-

https://doi.org/10.5194/amt-2020-295
Preprint. Discussion started: 8 September 2020

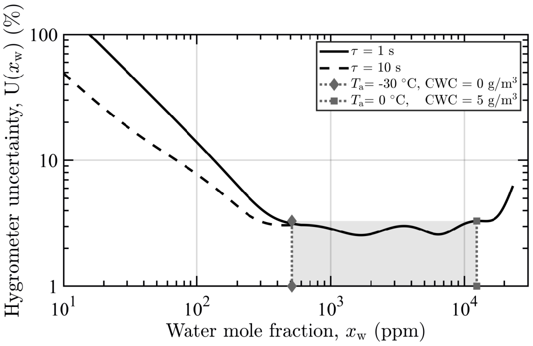

Figure 7. Relative measurement uncertainty (95 % coverage) of the photoacoustic hygrometer operated at 35 °C, 800 hPa and with integration times τ of 1 s and 10 s. The gray area bounded by dotted vertical lines marks the target range of background and total water contents, defined by the lower limit CWC of 0 g m^{-3} at -30 °C (512 ppm) and the upper limit of 5 g m^{-3} at 0 °C (12,361 ppm). The air is assumed fully saturated with respect to supercooled liquid.

rated air at 0 °C. These limits correspond to 512 ppm and 12,361 ppm at standard pressure, respectively. Fully saturated air is assumed, as high relative humidity is typical during measurement in closed circuit icing wind tunnels. Increasing lock-in integration time can be seen to not yield notable performance improvement, as in the range of interest accuracy is dominated by the uncertainty in the calibration humidity.

The determined PA hygrometer accuracy is lower than the accuracy specified for NDIR systems providing a similar measurement range (e.g., 1.5 %; LI-COR Inc., 2020). However, because the accuracy of the hygrometer is currently dominated by the accuracy of the humidity generator, it is expected that improvement of saturator temperature stability and temperature measurement, combined with the independent calibration of the HG, will further improve the accuracy of the hygrometer to similar levels.

4 CWC measurement and uncertainty

Derivation of the cloud condensed water content from the measured TW mole fraction $x_\mathrm{w,tot}$ and the ambient air BWV mole fraction $x_\mathrm{w,a}$ requires additional input from the instrument's flow measurement, together with input about the icing wind tunnel operating condition. Equations used to derive the actual condensed water content and the corresponding measurement uncertainty from the measured quantities are briefly described in the following subsections.

Measurement of the CWC, defined as the mass of condensed water in the form of hydrometeors per volume of air, is accompanied by hydrometeor and air sampling errors introduced by deviations from the ideal and isokinetic sampling at the TW inlet. These errors are corrected by accounting for the actual mass averaged hydrometeor aspiration efficiency of the probe for the given particle size distribution $\overline{\eta}_{\mathrm{asp}}$ (cf. Appendix B; Belyaev and Levin, 1974):

$$\mathrm{CWC_i} = \overline{\eta}_{\mathrm{asp}}\,\mathrm{CWC} = \frac{\overline{E}}{\mathrm{IKF}}\,\mathrm{CWC}\,. \tag{3}$$

Here, $\mathrm{CWC_i}$ is the indicated or measured condensed water content and $\overline{E}$ is the mass averaged hydrometeor collection efficiency of the probe.

Under ideal and isokinetic sampling conditions, the CWC is equal to the ratio of the mass flow rate of hydrometeors to the volumetric flow rate of air entering the probe TW inlet. At the inlet, the volume of air occupied and displaced by the liquid or solid hydrometeors can be assumed negligible for the water contents of interest (Davison et al., 2016). Indicated condensed water content $\mathrm{CWC_i}$ is the ratio of the actually sampled hydrometeor mass flow rate $\dot{m}_\mathrm{h}$ to the sampled volumetric flow rate of air q_a. Thus, using Eq. (3), CWC may be calculated from the expression

$$\mathrm{CWC} = \mathrm{CWC_i}\,\frac{\mathrm{IKF}}{\overline{E}} = \frac{\dot{m}_\mathrm{h}}{q_\mathrm{a}} \cdot \frac{\mathrm{IKF}}{\overline{E}}\,. \tag{4}$$

4.1 Indicated CWC

The flow rates $\dot{m}_\mathrm{h}$ and q_a may be expressed in terms of the total mass flow sampled through the TW inlet $\dot{m}_\mathrm{tot}$ (IWT air, including hydrometeors), the mass flow of humid ambient air $\dot{m}_\mathrm{a}$ (IWT air, excluding hydrometeors) and the ambient air density ρ_a. The indicated CWC is then calculated from

$$\begin{aligned}
\mathrm{CWC_i} &= \frac{\dot{m}_\mathrm{h}}{q_\mathrm{a}} = \frac{\dot{m}_\mathrm{tot} - \dot{m}_\mathrm{a}}{\dot{m}_\mathrm{a}/\rho_\mathrm{a}} && (5)\\
&= \rho_\mathrm{a}\left(\frac{\omega_\mathrm{da,a}}{\omega_\mathrm{da,tot}} - 1\right) && (6)\\
&= \frac{p_\mathrm{a}\,M_\mathrm{w}}{R\,T_\mathrm{a}} \cdot \frac{x_\mathrm{w,tot} - x_\mathrm{w,a}}{1 - x_\mathrm{w,tot}}\,, && (7)
\end{aligned}$$

where the density of the air has been calculated assuming an ideal gas mixture of dry air (subscript da) and water vapor,

$$\begin{aligned}
\rho_\mathrm{a} &= \rho_\mathrm{da} + \rho_\mathrm{w,a} && (8)\\
&= \frac{p_\mathrm{a}}{R\,T_\mathrm{a}}\left[M_\mathrm{da}(1 - x_\mathrm{w,a}) + M_\mathrm{w}\,x_\mathrm{w,a}\right]\,. && (9)
\end{aligned}$$

$\omega_\mathrm{da,tot}$ and $\omega_\mathrm{da,a}$ are the dry air mass fractions of the sampled TW air, which includes evaporated hydrometeors, and of the ambient air, respectively:

$$\begin{aligned}
\omega_\mathrm{da,tot} &= \frac{\dot{m}_\mathrm{da}}{\dot{m}_\mathrm{tot}} = \frac{M_\mathrm{da}(1 - x_\mathrm{w,tot})}{M_\mathrm{da}(1 - x_\mathrm{w,tot}) + M_\mathrm{w}\,x_\mathrm{w,tot}}\,, && (10)\\
\omega_\mathrm{da,a} &= \frac{\dot{m}_\mathrm{da}}{\dot{m}_\mathrm{a}} = \frac{M_\mathrm{da}(1 - x_\mathrm{w,a})}{M_\mathrm{da}(1 - x_\mathrm{w,a}) + M_\mathrm{w}\,x_\mathrm{w,a}}\,. && (11)
\end{aligned}$$

T_a and p_a are the icing wind tunnel static air temperature and pressure. M_da and M_w are the molar masses of dry air and water and R is the universal gas constant. Real gas effects at the measurement temperatures, pressures and humidities of interest are minor.

4.2 Isokinetic factor and collection efficiency

The TW inlet flow rate is only set to isokinetic sampling once before activation of the IWT spray system. As the inlet total mass flow rate is held constant and is measured downstream the evaporator, water vapor originating from hydrometeor evaporation reduces the inlet air flow rate during TW measurement, altering the flow field at the probe inlet and reducing the IKF. In addition to this reduction of the IKF, minor changes in the IWT air density ρ_a or airspeed U_a during measurement also lead to deviations from the initially set isokineticity.

The isokinetic factor in Eq. (4) corrects for these sources of disproportional sampling of ambient air in comparison to isokinetic sampling and is determined during measurement from

$$\mathrm{IKF} = \frac{\overline{U}_\mathrm{s}}{U_\mathrm{a}} = \frac{\dot{m}_\mathrm{a}}{U_\mathrm{a}\,\rho_\mathrm{a}\,A_\mathrm{inlet}} = \frac{4\,\dot{m}_\mathrm{a}}{U_\mathrm{a}\,\rho_\mathrm{a}\,d_\mathrm{inlet}^2\,\pi}\;, \qquad (12)$$

where d_inlet is the diameter of the circular probe TW inlet.

Since with a decrease of the IKF the collection efficiency at high particle Stokes numbers decreases sub-proportionally to the efficiency at lower Stokes numbers (cf. Fig. 3), condensed water content is overestimated for typical particle size distributions. For each specific particle size distribution encountered during measurement, the mass averaged collection efficiency $\overline{E}$ in Eq. (4) may be used to correct for the size and IKF dependent sampling efficiency.

4.2.1 Mass flow measurement

The ambient air mass flow rate $\dot{m}_\mathrm{a}$ required for the calculation of the IKF is determined from the total mass flow sampled through the TW inlet, i.e., the combined mass flow rates through the PA cell $\dot{m}_\mathrm{cell}$ and the bypass path $\dot{m}_\mathrm{bp}$. Together with Eqs. (10)-(11), the ambient air mass flow rate (excluding hydrometeors) through the TW inlet is given by

$$\dot{m}_\mathrm{a} = \frac{\omega_\mathrm{da,tot}}{\omega_\mathrm{da,a}}\,\dot{m}_\mathrm{tot} = \frac{\omega_\mathrm{da,tot}}{\omega_\mathrm{da,a}}\,(\dot{m}_\mathrm{cell} + \dot{m}_\mathrm{bp})\;. \qquad (13)$$

The thermal mass flow meters are calibrated for dry air, assuming dry air specific heat capacity for the gas to be measured. As humid air isobaric heat capacity increases by $1\,\%$ at the maximum expected TWC ($10\,\mathrm{g\,m^{-3}}$ CWC, fully saturated air at STP), the indicated volumetric standard flow rates of the flow meters, $q_\mathrm{cell,0}$ and $q_\mathrm{bp,0}$, are converted to humid air mass flow rates (Hardy et al., 1999):

$$\begin{aligned}\dot{m}_j &= \frac{c_\mathrm{p,da}}{c_\mathrm{p,tot}}\,\rho_\mathrm{da,0}\,q_{j,0}\\ &= \frac{c_\mathrm{p,da}}{c_\mathrm{p,da}\,\omega_\mathrm{da,tot} + c_\mathrm{p,w}\,(1-\omega_\mathrm{da,tot})}\,\rho_\mathrm{da,0}\,q_{j,0}\;, \qquad (14)\end{aligned}$$

where $j = \{\mathrm{cell},\mathrm{bp}\}$ refers to the cell or bypass measurement, $\rho_\mathrm{da,0}$ is the dry air density at standard temperature and $1013.25\,\mathrm{hPa}$, $c_\mathrm{p,da}$ is the isobaric specific heat capacity of dry air, and the specific heat capacity of humid air $c_\mathrm{p,tot}$ is calculated assuming an ideal mixture model. The remaining mass flow error after applying the above heat capacity correction has not yet been determined. However, the error is assumed below $1\,\%$, as the change in air specific heat capacity itself is below $1\,\%$ at the maximum expected total water content.

https://doi.org/10.5194/amt-2020-295
Preprint. Discussion started: 8 September 2020

Atmospheric Measurement Techniques Discussions

4.2.2 CWC estimation

The final expression used for icing wind tunnel CWC estimation is obtained by combining Eq. (4) with Eqs. (7) and (10)-(14):

$$\mathrm{CWC} = \frac{4\,M_\mathrm{w}}{\pi\,d_\mathrm{inlet}^2\,U_\mathrm{a}\,\overline{E}} \cdot \frac{\rho_\mathrm{da,0}\,c_\mathrm{p,da}\,(q_\mathrm{bp,0}+q_\mathrm{cell,0})}{c_\mathrm{p,da}\,M_\mathrm{da}\,(1-x_\mathrm{w,tot})+c_\mathrm{p,w}\,M_\mathrm{w}\,x_\mathrm{w,tot}} \cdot \frac{x_\mathrm{w,tot}-x_\mathrm{w,a}}{1-x_\mathrm{w,a}}\,. \tag{15}$$

Although IWT static air temperature and pressure are required to set the total sampling mass flow to isokinetic TW sampling, this result shows that if the isokinetic factor is not calculated explicitly, air temperature and pressure only appear in the hydrometeor collection efficiency (through air viscosity and slip correction) and otherwise are not required to calculate the condensed water content. For minor temperature and pressure fluctuations during IWT water content measurement, only marginal impact on CWC measurement and uncertainty is anticipated by disregarding changes in IWT air temperature and pressure.

4.3 CWC measurement uncertainty

Corrections and errors introduced by the collection efficiency are specific to the respective wind tunnel icing conditions and hence are not considered in the following general analysis. Instead, a mean mass averaged collection efficiency of one is assumed. With the numerically determined collection efficiency given in Fig. 3, maintaining this assumption for the evaluation of the presented measurements in icing conditions of freezing drizzle or rain, with median volume diameters (MVDs) in the range of $100\,\mu\mathrm{m}$ to $650\,\mu\mathrm{m}$, the potential CWC underestimation is below $1\,\%$ (size distribution data taken from Cober et al. (2009)).

The uncertainty of the condensed water content measurement is derived from a first-order propagation of the uncertainties of the quantities appearing in Eq. (15) according to the Guide to the Expression of Uncertainty in Measurement (GUM; Joint Committee for Guides in Metrology, 2008a). Uncertainties not distributed normally have been converted to standard uncertainties for the analytical calculations. Unless otherwise stated, all uncertainties are given in terms of the $95\,\%$ coverage interval. A summary of the individual uncertainties of the input quantities is given in Table C1 in Appendix C of this work.

The current single-hygrometer instrument only allows either TW or BWV content measurement. Alternating between both measurements to determine the CWC inevitably results in a measurement error due to the dynamic behavior of the background water content, which is mainly defined by the initial IWT air saturation level and stability of the temperature conditioning during the measurement. Depending on the saturation level preceding activation of the spray, the background water content during the probe intercomparison increased by up to $0.5\,\mathrm{g\,m^{-3}}$ for as long as five minutes after activation of the spray and before reaching a stable reading. As a consequence of alternating TW and BWV measurement, errors highly depend on subjective assessment during evaluation and are specific to the IWT operating conditions. With the goal of assessing instrument accuracy with a planned second dedicated PA cell for background humidity measurement, the uncertainties of the TW and BWV content measurement are both taken equal to the hygrometer measurement uncertainty given in Section 3.3. The presented uncertainties

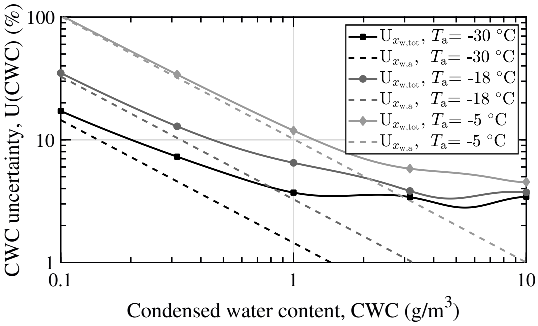

Figure 8. Hygrometer measurement uncertainty contributions to the $95\,\%$ CWC measurement uncertainty at three static air temperatures, an airspeed of $60\,\mathrm{m\,s^{-1}}$ and a static air pressure of $1013.25\,\mathrm{hPa}$. Condensed water content uncertainty contributions are given relative to the actual CWC and for isokinetic sampling. The ambient air is assumed fully saturated with respect to supercooled liquid.

may, however, be taken as upper limits for a different hygrometer used for background humidity measurement with similar or better accuracy.

Figure 8 shows the calculated hygrometer contribution to the condensed water content measurement uncertainty at three IWT static air temperatures. Temperatures of $-30\,^{\circ}\mathrm{C}$, $-18\,^{\circ}\mathrm{C}$ and $-5\,^{\circ}\mathrm{C}$ were examined, again assuming fully saturated air with respect to supercooled liquid water, as this is expected for the closed circuit icing wind tunnel. The measurement uncertainty contributions are given relative to the actual CWC. Contributions of the measurement of the background water vapor concentration ($\mathrm{U}_{x_{\mathrm{w,a}}}$, dashed lines) indicate constant background humidities with associated constant absolute measurement uncertainties.

The hygrometer's contribution to the CWC measurement uncertainty increases rapidly with lower water content and increasing temperature. The latter circumstance is a result of the rising absolute BWV concentration uncertainty with increasing background humidity, which dominates the difference of measured total and background water vapor concentrations at low CWCs (last term in Eq. (15)). For a condensed water content of $0.5\,\mathrm{g\,m^{-3}}$ and an IWT temperature of $-5\,^{\circ}\mathrm{C}$, the combined hygrometer uncertainty contribution (root of sum of squares) is $0.15\,\mathrm{g\,m^{-3}}$. At $-30\,^{\circ}\mathrm{C}$ the hygrometer's contribution is reduced to $0.03\,\mathrm{g\,m^{-3}}$.

Figure 9 shows the overall CWC measurement uncertainty at two of the above temperatures. Also shown are the individual contributions of the input quantities. At high condensed water contents the device is currently obviously limited by the large relative uncertainty in the probe TW inlet area ($\pm 9\,\%$), which contributes a constant $10.5\,\%$ to the overall uncertainty. This is a result of the particularly small size of the TW inlet diameter. However, deviation of the estimated nozzle inlet area from the true size only results in an invariant systematic error in the isokinetic factor. Hence the CWC measurement error should be proportional to the indicated CWC and should not affect instrument precision. The additional error in the projected probe TW inlet area due to misalignment to the direction of flow is below $0.5\,\%$, assuming an angle of attack within $\pm 5\,^{\circ}$. This does

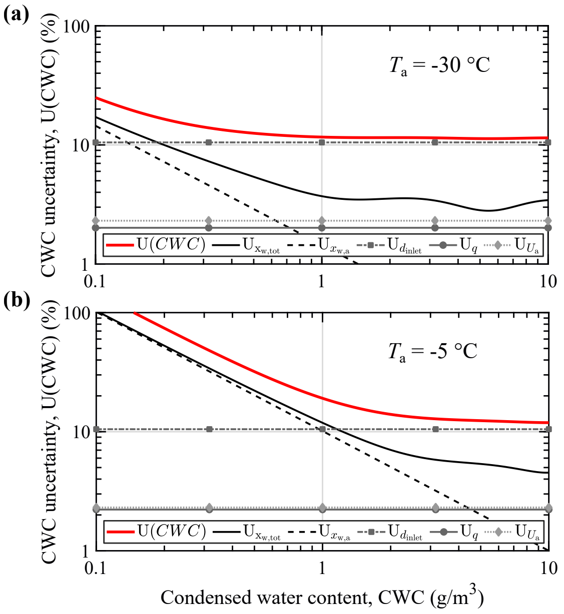

Figure 9. Condensed water content measurement uncertainty (95 %) and individual contributions at static air temperatures of **(a)** −30 °C and **(b)** −5 °C. Uncertainties are given relative to the actual CWC and for isokinetic sampling. Wind speed and static air pressure are 60 $\mathrm{m\,s^{-1}}$ and 1013.25 hPa, respectively. The ambient air is assumed fully saturated with respect to supercooled liquid.

not include errors induced by changes in collection efficiency, which again have to be considered separately for the respective particle size distribution.

Towards lower condensed water contents, the overall measurement uncertainty is dominated by the humidity measurement. As is typical for IKPs, the accuracy of the instrument is highest at low ambient temperatures or background humidities (Davison et al., 2016). Table 1 summarizes absolute and relative measurement uncertainties U(CWC) at static air temperatures of −5 °C and −30 °C for condensed water contents in the range of 0.25 $\mathrm{g\,m^{-3}}$ to 3 $\mathrm{g\,m^{-3}}$.

At the lower temperature, measurement uncertainty decreases below 20 % above a condensed water content of 0.14 $\mathrm{g\,m^{-3}}$. In warm air of −5 °C this is only the case above a CWC of 0.93 $\mathrm{g\,m^{-3}}$. Due to the high contributions of humidity measurement and inlet area uncertainty, the measurements of the total mass flow and IWT airspeed only marginally contribute to the overall uncertainty.

To validate the stated first-order analytic CWC uncertainties, a Monte Carlo method (Joint Committee for Guides in Metrology, 2008b) has been applied. The method takes into account and propagates the assumed uncertainty distributions of the input quantities. As the TW inlet diameter is assumed with uniform probability within the measured and specified bounds (cf. Table C1), analytic and numeric uncertainties are expected to differ at high CWCs where the inlet diameter contribution dominates. Numerically calculated shortest 95 % coverage intervals attained with the Monte Carlo method lie within the analytic

Table 1. Instrument absolute and relative CWC measurement uncertainties (95 % coverage) at selected cloud CWCs and at static air temperatures of $-5\,^{\circ}\mathrm{C}$ and $-30\,^{\circ}\mathrm{C}$. Wind tunnel airspeed and static air pressure for the calculations are $60\,\mathrm{m\,s^{-1}}$ and $1013.25\,\mathrm{hPa}$, respectively.

T_a	CWC	U(CWC)	
$-5\,^{\circ}\mathrm{C}$	$0.25\,\mathrm{g\,m^{-3}}$	$0.15\,\mathrm{g\,m^{-3}}$	60 %
	$0.50\,\mathrm{g\,m^{-3}}$	$0.16\,\mathrm{g\,m^{-3}}$	31 %
	$1.00\,\mathrm{g\,m^{-3}}$	$0.19\,\mathrm{g\,m^{-3}}$	19 %
	$3.00\,\mathrm{g\,m^{-3}}$	$0.39\,\mathrm{g\,m^{-3}}$	13 %
$-30\,^{\circ}\mathrm{C}$	$0.25\,\mathrm{g\,m^{-3}}$	$0.04\,\mathrm{g\,m^{-3}}$	15 %
	$0.50\,\mathrm{g\,m^{-3}}$	$0.06\,\mathrm{g\,m^{-3}}$	13 %
	$1.00\,\mathrm{g\,m^{-3}}$	$0.12\,\mathrm{g\,m^{-3}}$	12 %
	$3.00\,\mathrm{g\,m^{-3}}$	$0.34\,\mathrm{g\,m^{-3}}$	11 %

interval over the whole range of interest (cf. Appendix E, Fig. E1). Hence, the presented analytic uncertainties may be taken as upper bounds to a more realistic estimation of the uncertainty.

5 Icing wind tunnel probe intercomparison

The photoacoustic hygrometer in combination with the IKP was used for TW measurement during a water content probe intercomparison campaign at the RTA Rail Tech Arsenal Fahrzeugversuchsanlage GmbH (RTA) icing wind tunnel. The closed circuit IWT is capable of simulating air temperatures down to $-30\,^{\circ}\mathrm{C}$ and windspeeds up to $80\,\mathrm{m\,s^{-1}}$ in a test section of $(3.5{\times}2.5{\times}3)\,\mathrm{m}$ (width×height×length) at local ambient pressure. Test conditions included freezing drizzle and rain icing conditions with bi-modal particle size distributions (in close agreement to EASA CS-25 Appendix O) and with MVDs of approximately $100\,\mathrm{\mu m}$ and $550\,\mathrm{\mu m}$ to $650\,\mathrm{\mu m}$, respectively. Measurements in classical supercooled droplet icing conditions at higher cloud CWCs had to be disregarded due to the already described oscillations observed in the TW measurements at high loads, suspected to be caused by temporary obstructions of the small diameter inlet. All measurements were conducted at a target static air temperature of $-5\,^{\circ}\mathrm{C}$ and wind speed of $60\,\mathrm{m\,s^{-1}}$. Freezing drizzle is created by 264 pneumatic atomizing nozzles mounted on horizontal spray bars placed approximately $12\,\mathrm{m}$ upstream the test section. Freezing rain droplet size distributions with maximum diameters of approximately $1.5\,\mathrm{mm}$ were generated with an additional set of twelve rotating nozzles mounted on the IWT spray bar system (cf. Breitfuss et al., 2019).

The PA system was compared against a multi-element water content hot-wire probe (SEA, WCM-2000 Multi Element Water Content System) and an IKP from Cranfield University (CU-IKP; Bansmer et al., 2018), which utilizes commercial NDIR sensor based hygrometers for simultaneous BWV and isokinetic TW measurement via backward- and forward-facing inlets and was specifically designed for high water content IWT measurement. All probes were mounted side by side on a horizontal splitter-plate-like panel with the probe inlets positioned at the approximate vertical center of the test section (cf. Fig. 10) and

https://doi.org/10.5194/amt-2020-295
Preprint. Discussion started: 8 September 2020

Atmospheric Measurement Techniques
Discussions

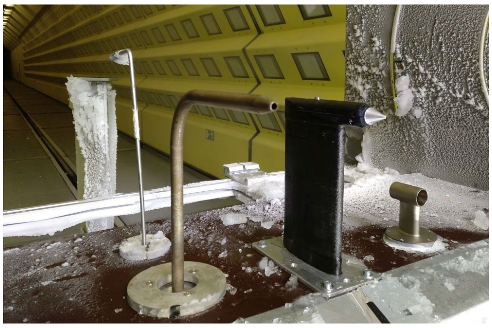

Figure 10. Positioning of the water content probes mounted on the splitter-plate-like panel in the RTA icing wind tunnel test section. Viewing direction is in the direction of flow. From left to right: Cranfield University IKP TW and backward facing BWV inlet, PA hygrometer IKP and SEA WCM-2000.

the measurements with the probes were conducted simultaneously. In the relevant area of the test section, LWC spatial cloud uniformity of the IWT is assumed better than $\pm 10\,\%$ and $\pm 15\,\%$ for freezing drizzle and freezing rain, respectively. The spatial cloud uniformity was determined with an icing cloud calibration grid (Breitfuss et al., 2019) and is within the SAE ARP-5905 recommended maximum allowable deviation ($\pm 20\,\%$).

During the intercomparison the PA hygrometer was primarily used for TWC measurement. Continuous background humidity measurement was thus performed with an external capacitive humidity sensor (E+E Elektronik, EE33) mounted to the IWT wall. The sensor (labeled *IWT humidity rear*) has a specified relative humidity and temperature measurement accuracy better than $\pm 2.3\,\%\mathrm{RH}$ and $\pm 0.25\,^\circ\mathrm{C}$, respectively, and is located downstream the PA system IKP at the rear end of the IWT. BWV concentrations measured by this sensor were time-shifted to correct for the time delay resulting from the displacement from the probe location. A second humidity sensor of the same type (*IWT humidity front*) is placed at the test section, but is not directly exposed to the main IWT air flow. This sensor is not used for evaluation, but gives an indication of the true background humidity at the sampling point of the hygrometer.

Figures 11 and 12 show two measurements in freezing rain with a drop MVD of approximately $550\,\mu\mathrm{m}$. The upper panels show the TW and BWV mole fractions measured by the PA system and the CU-IKP together with background humidities measured by both IWT humidity sensors over time. The lower panels of Figs. 11 and 12 show the corresponding derived CWC for the PA system and the CU-IKP, as well as the measured CWC by the multi-element hot-wire instrument. Activation of the IWT spray system is indicated by a calculated theoretical condensed water content (*IWT spray*), which, however, is known to underestimate the true CWC in SLD icing conditions. The high dispersion in the PA signal during cloud measurement is a result of the low averaging effect of the small probe TW inlet area in combination with the fast response time of the hygrometer ($\tau_{63} < 2\,\mathrm{s}$). Collection efficiency has been assumed $100\,\%$ for the evaluation, as the error is assumed below $1\,\%$ for the SLD size distributions (cf. Section 4.3).

https://doi.org/10.5194/amt-2020-295
Preprint. Discussion started: 8 September 2020

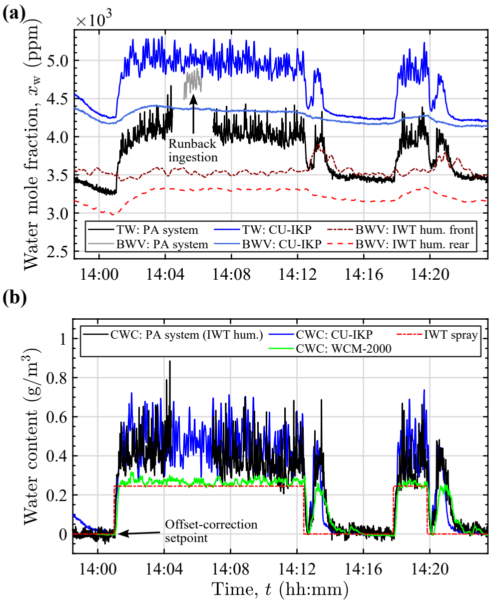

Figure 11. Water content measurements in freezing rain with a drop MVD of $550\,\mu\mathrm{m}$ at $-5\,^\circ\mathrm{C}$ and $60\,\mathrm{m\,s^{-1}}$. **(a)** PA instrument and CU-IKP TW and BWV mole fractions (erroneous PA instrument BWV sampling perpendicular to flow), together with BWV mole fractions calculated from the IWT humidity measurements. **(b)** CWCs determined by the PA system (in combination with *IWT humidity rear*), the CU-IKP and the hot-wire probe (WCM-2000). Spray activation is indicated by *IWT spray*.

The external background humidity reference (*IWT humidity rear*) can be seen to correlate well with the PA system total water measurement when the spray system is inactive (cloud-free air). Nevertheless, considerable offset (several hundred ppm) was measured in all conditions and was therefore subtracted for the estimation of the condensed water content. Points in time of the $10\,\mathrm{s}$ offset calculation period are indicated with arrows in Figs. 11(b) and 12(b). The observable offset is mainly attributed to the humidity sensor accuracy, as well as to gradients in the IWT air temperature and saturation between the measurement locations.

The CU-IKP likewise indicated a steady offset of approximately $100\,\mathrm{ppm}$ between the TW and BWV measurements when the spray system was inactive. This difference may have resulted from differing sensitivities or zero offset drift of the hygrometer channels and is corrected in a similar manner as with the PA system. Additionally, as the CU-IKP has not been calibrated for absolute measurement and the NDIR gas analyzer has been used without continuous reference measurement, exhibiting simultaneous but similar drift of both channels, measured concentrations were larger than determined by the IWT humidity sensors and the PA system. For some measurements the difference between PA system and CU-IKP exceeded $2{,}000\,\mathrm{ppm}$. As large parts of humidities measured by the CU-IKP are in excess of the saturation mole fraction with respect to supercooled liquid (even well before activation of the spray), it is concluded that the calculated CU-IKP values overestimate true absolute

https://doi.org/10.5194/amt-2020-295
Preprint. Discussion started: 8 September 2020

Atmospheric Measurement Techniques
Discussions
Open Access

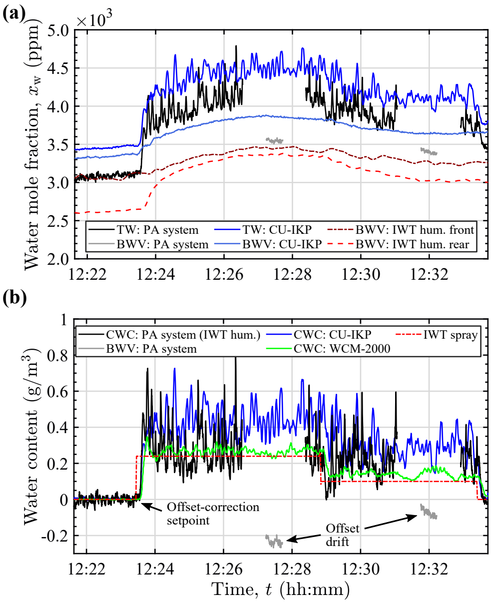

Figure 12. Water content measurement in freezing rain (MVD of 550 µm, $-5\,^\circ$C, $60\,\mathrm{m\,s^{-1}}$), showing underestimated CWC due to significant background humidity offset drift. **(a)** PA instrument and CU-IKP TW and BWV mole fraction (extended PA instrument probe BWV inlet), together with BWV mole fractions calculated from the IWT humidity measurements. **(b)** CWCs determined by the PA system (in combination with *IWT humidity rear*), the CU-IKP and the hot-wire probe (WCM-2000). *BWV: PA system* shows the residual background offset between the Pa system's BWV measurement and *IWT humidity rear* after offset correction. Spray activation is indicated by *IWT spray*.

TW and BWV contents. Effects on CWC derivation, however, are mitigated by the expected similar drift of both channels and the primarily differential nature of CWC measurement.

Background humidity measurement with the PA instrument's BWV inlet port oriented perpendicular to the direction of flow resulted in highly elevated BWV levels (Fig. 11(a)), due to ingestion of runback water or sampling of air from the humidified thermal boundary layer of the heated probe. Therefore, the latter half of the measurements was conducted with the probe BWV inlet extended by a backward-oriented tubing, which enabled intermittent and more reliable background humidity measurement in icing conditions. Differences (residuals) in background humidities measured by the PA system with the modified BWV inlet and the reference humidity sensor were used to identify measurements exhibiting considerable background humidity offset drift (cf. Fig. 12(a) and (b)), which were subsequently excluded from further evaluation. Due to the dynamic behavior of the background humidity, estimated offset drifts of up to $0.1\,\mathrm{g\,m^{-3}}$ could not be reliably detected with the described method and may have resulted in equivalent CWC measurement errors. For the water contents encountered during the intercomparison this may have resulted in relative errors of $11\,\%$ to $36\,\%$ for the highest and the lowest CWC, respectively.

https://doi.org/10.5194/amt-2020-295
Preprint. Discussion started: 8 September 2020

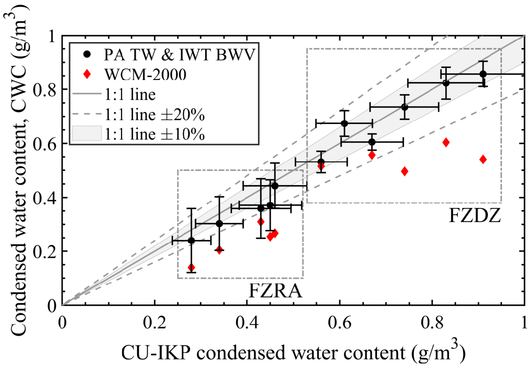

Figure 13. Mean measured CWC of the PA system in combination with the IWT background humidity measurement and of the hot-wire probe (WCM-2000) over the CWC measured by the Cranfield University IKP (CU-IKP). Dash-dotted rectangular boxes in the figure mark measurements of freezing rain (FZRA) and freezing drizzle (FZDZ) with MVDs of approximately 550 µm to 650 µm and 100 µm, respectively. Vertical error bars mark the standard deviations of the measurements. Horizontal error bars indicate the IWT cloud LWC uniformity (±15 % and ±10 % for freezing drizzle and freezing rain, respectively).

Figure 13 finally shows the comparison of the mean CWCs measured by all probes in conditions of freezing drizzle and freezing rain. Condensed water contents determined with the PA system and the hot-wire probe are plotted over the mean CWC measured by the Cranfield University IKP, as the device has been assumed the reference due to its superior probe design and the simultaneous background and TW measurement.

Precision of the presented measurements heavily depends on the stability of the background humidity during total water content measurement with the PA system and the correct identification of background humidity drifts. Although the measurement uncertainty cannot be quantified for the applied method of BWV estimation at the location of the IKP, the CWC derived from the PA system TW measurement is shown to agree within ±20 % of the reference measurement for conditions of freezing drizzle or rain. Condensed water contents determined in freezing drizzle are within ±10 % of the reference (best-fit slope of 0.98).

Total condensed water content determined by the hot-wire instrument continuously was below the CWC measured by the CU-IKP. This underestimation is partly attributed to splashing of large droplets from the hot-wire sensor-element (cylindrical half-pipe facing in the direction of flow), but is larger than is anticipated for freezing drizzle cloud droplet distributions (Steen et al., 2016) and may indicate the advantages of isokinetic evaporator probes for CWC measurement in these conditions. A detailed analysis of the severe differences is outside the scope of this work. However, measured deviations from the reference IKP may also be attributable to spatial IWT cloud non-uniformity for all systems. Accuracy of PA system CWC measurement is additionally decreased by the high absolute background humidity present at the relatively warm IWT temperature during the measurements (cf. Section 4.3).

https://doi.org/10.5194/amt-2020-295
Preprint. Discussion started: 8 September 2020

Atmospheric Measurement Techniques Discussions
Open Access

6 Conclusions and outlook

In this work a hygrometer based on intensity-modulated photoacoustic spectroscopy with a near-infrared laser diode has been realized and combined with a two-pressure humidity generator and an isokinetic evaporator probe to provide a new instrument capable of measuring total or background water contents in simulated atmospheric icing conditions. The dynamic range of the single-wavelength PA hygrometer has been shown to encompass water contents occurring in SLD, mixed-phase and high IWC environments, where classical water content probes are associated with lower accuracy. Laboratory calibration of the hygrometer using the instrument's calibration unit displayed a $1\,\mathrm{s}$ integration time limit of detection of $23\,\mathrm{ppm}$ and an accuracy ($95\,\%$ coverage) better than $2.5\,\%$ to $3.3\,\%$ in the range of $512\,\mathrm{ppm}$ to $12,361\,\mathrm{ppm}$ at standard pressure. The range corresponds to a saturated sea-level cloud-free air at $-30\,°\mathrm{C}$ and a CWC of $5\,\mathrm{g\,m^{-3}}$ in saturated $0\,°\mathrm{C}$ air. Since the determined accuracy is dominated by the uncertainty of the built-in humidity reference, further improvement of the hygrometer's measurement uncertainty may be achieved by using an independent traceable calibration.

For CWC measurements a major contribution to the overall measurement uncertainty is associated with the small diameter TW inlet of the IKP ($3.3\,\mathrm{mm}$), which currently constrains the device uncertainty ($95\,\%$ coverage) to above $10\,\%$ in all conditions. The small diameter also is suspected to cause temporary accumulation of water or ice in the inlet at high CWC loads. To further decrease the overall measurement uncertainty to the level of the hygrometer uncertainty, a redesign of the IKP inlet is the focus of ongoing research. The isokinetic aspiration efficiency of the probe at wind tunnel airspeeds above $60\,\mathrm{m\,s^{-1}}$ has been determined by numerical means and near standard pressures and has been shown to lie above $88\,\%$ for droplets of any size and above $99\,\%$ for droplets with diameters greater than $40\,\mu\mathrm{m}$. From the determined size dependent collection efficiency a bias of less than $1\,\%$ can be inferred for CWC measurement in absence of detailed droplet size distribution data in conditions of freezing drizzle or rain (EASA CS-25 Appendix O).

Uncertainty considerations showed that despite the current limitations given by the IKP inlet, an accuracy better than $20\,\%$ is achieved by the instrument for CWCs above $0.14\,\mathrm{g\,m^{-3}}$ in cold air ($-30\,°\mathrm{C}$) and when combined with a suitable background humidity measurement. For higher condensed water contents measurement accuracy further improves. In saturated warm air ($-5\,°\mathrm{C}$) the hygrometer uncertainty currently limits practical measurement to condensed water contents above $0.9\,\mathrm{g\,m^{-3}}$. With additional adaptations of the TW inlet and improvement of the calibration process, further extension of the useful operating range to lower water contents is expected. It has to be noted that the determined measurement uncertainty is higher than the $\pm 10\,\%$ LWC measurement instrumentation maximum uncertainty demanded by the SAE ARP-5905, which, however, has been defined for classical icing conditions (EASA CS-25 Appendix C) and may be increased in a similar recommended practice for the particularly challenging measurement in SLD icing conditions (SAE AIR-6341, 2015).

The system's TWC measurement capability has been deployed in a CWC measurement intercomparison with a reference IKP instrument in freezing drizzle and rain conditions in the RTA icing wind tunnel. Background humidity had to be estimated independently by an external humidity sensor which, together with the necessary method of offset correction, was determined to limit achievable measurement precision for the chosen setup. Measurements performed in warm air freezing drizzle and rain conditions with MVDs from $100\,\mu\mathrm{m}$ to $650\,\mu\mathrm{m}$, however, showed a CWC agreement of the two IKPs within $\pm 20\,\%$ for

https://doi.org/10.5194/amt-2020-295
Preprint. Discussion started: 8 September 2020

water contents in the range of $0.3\,\mathrm{g\,m^{-3}}$ to $0.9\,\mathrm{g\,m^{-3}}$. This is also within the recommended maximum LWC spatial deviation allowed by the SAE ARP-5905 ($\pm 20\,\%$).

Appendix A: Photoacoustic background signal correction

The signal returned by the PA hygrometer is the lock-in signal $\boldsymbol{S_m} = (S_{m,I}, S_{m,Q})^T$, where I and Q denote the in-phase and quadrature components of the lock-in amplifier, respectively. Prior to each calibration, a background photoacoustic signal, $\boldsymbol{S}_{BG} = (S_{BG,I}, S_{BG,Q})^T$ is recorded after flushing the PA cell with the zero air until a stable reading is attained.

The photoacoustic amplitude of all subsequent calibration or water content measurements is calculated on the digital signal processing unit of the hygrometer after phase-correct subtraction of the mean of the recorded PA background signal:

$$\begin{aligned} S &= \|\boldsymbol{S}_m - \overline{\boldsymbol{S}}_{BG}\| \\ &= \sqrt{(S_{m,I} - \overline{S}_{BG,I})^2 + (S_{m,Q} - \overline{S}_{BG,Q})^2}\,. \end{aligned} \tag{A1}$$

Appendix B: Calculation of inlet efficiencies, Stokes number and stopping distance

The aspiration efficiency η_asp of particles at a given particle size d_p is given by the particle mass concentration in the air entering the inlet divided by the ambient mass concentration at that size (Belyaev and Levin, 1974),

$$\eta_\mathrm{asp}(d_\mathrm{p}) = \frac{\mathrm{CWC_i}(d_\mathrm{p})}{\mathrm{CWC}(d_\mathrm{p})}\,, \tag{B1}$$

and may be written in terms of the limiting area A_lim in front of the inlet, within which all trajectories of sampled particles begin, and the freestream to mean sampling velocity ratio $U_\mathrm{a}/\overline{U}_\mathrm{s}$:

$$\eta_\mathrm{asp}(d_\mathrm{p}) = \frac{A_\mathrm{lim}(d_\mathrm{p})}{A_\mathrm{inlet}} \cdot \frac{U_\mathrm{a}}{\overline{U}_\mathrm{s}} = \frac{E(d_\mathrm{p})}{\mathrm{IKF}}\,. \tag{B2}$$

Here, $E = A_\mathrm{lim}/A_\mathrm{inlet}$ is the particle size dependent collection efficiency and $\mathrm{IKF} = \overline{U}_\mathrm{s}/U_\mathrm{a}$ is the isokinetic factor.

For the evaluation of the collection efficiencies, the particle Stokes number St_p is calculated according to Kulkarni et al. (2011):

$$St_\mathrm{p} = \frac{\rho_\mathrm{p}\, d_\mathrm{p}^2\, U_\mathrm{p}\, C_c}{18\,\eta\, d_\mathrm{inlet}}\,, \tag{B3}$$

where ρ_p is the droplet density calculated for supercooled liquid water (Hare and Sorensen, 1987), d_p is the droplet diameter, U_p is the initial droplet velocity equal to the freestream airspeed U_a, C_c is the Cunningham slip correction, η is the air dynamic viscosity and d_inlet is the probe inlet diameter.

The Cunningham slip correction for droplets is calculated by

$$C_c = 1 + \frac{2\,\lambda}{d_\mathrm{p}}\left[1.207 + 0.440\,\exp\left(-0.596\,d_\mathrm{p}/(2\,\lambda)\right)\right] \tag{B4}$$

https://doi.org/10.5194/amt-2020-295
Preprint. Discussion started: 8 September 2020

Table C1. Summary of uncertainties of the two-pressure humidity generator (HG) and the input quantities entering the condensed water content calculation. Uncertainties are given in terms of half-widths of the rectangular uncertainty distributions.

Variable	Description	Reference / Source	Uncertainty
$x_{\mathrm{w,BG}}$	Zero air residual water vapor volume fraction	calibrated	2 ppmv
T_{HG}	HG saturator air temperature	calibrated	0.16 K
p_{HG}	HG saturator air pressure	calibrated	200 Pa (2 %FS)
M_{w}	Molar mass of water ($18.01528\,\mathrm{g\,mol^{-1}}$)	Wieser and Berglund (2009)	negligible
M_{da}	Molar mass of dry air ($28.964\,\mathrm{g\,mol^{-1}}$)	Giacomo (1982)	negligible
$c_{\mathrm{p,w}}$	Water vapor specific heat capacity ($1874\,\mathrm{J\,kg^{-1}\,K^{-1}}$, $x_{\mathrm{w}} = 1\,\%$)	Bell et al. (2014)	negligible
$c_{\mathrm{p,da}}$	Dry air specific heat capacity ($1006.7\,\mathrm{J\,kg^{-1}\,K^{-1}}$)	Bell et al. (2014)	negligible
$\rho_{\mathrm{da,0}}$	Dry air density at 0 °C and 1013.25 hPa ($1.293\,\mathrm{kg\,m^{-3}}$)	Giacomo (1982)	negligible
$q_{\mathrm{bp,0}}$	Bypass path standard volumetric flow rate	calibrated	0.06 slpm (1 %FS)
$q_{\mathrm{cell,0}}$	PA cell standard volumetric flow rate	calibrated	0.6 slpm (1 %FS)
d_{inlet}	Probe TW inlet diameter	measurement	0.15 mm
U_{a}	Wind tunnel airspeed at probe	IWT	2 %

(Allen and Raabe, 1985; Rader, 1990), where the mean free path λ according to Willeke (1976) is given by:

$$\lambda = \lambda_r \left(\frac{101 \cdot 10^3}{p_{\mathrm{a}}}\right)\left(\frac{T_{\mathrm{a}}}{293}\right)\left(\frac{1+101/293}{1+101/T_{\mathrm{a}}}\right) . \tag{B5}$$

The air dynamic viscosity is calculated by

$$\eta = \eta_r \left(\frac{T_r + S_u}{T_{\mathrm{a}} + S_u}\right)\left(\frac{T_{\mathrm{a}}}{T_r}\right)^{3/2} \tag{B6}$$

5 (Kulkarni et al., 2011), where the reference viscosity η_r is 18.33×10^{-6} Pa s and the Sutherland interpolation constant S_u is 110.4 K at the reference temperature T_r of 293 K.

The particle stopping distance S_{p} for droplet or particle Reynolds numbers Re_{p} in the range of 1 to 400 is calculated with the correlation obtained by Mercer (1973):

$$S_{\mathrm{p}} = \frac{\rho_{\mathrm{p}} d_{\mathrm{p}}}{\rho_{\mathrm{a}}}\left(Re_{\mathrm{p}}^{1/3} - \sqrt{6}\,\mathrm{atan}\left(\frac{Re_{\mathrm{p}}^{2/3}}{\sqrt{6}}\right)\right) . \tag{B7}$$

10 Appendix C: Summary of input uncertainties

Table C1 summarizes individual uncertainty contributions to the overall instrument CWC measurement uncertainty.

Appendix D: Hygrometer uncertainty

The theoretical background corrected lock-in signal amplitude for a given water vapor mole fraction in air x_w and a parameter set $\boldsymbol{b}$ may be written as $S = f(x_\mathrm{w}, \boldsymbol{b})$ (Lang et al., 2020). To determine the parameters in the calibration function with the least-squares method (Eq. (2)) while considering the calibration humidity uncertainty $u(x_{\mathrm{w},i})$, the inverse function $x_\mathrm{w} = f^{\text{-}1}(S, \boldsymbol{b})$ is required. As no closed-form expression for x_w can be found, the water vapor mole fraction is obtained by numerically finding the root of

$$g(S, x_\mathrm{w}, \boldsymbol{b}) = S - f(x_\mathrm{w}, \boldsymbol{b}) \tag{D1}$$

for a measured signal amplitude and a given set of parameters:

$$x_\mathrm{w} = f^{\text{-}1}(S, \boldsymbol{b}) = \{x \,|\, g(S, x, \boldsymbol{b}) = 0\} \ . \tag{D2}$$

The measurement uncertainty of the PA hygrometer $u(x_\mathrm{w})$ is then evaluated from Eq. (D2) by combining the uncertainties of the measurement signal amplitude $u(S)$ and the correlated parameters determined from calibration, following the GUM (Joint Committee for Guides in Metrology, 2008a):

$$\begin{aligned} u^2(x_\mathrm{w}) = & \left(\frac{\partial f^{\text{-}1}}{\partial S}\right)^2 u^2(S) \\ & + \sum_{i=1}^{5}\sum_{j=1}^{5} \frac{\partial f^{\text{-}1}}{\partial b_i}\frac{\partial f^{\text{-}1}}{\partial b_j} u(b_i, b_j) \ , \end{aligned} \tag{D3}$$

where $u(b_i, b_j)$ is the covariance of the fit parameters b_i and b_j. $u(b_i, b_i) = u^2(b_i)$ is the variance of coefficient b_i.

The uncertainty in the measured signal amplitude is estimated from the Allan deviation analysis and is taken equivalent to the signal noise at the measurement integration time of 1 s.

The sensitivity coefficients in Eq. (D3), i.e., the partial derivatives of $f^{\text{-}1}$ with respect to the PA signal amplitude and the calibration function parameters, are calculated from Eqs. (D1) and (D2) by using standard rules of calculus (Lira, 2002):

$$\frac{\partial f^{\text{-}1}}{\partial S} = -\frac{\partial g/\partial S}{\partial g/\partial x_\mathrm{w}} = \frac{1}{\partial f/\partial x_\mathrm{w}} \ , \tag{D4}$$

$$\frac{\partial f^{\text{-}1}}{\partial b_i} = -\frac{\partial g/\partial b_i}{\partial g/\partial x_\mathrm{w}} = -\frac{\partial f/\partial b_i}{\partial f/\partial x_\mathrm{w}} \ . \tag{D5}$$

Errors introduced by finding the root in Eq. (D2) are assumed negligible, due to the high accuracy of the numerical solver with the chosen tolerance level.

Appendix E: Numerical CWC uncertainty evaluation

Figure E1 shows the comparison of the 95 % coverage intervals of the CWC measurement uncertainty calculated with the first-order analytical and the Monte Carlo method for an IWT static air temperature of −30 °C and an airspeed of $60\,\mathrm{m\,s^{-1}}$.

https://doi.org/10.5194/amt-2020-295
Preprint. Discussion started: 8 September 2020

Atmospheric Measurement Techniques
Discussions

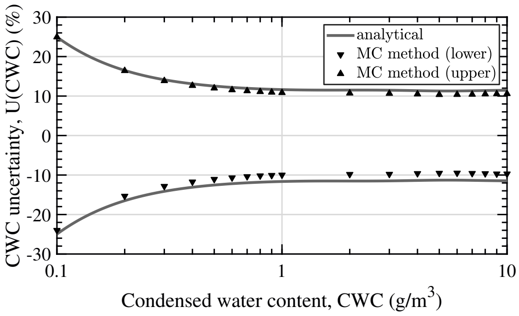

Figure E1. 95 % coverage intervals of the CWC measurement uncertainty calculated with the first-order analytical and the Monte Carlo (MC) method. Uncertainties are given relative to the actual CWC. Icing wind tunnel static air temperature, pressure and airspeed are set to $-30\,^\circ\mathrm{C}$, $1013.25\,\mathrm{hPa}$ and $60\,\mathrm{m\,s^{-1}}$, respectively, and the ambient air is assumed fully saturated with respect to supercooled liquid water. Monte Carlo intervals are shortest (non-symmetric) 95 % intervals indicated by the lower and upper bounds.

Uncertainties are given relative to the actual CWC. Shortest intervals obtained by the Monte Carlo method can be seen to lie within the analytical intervals over the whole CWC range of interest.

Author contributions. Conceptualization: B. Lang, W. Breitfuss, W. Hassler, A. Bergmann; Methodology and investigation: B. Lang, P. Breitegger, W. Breitfuss, A. Tramposch, H. Pervier; Software and material preparation: B. Lang, W. Breitfuss, S. Schweighart, H. Pervier; Writing - original draft preparation: B. Lang; Writing - review and editing: all authors; Funding acquisition: A. Tramposch, A. Bergmann, W. Hassler; Resources: A. Bergmann, A. Klug, W. Hassler; Supervision: A. Bergmann, W. Hassler; Project administration: A. Bergmann, A. Klug, W. Hassler.

Competing interests. The authors declare that they have no conflict of interest.

Acknowledgements. This work has been partly funded by the Austrian Aeronautics Programme TAKE OFF of the Federal Ministry of Transport, Innovation and Technology (BMVIT), managed by the FFG (Project number: 850457).

https://doi.org/10.5194/amt-2020-295
Preprint. Discussion started: 8 September 2020

References

Allen, M. D. and Raabe, O. G.: Slip correction measurements of spherical solid aerosol particles in an improved millikan apparatus, Aerosol Science and Technology, 4, 269–286, https://doi.org/10.1080/02786828508959055, 1985.

Bansmer, S. E., Baumert, A., Sattler, S., Knop, I., Leroy, D., Schwarzenboeck, A., Jurkat-Witschas, T., Voigt, C., Pervier, H., and Esposito, B.: Design, construction and commissioning of the Braunschweig Icing Wind Tunnel, Atmospheric Measurement Techniques, 11, 3221–3249, https://doi.org/10.5194/amt-11-3221-2018, 2018.

Bell, I. H., Wronski, J., Quoilin, S., and Lemort, V.: Pure and pseudo-pure fluid thermophysical property evaluation and the open-source thermophysical property library coolprop, Industrial and Engineering Chemistry Research, 53, 2498–2508, https://doi.org/10.1021/ie4033999, 2014.

Belyaev, S. P. and Levin, L. M.: Techniques for collection of representative aerosol samples, Journal of Aerosol Science, 5, 325–338, https://doi.org/10.1016/0021-8502(74)90130-X, 1974.

Bernstein, B. C., Ratvasky, T. P., Miller, D. R., and McDonough, F.: Freezing Rain as an In-Flight Icing Hazard, Nasa, 2000.

Breitegger, P. and Bergmann, A.: A Precise Gas Dilutor Based on Binary Weighted Critical Flows to Create NO2 Concentrations, Proceedings, 2, 998, https://doi.org/10.3390/proceedings2130998, 2018.

Breitfuss, W., Wannemacher, M., Knöbl, F., and Ferschitz, H.: Aerodynamic Comparison of Freezing Rain and Freezing Drizzle Conditions at the RTA Icing Wind Tunnel, SAE Technical Papers, 2019-June, 245–255, https://doi.org/10.4271/2019-01-2023, 2019.

Chalmers, J., Davison, C., Macleod, J., Neuteboom, M., and Fuleki, D.: Icing Test and Measurement Capabilities of the NRC's Gas Turbine Laboratory, in: SAE Technical Papers, pp. 2019–01–1943, SAE International, https://doi.org/10.4271/2019-01-1943, 2019.

Cober, S., Bernstein, B., Jeck, R., Hill, E., Isaac, G., Riley, J., and Shah, A.: Data and Analysis for the Development of an Engineering Standard for Supercooled Large Drop Conditions, Tech. Rep. March, U.S. Department of Transportation, Federal Aviation Administration, 2009.

Cober, S. G., Isaac, G. A., Korolev, A. V., and Strapp, J. W.: Assessing cloud-phase conditions, Journal of Applied Meteorology, 40, 1967–1983, https://doi.org/10.1175/1520-0450(2001)040<1967:ACPC>2.0.CO;2, 2001a.

Cober, S. G., Isaac, G. A., and Strapp, J. W.: Characterizations of aircraft icing environments that include supercooled large drops, Journal of Applied Meteorology, 40, 1984–2002, https://doi.org/10.1175/1520-0450(2001)040<1984:COAIET>2.0.CO;2, 2001b.

Davis, S. M., Hallar, A. G., Avallone, L. M., and Engblom, W.: Measurement of total water with a tunable diode laser hygrometer: Inlet analysis, calibration procedure, and ice water content determination, Journal of Atmospheric and Oceanic Technology, 24, 463–475, https://doi.org/10.1175/JTECH1975.1, 2007.

Davison, C., MacLeod, J. D., Strapp, J. W., and Buttsworth, D. R.: Isokinetic total water content probe in a naturally aspirating configuration: Initial aerodynamic design and testing, in: 46th AIAA Aerospace Sciences Meeting and Exhibit, January, 2008.

Davison, C. R., Walter Strapp, J., Lilie, L., Ratvasky, T. P., and Dumont, C.: Isokinetic TWC evaporator probe: Calculations and systemic uncertainty analysis, in: 8th AIAA Atmospheric and Space Environments Conference, https://doi.org/10.2514/6.2016-4060, 2016.

Dorsi, S. W., Kalnajs, L. E., Toohey, D. W., and Avallone, L. M.: A fiber-coupled laser hygrometer for airborne total water measurement, Atmospheric Measurement Techniques, 7, 215–223, https://doi.org/10.5194/amt-7-215-2014, 2014.

EASA CS-25: Certification Specifications and Acceptable Means of Compliance for Large Aeroplanes CS-25, Tech. rep., European Aviation Safety Agency, 2020.

https://doi.org/10.5194/amt-2020-295
Preprint. Discussion started: 8 September 2020

Atmospheric Measurement Techniques
Discussions

Emery, E. F., Miller, D. R., Plaskon, S. R., Strapp, W., and Lillie, L.: Ice particle impact on cloud water content instrumentation, in: AIAA Paper, March, pp. 8387–8398, https://doi.org/10.2514/6.2004-731, 2004.

FAA CFR-25: US Code of Federal Regulations - Title 14 Part 25, Airworthiness Standards - Transport Category Airplanes, 2019.

Gent, R. W., Dart, N. P., and Cansdale, J. T.: Aircraft icing, Philosophical Transactions of the Royal Society A: Mathematical, Physical and Engineering Sciences, 358, 2873–2911, https://doi.org/10.1098/rsta.2000.0689, 2000.

Giacomo, P.: Equation for the determination of the density of moist air (1981), Metrologia, 18, 33–40, https://doi.org/10.1088/0026-1394/18/1/006, 1982.

Gordon, I. E., Rothman, L. S., Hill, C., Kochanov, R. V., Tan, Y., Bernath, P. F., Birk, M., Boudon, V., Campargue, A., Chance, K. V., Drouin, B. J., Flaud, J. M., Gamache, R. R., Hodges, J. T., Jacquemart, D., Perevalov, V. I., Perrin, A., Shine, K. P., Smith, M. A., Tennyson, J., Toon, G. C., Tran, H., Tyuterev, V. G., Barbe, A., Császár, A. G., Devi, V. M., Furtenbacher, T., Harrison, J. J., Hartmann, J. M., Jolly, A., Johnson, T. J., Karman, T., Kleiner, I., Kyuberis, A. A., Loos, J., Lyulin, O. M., Massie, S. T., Mikhailenko, S. N., Moazzen-Ahmadi, N., Müller, H. S., Naumenko, O. V., Nikitin, A. V., Polyansky, O. L., Rey, M., Rotger, M., Sharpe, S. W., Sung, K., Starikova, E., Tashkun, S. A., Auwera, J. V., Wagner, G., Wilzewski, J., Wcisło, P., Yu, S., and Zak, E. J.: The HITRAN2016 molecular spectroscopic database, Journal of Quantitative Spectroscopy and Radiative Transfer, 203, 3–69, https://doi.org/10.1016/j.jqsrt.2017.06.038, 2017.

Greenspan, L.: Functional equations for the enhancement factors for CO2-free moist air, Journal of Research of the National Bureau of Standards Section A: Physics and Chemistry, 80A, 41, https://doi.org/10.6028/jres.080a.007, 1976.

Hardy, J. E., Hylton, J. O., and Mcknight, T. E.: Empirical correlations for thermal flowmeters covering a wide range of thermal-physical properties, in: National Conference of Standards Labs, 1999.

Hare, D. E. and Sorensen, C. M.: The density of supercooled water. II. Bulk samples cooled to the homogeneous nucleation limit, The Journal of Chemical Physics, 87, 4840–4845, https://doi.org/10.1063/1.453710, 1987.

Hodgkinson, J. and Tatam, R. P.: Optical gas sensing: a review, Measurement Science and Technology, 24, 012 004, https://doi.org/10.1088/0957-0233/24/1/012004, 2013.

Isaac, G. A., Korolev, A. V., Strapp, J. W., Cober, S. G., Boudala, F. S., Marcotte, D., and Reich, V. L.: Assessing the collection efficiency of natural cloud particles impacting the Nevzorov total water content probe, in: Collection of Technical Papers - 44th AIAA Aerospace Sciences Meeting, pp. 14 846–14 858, https://doi.org/10.2514/6.2006-1221, 2006.

Joint Committee for Guides in Metrology: Evaluation of measurement data — Guide to the expression of uncertainty in measurement, 2008a.

Joint Committee for Guides in Metrology: Evaluation of measurement data — Supplement 1 to the Guide to the expression of uncertainty in measurement — Propagation of distributions using a Monte Carlo method, 2008b.

Korolev, A., Strapp, J. W., Isaac, G. A., and Emery, E.: Improved airborne hot-wire measurements of ice water content in clouds, Journal of Atmospheric and Oceanic Technology, 30, 2121–2131, https://doi.org/10.1175/JTECH-D-13-00007.1, 2013.

Krämer, M. and Afchine, A.: Sampling characteristics of inlets operated at low U/U0 ratios: New insights from computational fluid dynamics (CFX) modeling, Journal of Aerosol Science, 35, 683–694, https://doi.org/10.1016/j.jaerosci.2003.11.011, 2004.

Kulkarni, P., Baron, P. A., and Willeke, K.: Aerosol measurement: principles, techniques, and applications, John Wiley \& Sons, third edn., 2011.

Lang, B., Breitegger, P., Brunnhofer, G., Prats Valero, J., Schweighart, S., Klug, A., Hassler, W., and Bergmann, A.: Molecular relaxation effects on vibrational water vapor photoacoustic spectroscopy in air, Applied Physics B: Lasers and Optics, 126, 1–18, https://doi.org/10.1007/s00340-020-7409-3, https://link.springer.com/article/10.1007/s00340-020-7409-3, 2020.

Langridge, J. M., Richardson, M. S., Lack, D. A., Brock, C. A., and Murphy, D. M.: Limitations of the photoacoustic technique for aerosol absorption measurement at high relative humidity, Aerosol Science and Technology, 47, 1163–1173, https://doi.org/10.1080/02786826.2013.827324, 2013.

LI-COR Inc.: Using the LI-830 and LI-850 Gas Analyzers, Tech. rep., LI-COR Inc., https://www.licor.com/documents/gz8gaf0ls5vhvpl52xtmyr8mfoh5kwe8, 2020.

Lira, I.: Evaluating the Measurement Uncertainty, IOP Publishing Ltd, https://doi.org/10.1887/0750308400, http://stacks.iop.org/0750308400, 2002.

Mason, J. G., Strapp, J. W., and Chow, P.: The ice particle threat to engines in flight, in: Collection of Technical Papers - 44th AIAA Aerospace Sciences Meeting, vol. 4, pp. 2445–2465, 2006.

Mercer, T. T.: Aerosol technology in hazard evaluation, ACADEMIC PRESS, 394 p., 394, https://doi.org/10.1016/0021-9797(74)90320-8, 1973.

Meyer, C. W., Hodges, J. T., Huang, P. H., Miller, W. W., Ripple, D. C., Scace, G. E., Gutierrez, C. M., and Gallagher, P.: Calibration of Hygrometers with the Hybrid Humidity Generator, NIST Special Publication, 250, https://doi.org/10.6028/NIST.SP.250-83, 2008.

Orchard, D. M., Szilder, K., and Davison, C. R.: Design of an icing wind tunnel contraction for supercooled large drop conditions, in: 2018 Atmospheric and Space Environments Conference, https://doi.org/10.2514/6.2018-3185, 2018.

Orchard, D. M., Clark, C., and Chevrette, G.: Measurement of Liquid Water Content for Supercooled Large Drop Conditions in the NRC's Altitude Icing Wind Tunnel, in: SAE Technical Papers, pp. 2019–01–2007, https://doi.org/10.4271/2019-01-2007, 2019.

Politovich, M. K.: Aircraft icing caused by large supercooled droplets, Journal of Applied Meteorology, 28, 856–868, https://doi.org/10.1175/1520-0450(1989)028<0856:AICBLS>2.0.CO;2, 1989.

Rader, D. J.: Momentum slip correction factor for small particles in nine common gases, Journal of Aerosol Science, 21, 161–168, https://doi.org/10.1016/0021-8502(90)90001-E, 1990.

Rader, D. J. and Marple, V. A.: A study of the effects of anisokinetic sampling, Aerosol Science and Technology, 8, 283–299, https://doi.org/10.1080/02786828808959190, 1988.

Ratvasky, T., Harrah, S., Strapp, J. W., Lilie, L., Proctor, F., Strickland, J., Hunt, P., Bedka, K., Diskin, G., Nowak, J. B., Bui, T. P., Bansemer, A., and Dumont, C.: Summary of the High Ice Water Content (HIWC) RADAR Flight Campaigns, in: SAE Technical Papers, pp. 2019–01–2027, https://doi.org/10.4271/2019-01-2027, 2019.

Riley, J. T.: Mixed-Phase Icing Conditions: A Review, Tech. rep., FAA, 1998.

SAE AIR-6341: SLD capabilities of icing wind tunnels (Work in progress), SAE International, https://www.sae.org/standards/content/air6341/, 2015.

SAE ARP-5905: Calibration and Acceptance of Icing Wind Tunnels, SAE International, 2015.

Selamet, A. and Radavich, P. M.: The effect of length on the acoustic attenuation performance of concentric expansion chambers: An analytical, computational and experimental investigation, Journal of Sound and Vibration, 201, 407–426, https://doi.org/10.1006/jsvi.1996.0720, 1997.

Steen, L.-C. E., Ide, R. F., and Van Zante, J. F.: An assessment of the icing blade and the SEA multi-element sensor for liquid water content calibration of the NASA GRC icing research tunnel, in: 8th AIAA Atmospheric and Space Environments Conference, https://doi.org/10.2514/6.2016-4051, 2016.

https://doi.org/10.5194/amt-2020-295
Preprint. Discussion started: 8 September 2020

Strapp, J., Lilie, L. E., Ratvasky, T. P., Davison, C., and Dumont, C.: Isokinetic TWC evaporator probe: Development of the IKP2 and performance testing for the HAIC-HIWC darwin 2014 and cayenne-2015 field campaigns, in: 8th AIAA Atmospheric and Space Environments Conference, pp. 1–28, https://doi.org/10.2514/6.2016-4059, 2016.

Strapp, J. W., Oldenburg, J., Ide, R., Lilie, L., Bacic, S., Vukovic, Z., Oleskiw, M., Miller, D., Emery, E., and Leone, G.: Wind tunnel measurements of the response of hot-wire liquid water content instruments to large droplets, Journal of Atmospheric and Oceanic Technology, 20, 791–806, https://doi.org/10.1175/1520-0426(2003)020<0791:WTMOTR>2.0.CO;2, 2003.

Szakáll, M., Bozóki, Z., Kraemer, M., Spelten, N., Moehler, O., and Schurath, U.: Evaluation of a photoacoustic detector for water vapor measurements under simulated tropospheric/lower stratospheric conditions, Environmental Science and Technology, 35, 4881–4885, https://doi.org/10.1021/es015564x, 2001.

Szakáll, M., Varga, A., Pogány, A., Bozóki, Z., and Szabó, G.: Novel resonance profiling and tracking method for photoacoustic measurements, Applied Physics B: Lasers and Optics, 94, 691–698, https://doi.org/10.1007/s00340-009-3391-5, 2009.

Tátrai, D., Bozóki, Z., Smit, H., Rolf, C., Spelten, N., Krämer, M., Filges, A., Gerbig, C., Gulyás, G., and Szabó, G.: Dual-channel photoacoustic hygrometer for airborne measurements: Background, calibration, laboratory and in-flight intercomparison tests, Atmospheric Measurement Techniques, 8, 33–42, https://doi.org/10.5194/amt-8-33-2015, 2015.

Van Zante, J. F., Ratvasky, T. P., Bencic, T. J., Challis, C. C., Timko, E. N., and Woike, M. R.: Update on the nasa glenn propulsion systems lab icing and ice crystal cloud characterization (2017), in: 2018 Atmospheric and Space Environments Conference, pp. 77–83, https://doi.org/10.2514/6.2018-3969, 2018.

Vukits, T. J.: Overview and risk assessment of icing for transport category aircraft and components, in: 40th AIAA Aerospace Sciences Meeting and Exhibit, January 2002, https://doi.org/10.2514/6.2002-811, 2002.

Wagner, W. and Pruss, A.: International Equations for the Saturation Properties of Ordinary Water Substance. Revised According to the International Temperature Scale of 1990. Addendum to J. Phys. Chem. Ref. Data 16, 893 (1987), Journal of Physical and Chemical Reference Data, 22, 783–787, https://doi.org/10.1063/1.555926, http://aip.scitation.org/doi/10.1063/1.555926, 1993.

Werle, P., Mücke, R., and Slemr, F.: The limits of signal averaging in atmospheric trace-gas monitoring by tunable diode-laser absorption spectroscopy (TDLAS), Applied Physics B Photophysics and Laser Chemistry, 57, 131–139, https://doi.org/10.1007/BF00425997, 1993.

Wernecke, J. and Wernecke, R.: Industrial Moisture and Humidity Measurement: A Practical Guide, Wiley-VCH, 2013.

Wieser, M. E. and Berglund, M.: Atomic weights of the elements 2007 (IUPAC technical report), in: Pure and Applied Chemistry, pp. 2131–2156, https://doi.org/10.1351/PAC-REP-09-08-03, 2009.

Willeke, K.: Temperature dependence of particle slip in a gaseous medium, Journal of Aerosol Science, 7, 381–387, https://doi.org/10.1016/0021-8502(76)90024-0, 1976.

Zuckerwar, A. J.: Handbook of the Speed of Sound in Real Gases, Academic Press, Inc, 2002.

PAPER III. INTENSITY MODULATED PHOTOTHERMAL MEASUREMENTS OF NO_2 WITH A COMPACT FIBER-COUPLED FABRY–PÉROT INTERFEROMETER

Author contributions: The author of this thesis contributed in the conceptualization of the PT sensor, the design of the gas cell, the experimental investigation and data evaluation. The author contributed to the original draft and the revisions of the manuscript.

Publication status: This article is an accepted and published version of [3]: Breitegger, P., Lang, B. and Bergmann, A.: Intensity Modulated Photothermal Measurements of NO2 with a Compact Fiber-Coupled Fabry–Pérot Interferometer, Sensors, 19(15), 3341, doi.org/10.3390/s19153341, 2019.

sensors MDPI

Article

Intensity Modulated Photothermal Measurements of NO_2 with a Compact Fiber-Coupled Fabry–Pérot Interferometer

Philipp Breitegger *, Benjamin Lang and Alexander Bergmann

Institute of Electronic Sensor Systems, Graz University of Technology, Graz 8010, Austria
* Correspondence: p.breitegger@tugraz.at; Tel.: +43-316-873-3344

Received: 27 June 2019; Accepted: 27 July 2019; Published: 30 July 2019

Abstract: Sensors for the reliable measurement of nitrogen dioxide concentrations are of high interest due the adverse health effects of this pollutant. This work employs photothermal spectroscopy to measure nitrogen dioxide concentrations at the parts per billion level. Absorption induced temperature changes are detected by means of a fiber-coupled Fabry–Pérot interferometer. The small size of the interferometer enables small detection volumes, paving the way for miniaturized sensing concepts as well as fast response times, demonstrated down to 3 s. A normalized noise equivalent absorption of $7.5 \times 10^{-8}\,\mathrm{cm^{-1}W/\sqrt{Hz}}$ is achieved. Additionally, due to the rigid structure of the interferometer, the sensitivity to mechanical vibrations is shown to be minor.

Keywords: nitrogen dioxide; photothermal interferometry; gas sensor; optical microphone

1. Introduction

Due to the adverse health effects of NO_2 [1], monitoring ambient NO_2 concentrations as well as NO_2 emissions from vehicles is of interest for citizens, researchers, and legislative purposes [2–5]. WHO recommends an hourly mean of $200\,\mathrm{\mu g\,m^{-3}}$ (106.4 ppb) and an annual mean of $40\,\mathrm{\mu g\,m^{-3}}$ (21.3 ppb) not to be exceeded [1]. A variety of sensing principles exist for the sensing of NO_2. For example, electrochemical and metal oxide sensors are low-cost, but lack sensitivity, selectivity, and long-term stability [6]. On the other hand, chemiluminescence detectors are expensive and large in size, but offer reliable measurements and are commonly used to measure NO_2 concentrations for legislative purposes [5]. Further, optical sensors exist, which provide high spectral selectivity by choosing a light source that matches one or more absorption bands of NO_2. Among those are photoacoustic and photothermal sensing concepts.

Photoacoustic spectroscopy uses intensity or wavelength modulated light sources, which match one ore more absorption bands of the gas of interest, exciting transitions into higher molecular energy levels. Subsequent collisional deactivation leads to the production of a fast decaying thermal and a propagating, slowly decaying acoustic wave [7]. The detection of the acoustic wave, usually after acoustically resonant amplification, is utilized in photoacoustic spectroscopy [8–10] and quartz-enhanced photoacoustic spectroscopy [11–14].

This work focuses on an interferometric detection scheme, where the temperature change is measured by a refractive index change, induced by the absorption-based heating. As an excitation source, we use an intensity modulated 450 nm laser. The generated refractive index change is measured by means of a fiber-coupled Fabry–Pérot interferometer as the sensing element. Previous publications have demonstrated noise equivalent absorptions of $1.3 \times 10^{-7}\,\mathrm{cm^{-1}W/\sqrt{Hz}}$ with intensity modulation for NO_2 (equal to 700 ppb for 30 mW average laser power) [15] and $1.8 \times 10^{-6}\,\mathrm{cm^{-1}W/\sqrt{Hz}}$ [16] or $7.5 \times 10^{-9}\,\mathrm{cm^{-1}W/\sqrt{Hz}}$ [17], with wavelength modulation for detection of SO_2. Similar normalized noise equivalent absorptions (NNEAs) can be achieved with microstructured hollow-core fibers in combination with photothermal interferometry [18,19]. The response of hollow-core fiber gas sensors, however, is diffusion limited and response times for long, high-sensitivity fibers are usually limited to several tens of seconds [18,20]. Exceptions with response times down to 3 s and detection limits of $7.4 \times 10^{-5}\,\mathrm{cm}^{-1}$ for methane have been reported for short fibers [18,21], but lacking statements about the laser power coupled into the fiber prohibit a comparison to other methods.

In this work, we demonstrate sensing of NO_2 by photothermal interferometry, utilizing a membrane-free optical microphone as interferometer. The $1\,\sigma$ detection limit for 1 s integration time is 348 ppb, equal to a normalized noise equivalent absorption of $7.5 \times 10^{-8}\,\mathrm{cm}^{-1}\mathrm{W}/\sqrt{\mathrm{Hz}}$. The work is meant to demonstrate the advantages of photothermal interferometry for NO_2, such as miniaturization potential of the sensing volume, fast response times, and a robust setup.

2. Materials and Methods

2.1. Photothermal Interferometry

In this work, photothermal interferometry (PTI) is realized with a fiber-coupled Fabry–Pérot interferometer (FPI). Intensity modulation of the 450 nm excitation laser produces a thermal wave, with a temperature change directly proportional to the concentration of NO_2 [22]. The thermal wave is heavily damped, and is therefore only observed close to the probe beam [7]. The local heating leads to a change in refractive index Δn, described by the Clausius–Mosotti equation [22], with ΔT temperature rise and T_{abs} absolute temperature of the gas:

$$\Delta n = -(n-1)\frac{\Delta T}{T_{abs}}. \tag{1}$$

Due to the constant gas flow through the cell, incremental heating of the gas sample due to the excitation laser can be neglected and constant absolute temperature of the gas can be assumed in our experiments. Hence, the detected change in refractive index is directly proportional to the NO_2 concentration within the FPI cavity.

The FPI used for this work measures the intensity of the reflected probe laser. The reflected intensity I_r is given by [23]

$$I_r = I_i\left(1 - \frac{1}{1 + F\sin^2(\delta/2)}\right), \tag{2}$$

where I_i is the incident intensity and F is the finesse of the mirrors. The phase shift δ depends on the refractive index in the cavity n, the distance between the mirrors d, and the wavelength λ as

$$\delta = \frac{4\pi n d}{\lambda}. \tag{3}$$

Changes in n change the phase shift δ and, thus, the reflected intensity I_r.

2.2. Experimental Setup

For this work, a commercial optical microphone was used as detector, which consists of a fiber-coupled FPI cavity, machined as a rigid structure, which offers low sensitivity to mechanical vibrations [24]. The FPI is formed by a machined opening with semitransparent mirror surfaces, each approximately 1.5 mm × 1.5 mm in size, which are facing parallel to each other at a distance of approximately 3.3 mm. A 1550 nm probe laser of 1 mW optical power is reflected back and forth between the mirrors, and the reflected intensity is measured [24]. The probe laser is of approximately Gaussian shape, with 205 µm full width at half maximum within the cavity, and the reflectivity of the etalon mirrors is in the range of 0.6 [25]. The commercial microphone head comes with protective membranes covering the cavity, which were removed to allow for a free gas exchange and an overlap of the probe and excitation beams (cf. Figure 1).

The optical microphone is placed in a 3D-printed cell with a sample volume smaller than 9 cm^3 (Figure 1). The cell was optimized with multiphysical simulations to suppress unwanted acoustic resonances. The beam of the excitation laser (blue) is focused through a window and horizontally centered to cross the probe laser of the optical microphone at the position of maximum intensity. A neutral density (ND) filter is mounted opposite the window to attenuate the excitation beam. A 40 mW continuous-wave optical power laser module (Laser Components GmbH, Olching, Germany: FLEXPOINT® Dot Laser Module) with 450 nm wavelength serves as excitation laser. At this wavelength, NO_2 yields high absorption with little cross-sensitivity to other gases. Also, this wavelength is above the photodissociation threshold [26].

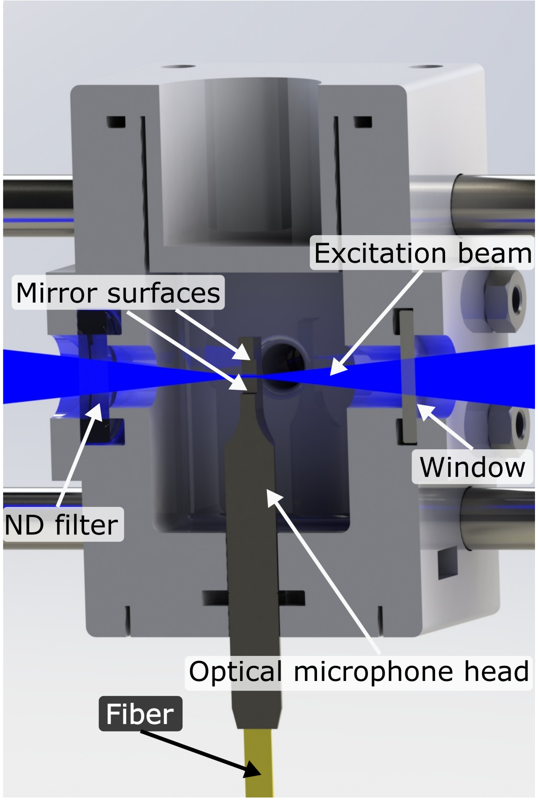

Figure 1. Cut through the 3D-printed cell, carrying the head of the optical microphone. Excitation laser beam is shown in blue. The probe beam is reflected within the microphone cavity between the top and bottom mirror surfaces.

The experimental setup allows to study the sensor response for different concentrations of NO_2, flow rates, and modulation frequencies. This is shown in Figure 2. Gas mixtures were produced with a temperature stabilized custom gas diluter based on binary weighted critical orifices [27], which offer low uncertainties over a broad range of dilution ratios. The NO_2 gas cylinder contains a mixture of NO_2 and synthetic air (Messer Austria GmbH, Gumpoldskirchen, Austria: 19.2 ppm NO_2), which was further diluted with synthetic air (Messer Austria GmbH: Synthetic Air, Scientific). The flow rate to the PTI cell is controlled by a mass flow controller (MFC; Vögtlin, Aesch, Switzerland: Model GSC-B).

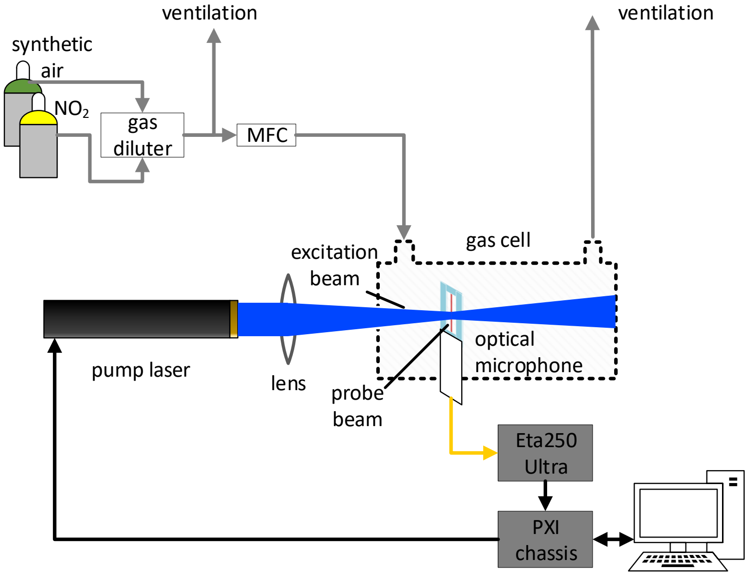

Figure 2. Schematic of the experimental setup for characterizing the photothermal interferometry setup with NO_2. Gas mixtures are created with a gas diluter. The excitation beam is perpendicular to the probe beam and is focused and centered into the cavity of the optical microphone.

The signal from the optical microphone control unit (XARION Laser Acoustics GmbH, Vienna, Austria: Eta 250 Ultra—settings: Cutoff frequency 100 Hz, gain 20 dB) is recorded with a data acquisition card (National Instruments, Austin, TX, United States: Model PXI-6281) at 250 ksps and post-processed on a personal computer (PC). The same chassis carrying the PXI-6281 also houses a function generator (National Instruments: Model PXI-5402). The function generator provides the square-wave modulation signal (duty cycle 50%) for the excitation laser. The PTI signal is filtered with a digital lock-in amplifier, realized in LabVIEW code on a PC, with an integration time of 1 s. Due to the high sampling rate and limited buffer size of the DAQ card, data acquisition and modulation is stopped and restarted after each measurement to obtain a constant phase relation.

To investigate the sensitivity of the FPI and the signal to mechanical vibrations, the sensor was mounted on a platform connected to an electrodynamic shaker (TIRA GmbH, Schalkau, Germany: TIRAvib S502). Applied vertical accelerations and vibration spectral densities were measured with a piezoelectric accelerometer (PCB Piezotronics Inc., Depew, NY, United States: 333B30) placed next to the cell mounting, as shown in Figure 3. In this configuration the operating sensor was exposed to two different broadband quasi-random vibration distributions over the frequency range of 1 Hz to 500 Hz—characteristic for highway truck vibration exposure [28]—to test mobile operation of the PTI sensor. The sensor was exposed to the acceleration spectra at different root mean square accelerations for several minutes and signal noise was recorded at multiple points in time. Additionally, the sensor was accelerated sinusoidally and maximum tolerable vertical accelerations (insignificantly increased signal noise) at a range of frequencies between 10 Hz and 300 Hz were determined. Due to the low anticipated effect on the noise level, the interferometer interrogation unit was not exposed to the vibrations.

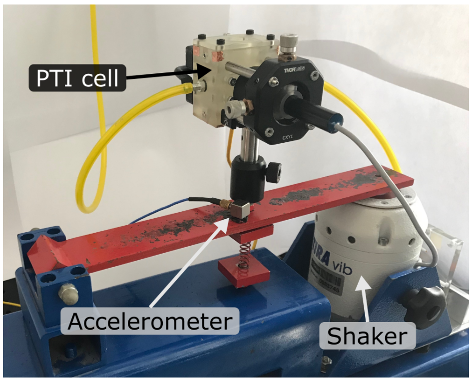

Figure 3. Photograph of the vibration test setup, showing the full photothermal interferometry (PTI) cell with gas lines and laser, mounted on an electrodynamic shaker. The piezoelectric accelerometer, measuring applied accelerations, is placed next to the cell mounting.

3. Results

3.1. Influence of Flow Rate on Sensor Noise

The selection of the flow rate is a balance of response time and detection limit, as higher flow rates offer faster gas exchange rates, but are associated to higher flow noise, which negatively effect the detection limit. Figure 4 shows the noise spectrum of the flow noise, measured by the optical microphone without the excitation laser being switched on. The noise spectrum was calculated as the Welch power spectral density estimate with a 0.5 s Hanning window. The flow rate was varied between 0.2 slpm and 4 slpm. Only a slight increase in noise is seen up to flow rates of 1 slpm, but higher flow rates significantly increase present $1/f^{\alpha}$ noise [29] and are accompanied by flow-rate-dependent tonal noise.

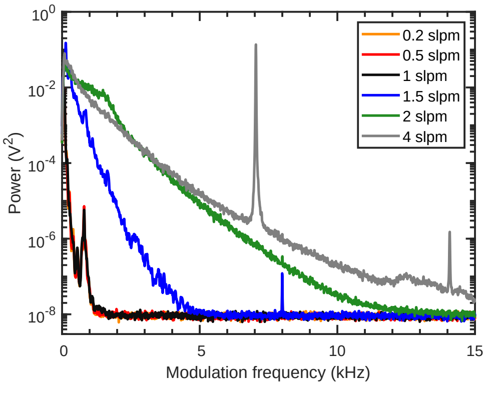

Figure 4. Welch spectra of the background noise without excitation laser at different flow rates. Welch spectra are calculated over 0.1 s windows and averaged over 9 s. The noise spectra of 0.2 slpm and 0.5 slpm are identical and covered by the spectrum at 1 slpm.

Due to the small cell volume of less than 9 cm^3, a flow rate of 0.5 slpm with a nominal gas exchange rate of ≈1 s/cell volume was considered sufficient with a 1 s integration time, and was used in the subsequent measurements.

3.2. Selection of the Optimal Modulation Frequency

From Figure 4, the additional presence of flow-rate-independent noise around 800 Hz is visible, and a higher modulation frequency should be chosen. However, as the photothermal signal is inversely proportional to the modulation frequency [22], a low modulation frequency is desired. Therefore, the signal with 19.2 ppm NO_2 (black circles) and the background noise with synthetic air (blue diamonds) was recorded with the lock-in amplifier for different modulation frequencies (Figure 5a). The inverse signal strength of the photothermal signal can nicely be seen (black circles). To find the optimal modulation frequency, the signal-to-noise ratio (SNR) was calculated (black dots in Figure 5b). Due to the variation in the calculated SNR values, a moving average filter was applied (blue curve) and a modulation frequency of 1.4 kHz, in the region where best results were achieved, was selected.

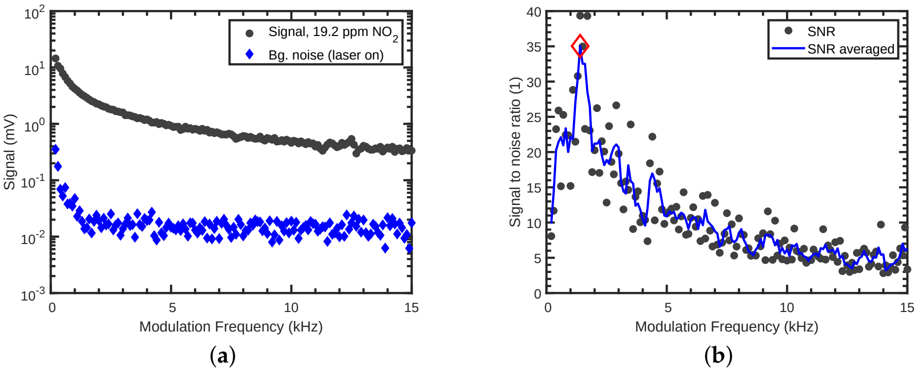

Figure 5. Noise investigations of the PTI sensor: (**a**) Signal with 19.2 ppm NO_2 (black circles), background noise for different modulation frequencies with the laser switched on (blue diamonds), measured with lock-in amplifier. Background noise with the laser switched off equals the noise with the modulated laser switched on. (**b**) Signal-to-noise ratio as a function of the modulation frequency. The selected modulation frequency is marked with a red diamond.

3.3. Limit of Detection and Long Term Stability

The linearity of the PTI sensor was confirmed by applying concentrations ranging from 606 ppb to 19.2 ppm NO_2 to the sensor. The PTI signal, as a function of applied NO_2 concentration, is shown in Figure 6. Each data point was averaged for approximately 40 values, i.e., 40 s. All signals are background-corrected with respect to their phase. The sensitivity was determined to be $(0.149 \pm 0.002)\,\mathrm{mV\,ppm^{-1}}$ from a weighted linear regression. The coefficient of determination for the fit is $R^2 = 0.999$.

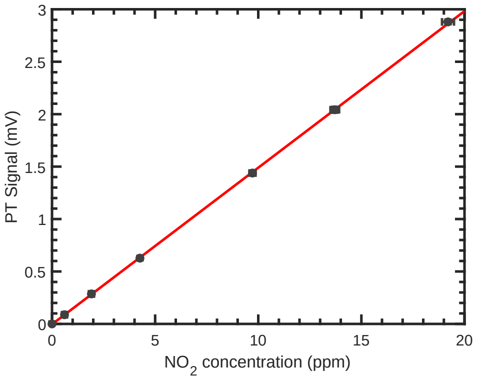

Figure 6. Linear fit (red) of the background-corrected photothermal signal as a function of the NO_2 concentration. Error bars of the photothermal signals are the standard deviation relative to the mean. Error bars of the concentrations are too small to be visible on this scale.

Long-term stability was investigated by calculating the Allan deviation for the signal at constant flow of synthetic air. The corresponding plot is shown in Figure 7. Even though the sensor was mounted on an optical table without vibration isolation, no interferences from mechanical vibrations were observed, due to the rigid structure of the FPI.

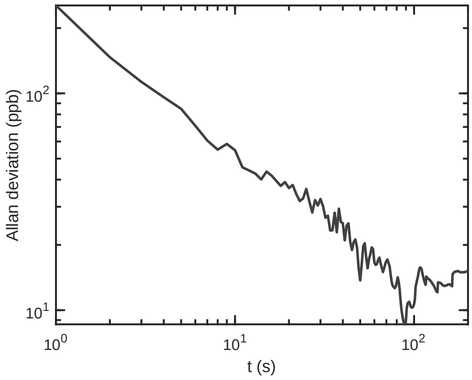

Figure 7. Allan deviation of the photothermal signal in units of NO_2 concentration as a function of averaging time. Allan deviation was calculated with MATLAB.

From Figure 7, it can be seen that the 1σ detection limit is 348 ppb for 1 s averaging time. The detection limit can be further improved to 75 ppb (10 s) and 26 ppb (100 s), by using longer averaging times. The increase in standard deviation after approximately 200 s, and the therefore limited maximum integration time, stems from the laser module, which is not temperature stabilized (cf. Appendix A). This, however, could be easily improved by changing to a temperature stabilized laser. The optical microphone itself uses a feedback current to stabilize the wavelength of the probe laser to maintain a steady operating point, i.e., compensating for slow temperature and pressure changes [24].

The normalized noise equivalent absorption was calculated by assuming a Gaussian wavelength distribution around 450 nm with FWHM of 0.5 nm, and using the corresponding absorption coefficient from the HITRAN database [30]. For 1 s integration time of the lock-in amplifier, this corresponds to an NNEA of $7.5 \times 10^{-8}\,\mathrm{cm}^{-1}\mathrm{W}/\sqrt{\mathrm{Hz}}$.

Low sensitivity of the PTI sensor to mechanical vibrations is essential for mobile applications and is usually hard to achieve for interferometric setups. Results of the vibration analysis, however, suggest low sensitivity of the proposed interferometric sensor concept, due to the rigid structure of the FP cavity. Figure 8a shows the applied acceleration spectral densities in the frequency range of interest and, for comparison purposes, a military standard vibration schedule for highway truck vertical vibration exposure, often used for commercial product testing (MIL-STD-810H, Method 514.8C-I [28]). The peak visible at 50 Hz in both spectra is noise at the power line frequency, amplified by the accelerometer amplifier, and has to be disregarded from the acceleration spectrum. Although a strong mechanical resonance of the setup is excited near 150 Hz for vibrations up to 500 Hz (black curve), the measured signal noise level only increases marginally from 30 µV to 40 µV. During application of the low-frequency vibration spectrum with components up to 100 Hz (yellow curve), no changes in the measured noise level were observed and the noise remained at the background level.

Achieved peak accelerations for sinusoidal vibrations are plotted in Figure 8b together with the measured noise. It can be seen that, for frequencies between 20 Hz and 300 Hz, the PTI sensor was exposed to accelerations at or above 0.5 g up to 1.7 g, with the noise level still well within the 3σ noise band. At 10 Hz, the large motion amplitude of the electrodynamic shaker was causing a repeated mechanical impulse to the PTI setup, and applied peak accelerations were reduced to prevent impulse excitation.

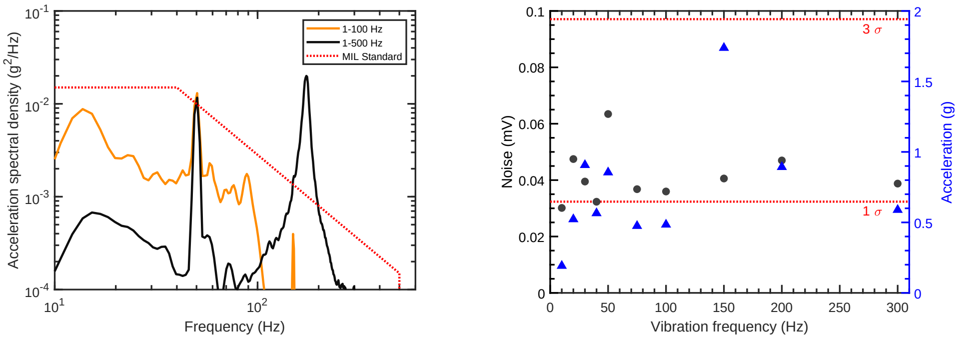

(**a**) (**b**)

Figure 8. Vibration analysis: (**a**) Broadband acceleration spectral densities applied to the measurement setup during operation (yellow and black curves). Military standard vibration schedule for highway truck vertical vibration exposure (MIL-STD-810H, Method 514.8C-I [28]; red dotted line). (**b**) Measured signal noise (black circles) at the applied sinusoidal vertical peak accelerations (blue triangles) for zero air. Horizontal dotted lines mark 1 σ and 3 σ noise levels.

3.4. Response Time

As short response times are critical for a wide variety of applications, the response of the proposed PTI sensor to steps in concentration was investigated. Repeated steps from synthetic air (zero concentration) to concentrations of 19.2 ppm NO_2 at 0.5 slpm and 1 s integration time revealed reproducible response times to 90% signal level (τ_{90}) below 3 s; and recovery times to 10% signal level (τ_{10}) below 2 s. An exemplary response curve is shown in Figure 9.

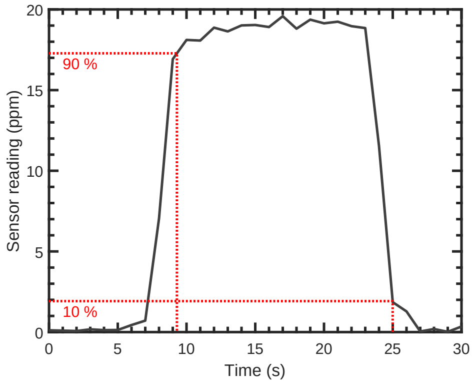

Figure 9. Sensor step response for a step from zero air to a concentration of 19.2 ppm NO_2 and back at 0.5 slpm and 1 s integration time. Response time to 90% (τ_{90}) and recovery time to 10% (τ_{10}) signal level are below 3 s and 2 s, respectively.

4. Discussion and Conclusions

The presented sensor concept, using a compact fiber-coupled Fabry–Pérot interferometer for photothermal spectroscopy, offers a reliable sensing scheme for NO_2 with high spectral selectivity and sensitivity. The NNEA was determined to be $7.5 \times 10^{-8}\,\mathrm{cm^{-1}W/\sqrt{Hz}}$, which is lower than previous PTI implementations [15,16], but can still be improved in future realizations, e.g., by applying a balanced detection scheme [17].

QEPAS implementations reach slightly better NNEAs (e.g., $2.5 \times 10^{-8}\,\mathrm{cm^{-1}W/\sqrt{Hz}}$ [10], $4.2 \times 10^{-9}\,\mathrm{cm^{-1}W/\sqrt{Hz}}$ [13]) and, compared to conventional PAS implementations, the NNEA is up to a factor 100 worse ($7.0 \times 10^{-10}\,\mathrm{cm}^{-1}\mathrm{W}/\sqrt{\mathrm{Hz}}$ [10]). However, the proposed PTI sensor approach offers the possibility for a much smaller detection volume, capable of faster response times and higher miniaturization potential.

The developed, non-optimized cell has a volume smaller than $9\,\mathrm{cm}^3$, for which an integration time of 1 s combined with a flow rate of 0.5 slpm proved to provide a good balance of response time and detection limit. Even though the given cell geometry comprises poorly flushed dead volumes, a response time of $\tau_{90} = 3\,\mathrm{s}$ and a recovery time of $\tau_{10} = 2\,\mathrm{s}$ were achieved. For applications requiring faster response times, a combination of smaller integration time and higher flow rate can be easily realized. Due to the small size of the optical microphone, the cell volume could be ultimately decreased to the dimensions of the FPI cavity, which is $1.5\,\mathrm{mm} \times 1.5\,\mathrm{mm} \times 3.3\,\mathrm{mm} \approx 7.5\,\mathrm{mm}^3$, without major drawbacks. This is highly advantageous when compared to microstructured hollow-core fiber-based PTI approaches, where long fibers are needed to reach comparable NNEAs. To fully demonstrate the miniaturization potential of the presented method, future research should focus on the downscaling of the cell down to the FPI cavity volume.

On the other hand, applications like environmental monitoring require lower detection limits, at averaging times of up to one hour [5]. In this case, a stabilized laser source could be used, which would enable longer averaging times to improve the detection limit. Additionally, higher laser power could be used to improve the detection limit, as the photothermal signal scales directly with the laser power.

A low sensitivity of the PTI sensor to mechanical vibrations was demonstrated with broadband vibrations in a frequency range similar to vehicular vibration profiles. Although the applied vibration power was below the specified root mean square acceleration of $g_{rms} = 1.04\,\mathrm{g}$ in the cited military vibration test standard, future commercial application possibilities in mobile gas sensing should be realizable with minor improvements in setup stability. This is underlined by the fact that, for sinusoidal vibrations, peak accelerations of 1.7 g could be applied to the described setup, without significantly increasing signal noise.

Although an expensive lab grade optical microphone was used for the proof of principle experiments, chip-level miniaturization of the sensor is possible, offering interesting potential for large-scale production of the sensor. Possible fields of application include exhaust gas and emission measurements. Furthermore, measurement of different gases can easily be achieved by using excitation lasers of different wavelengths.

Author Contributions: Conceptualization, P.B. and B.L.; methodology, P.B. and B.L.; software, P.B.; validation, P.B., B.L., and A.B.; formal analysis, P.B. and B.L.; investigation, P.B. and B.L.; resources, P.B., B.L., and A.B.; data curation, P.B. and B.L.; writing—original draft preparation, P.B.; writing—review and editing, P.B., B.L., and A.B.; visualization, P.B. and B.L.; supervision, A.B.; project administration, A.B.

Funding: This research received no external funding.

Acknowledgments: The authors would like to thank Wolfgang Rohringer and Balthasar Fischer from XARION Laser Acoustics GmbH for the constructive discussions. Open access publication is supported by the TU Graz Open Access Publishing Fund.

Conflicts of Interest: The authors declare no conflict of interest.

Abbreviations

The following abbreviations are used in this manuscript:

PTI	photothermal interferometry
PAS	photoacoustic spectroscopy
QEPAS	quartz-enhanced photoacoustic spectroscopy
ksps	kilosamples per second
NNEA	noise normalized equivalent absorption

Appendix A. Drift of the Laser Power

To investigate whether drift is dominated by fluctuations of the laser power, an Allan deviation analysis was carried out. As can be seen in Figure A1, a drift of the laserpower is appearing at the same timescale as the drift of the FPI sensor (around 200 s), which indicates that drift is caused by fluctuations of the laser power.

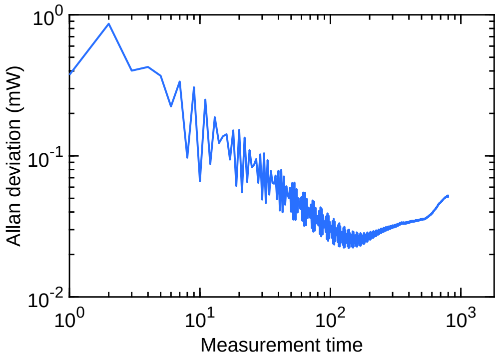

Figure A1. Allan deviation of the laser power as a function of the averaging time.

References

1. World Health Organisation. *Air Quality Guidelines for Particulate Matter, Ozone, Nitrogen Dioxide and Sulfur Dioxide—Global Update 2005*; WHO Press: Geneva, Switzerland, 2006.
2. Wild, R.J.; Dubé, W.P.; Aikin, K.C.; Eilerman, S.J.; Neuman, J.A.; Peischl, J.; Ryerson, T.B.; Brown, S.S. On-road measurements of vehicle NO2/NOx emission ratios in Denver, Colorado, USA. *Atmos. Environ.* **2017**, *148*, 182–189, doi:10.1016/j.atmosenv.2016.10.039. [CrossRef]
3. Hagemann, R.; Corsmeier, U.; Kottmeier, C.; Rinke, R.; Wieser, A.; Vogel, B. Spatial variability of particle number concentrations and NOx in the Karlsruhe (Germany) area obtained with the mobile laboratory 'AERO-TRAM'. *Atmos. Environ.* **2014**, *94*, 341–352.10.1016/j.atmosenv.2014.05.051. [CrossRef]
4. Mead, M.I.; Popoola, O.A.M.; Stewart, G.B.; Landshoff, P.; Calleja, M.; Hayes, M.; Baldovi, J.J.; McLeod, M.W.; Hodgson, T.F.; Dicks, J.; et al. The use of electrochemical sensors for monitoring urban air quality in low-cost, high-density networks. *Atmos. Environ.* **2013**, *70*, 186–203.10.1016/j.atmosenv.2012.11.060. [CrossRef]
5. European Parliament, Council of the European Union. Directive 2008/50/EC of the European Parliament and of the Council of 21 May 2008 on ambient air quality and cleaner air for Europe. *Off. J. Eur. Union* **2008**, *L 152*, 1–44.
6. Castell, N.; Dauge, F.R.; Schneider, P.; Vogt, M.; Lerner, U.; Fishbain, B.; Broday, D.; Bartonova, A. Can commercial low-cost sensor platforms contribute to air quality monitoring and exposure estimates? *Environ. Int.* **2017**, *99*, 293–302.10.1016/j.envint.2016.12.007. [CrossRef] [PubMed]
7. Miklós, A.; Hess, P.; Bozóki, Z. Application of acoustic resonators in photoacoustic trace gas analysis and metrology. *Rev. Sci. Instrum.* **2001**, *72*, 1937–1955.10.1063/1.1353198. [CrossRef]
8. Kalkman, J.; van Kesteren, H. Relaxation effects and high sensitivity photoacoustic detection of NO2 with a blue laser diode. *Appl. Phys. B* **2008**, *90*, 197–200.10.1007/s00340-007-2895-0. [CrossRef]
9. Yin, X.; Dong, L.; Wu, H.; Zheng, H.; Ma, W.; Zhang, L.; Yin, W.; Jia, S.; Tittel, F.K. Sub-ppb nitrogen dioxide detection with a large linear dynamic range by use of a differential photoacoustic cell and a 3.5 W blue multimode diode laser. *Sens. Actuators B Chem.* **2017**, *247*, 329–335.10.1016/j.snb.2017.03.058. [CrossRef]
10. Rück, T.; Bierl, R.; Matysik, F.M. Low-cost photoacoustic NO2 trace gas monitoring at the pptV-level. *Sens. Actuators A Phys.* **2017**, *263*, 501–509.10.1016/j.sna.2017.06.036. [CrossRef]
11. Kosterev, A.A.; Bakhirkin, Y.A.; Curl, R.F.; Tittel, F.K. Quartz-enhanced photoacoustic spectroscopy. *Opt. Lett.* **2002**, *27*, 1902–1904.10.1364/OL.27.001902. [CrossRef]

12. Yi, H.; Liu, K.; Chen, W.; Tan, T.; Wang, L.; Gao, X. Application of a broadband blue laser diode to trace NO2 detection using off-beam quartz-enhanced photoacoustic spectroscopy. *Opt. Lett.* **2011**, *36*, 481–483.10.1364/OL.36.000481. [CrossRef] [PubMed]
13. Zheng, H.; Dong, L.; Yin, X.; Liu, X.; Wu, H.; Zhang, L.; Ma, W.; Yin, W.; Jia, S. Ppb-level QEPAS NO2 sensor by use of electrical modulation cancellation method with a high power blue LED. *Sens. Actuators B Chem.* **2015**, *208*, 173–179.10.1016/j.snb.2014.11.015. [CrossRef]
14. Rück, T.; Bierl, R.; Matysik, F.M. NO2 trace gas monitoring in air using off-beam quartz enhanced photoacoustic spectroscopy (QEPAS) and interference studies towards CO2, H2O and acoustic noise. *Sens. Actuators B Chem.* **2018**, *255*, 2462–2471.10.1016/j.snb.2017.09.039. [CrossRef]
15. Campillo, A.J.; Petuchowski, S.J.; Davis, C.C.; Lin, H.B. Fabry-perot photothermal trace detection. *Appl. Phys. Lett.* **1982**, *41*, 327–329.10.1063/1.93524. [CrossRef]
16. Waclawek, J.P.; Bauer, V.C.; Moser, H.; Lendl, B. 2f-wavelength modulation Fabry-Perot photothermal interferometry. *Opt. Express* **2016**, *24*, 28958–28967.10.1364/OE.24.028958. [CrossRef]
17. Waclawek, J.P.; Kristament, C.; Moser, H.; Lendl, B. Balanced-detection interferometric cavity-assisted photothermal spectroscopy. *Opt. Express* **2019**, *27*, 12183–12195.10.1364/OE.27.012183. [CrossRef]
18. Yang, F.; Jin, W.; Lin, Y.; Wang, C.; Lut, H.; Tan, Y. Hollow-core microstructured optical fiber gas sensors. *J. Lightwave Technol.* **2016**, *35*, 3413–3424. [CrossRef]
19. Krzempek, K. A Review of Photothermal Detection Techniques for Gas Sensing Applications. *Appl. Sci.* **2019**, *9*, 2826.10.3390/app9142826. [CrossRef]
20. Wynne, R.M.; Barabadi, B.; Creedon, K.J.; Ortega, A. Sub-Minute Response Time of a Hollow-Core Photonic Bandgap Fiber Gas Sensor. *J. Lightwave Technol.* **2009**, *27*, 1590–1596.10.1109/JLT.2009.2019258. [CrossRef]
21. Hoo, Y.L.; Liu, S.; Ho, H.L.; Jin, W. Fast response microstructured optical fiber methane sensor with multiple side-openings. *IEEE Photonics Technol. Lett.* **2010**, *22*, 296–298.10.1109/LPT.2009.2039016. [CrossRef]
22. Davis, C.C.; Petuchowski, S.J. Phase fluctuation optical heterodyne spectroscopy of gases. *Appl. Opt.* **1981**, *20*, 2539–2554.10.1364/AO.20.002539. [CrossRef] [PubMed]
23. Hecht, E. *Optics, Global Edition*, 5th ed.; Pearson: London, UK, 2017.
24. Preisser, S.; Rohringer, W.; Liu, M.; Kollmann, C.; Zotter, S.; Fischer, B.; Drexler, W. All-optical highly sensitive akinetic sensor for ultrasound detection and photoacoustic imaging. *Biomed. Opt. Express* **2016**, *7*, 4171–4186.10.1364/BOE.7.004171. [CrossRef] [PubMed]
25. Fischer, B.; Wintner, E. Sound Recording by Laser Interferometry. In Proceedings of the Conference on Lasers and Electro-Optics/International Quantum Electronics Conference, Baltimore, MD, USA, 31 May–5 June 2009; OSA: Washington, DC, USA, 2009; p. JWA64.10.1364/CLEO.2009.JWA64. [CrossRef]
26. Roehl, C.M.; Orlando, J.J.; Tyndall, G.S.; Shetter, R.E.; Vazquez, G.J.; Cantrell, C.A.; Calvert, J.G. Temperature Dependence of the Quantum Yields for the Photolysis of NO2 Near the Dissociation Limit. *J. Phys. Chem.* **1994**, *98*, 7837–7843.10.1021/j100083a015. [CrossRef]
27. Breitegger, P.; Bergmann, A. A Precise Gas Dilutor Based on Binary Weighted Critical Flows to Create NO2 Concentrations. *Proceedings* **2018**, *2*, 998.10.3390/proceedings2130998. [CrossRef]
28. *Mil-STD-810H: Department of Defense Test Method Standard for Environmental Engineering Considerations and Laboratory Tests*; US Department of Defense (DoD): Washington, DC, USA, 2019.
29. Herault, J.; Pétrélis, F.; Fauve, S. $1/f^{\alpha}$ Low Frequency Fluctuations in Turbulent Flows. *J. Stat. Phys.* **2015**, *161*, 1379–1389.10.1007/s10955-015-1408-5. [CrossRef]
30. Vandaele, A.; Hermans, C.; Simon, P.; Carleer, M.; Colin, R.; Fally, S.; Mérienne, M.; Jenouvrier, A.; Coquart, B. Measurements of the NO2 absorption cross-section from 42,000 cm^{-1} to 10,000 cm^{-1} (238–1000 nm) at 220 K and 294 K. *J. Quant. Spectrosc. Radiat. Transf.* **1998**, *59*, 171–184.10.1016/S0022-4073(97)00168-4. [CrossRef]

REFERENCES

[1] Benjamin Lang, Philipp Breitegger, Georg Brunnhofer, Jordi Prats Valero, Simon Schweighart, Andreas Klug, Wolfgang Hassler, and Alexander Bergmann. Molecular relaxation effects on vibrational water vapor photoacoustic spectroscopy in air. *Applied Physics B: Lasers and Optics*, 126(4):1–18, apr 2020. ISSN 09462171. doi: 10.1007/s00340-020-7409-3. URL https://link.springer.com/article/10.1007/s00340-020-7409-3.

[2] Benjamin Lang, Wolfgang Breitfuss, Simon Schweighart, Philipp Breitegger, Hugo Pervier, Andreas Tramposch, Andreas Klug, Wolfgang Hassler, and Alexander Bergmann. Photoacoustic hygrometer for icing wind tunnel water content measurement: Design, analysis and intercomparison. 2020. doi: 10.5194/amt-2020-295. URL https://doi.org/10.5194/amt-2020-295.

[3] Philipp Breitegger, Benjamin Lang, and Alexander Bergmann. Intensity modulated photothermal measurements of NO2 with a compact fiber-coupled fabry–pérot interferometer. *Sensors (Switzerland)*, 19(15):3341, jul 2019. ISSN 14248220. doi: 10.3390/s19153341. URL https://www.mdpi.com/1424-8220/19/15/3341.

[4] Jeffery T. Kiehl and Kevin E. Trenberth. Earth's Annual Global Mean Energy Budget. *Bulletin of the American Meteorological Society*, 78(2):197–208, feb 1997. ISSN 00030007. doi: 10.1175/1520-0477(1997)078<0197:EAGMEB>2.0.CO;2. URL http://journals.ametsoc.org/bams/article-pdf/78/2/197/3729125/1520-0477.

[5] K. H. Rosenlof, S. J. Oltmans, D. Kley, J. M. Russell, E. W. Chiou, W. P. Chu, D. G. Johnson, K. K. Kelly, H. A. Michelsen, G. E. Nedoluha, E. E. Remsberg, G. C. Toon, and M. P. McCormick. Stratospheric water vapor increases over the past half-century. *Geophysical Research Letters*, 28(7): 1195–1198, apr 2001. ISSN 00948276. doi: 10.1029/2000GL012502. URL https://agupubs.onlinelibrary.wiley.com/doi/full/10.1029/2000GL012502https://agupubs.onlinelibrary.wiley.com/doi/abs/10.1029/2000GL012502https://agupubs.onlinelibrary.wiley.com/doi/10.1029/2000GL012502.

[6] Kevin E. Trenberth, John T. Fasullo, and Jeffrey Kiehl. Earth's global energy budget. *Bulletin of the American Meteorological Society*, 90(3):311–323, mar 2009. ISSN 00030007. doi: 10.1175/2008BAMS2634.1. URL http://journals.ametsoc.org/bams/article-pdf/90/3/311/3737077/2008bams2634{_}1.pdf.

[7] Susan Solomon, Karen H. Rosenlof, Robert W. Portmann, John S. Daniel, Sean M. Davis, Todd J. Sanford, and Gian Kasper Plattner. Contributions of stratospheric water vapor to decadal changes in the rate of global warming. *Science*, 327(5970): 1219–1223, mar 2010. ISSN 00368075. doi: 10.1126/science.1182488. URL www.esrl.noaa.gov/psd.

[8] Masoud Farzaneh. *Atmospheric icing of power networks*. Springer Netherlands, 2008. ISBN 9781402085307. doi: 10.1007/978-1-4020-8531-4.

[9] Clement Hochart, Guy Fortin, Jean Perron, and Adrian Ilinca. Wind turbine performance under icing conditions. *Wind Energy*, 11(4):319–333, 2008. ISSN 10954244. doi: 10.1002/we.258. URL www.interscience.wiley.com.

[10] A. R. Dehghani-Sanij, S. R. Dehghani, G. F. Naterer, and Y. S. Muzychka. Marine icing phenomena on vessels and offshore structures: Prediction and analysis, oct 2017. ISSN 00298018.

[11] R. W. Gent, N. P. Dart, and J. T. Cansdale. Aircraft icing. *Philosophical Transactions of the Royal Society A: Mathematical, Physical and Engineering Sciences*, 358(1776): 2873–2911, 2000. ISSN 1364503X. doi: 10.1098/rsta.2000.0689.

[12] Jeanne G Mason, J Walter Strapp, and Philip Chow. The ice particle threat to engines in flight. In *Collection of Technical Papers - 44th AIAA Aerospace Sciences Meeting*, volume 4, pages 2445–2465, 2006. ISBN 1563478072.

[13] M. K. Politovich. Aircraft icing caused by large supercooled droplets. *Journal of Applied Meteorology*, 28(9):856–868, 1989. ISSN 08948763. doi: 10.1175/1520-0450(1989)028<0856:AICBLS>2.0.CO;2.

[14] NATO Fluid Dynamics Panel Working Group 20. Ice Accretion Simulation (AGARD-AR-344). Technical Report December 1997, ADVISORY GROUP FOR AEROSPACE RESEARCH & DEVELOPMENT, 1997.

[15] Ben C Bernstein, Thomas P. Ratvasky, Dean R Miller, and Frank McDonough. Freezing Rain as an In-Flight Icing Hazard. Technical Report June, 2000.

[16] Thomas J. Vukits. Overview and risk assessment of icing for transport category aircraft and components. In *40th AIAA Aerospace Sciences Meeting and Exhibit*, number January 2002, 2002. doi: 10.2514/6.2002-811.

[17] New Zealand Civil Aviation Authority. Aircraft Icing Handbook. Technical report, Civil Aviation Authority, 2000.

[18] EASA CS-25. Certification Specifications and Acceptable Means of Compliance for Large Aeroplanes CS-25. Technical report, European Aviation Safety Agency, 2020.

[19] FAA CFR-25. US Code of Federal Regulations - Title 14 Part 25, Airworthiness Standards - Transport Category Airplanes, 2019.

[20] Stewart G. Cober and George A. Isaac. Characterization of aircraft icing environments with Supercooled Large Drops for application to commercial aircraft certification. *Journal of Applied Meteorology and Climatology*, 51(2):265–284, 2012. ISSN 15588424. doi: 10.1175/JAMC-D-11-022.1.

[21] J W Strapp, A Korolev, T Ratvasky, R Potts, A Protat, P May, A Ackerman, A Fridlind, P Minnis, J Haggerty, and Others. The High Ice Water Content (HIWC) Study of Deep Convective Clouds: Science and Technical Plan. Technical report, 2015. URL http://www.tc.faa.gov/its/worldpac/techrpt/tc14-31.pdf.

[22] Alfons. Schwarzenboeck, Fabian. Dezitter, Alice. Grandin, Alain. Protat, and EASA. HighIWC — Ice Water Content of clouds at High altitude. Technical report, 2012. URL http://www.easa.europa.eu/safety-and-research/research-projects/docs/large-aeroplanes/HighIWC{_}Final{_}Study{_}Report{_}4-2011.pdf.

[23] EASA. ED Decision 2015/008/R ,CS-25 - Amendment 16. Technical report, 2015. URL https://www.easa.europa.eu/document-library/agency-decisions/ed-decision-2015008r.

[24] US Federal Aviation Administration. Airplane and Engine Certification Requirements in Supercooled Large Drop, Mixed Phase, and Ice Crystal Icing Conditions. Technical report, 2014. URL http://www.gpo.gov/fdsys/.

[25] Robert S. Mazzawy and J. Walter Strapp. Appendix D - An interim icing envelope. In *SAE Technical Papers*. SAE International, 2007. doi: 10.4271/2007-01-3311.

[26] Craig Davison, Thomas Ratvasky, and Lyle Lilie. Naturally aspirating isokinetic total water content probe: Wind tunnel test results and design modifications. *SAE Technical Papers*, 2011. ISSN 26883627. doi: 10.4271/2011-38-0036.

[27] Alexei Korolev, J W Strapp, G A Isaac, and E. Emery. Improved airborne hot-wire measurements of ice water content in clouds. *Journal of Atmospheric and Oceanic Technology*, 30(9):2121–2131, 2013. ISSN 07390572. doi: 10.1175/JTECH-D-13-00007.1.

[28] Laura-Cheri E Steen, Robert F Ide, and Judith Foss Van Zante. An assessment of the icing blade and the SEA multi-element sensor for liquid water content calibration of the NASA GRC icing research tunnel. In *8th AIAA Atmospheric and Space Environments Conference*, 2016. ISBN 9781624104336. doi: 10.2514/6.2016-4051.

[29] D. Baumgardner, S. J. Abel, D. Axisa, R. Cotton, J. Crosier, P. Field, C. Gurganus, A. Heymsfield, A. Korolev, M. Krämer, P. Lawson, G. McFarquhar, Z. Ulanowski, J. Um, Um, and J. Cloud Ice Properties: In Situ Measurement Challenges. *Meteorological Monographs*, 58:9.1–9.23, 2017. ISSN 0065-9401. doi: 10.1175/AMSMONOGRAPHS-D-16-0011.1. URL http://www.artium.comhttp://journals.ametsoc.org/doi/10.1175/AMSMONOGRAPHS-D-16-0011.1.

[30] Jennifer Chalmers, Craig Davison, James Macleod, Martin Neuteboom, and Dan Fuleki. Icing Test and Measurement Capabilities of the NRC's Gas Turbine Laboratory. In *SAE Technical Papers*, pages 2019–01–1943. SAE International, 2019. doi: 10.4271/2019-01-1943.

[31] A. Baumert, S. Bansmer, P. Trontin, and P. Villedieu. Experimental and numerical investigations on aircraft icing at mixed phase conditions. *International Journal of Heat and Mass Transfer*, 123:957–978, aug 2018. ISSN 00179310. doi: 10.1016/j.ijheatmasstransfer.2018.02.008.

[32] Oloufemi Fakorede, Zoé Feger, Hussein Ibrahim, Adrian Ilinca, Jean Perron, and Christian Masson. Ice protection systems for wind turbines in cold climate: characteristics, comparisons and analysis, nov 2016. ISSN 18790690.

[33] HAIC Consortium. High Altitude Ice Crystals Final Forum Booklet of Abstracts. Technical report, HAIC Consortium, 2016. URL http://www.haic.eu/wp-content/uploads/2017/01/HAIC{_}Booklet-of-Abstracts{_}FINAL-FORUM{_}approved.pdf.

[34] Peter M Struk, Tadas P Bartkus, Timothy J Bencic, Michael C King, Thomas P Ratvasky, Judith F Van Zante, and Jen Ching Tsao. An initial study of the fundamentals of ice crystal icing physics in the NASA propulsion systems laboratory. In *9th AIAA Atmospheric and Space Environments Conference, 2017*, pages 110–113, 2017. ISBN 9781624104961. doi: 10.2514/6.2017-4242.

[35] Tom (CSTA-Aircraft-Icing) Bond. FAA Aircraft Icing Research - Update on Research Plans, 2019.

[36] SAE ARP-5905. Calibration and Acceptance of Icing Wind Tunnels. *SAE International*, 2015.

[37] Stewart G Cober, George A Isaac, and J Walter Strapp. Characterizations of aircraft icing environments that include supercooled large drops. *Journal of Applied Meteorology*, 40(11):1984–2002, 2001. ISSN 08948763. doi: 10.1175/1520-0450(2001)040<1984:COAIET>2.0.CO;2.

[38] Richard K Jeck. Models and Characteristics of Freezing Rain and Freezing Drizzle for Aircraft Icing Applications. (January):113, 2010.

[39] Stephan E Bansmer, Arne Baumert, Stephan Sattler, Inken Knop, Delphine Leroy, Alfons Schwarzenboeck, Tina Jurkat-Witschas, Christiane Voigt, Hugo Pervier, and Biagio Esposito. Design, construction and commissioning of the Braunschweig Icing Wind Tunnel. *Atmospheric Measurement Techniques*, 11(6):3221–3249, 2018. ISSN 18678548. doi: 10.5194/amt-11-3221-2018.

[40] Dean R. Miller, Mark G. Potapczuk, and Thomas H. Bond. Update On SLD Engineering Tools Development. jun 2003. doi: 10.4271/2003-01-2127. URL https://www.sae.org/content/2003-01-2127/.

[41] Aviation Rulemaking Advisory Committee - Ice Protection Harmonization Working Group. Task 2 Working Group Report on Supercooled Large Droplet Rulemaking. Technical report, 2005.

[42] J. W. Strapp, J. Oldenburg, R. Ide, L. Lilie, S. Bacic, Z. Vukovic, M. Oleskiw, D. Miller, E. Emery, and G. Leone. Wind tunnel measurements of the response of hot-wire liquid water content instruments to large droplets. *Journal of Atmospheric and Oceanic Technology*, 20(6):791–806, jun 2003. ISSN 07390572. doi: 10.1175/1520-0426(2003)020<0791:WTMOTR>2.0.CO;2.

[43] David M. Orchard, Catherine Clark, and Gislain Chevrette. Measurement of Liquid Water Content for Supercooled Large Drop Conditions in the NRC's Altitude Icing Wind Tunnel. In *SAE Technical Papers*, pages 2019–01–2007, 2019. doi: 10.4271/2019-01-2007.

[44] George A Isaac, Alexei V Korolev, J Walter Strapp, Stewart G Cober, Faisal S. Boudala, Dave Marcotte, and Vincent L. Reich. Assessing the collection efficiency of natural cloud particles impacting the Nevzorov total water content probe. In *Collection of Technical Papers - 44th AIAA Aerospace Sciences Meeting*, pages 14846–14858, 2006. ISBN 1563478072. doi: 10.2514/6.2006-1221.

[45] D. Baumgardner, J. L. Brenguier, A. Bucholtz, H. Coe, P. DeMott, T. J. Garrett, J. F. Gayet, M. Hermann, A. Heymsfield, A. Korolev, M. Krämer, A. Petzold, W. Strapp, P. Pilewskie, J. Taylor, C. Twohy, M. Wendisch, W. Bachalo, and P. Chuang. Airborne instruments to measure atmospheric aerosol particles, clouds and radiation: A cook's tour of mature and emerging technology. *Atmospheric Research*, 102(1-2):10–29, 2011. ISSN 01698095. doi: 10.1016/j.atmosres.2011.06.021.

[46] David M. Orchard, Krzysztof Szilder, and Craig R. Davison. Design of an icing wind tunnel contraction for supercooled large drop conditions. In *2018 Atmospheric and Space Environments Conference*, 2018. ISBN 9781624105586. doi: 10.2514/6.2018-3185.

[47] Laura E. King-Steen and Robert F. Ide. Creating a bimodal drop-size distribution in the NASA glenn icing research tunnel. In *9th AIAA Atmospheric and Space Environments Conference, 2017*. American Institute of Aeronautics and Astronautics Inc, AIAA, 2017. ISBN 9781624104961. doi: 10.2514/6.2017-4477. URL https://arc.aiaa.org/doi/abs/10.2514/6.2017-4477.

[48] Hermann Ferschitz, Michael Wannemacher, Otto Bucek, Florian Knöbel, and Wolfgang Breitfuß. Development of SLD Capabilities in the RTA Icing Wind Tunnel. *SAE International Journal of Aerospace*, 10(1):2017–01–9001, jun 2017. ISSN 1946-3901. doi: 10.4271/2017-01-9001.

[49] Wolfgang Breitfuss, Michael Wannemacher, Florian Knöbl, and Hermann Ferschitz. Aerodynamic Comparison of Freezing Rain and Freezing Drizzle Conditions at the RTA Icing Wind Tunnel. *SAE Technical Papers*, 2019-June(June):245–255, 2019. ISSN 01487191. doi: 10.4271/2019-01-2023.

[50] AQUASENSE - Erforschung und Validierung eines Demonstrators zur simultanen LWC/IWC-Bestimmung in Vereisungswindkanälen, 2015. URL https://open4aviation.at/de/projekte/aquasense.php.

[51] M.L. Grzych and J.G. Mason. Weather Conditions Associated with Jet Engine Power Loss and Damage Due to Ingestion of Ice Particles: What We've Learned Through 2009. *14th Conference on Aviation, Range, and Aerospace Meteorology*, 2010. URL http://www.wxforecastnow.com/documents/grzych{_}ams{_}2010.pdf.

[52] Edward F Emery, Dean R Miller, Stephen R Plaskon, Walter Strapp, and Lyle Lillie. Ice particle impact on cloud water content instrumentation. In *AIAA Paper*, number March, pages 8387–8398, 2004. ISBN 978-1-62410-078-9. doi: 10.2514/6.2004-731.

[53] FAA CFR-33. US Code of Federal Regulations - Title 14 Appendix D to Part 33 - Mixed Phase and Ice Crystal Icing Envelope (Deep Convective Clouds), 2019. URL https://www.law.cornell.edu/cfr/text/14/appendix-D{_}to{_}part{_}33.

[54] D R Buttsworth, C Davison, J. D. MacLeod, and J W Strapp. Evaporator design for an isokinetic total water content probe in a naturally aspirating configuration. In *Proceedings of the 16th Australasian Fluid Mechanics Conference, 16AFMC*, number December, pages 825–830, 2007. ISBN 9781864998948.

[55] Craig Davison, James MacLeod, J. Strapp, and David Buttsworth. Isokinetic Total Water Content Probe in a Naturally Aspirating Configuration: Initial Aerodynamic Design and Testing. In *46th AIAA Aerospace Sciences Meeting and Exhibit*, number January, Reston, Virigina, jan 2008. American Institute of Aeronautics and Astronautics. ISBN 978-1-62410-128-1. doi: 10.2514/6.2008-435. URL http://arc.aiaa.org/doi/10.2514/6.2008-435.

[56] Andrew L Reehorst, Dean R Miller, and Colin S Bidwell. Total Water Content Measurements With an Isokinetic Sampling Probe. Technical report, 2010.

[57] Craig Davison, Thomas Ratvasky, and Lyle Lilie. Naturally Aspirating Isokinetic Total Water Content Probe: Wind Tunnel Test Results and Design Modifications. In *SAE Technical Paper Series*, volume 1, 2011. doi: 10.4271/2011-38-0036.

[58] J.W. Strapp, Lyle E. Lilie, Thomas P. Ratvasky, Craig Davison, and Chris Dumont. Isokinetic TWC evaporator probe: Development of the IKP2 and performance testing for the HAIC-HIWC darwin 2014 and cayenne-2015 field campaigns. In *8th AIAA Atmospheric and Space Environments Conference*, pages 1–28, 2016. ISBN 9781624104336. doi: 10.2514/6.2016-4059.

[59] LI-COR Inc. Using the LI-830 and LI-850 Gas Analyzers. Technical report, LI-COR Inc., 2020. URL https://www.licor.com/documents/gz8gaf0ls5vhvpl52xtmyr8mfoh5kwe8.

[60] D. Baumgardner, S. J. Abel, D. Axisa, R. Cotton, J. Crosier, P. Field, C. Gurganus, A. Heymsfield, A. Korolev, M. Krämer, P. Lawson, G. McFarquhar, Z. Ulanowski, and J. Um. Cloud Ice Properties: In Situ Measurement Challenges. *Meteorological Monographs*, 58:9.1–9.23, 2017. ISSN 0065-9401. doi: 10.1175/AMSMONOGRAPHS-D-16-0011.1. URL http://journals.ametsoc.org/doi/10.1175/AMSMONOGRAPHS-D-16-0011.1.

[61] Astrid Lampert, Jörg Hartmann, Falk Pätzold, Lennart Lobitz, Peter Hecker, Katrin Kohnert, Eric Larmanou, Andrei Serafimovich, and Torsten Sachs. Comparison of Lyman-alpha and LI-COR infrared hygrometers for airborne measurement of turbulent fluctuations of water vapour. *Atmospheric Measurement Techniques*, 11 (4):2523–2536, may 2018. ISSN 18678548. doi: 10.5194/amt-11-2523-2018. URL https://amt.copernicus.org/articles/11/2523/2018/.

[62] D W Fahey, R. S. Gao, O Möhler, H Saathoff, C Schiller, V Ebert, M Krämer, T Peter, N Amarouche, L M Avallone, R Bauer, Z Bozóki, L E Christensen, S M Davis, G Durry, C Dyroff, R L Herman, S Hunsmann, S M Khaykin, P Mackrodt, J Meyer, J B Smith, N Spelten, R F Troy, H Vömel, S Wagner, and F G Wienhold. The AquaVIT-1 intercomparison of atmospheric water vapor measurement techniques. *Atmospheric Measurement Techniques*, 7(9):3177–3213, 2014. ISSN 18678548. doi: 10.5194/amt-7-3177-2014. URL www.atmos-meas-tech.net/7/3177/2014/.

[63] S. Nicholls, J. Leighton, and R. Barker. A New Fast Response Instrument for Measuring Total Water Content from Aircraft. *Journal of Atmospheric and Oceanic Technology*, 7(5):706–718, oct 1990. ISSN 0739-0572. doi: 10.1175/1520-0426(1990)007<0706:anfrif>2.0.co;2. URL http://journals.ametsoc.org/doi/abs/10.1175/1520-0426{%}281990{%}29007{%}3C0706{%}3AANFRIF{%}3E2.0.CO{%}3B2.

[64] M. Zöger, A. Afchine, N. Eicke, M. T. Gerhards, E. Klein, D. S. McKenna, U. Mörschel, U. Schmidt, V. Tan, F. Tuitjer, T. Woyke, and C. Schiller. Fast in situ stratospheric hygrometers: A new family of balloon-borne and airborne Lyman α photofragment fluorescence hygrometers. *Journal of Geophysical Research Atmospheres*, 104 (D1):1807–1816, jan 1999. ISSN 01480227. doi: 10.1029/1998JD100025. URL http://doi.wiley.com/10.1029/1998JD100025.

[65] Elliot M Weinstock, J B Smith, D Sayres, J V Pittman, N Allen, and J G Anderson. Measurements of the total water content of cirrus clouds. Part II: Instrument performance and validation. *Journal of Atmospheric and Oceanic Technology*, 23(11):1410–1421, 2006. ISSN 07390572. doi: 10.1175/JTECH1929.1. URL https://journals.ametsoc.org/doi/pdf/10.1175/JTECH1929.1.

[66] J. Meyer, C. Rolf, C. Schiller, S. Rohs, N. Spelten, A. Afchine, M. Zöger, N. Sitnikov, T. D. Thornberry, A. W. Rollins, Z. Bozóki, D. Tátrai, V. Ebert, B. Kühnreich, P. Mackrodt, O. Möhler, H. Saathoff, K. H. Rosenlof, and M. Krämer. Two decades of water vapor measurements with the FISH fluorescence hygrometer: A review, jul 2015. ISSN 16807324. URL https://acp.copernicus.org/articles/15/8521/2015/.

[67] S J Abel, R J Cotton, P A Barrett, and A K Vance. A comparison of ice water content measurement techniques on the FAAM BAe-146 aircraft. *Atmospheric Measurement Techniques*, 7(9):3007–3022, 2014. ISSN 18678548. doi: 10.5194/amt-7-3007-2014.

[68] Ghenadii Korotcenkov. *Handbook of Humidity Measurement*. CRC Press, jan 2018. ISBN 9780203731888. doi: 10.1201/b22370. URL https://www.taylorfrancis.com/books/9781351400565.

[69] A K Vance, S J Abel, R J Cotton, and A M Woolley. Performance of WVSS-II hygrometers on the FAAM research aircraft. *Atmospheric Measurement Techniques*, 8(3):1617–1625, 2015. ISSN 18678548. doi: 10.5194/amt-8-1617-2015. URL www.atmos-meas-tech.net/8/1617/2015/.

[70] Sean M Davis, A Gannet Hallar, Linnea M Avallone, and William Engblom. Measurement of total water with a tunable diode laser hygrometer: Inlet analysis, calibration procedure, and ice water content determination. *Journal of Atmospheric and Oceanic Technology*, 24(3):463–475, 2007. ISSN 07390572. doi: 10.1175/JTECH1975.1.

[71] S W Dorsi, L E Kalnajs, D W Toohey, and L M Avallone. A fiber-coupled laser hygrometer for airborne total water measurement. *Atmospheric Measurement Techniques*, 7(1):215–223, 2014. ISSN 18678548. doi: 10.5194/amt-7-215-2014.

[72] Bernhard Buchholz, Sören Kallweit, and Volker Ebert. SEALDH-II—An autonomous, holistically controlled, first principles TDLAS hygrometer for field and airborne applications: Design–setup–accuracy/stability stress test. *Sensors (Switzerland)*, 17

(1):68, dec 2017. ISSN 14248220. doi: 10.3390/s17010068. URL http://www.mdpi.com/1424-8220/17/1/68.

[73] Bernhard Buchholz, Armin Afchine, Alexander Klein, Cornelius Schiller, Martina Krämer, and Volker Ebert. HAI, a new airborne, absolute, twin dual-channel, multi-phase TDLAS-hygrometer: Background, design, setup, and first flight data. *Atmospheric Measurement Techniques*, 10(1):35–57, 2017. ISSN 18678548. doi: 10.5194/amt-10-35-2017.

[74] E. R. Crosson. A cavity ring-down analyzer for measuring atmospheric levels of methane, carbon dioxide, and water vapor. In *Applied Physics B: Lasers and Optics*, volume 92, pages 403–408. Springer, sep 2008. doi: 10.1007/s00340-008-3135-y. URL https://link.springer.com/article/10.1007/s00340-008-3135-y.

[75] Scott J Richardson, Natasha L Miles, Kenneth J Davis, Eric R Crosson, Chris W Rella, and Arlyn E Andrews. Field testing of cavity ring-down spectroscopy analyzers measuring carbon dioxide and water vapor. *Journal of Atmospheric and Oceanic Technology*, 29(3):397–406, 2012. ISSN 07390572. doi: 10.1175/JTECH-D-11-00063.1. URL http://journals.ametsoc.org/jtech/article-pdf/29/3/397/3350008/jtech-d-11-00063{_}1.pdf.

[76] Picarro Inc. G2301 Analyzer Datasheet. URL https://www.picarro.com/support/library/documents/g2301{_}analyzer{_}datasheet.

[77] Jane Hodgkinson and Ralph P Tatam. Optical gas sensing: a review. *Measurement Science and Technology*, 24(1):012004, jan 2013. ISSN 0957-0233. doi: 10.1088/0957-0233/24/1/012004.

[78] Zoltán Bozóki, Miklós Szakáll, Árpád Mohácsi, Gábor Szabó, and Zsolt Bor. Diode laser based photoacoustic humidity sensors. *Sensors and Actuators, B: Chemical*, 91 (1-3):219–226, 2003. ISSN 09254005. doi: 10.1016/S0925-4005(03)00120-5.

[79] Miklós Szakáll, Zoltán Bozóki, Árpád Mohácsi, Attila Varga, and Gábor Szabó. Diode laser based photoacoustic water vapor detection system for atmospheric research. *Applied Spectroscopy*, 58(7):792–798, 2004. ISSN 00037028. doi: 10.1366/0003702041389373.

[80] Miklós Szakáll, János Csikós, Zoltán Bozóki, and Gábor Szabó. On the temperature dependent characteristics of a photoacoustic water vapor detector for airborne application. *Infrared Physics and Technology*, 51(2):113–121, 2007. ISSN 13504495. doi: 10.1016/j.infrared.2007.04.001.

[81] Zoltán Bozóki, Anna Szabó, Árpád Mohácsi, and Gábor Szabó. A fully opened photoacoustic resonator based system for fast response gas concentration measurements. *Sensors and Actuators, B: Chemical*, 147(1):206–212, 2010. ISSN 09254005. doi: 10.1016/j.snb.2010.02.060.

[82] D. Tátrai, Z. Bozóki, H. Smit, C. Rolf, N. Spelten, M. Krämer, A. Filges, C. Gerbig, G. Gulyás, and G. Szabó. Dual-channel photoacoustic hygrometer for airborne measurements: background, calibration, laboratory and in-flight intercomparison tests. *Atmospheric Measurement Techniques*, 8(1):33–42, jan 2015. ISSN 1867-8548. doi: 10.5194/amt-8-33-2015.

[83] Joh-Han Pao. *Optoacoustic spectroscopy and detection*. Academic Press, Inc, 1977. ISBN 9780323158817.

[84] Stephen E. Bialkowski, Nelson G. C. Astrath, and Mikhail A. Proskurnin. *Photothermal Spectroscopy Methods*. Wiley, apr 2019. ISBN 9781119279075. doi: 10.1002/9781119279105. URL https://onlinelibrary.wiley.com/doi/book/10.1002/9781119279105.

[85] Bogdan Wozniak and Jerzy Dera. Light Absorption by Water Molecules and Inorganic Substances Dissolved in Sea Water. In *Light Absorption in Sea Water*, pages 11–81. 2007. doi: 10.1007/978-0-387-49560-6_2.

[86] Chandrasekhar S. Radiative Transfer. In *Mathematical Principles of Remote Sensing:*. Dover Publications, Inc., New York, 2010. ISBN 9780486605906. doi: 10.4324/9780203305782_chapter_4.

[87] Walter Regula. Berichte des Deutschen Wetterdienstes 44 Das Spektrum des Wasserdampfes. Technical report, 1958. URL www.dwd.de.

[88] Zoltán Bozóki, Andrea Pogány, and Gábor Szabó. Photoacoustic instruments for practical applications: Present, potentials, and future challenges. *Applied Spectroscopy Reviews*, 46(1):1–37, 2011. ISSN 05704928. doi: 10.1080/05704928.2010.520178.

[89] David S Sayres, E J Moyer, T F Hanisco, J. M. St. Clair, F N Keutsch, A. O'Brien, N T Allen, L Lapson, J N Demusz, M Rivero, T Martin, M Greenberg, C Tuozzolo, G S Engel, J H Kroll, J B Paul, and J G Anderson. A new cavity based absorption instrument for detection of water isotopologues in the upper troposphere and lower stratosphere. *Review of Scientific Instruments*, 80(4):693, 2009. ISSN 00346748. doi: 10.1063/1.3117349. URL http://scitation.aip.org/content/aip/journal/rsi/80/4?ver=pdfcov.

[90] Marie Šimečková, David Jacquemart, Laurence S. Rothman, Robert R. Gamache, and Aaron Goldman. Einstein A-coefficients and statistical weights for molecular absorption transitions in the HITRAN database. *Journal of Quantitative Spectroscopy and Radiative Transfer*, 98(1):130–155, mar 2006. ISSN 00224073. doi: 10.1016/j.jqsrt.2005.07.003.

[91] L. S. Rothman, C P Rinsland, A Goldman, S. T. Massie, D. P. Edwards, J. M. Flaud, A Perrin, C Camy-Peyret, V Dana, J. Y. Mandin, J Schroeder, A. McCann, R. R. Gamache, R B Wattson, K. Yoshino, K V Chance, K W Jucks, L R Brown, V. Nemtchinov, and P. Varanasi. The HITRAN molecular spectroscopic database and HAWKS (HITRAN Atmospheric Workstation): 1996 edition. *Journal of Quantitative Spectroscopy and Radiative Transfer*, 60(5):665–710, 1998. ISSN 00224073. doi: 10.1016/S0022-4073(98)00078-8. URL http://www.hitran.com.

[92] I. E. Gordon, L. S. Rothman, C. Hill, R. V. Kochanov, Y. Tan, P. F. Bernath, M. Birk, V. Boudon, A. Campargue, K. V. Chance, B. J. Drouin, J. M. Flaud, R. R. Gamache, J. T. Hodges, D. Jacquemart, V. I. Perevalov, A. Perrin, K. P. Shine, M. A.H. Smith, J. Tennyson, G. C. Toon, H. Tran, V. G. Tyuterev, A. Barbe, A. G. Császár, V. M. Devi, T. Furtenbacher, J. J. Harrison, J. M. Hartmann, A. Jolly, T. J. Johnson, T. Karman, I. Kleiner, A. A. Kyuberis, J. Loos, O. M. Lyulin, S. T. Massie, S. N. Mikhailenko,

N. Moazzen-Ahmadi, H. S.P. Müller, O. V. Naumenko, A. V. Nikitin, O. L. Polyansky, M. Rey, M. Rotger, S. W. Sharpe, K. Sung, E. Starikova, S. A. Tashkun, J. Vander Auwera, G. Wagner, J. Wilzewski, P. Wcisło, S. Yu, and E. J. Zak. The HITRAN2016 molecular spectroscopic database. *Journal of Quantitative Spectroscopy and Radiative Transfer*, 203:3–69, dec 2017. ISSN 00224073. doi: 10.1016/j.jqsrt.2017.06.038.

[93] Wolfgang Demtröder. *Experimentalphysik 3*. Springer-Lehrbuch. Springer-Verlag, Berlin/Heidelberg, 2016. ISBN 3-540-21473-9. doi: 10.1007/b139046. URL http://link.springer.com/10.1007/978-3-662-49094-5http://link.springer.com/10.1007/b139046.

[94] D. Lisak, A. Cygan, D. Bermejo, J. L. Domenech, J. T. Hodges, and H. Tran. Application of the Hartmann-Tran profile to analysis of H2O spectra. *Journal of Quantitative Spectroscopy and Radiative Transfer*, 164:221–230, jul 2015. ISSN 00224073. doi: 10.1016/j.jqsrt.2015.06.012.

[95] N. H. Ngo, D. Lisak, H. Tran, and J. M. Hartmann. An isolated line-shape model to go beyond the Voigt profile in spectroscopic databases and radiative transfer codes. *Journal of Quantitative Spectroscopy and Radiative Transfer*, 129:89–100, nov 2013. ISSN 00224073. doi: 10.1016/j.jqsrt.2013.05.034.

[96] R. V. Kochanov, I. E. Gordon, L. S. Rothman, P. Wcisło, C. Hill, and J. S. Wilzewski. HITRAN Application Programming Interface (HAPI): A comprehensive approach to working with spectroscopic data. *Journal of Quantitative Spectroscopy and Radiative Transfer*, 177:15–30, jul 2016. ISSN 00224073. doi: 10.1016/j.jqsrt.2016.03.005.

[97] M S Shumate, R T Menzies, J S Margolis, and L.-G. Rosengren. Water vapor absorption of carbon dioxide laser radiation. *Applied Optics*, 15(10):2480, 1976. ISSN 0003-6935. doi: 10.1364/ao.15.002480.

[98] Anikó Veres, Zoltán Bozóki, Árpád Mohácsi, Miklós Szakáll, and Gábor Szabó. External cavity diode laser based photoacoustic detection of CO 2 at 1.43 μm: The effect of molecular relaxation. In *Applied Spectroscopy*, volume 57, pages 900–905, 2003. doi: 10.1366/000370203322258841.

[99] G. Wysocki, A. A. Kosterev, and F. K. Tittel. Influence of molecular relaxation dynamics on quartz-enhanced photoacoustic detection of CO2 at λ =2 μm. *Applied Physics B: Lasers and Optics*, 85(2-3):301–306, 2006. ISSN 09462171. doi: 10.1007/s00340-006-2369-9.

[100] S. Schilt, J. P. Besson, and L. Thévenaz. Near-infrared laser photoacoustic detection of methane: The impact of molecular relaxation. *Applied Physics B: Lasers and Optics*, 82(2 SPEC. ISS.):319–329, 2006. ISSN 09462171. doi: 10.1007/s00340-005-2076-y.

[101] J. P. Besson, S. Schilt, and L. Thévenaz. Molecular relaxation effects in hydrogen chloride photoacoustic detection. *Applied Physics B: Lasers and Optics*, 90(2): 191–196, 2008. ISSN 09462171. doi: 10.1007/s00340-007-2821-5.

[102] W. P. Arnott, H. Moosmüller, P. J. Sheridan, J. A. Ogren, R. Raspet, W. V. Slaton, J. L. Hand, S. M. Kreidenweis, and J. L. Collett. Photoacoustic and filter-based ambient aerosol light absorption measurements: Instrument comparisons and the role

of relative humidity. *Journal of Geophysical Research: Atmospheres*, 108(1):4034, 2003. ISSN 01480227. doi: 10.1029/2002jd002165. URL http://doi.wiley.com/10.1029/2002JD002165.

[103] Justin M Langridge, Mathews S Richardson, Daniel A Lack, Charles A Brock, and Daniel M Murphy. Limitations of the photoacoustic technique for aerosol absorption measurement at high relative humidity. *Aerosol Science and Technology*, 47(11): 1163–1173, 2013. ISSN 02786826. doi: 10.1080/02786826.2013.827324.

[104] Vladimir P. Zharov and Vladilen S. Letokhov. *Laser Optoacoustic Spectroscopy*, volume 37 of *Springer Series in Optical Sciences*. Springer Berlin Heidelberg, Berlin, Heidelberg, 1986. ISBN 978-3-662-14479-4. doi: 10.1007/978-3-540-39492-1. URL http://link.springer.com/10.1007/978-3-540-39492-1.

[105] J Yardley. *Introduction to Molecular Energy Transfer*. Elsevier, 2012. ISBN 9780127685502. doi: 10.1016/B978-0-12-768550-2.X5001-4. URL https://books.google.at/books?hl=de{&}lr={&}id=FdsPPewZxCQC{&}oi=fnd{&}pg=PP1{&}dq=Introduction+to+Molecular+Energy+Transfer+von+James+Yardley{&}ots=whui1VDtH9{&}sig=p4Bx5oKSIi2KEpIZupNkaCm78nwhttps://linkinghub.elsevier.com/retrieve/pii/B9780127685502X50014.

[106] M. Lopez-Puertas and F. W. Taylor. *NON-LTE Radiative Transfer in the Atmosphere*. World Scientific, 2001. ISBN 981-02-4566-1.

[107] N Barreiro, A Peuriot, G Santiago, and V Slezak. Water-based enhancement of the resonant photoacoustic signal from methane-air samples excited at 3.3 μm. *Applied Physics B: Lasers and Optics*, 108(2):369–375, 2012. ISSN 09462171. doi: 10.1007/s00340-012-5018-5.

[108] Xukun Yin, Lei Dong, Huadan Zheng, Xiaoli Liu, Hongpeng Wu, Yanfang Yang, Weiguang Ma, Lei Zhang, Wangbao Yin, Liantuan Xiao, and Suotang Jia. Impact of humidity on quartz-enhanced photoacoustic spectroscopy based CO detection using a near-IR telecommunication diode laser. *Sensors (Switzerland)*, 16(2), jan 2016. ISSN 14248220. doi: 10.3390/s16020162.

[109] Peter Hess. *Photoacoustic, Photothermal and Photochemical Processes in Gases*, volume 46 of *Topics in Current Physics*. Springer Berlin Heidelberg, Berlin, Heidelberg, 1989. ISBN 978-3-642-83853-8. doi: 10.1007/978-3-642-83851-4. URL http://link.springer.com/10.1007/978-3-642-83851-4.

[110] Thomas F Hunter, David Rumbles, and Malcolm G Stock. Photophysical processes in the vapour-phase measured by the optic-acoustic effect. Part 1. - The model and apparatus for the study of radiationless processes. *Journal of the Chemical Society, Faraday Transactions 2: Molecular and Chemical Physics*, 70:1010–1021, 1974. ISSN 03009238. doi: 10.1039/F29747001010.

[111] E. L. Cussler. *Diffusion*. Cambridge University Press, Cambridge, 2009. ISBN 9780511805134. doi: 10.1017/CBO9780511805134. URL /core/books/diffusion/52ADCBD2746CA771AFF0CC572CE190A6http://ebooks.cambridge.org/ref/id/CBO9780511805134.

[112] Christopher C. Davis and Samuel J. Petuchowski. Phase fluctuation optical heterodyne spectroscopy of gases. *Applied Optics*, 20(14):2539, jul 1981. ISSN 0003-6935. doi: 10.1364/AO.20.002539. URL https://www.osapublishing.org/abstract.cfm?URI=ao-20-24-4151https://www.osapublishing.org/abstract.cfm?URI=ao-20-14-2539.

[113] Richard Raspet, William V. Slaton, W. Patrick Arnott, and Hans Moosmüller. Evaporation-condensation effects on resonant photoacoustics of volatile aerosols. *Journal of Atmospheric and Oceanic Technology*, 20(5):685–695, 2003. ISSN 07390572. doi: 10.1175/1520-0426(2003)20<685:ECEORP>2.0.CO;2.

[114] H. Moosmüller, R K Chakrabarty, and W P Arnott. Aerosol light absorption and its measurement: A review, 2009. ISSN 00224073.

[115] P. M. Morse, K. U. Ingard, and F. B. Stumpf. Theoretical Acoustics. *American Journal of Physics*, 38(5):666–667, 1970. ISSN 0002-9505. doi: 10.1119/1.1976432.

[116] Ronald L. Panton. *Incompressible Flow*. John Wiley & Sons, Inc., Hoboken, NJ, USA, jul 2013. ISBN 9781118713075. doi: 10.1002/9781118713075. URL http://doi.wiley.com/10.1002/9781118713075.

[117] H L Toor. The Energy Equation for Viscous Flow - Effect of Expansion on Temperature Profiles. *Industrial & Engineering Chemistry*, 48(5):922–926, may 1956. ISSN 0019-7866. doi: 10.1021/ie50557a035. URL https://pubs.acs.org/sharingguidelineshttps://pubs.acs.org/doi/abs/10.1021/ie50557a035.

[118] N H Johannesen and J P Hodgson. The physics of weak waves in gases. *Reports on Progress in Physics*, 42(4):629–676, apr 1979. ISSN 0034-4885. doi: 10.1088/0034-4885/42/4/002. URL https://iopscience.iop.org/article/10.1088/0034-4885/42/4/002.

[119] Jeffrey A Sell. *Photothermal Investigations of Solids and Fluids*. Elsevier, 1989. ISBN 9780126363456. doi: 10.1016/B978-0-12-636345-6.X5001-4. URL https://linkinghub.elsevier.com/retrieve/pii/B9780126363456X50014.

[120] David L. Huestis. Vibrational energy transfer and relaxation in O2 and H2O. *Journal of Physical Chemistry A*, 110(21):6638–6642, 2006. ISSN 10895639. doi: 10.1021/jp054889n.

[121] Ian H. Bell, Jorrit Wronski, Sylvain Quoilin, and Vincent Lemort. Pure and pseudo-pure fluid thermophysical property evaluation and the open-source thermophysical property library coolprop. *Industrial and Engineering Chemistry Research*, 53(6): 2498–2508, feb 2014. ISSN 08885885. doi: 10.1021/ie4033999.

[122] Anatoliy A Kosterev, Frank K Tittel, Dmitry V Serebryakov, Alexander L Malinovsky, and Igor V Morozov. Applications of quartz tuning forks in spectroscopic gas sensing. *Review of Scientific Instruments*, 76(4):1–9, 2005. ISSN 00346748. doi: 10.1063/1.1884196.

[123] Jaakko Saarela, Tapio Sorvajärvi, Toni Laurila, and Juha Toivonen. Phase-sensitive method for background-compensated photoacoustic detection of NO_2 using high-power LEDs. *Optics Express*, 19(S4):A725, 2011. ISSN 1094-4087. doi: 10.1364/oe.19.00a725.

[124] Stefan Weigl, Florian Feldmeier, Rudolf Bierl, and Frank Michael Matysik. Photoacoustic detection of acetone in N2 and synthetic air using a high power UV LED. *Sensors and Actuators, B: Chemical*, 316, 2020. ISSN 09254005. doi: 10.1016/j.snb.2020.128109.

[125] Stéphane Schilt and Luc Thévenaz. Wavelength modulation photoacoustic spectroscopy: Theoretical description and experimental results. *Infrared Physics and Technology*, 48 (2):154–162, 2006. ISSN 13504495. doi: 10.1016/j.infrared.2005.09.001.

[126] Peter Werle. A review of recent advances in semiconductor laser based gas monitors, feb 1998. ISSN 13861425.

[127] Metin Ilke, Ralf Bauer, and Michael Lengden. A Calibration-Free Methodology for Resonantly Enhanced Photoacoustic Spectroscopy Using Quantum Cascade Lasers. *IEEE Sensors Journal*, 20(18):10530–10538, sep 2020. ISSN 15581748. doi: 10.1109/JSEN.2020.2964279.

[128] András Miklós, Peter Hess, and Zoltán Bozóki. Application of acoustic resonators in photoacoustic trace gas analysis and metrology, 2001. ISSN 00346748.

[129] H Bruhns, A Marianovich, and · M Wolff. Photoacoustic Spectroscopy Using a MEMS Microphone with Inter-IC Sound Digital Output. *Int J Thermophys*, 35:2292–2301, 2014. doi: 10.1007/s10765-014-1690-5. URL https://link.springer.com/content/pdf/10.1007{%}2Fs10765-014-1690-5.pdf.

[130] Pietro Patimisco, Angelo Sampaolo, Lei Dong, Frank K Tittel, and Vincenzo Spagnolo. Recent advances in quartz enhanced photoacoustic sensing, 2018. ISSN 19319401.

[131] Pietro Patimisco, Gaetano Scamarcio, Frank Tittel, and Vincenzo Spagnolo. Quartz-Enhanced Photoacoustic Spectroscopy: A Review. *Sensors*, 14(4):6165–6206, mar 2014. ISSN 1424-8220. doi: 10.3390/s140406165. URL http://www.mdpi.com/1424-8220/14/4/6165/.

[132] Qiaoyun Wang, Jianwei Wang, Liang Li, and Qingxu Yu. An all-optical photoacoustic spectrometer for trace gas detection. *Sensors and Actuators B: Chemical*, 153(1): 214–218, mar 2011. ISSN 0925-4005. doi: 10.1016/J.SNB.2010.10.035. URL http://www.sciencedirect.com/science/article/pii/S0925400510008531.

[133] Jyrki Kauppinen, Klaus Wilcken, Ismo Kauppinen, and Vesa Koskinen. High sensitivity in gas analysis with photoacoustic detection. *Microchemical Journal*, 76(1-2):151–159, feb 2004. ISSN 0026265X. doi: 10.1016/j.microc.2003.11.007.

[134] A. Miklos, C. Brand, A. Winkler, and P. Hess. Effective noise reduction on pulsed laser excitation of modes in a high-Q photoacoustic resonator. *Journal De Physique. IV : JP*, 4(7):C7–781–C7–784, jul 1994. ISSN 11554339. doi: 10.1051/jp4:19947184. URL http://www.edpsciences.org/10.1051/jp4:19947184.

[135] Jean-Philippe Besson, Stéphane Schilt, and Luc Thévenaz. Sub-ppm multi-gas photoacoustic sensor. *Spectrochimica Acta Part A*, 63:899–904, 2006. doi: 10.1016/j.saa.2005.10.034. URL https://ac.els-cdn.com/S1386142505005822/1-s2.0-S1386142505005822-main.pdf?{_}tid=8c924cb8-1e06-44dd-9158-bed886fb0861{&}acdnat=1520583298{_}3178526a35baacbf866d5cb04274075f.

[136] T. Starecki. Windowless open photoacoustic helmholtz cell. *Acta Physica Polonica A*, 114(6 A):211–216, 2008. ISSN 05874246. doi: 10.12693/APhysPolA.114.A-211.

[137] Alain Glière, Justin Rouxel, Mickael Brun, Bertrand Parvitte, Virginie Zéninari, and Sergio Nicoletti. Challenges in the design and fabrication of a lab-on-a-chip photoacoustic gas sensor. *Sensors (Switzerland)*, 14(1):957–974, 2014. ISSN 14248220. doi: 10.3390/s140100957.

[138] N Barreiro, A Peuriot, G Santiago, · V Slezak, and V Slezak. Water-based enhancement of the resonant photoacoustic signal from methane–air samples excited at 3.3 µm. *Appl Phys B*, 108:369–375, 2012. doi: 10.1007/s00340-012-5018-5. URL https://link.springer.com/content/pdf/10.1007{%}2Fs00340-012-5018-5.pdf.

[139] A. L. Ulasevich, A. V. Gorelik, A. A. Kouzmouk, and V. S. Starovoitov. A miniaturized prototype of resonant banana-shaped photoacoustic cell for gas sensing. *Infrared Physics and Technology*, 60:174–182, 2013. ISSN 13504495. doi: 10.1016/j.infrared.2013.04.011. URL http://dx.doi.org/10.1016/j.infrared.2013.04.011.

[140] Miklós Szakáll, Zoltán Bozóki, Martina Kraemer, Nicole Spelten, Ottmar Moehler, and Ulrich Schurath. Evaluation of a photoacoustic detector for water vapor measurements under simulated tropospheric/lower stratospheric conditions. *Environmental Science and Technology*, 35(24):4881–4885, 2001. ISSN 0013936X. doi: 10.1021/es015564x.

[141] M. L. Mujal. Acoustics of ducts and mufflers with application to exhaust and ventilation system design., 1987.

[142] A. Miklos, P. Hess, A. Mohacsi, J. Sneider, S. Kamm, and S. Schaefer. Improved photoacoustic detector for monitoring polar molecules such as ammonia with a 1.53 μm DFB diode laser. In *Proceedings of the 10th international conference on photoacoustic and photothermal phenomena*, volume 126, pages 126–128. ASCE, 1999. ISBN 1563968053. doi: 10.1063/1.58187. URL http://aip.scitation.org/doi/abs/10.1063/1.58187.

[143] Andreas Schmohl, Andras Miklos, and Peter Hess. Effects of adsorption–desorption processes on the response time and accuracy of photoacoustic detection of ammonia. *Applied Optics*, 40(15):2571, 2007. ISSN 0003-6935. doi: 10.1364/ao.40.002571.

[144] Uno Ingard. *Notes on acoustic*. INFINITY SCIENCE PRESS LLC, 2008. ISBN 9781934015087.

[145] Gustavo Rubio, Wim De Roeck, J. Meyers, Martine Baelmans, Paul Sas, and Wim Desmet. Aeroacoustic Noise Source Mechanisms in Simple Expansion Chambers. *12th AIAA/CEAS Aeroacoustics Conference (27th AIAA Aeroacoustics Conference)*, (May):8–10, 2006. doi: 10.2514/6.2006-2700. URL http://arc.aiaa.org/doi/abs/10.2514/6.2006-2700.

[146] J Herault, F. Pétrélis, and S. Fauve. 1/fα Low Frequency Fluctuations in Turbulent Flows: Transitions with Heavy-Tailed Distributed Interevent Durations. *Journal of Statistical Physics*, 161(6):1379–1389, 2015. ISSN 00224715. doi: 10.1007/s10955-015-1408-5.

[147] Thomas Rück, Rudolf Bierl, and Frank-Michael Matysik. Low-cost photoacoustic NO2 trace gas monitoring at the pptV-level. *Sensors and Actuators A: Physical*, 263:501–509, aug 2017. ISSN 0924-4247. doi: 10.1016/J.SNA.2017.06.036. URL https://www.sciencedirect.com/science/article/pii/S0924424717304843{#}fig0010.

[148] Miklós Szakáll, János Csikós, Zoltán Bozóki, and Gábor Szabó. On the temperature dependent characteristics of a photoacoustic water vapor detector for airborne application. *Infrared Physics and Technology*, 51(2):113–121, oct 2007. ISSN 13504495. doi: 10.1016/j.infrared.2007.04.001.

[149] G. R. Lima, L. Mota, A. Miklós, J. Angster, Z. Dubovski, M. G. da Silva, M. Sthel, and H. Vargas. Sensitive harmonic detection of ammonia trace using a compact photoacoustic resonator at double-pass configuration and a wavelength-modulated distributed feedback diode laser. *Applied Physics B: Lasers and Optics*, 117(1): 333–341, 2014. ISSN 09462171. doi: 10.1007/s00340-014-5840-z.

[150] Christophe Risser, Bertrand Parvitte, Raphael Vallon, and Virginie Zeninari. Optimization and complete characterization of a photoacoustic gas detector. *Applied Physics B: Lasers and Optics*, 118(2):319–326, 2014. ISSN 09462171. doi: 10.1007/s00340-014-5988-6.

[151] Pramod Kulkarni, Paul A Baron, and Klaus Willeke. *Aerosol measurement: principles, techniques, and applications*. John Wiley \& Sons, third edition, 2011. ISBN 978-0-470-38741-2.

[152] T. Ajtai, Á. Filep, A. Varga, G. Motika, Z. Bozóki, and G. Szabó. Ozone concentration-monitoring photoacoustic system based on a frequency-quadrupled Nd:YAG laser. *Applied Physics B*, 101(1-2):403–409, oct 2010. ISSN 0946-2171. doi: 10.1007/s00340-010-4174-8. URL http://link.springer.com/10.1007/s00340-010-4174-8.

[153] Thomas Rück, Rudolf Bierl, and Frank Michael Matysik. NO2 trace gas monitoring in air using off-beam quartz enhanced photoacoustic spectroscopy (QEPAS) and interference studies towards CO2, H2O and acoustic noise. *Sensors and Actuators, B: Chemical*, 255:2462–2471, feb 2018. ISSN 09254005. doi: 10.1016/j.snb.2017.09.039. URL https://www.sciencedirect.com/science/article/pii/S0925400517317021{#}fig0055.

[154] A. J. Zuckerwar. *Handbook of the Speed of Sound in Real Gases*. Academic Press, Inc, 2002. ISBN 012782510X.

[155] M. Suchenek and T. Starecki. Pulse measurements of the frequency response of a photoacoustic cell. *International Journal of Thermophysics*, 32(4):893–900, apr 2011. ISSN 0195928X. doi: 10.1007/s10765-011-0955-5. URL http://link.springer.com/10.1007/s10765-011-0955-5.

[156] M. Szakáll, A. Varga, A. Pogány, Z. Bozóki, and G. Szabó. Novel resonance profiling and tracking method for photoacoustic measurements. *Applied Physics B: Lasers and Optics*, 94(4):691–698, 2009. ISSN 09462171. doi: 10.1007/s00340-009-3391-5.

[157] W B Jackson, N M Amer, A C Boccara, and D Fournier. Photothermal deflection spectroscopy and detection. Technical report, 1981. URL https://www.osapublishing.org/DirectPDFAccess/6986A62A-0706-7D17-EA2C7E328C21EA61{_}24810/ao-20-8-1333.pdf?da=1{&}id=24810{&}seq=0{&}mobile=no.

[158] Christopher C Davis. Trace detection in gases using phase fluctuation optical heterodyne spectroscopy. *Applied Physics Letters*, 36(7):515–518, 1980. ISSN 00036951. doi: 10.1063/1.91590. URL https://doi.org/10.1063/1.91590.

[159] Neil D Weston, Palanikumaran Sakthivel, and Pritish Mukherjee. Ultrasensitive spectral trace detection of individual molecular components in an atmospheric binary mixture. *Applied Optics*, 32(6):828, 1993. ISSN 0003-6935. doi: 10.1364/ao.32.000828.

[160] David L Mazzoni and Christopher C Davis. Trace detection of hydrazines by optical homodyne interferometry. *Applied Optics*, 30(7):756, 1991. ISSN 0003-6935. doi: 10.1364/ao.30.000756.

[161] H. Moosmüller and W. P. Arnott. Folded Jamin interferometer: a stable instrument for refractive-index measurements. *Optics Letters*, 21(6):438, 1996. ISSN 0146-9592. doi: 10.1364/ol.21.000438.

[162] A J Campillo, S J Petuchowski, Christopher C Davis, and H. B. Lin. Fabry-perot photothermal trace detection. *Applied Physics Letters*, 41(4):327–329, 1982. ISSN 00036951. doi: 10.1063/1.93524. URL https://doi.org/10.1063/1.93524.

[163] Johannes P Waclawek, Volker C Bauer, Harald Moser, and Bernhard Lendl. 2f-wavelength modulation Fabry-Perot photothermal interferometry. *Optics Express*, 24(25):28958, 2016. ISSN 1094-4087. doi: 10.1364/oe.24.028958. URL http://dx.doi.org/10.1364/OE.24.028957.

[164] Stefan Preisser, Wolfgang Rohringer, Mengyang Liu, Christian Kollmann, Stefan Zotter, Balthasar Fischer, and Wolfgang Drexler. All-optical highly sensitive akinetic sensor for ultrasound detection and photoacoustic imaging. *Biomedical Optics Express*, 7(10):4171, 2016. ISSN 2156-7085. doi: 10.1364/boe.7.004171. URL http://dx.doi.org/10.1364/BOE.7.004171.

[165] Wolfgang Demtröder. *Experimentalphysik 2*. Springer-Lehrbuch. Springer Berlin Heidelberg, Berlin, Heidelberg, 2009. ISBN 978-3-642-29943-8. doi: 10.1007/978-3-540-68219-6. URL http://link.springer.com/10.1007/978-3-642-29944-5.

[166] James C Owens. Optical Refractive Index of Air: Dependence on Pressure, Temperature and Composition. *Applied Optics*, 6(1):51, 1967. ISSN 0003-6935. doi: 10.1364/ao.6.000051.

[167] Philip E Ciddor. Refractive index of air: new equations for the visible and near infrared. *Applied Optics*, 35(9):1566, 1996. ISSN 0003-6935. doi: 10.1364/ao.35.001566.

[168] P Werle, R. Mücke, and F Slemr. The limits of signal averaging in atmospheric trace-gas monitoring by tunable diode-laser absorption spectroscopy (TDLAS). *Applied Physics B Photophysics and Laser Chemistry*, 57(2):131–139, 1993. ISSN 07217269. doi: 10.1007/BF00425997.

[169] Baudelet. *Laser Spectroscopy for Sensing*. Elsevier, 2014. ISBN 9780857092731. doi: 10.1016/c2013-0-16220-4. URL https://linkinghub.elsevier.com/retrieve/pii/C20130162204.

[170] Wim C. Van Etten. *Introduction to Random Signals and Noise*. John Wiley & Sons, Ltd, Chichester, UK, aug 2006. ISBN 0470024119. doi: 10.1002/0470024135. URL http://doi.wiley.com/10.1002/0470024135.

[171] Teemu Tomberg, Markku Vainio, Tuomas Hieta, and Lauri Halonen. Sub-parts-per-trillion level sensitivity in trace gas detection by cantilever-enhanced photo-acoustic spectroscopy. *Scientific Reports*, 8(1):1848, 2018. ISSN 20452322. doi: 10.1038/s41598-018-20087-9. URL www.nature.com/scientificreports/.

[172] P. Werle. Accuracy and precision of laser spectrometers for trace gas sensing in the presence of optical fringes and atmospheric turbulence. In *Applied Physics B: Lasers and Optics*, volume 102, pages 313–329. Springer, feb 2011. doi: 10.1007/s00340-010-4165-9. URL https://link.springer.com/article/10.1007/s00340-010-4165-9.

[173] Marilena Giglio, Pietro Patimisco, Angelo Sampaolo, Gaetano Scamarcio, Frank K. Tittel, and Vincenzo Spagnolo. Allan Deviation Plot as a Tool for Quartz-Enhanced Photoacoustic Sensors Noise Analysis. *IEEE Transactions on Ultrasonics, Ferroelectrics, and Frequency Control*, 63(4):555–560, apr 2016. ISSN 08853010. doi: 10.1109/TUFFC.2015.2495013. URL http://ieeexplore.ieee.org/document/7307704/.

[174] Johannes P Waclawek, Christian Kristament, Harald Moser, and Bernhard Lendl. Balanced-detection interferometric cavity-assisted photothermal spectroscopy. *Optics Express*, 27(9):12183, 2019. ISSN 1094-4087. doi: 10.1364/oe.27.012183. URL https://doi.org/10.1364/OE.27.012183.

[175] N Barreiro, A Peuriot, V Slezak, and G Santiago. Study of the dependence of the photoacoustic signal amplitude from methane on different collisional partners. *Vibrational Spectroscopy*, 68:158–161, 2013. ISSN 09242031. doi: 10.1016/j.vibspec.2013.07.005.

[176] T D Thornberry, A W Rollins, R S Gao, L A Watts, S J Ciciora, R. J. McLaughlin, and D W Fahey. A two-channel, tunable diode laser-based hygrometer for measurement of water vapor and cirrus cloud ice water content in the upper troposphere and lower stratosphere. *Atmospheric Measurement Techniques*, 8(1):211–224, 2015. ISSN 18678548. doi: 10.5194/amt-8-211-2015.

[177] Pieter R. Wiederhold. *Water Vapor Measurement: Methods and Instrumentation*. 1997. ISBN 0-8247-9319-6.

[178] Jan Wernecke and Roland Wernecke. *Industrial Moisture and Humidity Measurement: A Practical Guide*. Wiley-VCH, 2013. ISBN 978-3-527-31554-3.

[179] P J Brewer, B Gieseking, V F Ferracci, M Ward, J Van Wijk, A. M.H. Van Der Veen, A A Lima, C R Augusto, S H Oh, B M Kim, S Lee, L A Konopelko, Y Kustikov, T Shimosaka, B. NieDerhauser, M Guillevic, C Pascale, Z Zhou, D Wang, and S Hu. International comparison CCQM-K116: 10 μmol mol-1 water vapour in nitrogen. *Metrologia*, 55(1A), 2018. ISSN 16817575. doi: 10.1088/0026-1394/55/1A/08018.

[180] P. Mackrodt. A New Attempt on a Coulometric Trace Humidity Generator. *International Journal of Thermophysics*, 33(8-9):1520–1535, sep 2012. ISSN 0195928X. doi: 10.1007/s10765-012-1348-0. URL https://link.springer.com/article/10.1007/s10765-012-1348-0.

[181] A. W. Rollins, T. D. Thornberry, R. S. Gao, B. D. Hall, and D. W. Fahey. Catalytic oxidation of H 2 on platinum: A robust method for generating low mixing ratio H 2O standards. *Atmospheric Measurement Techniques*, 4(10):2059–2064, oct 2011. ISSN 18671381. doi: 10.5194/amt-4-2059-2011. URL https://amt.copernicus.org/articles/4/2059/2011/.

[182] A. Saul and W. Wagner. International Equations for the Saturation Properties of Ordinary Water Substance. *Journal of Physical and Chemical Reference Data*, 16(4): 893–901, 1987. ISSN 15297845. doi: 10.1063/1.555787.

[183] Wolfgang Wagner and A. Pruss. International Equations for the Saturation Properties of Ordinary Water Substance. Revised According to the International Temperature Scale of 1990. Addendum to J. Phys. Chem. Ref. Data 16, 893 (1987). *Journal of Physical and Chemical Reference Data*, 22(3):783–787, may 1993. ISSN 15297845. doi: 10.1063/1.555926. URL http://aip.scitation.org/doi/10.1063/1.555926.

[184] Wolfgang Wagner and A. Pruß. The IAPWS Formulation 1995 for the Thermodynamic Properties of Ordinary Water Substance for General and Scientific Use. *Journal of Physical and Chemical Reference Data*, 31 (2):387–535, jun 2002. ISSN 0047-2689. doi: 10.1063/1.1461829. URL http://dx.doi.org/10.1063/1.1461829http://aip.scitation.org/toc/jpr/31/2http://aip.scitation.org/doi/10.1063/1.555926http://aip.scitation.org/doi/10.1063/1.1461829.

[185] Arnold Wexler. VAPOR PRESSURE FORMULATION FOR ICE. *J Res Natl Bur Stand Sect A Phys Chem*, 81 A(1):5–20, 1977. ISSN 0022-4332. doi: 10.6028/jres.081A.003.

[186] C. W. Meyer, W. W. Miller, D. C. Ripple, and G. E. Scace. Design and Performance of the New NIST Hybrid Humidity Generator. *NCSLI Measure*, 4(2):28–36, jun 2009. ISSN 1931-5775. doi: 10.1080/19315775.2009.11721470. URL https://ws680.nist.gov/publication/get{_}pdf.cfm?pub{_}id=832270https://www.tandfonline.com/doi/full/10.1080/19315775.2009.11721470.

[187] Lewis Greenspan. Functional equations for the enhancement factors for CO2-free moist air. *Journal of Research of the National Bureau of Standards Section A: Physics and Chemistry*, 80A(1):41, 1976. ISSN 0022-4332. doi: 10.6028/jres.080a.007.

[188] C W Meyer, J T Hodges, P H Huang, W W Miller, D C Ripple, G E Scace, Carlos M Gutierrez, and Patrick Gallagher. Calibration of Hygrometers with the Hybrid Humidity Generator. *NIST Special Publication*, 250(83), 2008. doi: 10.6028/NIST.SP.250-83.

[189] P. J. Brewer, B. A. Goody, T. Gillam, R. J.C. Brown, and M. J.T. Milton. High-accuracy stable gas flow dilution using an internally calibrated network of critical flow orifices. *Measurement Science and Technology*, 21(11):115902, oct 2010. ISSN 13616501. doi: 10.1088/0957-0233/21/11/115902. URL https://iopscience.iop.org/article/10.1088/0957-0233/21/11/115902https://iopscience.iop.org/article/10.1088/0957-0233/21/11/115902/meta.

[190] Philipp Breitegger and Alexander Bergmann. A Precise Gas Dilutor Based on Binary Weighted Critical Flows to Create NO2 Concentrations. *Proceedings*, 2(13):998, dec 2018. ISSN 2504-3900. doi: 10.3390/proceedings2130998.

[191] Joint Committee for Guides in Metrology. Evaluation of measurement data — Guide to the expression of uncertainty in measurement, 2008.

[192] Randall F Barron. *Industrial noise control $ and sense*. Marcel Dekker, Inc., 2002.

[193] Anatoliy A Kosterev, Frank K Tittel, Trevor S Knittel, Alan Cowie, and James D Tate. Trace Humidity Sensor based on Quartz-Enhanced Photoacoustic Spectroscopy. *Lacsea*, pages Paper TuA2 1–3, 2006. ISSN 21622701.

[194] Julien M Rey and Markus W Sigrist. New differential mode excitation photoacoustic scheme for near-infrared water vapour sensing. *Sensors and Actuators, B: Chemical*, 135(1):161–165, 2008. ISSN 09254005. doi: 10.1016/j.snb.2008.08.002.

[195] Zoltán Bozóki, János Sneider, Zoltán Gingl, Árpád Mohácsi, Miklós Szakáll, Zsolt Bor, and Gábor Szabó. A high-sensitivity, near-infrared tunable-diode-laser-based photoacoustic water-vapour-detection system for automated operation. *Measurement Science and Technology*, 10(11):999–1003, nov 1999. ISSN 09570233. doi: 10.1088/0957-0233/10/11/304.

[196] Miklós Szakáll, Árpád Mohácsi, Dávid Tátrai, Anna Szabó, Helga Huszár, Tibor Ajtai, Gábor Szabó, and Zoltán Bozóki. Twenty Years of Airborne Water Vapor and Total Water Measurements of a Diode Laser Based Photoacoustic Instruments. *Frontiers in Physics*, 8:384, oct 2020. ISSN 2296-424X. doi: 10.3389/fphy.2020.00384. URL https://www.frontiersin.org/article/10.3389/fphy.2020.00384/full.

[197] Xukun Yin, Lei Dong, Huadan Zheng, Xiaoli Liu, Hongpeng Wu, Yanfang Yang, Weiguang Ma, Lei Zhang, Wangbao Yin, Liantuan Xiao, and Suotang Jia. Impact of humidity on quartz-enhanced photoacoustic spectroscopy based CO detection using a near-IR telecommunication diode laser. *Sensors (Switzerland)*, 16(2), 2016. ISSN 14248220. doi: 10.3390/s16020162.

[198] H E Bass and F D Shields. Vibrational relaxation and sound absorption in 02/H20 mixtures. *Journal of the Acoustical Society of America*, 56(3):856–859, 1974. ISSN NA. doi: 10.1121/1.1903337.

[199] Henry E Bass. Absorption of sound by air: High temperature predictions. *Journal of the Acoustical Society of America*, 69(1):124–138, 1981. ISSN NA. doi: 10.1121/1.385356.

[200] R. O. Manuilova, A. G. Feofilov, A. A. Kutepov, and V. A. Yankovsky. Effect of updated relaxation rate constants on the H2O vibrational level populations and ro-vibrational spectra in the mesosphere and lower thermosphere. *Advances in Space Research*, 56 (9):1806–1814, 2015. ISSN 18791948. doi: 10.1016/j.asr.2014.12.002.

[201] A. G. Feofilov, A. A. Kutepov, W. D. Pesnell, R. A. Goldberg, B. T. Marshall, L. L. Gordley, M. García-Comas, M. López-Puertas, R. O. Manuilova, V. A. Yankovsky, S. V. Petelina, and J. M. Russell. Daytime SABER/TIMED observations of water vapor in the mesosphere: Retrieval approach and first results. *Atmospheric Chemistry and Physics*, 9(21):8139–8158, nov 2009. ISSN 16807324. doi: 10.5194/acp-9-8139-2009.

[202] H. E. Bass, Roy G. Keeton, and David Williams. Vibrational and rotational relaxation in mixtures of water vapor and oxygen. *The Journal of the Acoustical Society of America*, 60(1):74–77, 1976. ISSN 0001-4966. doi: 10.1121/1.381050.

[203] Craig R Davison, J. Walter Strapp, Lyle Lilie, Thomas P Ratvasky, and Christopher Dumont. Isokinetic TWC evaporator probe: Calculations and systemic uncertainty analysis. In *8th AIAA Atmospheric and Space Environments Conference*, 2016. ISBN 9781624104336. doi: 10.2514/6.2016-4060.

[204] David M. Orchard. AIR6341 - SLD capabilities of icing wind tunnels (Work in progress). Technical report, SAE International, 2015. URL https://www.sae.org/works/documentHome.do?comtID=TEAAC9C{&}docID=AIR6341{&}inputPage=wIpSdOcDeTaIlS.

[205] Judith F Van Zante, Thomas P Ratvasky, Timothy J Bencic, Clark C Challis, Emily N Timko, and Mark R Woike. Update on the nasa glenn propulsion systems lab icing and ice crystal cloud characterization (2017). In *2018 Atmospheric and Space Environments Conference*, pages 77–83, 2018. ISBN 9781624105586. doi: 10.2514/6.2018-3969.

[206] Juan H. Agui, Peter Struk, and Tadas Bartkus. Total Temperature Measurements in Icing Cloud Flows Using a Rearward Facing Probe. *SAE Technical Papers*, 2019-June (June):1–11, 2019. ISSN 01487191. doi: 10.4271/2019-01-1923.

[207] Thomas Ratvasky, Steven Harrah, J Walter Strapp, Lyle Lilie, Fred Proctor, Justin Strickland, Patricia Hunt, Kristopher Bedka, Glenn Diskin, John B Nowak, T Paul Bui, Aaron Bansemer, and Christopher Dumont. Summary of the High Ice Water Content (HIWC) RADAR Flight Campaigns. In *SAE Technical Papers*, volume 2019-June, 2019. doi: 10.4271/2019-01-2027. URL https://ntrs.nasa.gov/search.jsp?R=20190026988.

[208] Huadan Zheng, Lei Dong, Xukun Yin, Xiaoli Liu, Hongpeng Wu, Lei Zhang, Weiguang Ma, Wangbao Yin, and Suotang Jia. Ppb-level QEPAS NO2 sensor by use of electrical modulation cancellation method with a high power blue LED. *Sensors and Actuators, B: Chemical*, 208(2):173–179, 2015. ISSN 09254005. doi: 10.1016/j.snb.2014.11.015. URL http://dx.doi.org/10.1016/j.snb.2014.11.015.

[209] Jari Peltola, Markku Vainio, Tuomas Hieta, Juho Uotila, Sauli Sinisalo, Mikael Siltanen, and Lauri Halonen. High sensitivity trace gas detection by cantilever-enhanced photoacoustic spectroscopy using a mid-infrared continuous-wave optical parametric oscillator. *Optics Express*, 21(8):2103–2109, 2013. ISSN 1094-4087. doi: 10.1364/OE.21.010240. URL https://www.osapublishing.org/oe/abstract.cfm?uri=oe-21-8-10240.

APPENDIX A

PUBLICATIONS, CONFERENCE AND OTHER SCIENTIFIC CONTRIBUTIONS

Below, peer reviewed publications, conference contributions, as well as other scientific contributions generated and co-authored within the scope of this thesis are listed.

Journal Publications

1. Lang, B., Breitegger, P., Brunnhofer, G. et al.: Molecular relaxation effects on vibrational water vapor photoacoustic spectroscopy in air. Appl. Phys. B 126, 64, doi.org/10.1007/s00340-020-7409-3, 2020.

2. Lang, B., Breitfuss, W., Schweighart, S. et al.: Photoacoustic hygrometer for icing wind tunnel water content measurement: Design, analysis and intercomparison, Atmos. Meas. Tech. Discuss., doi.org/10.5194/amt-2020-295, in review, 2020.

3. Breitegger, P., Lang, B. and Bergmann, A.: Intensity Modulated Photothermal Measurements of NO2 with a Compact Fiber-Coupled Fabry–Pérot Interferometer, Sensors, 19(15), 3341, doi.org/10.3390/s19153341, 2019.

Conference Proceedings

1. Lang, B., Bergmann, A.: Design framework for a gas sensor based on an open photoacoustic resonator, 2016 IEEE SENSORS, Orlando, FL, pp. 1-3, doi: 10.1109/ICSENS.2016.7808433, 2016.

Oral Presentations

1. Lang, B., Bergmann, A., Hassler, W.: A photoacoustic cell for high flow rate environments, 19th International Conference on Photoacoustic and Photothermal Phenomena, 2017.
2. Lang, B., Bergmann, A., Hassler, W.: A resonant photoacoustic cell for high flow rate gas concentration measurement, EUROSENSORS 32, 2018.

Poster Presentations

1. Lang, B., Bergmann, A.: Design framework for a gas sensor based on an open photoacoustic resonator, 2016 IEEE SENSORS, Orlando, FL, pp. 1-3, doi: 10.1109/ICSENS.2016.7808433, 2016.

Contributions to Granted Research Proposals

1. AquaPhase - Infrared spectroscopic cloud water phase determination in icing conditions, FFG TAKEOFF, 2018.
2. JOICE - Joint Austrian In-flight Icing Research Venture 2020+, FFG TAKEOFF, 2020.

Applied Patents

1. Lang, B., Bergmann, A.: WO2019014697 - PHOTOACOUSTIC MEASURING DEVICE HAVING RESONATOR ELEMENTS, 2019.